Technische Universität München
TUM School of Natural Sciences

Characterization of Silicon Anodes for Lithium-Ion Batteries

Maximilian Simon Graf

Vollständiger Abdruck der von der TUM School of Natural Sciences der Technischen Universität München zur Erlangung eines

Doktors der Naturwissenschaften (Dr. rer. nat.)

genehmigten Dissertation.

Vorsitz: Prof. Dr. Marc-Georg Willinger

Prüfende der Dissertation:

1. Prof. Dr. Hubert A. Gasteiger
2. Prof. Brett L. Lucht

Die Dissertation wurde am 31.10.2024 bei der Technischen Universität München eingereicht und durch die TUM School of Natural Sciences am 09.12.2024 angenommen.

Abstract

Silicon as an anode-active material for lithium-ion batteries (LIBs) has been the focus of research for a long time. Until now, commercialization has been challenging due to the drastic volume changes upon (de-)lithiation. In the last few years, new silicon material concepts have been employed, some of which have recently reached mass production and can be found in their first applications on the market. This work investigates microscale silicon particles, which can be produced cost-effectively and are available on a large scale. A partial lithiation strategy achieves reasonable cycling stability with such a material concept, whereby the crystalline silicon particle is only amorphized to a certain extent, thus maintaining the integrity of the particle during cycling.

The investigation of the amorphization process with respect to the lithiation cutoff potential was analyzed by in-situ X-ray diffraction (XRD) in the first part of this thesis. It enabled an XRD-based quantification of the amorphous phase fraction over the course of extended charge/discharge cycling.

The second part of this thesis focuses on the mechanism of lithium nitrate ($LiNO_3$) as an electrolyte additive in carbonate-based electrolyte systems for silicon-based anodes. The reduction and oxidation reactions are studied on carbon electrodes using on-line electrochemical mass spectrometry (OEMS) and X-ray photoelectron spectroscopy (XPS). In addition, the cycling stability is examined in coin full-cells using silicon-based anodes and NCM622 cathodes.

With its high specific capacity of 3579 mAh g^{-1}_{Si}, silicon allows for high areal capacities and thin electrode coatings, making it a promising choice for fast-charging applications. The final part of this thesis provides a practical comparison between silicon-based anodes and

graphite anodes in terms of their temperature-dependent kinetic charge transfer resistance and ion transport resistance using impedance spectroscopy.

Kurzfassung

Silicium als Aktivmaterial für Anoden in Lithium-Ionen Batterien ist schon seit längerem im Fokus der Forschung. Bisher gestaltete sich die Kommerzialisierung als sehr herausfordernd, da Silicium über die (De-)Lithiierung eine große Volumenänderung aufweist. In den letzten Jahren wurden neue Materialkonzepte entwickelt, von denen es zuletzt einige in die Serienproduktion geschafft haben und in ersten Anwendungen auf dem Markt zu finden sind. In dieser Arbeit werden mikroskalige Siliciumpartikel untersucht, welche kostengünstig hergestellt werden können und in großem Maßstab verfügbar sind. Um mit einem solchem Materialkonzept eine angemessene Zyklenstabilität erreichen zu können, wird der Ansatz einer partiellen Lithiierung verfolgt. Dabei werden die kristallinen Siliciumpartikel nur bis zu einem gewissen Grad amorphisiert, um so die Integrität der Partikel über den Zyklenverlauf zu erhalten. Im ersten Teil dieser Arbeit, wird der Amorphisierungsprozess im Hinblick auf die Lithiierungs-Abschaltspannung mittels in-situ Röntgendiffraktometrie (XRD) untersucht und der Anteil der amorphen Phase quantitativ über XRD bestimmt.

Der zweite Teil der Arbeit befasst sich mit dem Mechanismus von Lithiumnitrat ($LiNO_3$) als Additiv in karbonatbasierten Elektrolytsystemen für siliciumhaltige Anoden. Reduktions- und Oxidationsreaktionen wurden an Kohlenstoffelektroden mittels elektrochemischer Online-Massenspektrometrie (OEMS) und Röntgenphotonenelektronenspektroskopie (XPS) untersucht. Zusätzlich wurde die Zyklenstabilität in Vollzellen im Knopfzellformat mit siliciumhaltigen Anoden und NCM622 Kathoden getestet.

Mit seiner hohen spezifischen Kapazität von 3579 mAh $g^{-1}{}_{Si}$, ermöglicht Silicium hohe Flächenkapazitäten bei Elektrodenbeschichtungen mit gleichzeitig geringen Schichtdicken

für Schnelladeanwendungen. Im letzten Teil dieser Arbeit werden Siliciumanoden mit Graphitanoden hinsichtlich ihres temperaturabhängigen kinetischen Ladungsübergangswiderstands und ihres ionischen Transportwiderstands mittels Impedanzspektroskopie gemessen.

List of Acronyms

CE	Coulombic efficiency
CPE	Constant phase element
CVD	Chemical vapor deposition
DEC	Diethylene carbonate
DMC	Dimethyl carbonate
EC	Ethylene carbonate
EIS	Electrochemical impedance spectroscopy
EUCAR	European Council for Automotive R&D
EV	Electric vehicle
FEC	Fluoro ethylene carbonate
GEIS	Galvanostatic electrochemical impedance spectroscopy
ICE	Internal combustion engine
LEDC	Lithium ethylene dicarbonate
LIB	Lithium-ion-battery
$LMPO_4$	Transition metal phosphate ($LiMPO_4$ with M = transition metal)
LTO	Lithium titanium oxide
NCM	Lithium nickel cobalt manganese oxide ($LiMO_2$ with M = Ni, Co, Mn)
OCV	Open circuit voltage
OEMS	On-Line electrochemical mass spectrometry
PEIS	Potentiostatic electrochemical impedance spectroscopy
ROLi	Li-alkoxides

SEI	Solid electrolyte interface
SiNW	Silicon nanowire
SiO_x	Silicon oxide
SOC	State of charge
TCHZ	Thompson-Cox-Hastings pseudo Voigt function
TEM	Transmission electron microscopy
TLM	Transmission line model
VC	Vinylene carbonate
XRD	X-ray powder diffraction
XPS	X-ray photoelectron spectroscopy

Contents

1.0 Introduction

In recent years, there has been a growing focus on the electrification of the mobility sector. In 2021, several countries, including the European Union and the United States, announced an internal combustion engine (ICE) sales ban by 2035, with the goal of a market share by electric vehicles (EVs) of at least 50% by 2030.[1] Such government regulations accelerate the transition towards more sustainable mobility. The automotive sector plays a vital role as the driving force for developing new battery technologies and ramping up production capacities. 90% of the European Union's estimated battery cell demand of 874 GWh in 2030 is for passenger cars and commercial vehicles and only 10% for other applications such as consumer electronics. Compared to consumer electronics, automotive applications require more stringent demands on battery technology with regard to safety, energy density, and fast charging capability. Target requirements by the European Council for Automotive R&D (EUCAR) for 2030 on the cell level are a specific energy density of 450 Wh kg^{-1}, a charging rate from 0%-80% SOC at a rate of 3.5C (i.e., a charging time of <20 min), and a cost of 70 € kWh^{-1}. Besides, calendaric lifetime, safety, and operating temperature are important parameters. Current commercial LiBs based on graphite and NCM cathode cell chemistry have a specific energy density of ~250 Wh kg^{-1} at costs of ~150 € kWh^{-1}.[2,3]

To achieve these challenging goals, it is necessary to develop new anode and cathode material concepts as well as novel cell technologies. Currently, the most widely used cathode active materials are nickel-rich NCM ($LiMO_2$, with M = Ni, Co, and Mn) and NCA ($LiMO_2$ with M = Ni, Co, Al) due to their high specific capacities and high discharge potentials versus Li^+/Li.

Carbonaceous materials, such as natural and artificial graphites, are commonly used as state-of-the-art materials on the anode side. To accommodate high-capacity cathode active materials with increased amounts of cyclable lithium, the graphite anode electrode thickness has to be increased. However, thick anodes can become a bottleneck for high-rate applications and may lead to severe cell failures upon fast-charging due to lithium plating. Therefore, alternative materials with higher specific capacities are necessary to enable thin anode designs that are particularly critical for fast charging. Silicon, the second most abundant element in the Earth's crust, exhibits a ten times higher theoretical specific capacity (3579 mAh g_{Si}^{-1}) as compared to commonly used graphite (372 mAh g_C^{-1}).[4,5,6]

Silicon is one of the most promising candidates among alternative materials, due to its low operating voltage (0.1-0.5 V vs. Li^+/Li).[7,8] However, the practical application of pure silicon is still hindered by several challenges originating from its intrinsic material properties. The volume expansion of ~280% upon (de-)alloying with lithium results in particle cracking and excessive electrolyte consumption due to the rupture of the solid electrolyte interphase (SEI).[9,10,11] This cracking, in turn, leads to the electrode's disintegration, resulting in the electrical isolation of individual silicon particles. As a result, low coulombic efficiencies, irreversible lithium loss, and increased internal resistances generally cause an inferior cycling performance and a short lifetime of the lithium-ion battery cells with silicon anodes.[4]

To reduce the effects described above at the electrode level, researchers have investigated the possibility of enhancing the anode's performance by combining silicon with graphite. This can be achieved by blending the two materials during electrode fabrication or designing a single Si-graphite composite (Si-Gr) material.[8,12,13] Although there are potential benefits, it is still a challenge to incorporate high amounts of Si (> 30%). Currently, only a small mass fraction of silicon (<5%) - often incorporated in the form of silicon oxide (SiO_x, 1700 mAh g^{-1}) - is used in commercial cells to increase the energy density.[6,14]

Possible strategies to increase the amount of silicon in the future include novel structural designs of the silicon active material, electrolyte additives, and silicon prelithiation. However, the latter only compensates for the loss of lithium and does not affect the effects of the volume expansion itself.

1.1 Lithium-ion batteries

In 2019, John B. Goodenough, M. Stanley Whittingham, and Akira Yoshino were awarded the Nobel Prize in Chemistry for their work on developing lithium-ion batteries, first commercialized by Sony in 1991.[15,16] In the 1970s, Whittingham discovered that intercalating lithium ions in titanium disulphide resulted in a material with surprisingly high energy density, operating at 2 V vs. Li^+/Li.[17] However, commercialization of this technology was hindered by the poor safety of the lithium metal electrode, resulting in fires and explosions through dendrite formation causing short circuits. In 1980, John Goodenough published the discovery of a new cathode active material operating at 4 V vs. Li^+/Li, which offered almost twice the energy density as Whittingham's titanium disulphide: lithium cobalt oxide, a transition metal oxide, allowed for a high operating potential at high energy density without structural collapse when lithium-ions were de-intercalated. The consumer electronics industry drove the development of the lithium-ion battery at that time, as oil prices were low and interest in alternatives to combustion engines had declined. It was essential to commercialize rechargeable and lightweight batteries to facilitate using portable and compact electronic devices, such as video cameras, music players, telephones, and computers. Akira Yoshino, who worked for the Asahi Kasei Corporation, aimed to develop such a battery. He combined Goodenough's lithium cobalt oxide cathode active material as positive electrode with petroleum coke as the negative electrode. This resulted in a stable and safe battery system with a high energy density operating up to 4 V vs. Li^+/Li.[18] Lithium-ion batteries have not undergone significant changes since their inception, except for using alternative materials as active components for the cathode and anode.

Currently, state-of-the-art cathode active materials fall into two categories: transition metal oxides ($LiMO_2$, where M represents the transition metal) or phosphates ($LiMPO_4$, where M represents the transition metal). Anode active materials consist of natural or synthetic graphite (C_6) or, more recently, a blend of graphite and silicon (Si) or silicon oxide (SiO_x). The cathode and anode active materials are integrated into a porous electrode matrix. This matrix includes conductive additives, such as carbon particles or fibers, to enhance the electrical conductivity within the electrode. A polymeric binder is also included to ensure the electrode's mechanical stability and flexibility. The electrode materials are coated onto metal foils that act as current collectors, conducting electrons to and from the reaction site and the external circuit (see **Figure 1**). To account for the different operating potentials of the electrodes, cathodes (positive electrodes) are coated onto aluminum foil, while anodes (negative electrodes) are coated onto copper foil. A porous polymer separator within the battery prevents physical contact between the cathode and anode, thus avoiding an electrical short circuit. The pores of the electrodes and of the porous separator are filled with electrolyte, comprising lithium salts dissolved in alkyl-carbonate-based solvents and often including additional electrolyte additives.

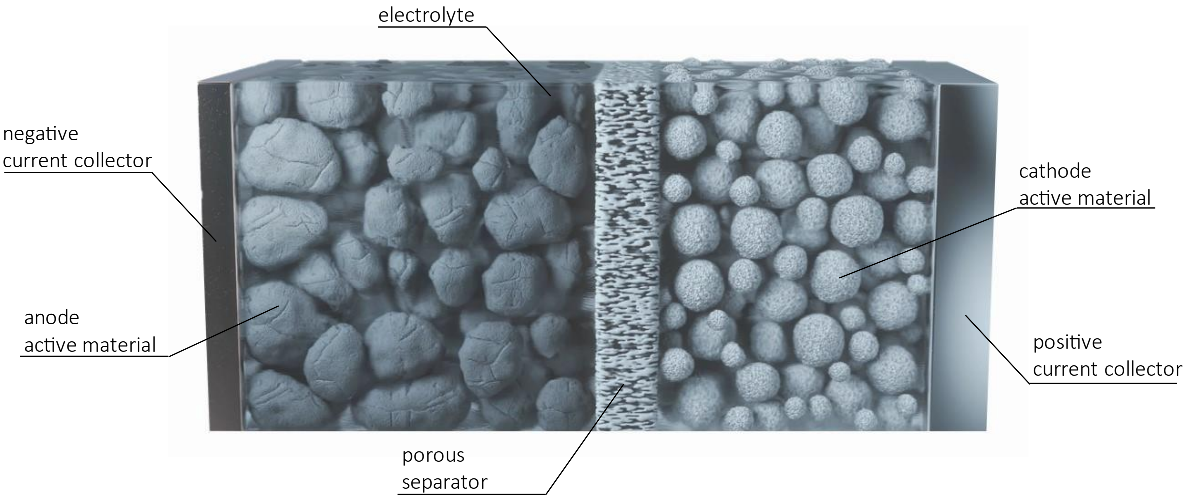

Figure 1 Schematic view of the main components of a lithium-ion battery, consisting of (from left to right): the negative copper current collector, the negative electrode with anode active material, the porous separator, the positive electrode with cathode active material, and the positive aluminum current collector. The void space of the porous electrodes and the separator is filled with electrolyte. Reprinted with permission from Jordan Giesige.[19]

Upon charging a secondary (i.e., a rechargeable) battery, lithium ions (Li^+) are de-intercalated from the positive cathode and intercalated into the negative anode. This process requires external energy; thus, the Gibbs free energy for this reaction is $\Delta G > 0$. Hence, upon discharging the battery, energy is released when Li^+ ions are deintercalated from the anode and intercalated into the positive cathode (i.e., for this reaction direction $\Delta G < 0$). The half-cell reactions for the cathode (equation 1.1) and the anode (equation 1.2) for $LiMO_2$ and C_6 can be given as follows:

$$\mathrm{LiMO_2} \rightleftharpoons \mathrm{Li_{1\text{-}x}MO_2} + \mathrm{x\,Li^+} + \mathrm{x\,e^-} \tag{1.1}$$

$$\mathrm{C_6} + \mathrm{x\,Li^+} + \mathrm{x\,e^-} \rightleftharpoons \mathrm{Li_xC_6} \tag{1.2}$$

Here, x ranges between 0 and 1. The combination of both reactions then gives the reaction of the full cell, whereby the charging reaction takes place from left to right and the discharge reaction from right to left accordingly.

$$\mathrm{LiMO_2 + C_6 \rightleftharpoons Li_{1\text{-}x}MO_2 + Li_xC_6} \qquad 1.3$$

The specific capacity of an active material, i.e., the amount of lithium that can be stored in a certain mass of material, is defined as:

$$q = \frac{Q}{m} = \frac{z * F}{M} \qquad 1.4$$

Here, *Q* is the total exchanged capacity, *m* is the active material mass, *z* is the valency of the active species (z = 1 for Li^+), F is the Faraday constant of 96,485 As mol^{-1}, and *M* is the molar mass of the active material. For anode active materials like graphite and silicon, commonly the molecular mass of the delithiated anode active material is used.

Since electrode potentials cannot be measured directly but always need to be measured against a reference electrode, potentials are commonly referenced to the redox potential of lithium (Li^+/Li). Thereby, 0 V vs. Li^+/Li corresponds to -3.04 V against the standard hydrogen electrode (SHE). The cell voltage can be calculated by the difference of the potentials of the two electrodes.

$$E_{\mathrm{cell}} = E_{\mathrm{cathode}} - E_{\mathrm{anode}} \qquad 1.5$$

Without any external current flowing, this voltage equals the cell's so-called open circuit voltage (OCV). Upon charge or discharge of the cell, each electrode follows a distinct profile of the electrode potential versus the degree of (de-)lithiation and the difference in electrode potentials in the absence of current flow corresponds to the open circuit voltage (OCV) of the cell. Overpotentials developed by kinetic, ohmic, or mass-transport-related resistances can also affect the cell voltage. The gravimetric energy density *w* (Wh kg^{-1}) of a cell or electrode is defined by the potential integrated over the capacity. It is typically referenced to either the mass of the electrode, the cell, or the battery module.

$$w = \frac{W}{m} = \int_0^q E(q')\,dq' = q * \bar{E} \qquad 1.6$$

With $\bar{E}$ being the charge averaged potential, the energy density can simply be compressed by the product of $\bar{E}$ and the specific capacity q of the cell or electrode.

For an ideal cell, the flow of Li^+ ions from the cathode to the anode, i.e., the charge capacity Q_{charge}, equals the flow of Li^+ ions back to the cathode upon discharge, i.e., the discharge capacity $Q_{discharge}$. The ratio of the discharge capacity over charge capacity is called coulombic efficiency (CE).

$$CE = \frac{Q_{\mathrm{discharge}}}{Q_{\mathrm{charge}}} \qquad 1.7$$

However, chemical or electrochemical side reactions are ubiquitous in a real cell. Accordingly, the CE is less than 100%. Generally, the number of Li^+ ions exchanged during charge and discharge equals that of the electrons, determining the reversible capacity during cycling. There are a few exceptions where irreversible parasitic reactions can contribute with additional electrons to this calculation. In the case where these parasitic reactions and other nonlinear degradation phenomena can be neglected. The status of a battery's life, commonly described by capacity retention, can be calculated by the CE for a specific number of cycles n.

$$\mathrm{Capacity\ retention}=(\mathrm{CE})^{\mathrm{n}} \qquad 1.8$$

This would predict that in order to reach 1000 cycles with a capacity retention of 90%, the coulombic efficiency must be at least 99.99%.[20] The charge and discharge current is usually normalized to the battery's capacity and is expressed as C-rate. The C-rate is typically given in units of 1 h^{-1} and corresponds to the current to charge or discharge the cell entirely in a given time. If a cell is charged within 5 hours, the applied current would correspond to a C-rate of C/5 and for a 10 Ah cell would correspond to a nominal current of 2 A.

1.2 Silicon as anode active material

The reaction mechanisms of anode active materials with the charge carrier in lithium-ion battery systems can be classified into three categories, as depicted in **Figure 2**. These categories include a) intercalation materials, e.g., graphite and lithium titanium oxide (LTO), b) single-phase conversion materials or alloy materials such as silicon or lithium, and c) multiple-phase conversion materials often described as conversion materials, including a wide range of transition metal -oxides,-phosphides and –nitrides.[21] Intercalation materials have the advantage of minimal structural changes during (de-) lithiation, limiting the volume expansion to usually below 25%.[22,23] Additionally, intercalation materials exhibit the advantage of having an only small difference between the lithiation and delithiation potential i.e., they have no significant voltage hysteresis. The major drawback of intercalation materials are their low volumetric and gravimetric capacities (<1500 mAh cm^3 and <500 mAh g^{-1}). However, despite its comparably low gravimetric capacity of 372 mAh g^{-1}, graphite is the most commonly used anode active material for lithium-ion batteries. The low (de-) lithiation potential of ~0.1 V vs. Li$^+$/Li and the high electronic and ionic (Li$^+$) conductivity are ideal properties for an anode active material.

In contrast to intercalation materials, alloy and conversion materials undergo significant structural changes and show a pronounced voltage hysteresis upon (de-) lithiation. Comparing conversion materials and alloy materials, the latter exhibit lower operation voltages (0.2-1.0 compared to 1.0-2.2 V vs. Li$^+$/Li), higher gravimetric capacities (400-3500 mAh g^{-1} compared to 650-1000 mAh g^{-1}), and improved electronic and ionic conductivities.[21,22] Thus, alloy materials are more interesting candidates than conversion materials to replace graphite in next-generation lithium-ion batteries.

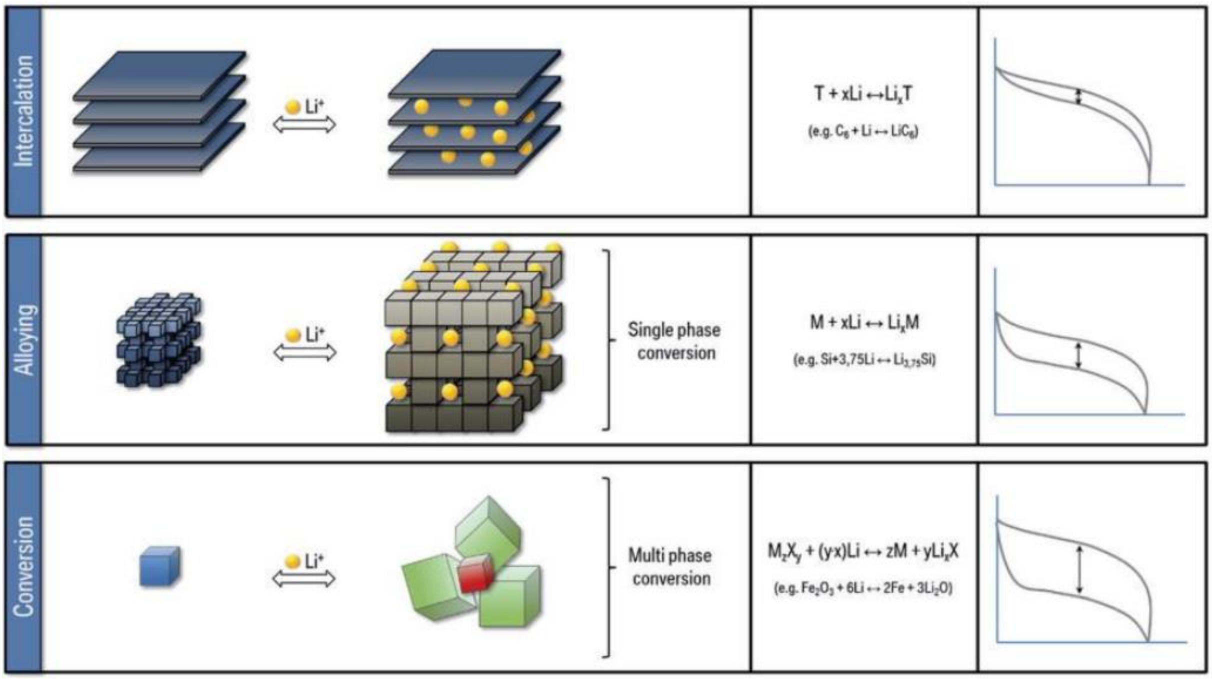

Figure 2 Schematic illustration of different types of anode active materials. Reprinted from “Future high-energy density anode materials from an automotive application perspective” by Stiaszny et al., with permission from the Royal Society of Chemistry.[21]

Amongst them, silicon is the most promising candidate. Sharma and Seefurth from General Motors reported the first electrochemical lithiation studies on silicon in the late 1970s.[24,25] Later, Wen and Huggins observed distinct crystalline Li-Si Phases by coulometric titration at 415 °C, resulting in a stepped galvanostatic voltage profile.[26] The compositions of these phases are $Li_{12}Si_7$, Li_7Si_3, $Li_{13}Si_4$, and $Li_{22}Si_5$, with the latter being the highest lithiated phase. However, electrochemical lithiation at room temperature involves electrochemical solid-state amorphization, forming amorphous Li_xSi phases.[27] In this case, the formation of the crystalline equilibrium phases is kinetically hindered; thus, the amorphous phase with a lower Gibbs free energy than the reactants is formed. Hence, the voltage profile for electrochemical (de-) lithiation at room temperature reveals a sloping behavior and depends on the silicon's applied current, as well as on the size, and morphology of the silicon material.[28,29] In 2004, Obrovac and Christensen found that a new crystalline phase $Li_{15}Si_4$ is formed during electrochemical lithiation, employing Rietveld refinement.[30] The formation of $Li_{15}Si_4$ ($Li_{3.75}Si$) corresponds to a specific capacity of 3579 mAh g^{-1} and is the highest lithiated phase that can be formed by electrochemical lithiation at room temperature.

Lithiation: $$cr\text{-Si} \xrightarrow{+\text{Li}} a\text{-Li}_{2.0}\text{Si} \xrightarrow{+\text{Li}} a\text{-Li}_{3.5}\text{Si} \xrightarrow{+\text{Li}} cr\text{-Li}_{3.75}\text{Si} \qquad 1.9$$

Delithiation: $$cr\text{-Li}_{3.75}\text{Si} \overset{\text{-Li}}{\rightarrow} a\text{-Li}_{2.0}\text{Si} + cr\text{-Li}_{3.75}\text{Si} \overset{\text{-Li}}{\rightarrow} a\text{-Si} \qquad 2.0$$

Subsequent cycling: $$a\text{-Si} \xrightarrow{+\text{Li}} a\text{-Li}_{2.0}\text{Si} \xrightarrow{+\text{Li}} a\text{-Li}_{3.5}\text{Si} \xrightarrow{+\text{Li}} cr\text{-Li}_{3.75}\text{Si} \qquad 2.1$$

Along with the (de-)lithiation process, silicon undergoes a volume change of ~280%.[17–19] The volume expansion follows Vegard's law and is the same for all binary Li-Metal alloys (except amorphous carbon, which follows an intercalation mechanism). Obrovac et al. found that the molar volume that lithium occupies in the alloy is about 8.9 mL mol^{-1} and shows a linear behavior with the amount of lithium inserted.[9] This implies that the total volume expansion of the alloy does not depend on the active element itself but rather on the amount of lithium that can be incorporated into the structure. Moreover, the volume expansion of an alloy can be restricted by the amount of lithium being inserted and, thus, the fraction of the total capacity of the active material used during operation. This strategy to limit the volume expansion will be discussed in more detail later. There is a fundamental difference in the lithiation mechanism, depending on whether crystalline or amorphous silicon is present initially in the active material. In dependence on the production process of the silicon active material and its design, silicon can be present in its crystalline or amorphous phase (see Chapter 1.3). Crystalline silicon undergoes electrochemical lithiation through a two-phase mechanism, where the silicon is consumed to generate lithiated amorphous silicon (Li_xSi). This process is characterized by a distinct reaction front with a thickness on the nanometer scale where crystalline and amorphous phases are present at the same time.[27,29,32,33] This two-phase behavior occurs due to the substantial activation energy required to break the crystalline silicon network.[34,35,36]

It is kinetically more favorable to further lithiate silicon clusters in the amorphous phase forming isolated silicon ions or smaller clusters, than to break up the pristine crystalline silicon network.[32] A high lithium concentration near the reaction front is needed to break the crystalline network's Si-Si bonds. Thus, the amorphous phase must reach a stoichiometry of $Li_{3.5}Si$ to further lithiate the remaining crystalline phase.[37] Accordingly, the voltage plateau for the initial lithiation of crystalline silicon drops to ≤ 170 mV vs. Li^+/Li, where the $Li_{3.5}Si$ phase is formed. At potentials ≤ 60 mV vs. Li^+/Li, the amorphous Li_xSi phase crystallizes into $Li_{15}Si_4$, as shown by the XRD analysis of Dahn and Li.[37] Structural investigations by in-situ NMR have demonstrated that a significant fraction of isolated Si atoms are present in this phase, allowing for a nucleation from the previous amorphous phase.[32,38] Lower lithiated amorphous phases do not readily nucleate, as this would involve rearrangement of the silicon clusters present at this stoichiometry and, thus, Si-Si bond breakage.

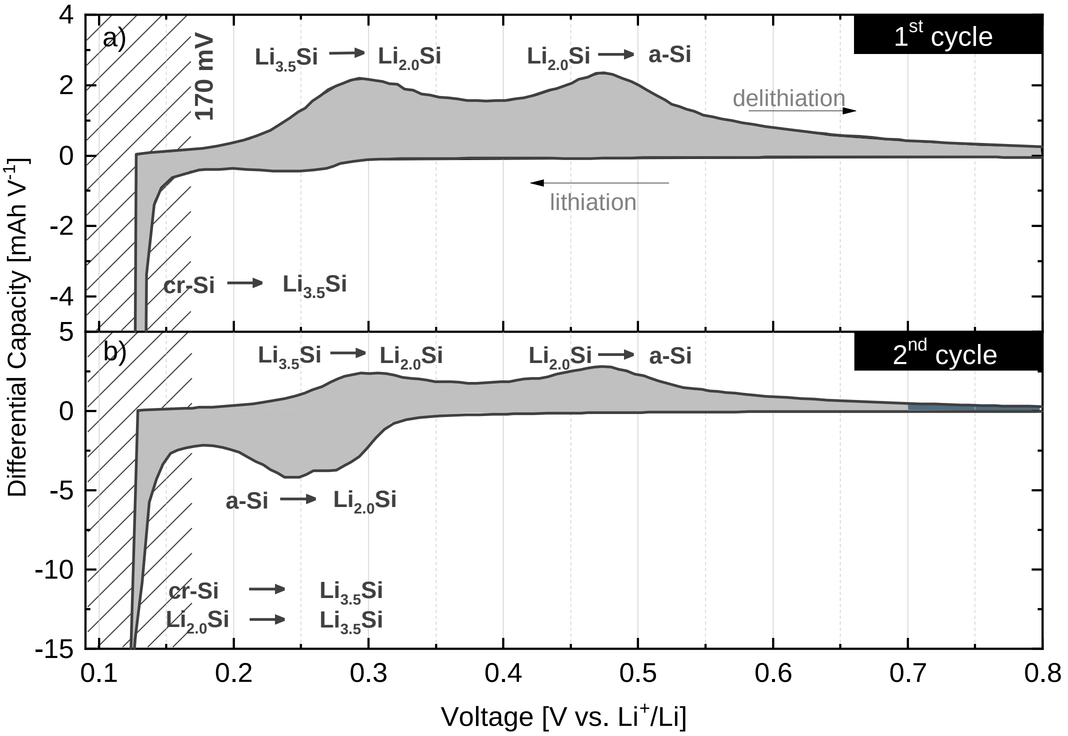

Figure 3 Differential capacity vs. voltage obtained from Si-C65//Li Swagelok T-cells with a lithium metal reference electrode (Li-RE). **(a)** In the first cycle, the lithiation step was limited to 1500 mAh g_{Si}^{-1}, followed by consecutive delithiation to a cutoff potential of 1.5 V vs. Li^+/Li. **(b)** Second cycle with a lithiation limit set by a capacity cutoff of 1500 mAh g_{Si}^{-1}. Electrochemical testing was done with Si-C65 electrodes (1.4 mg_{Si} cm^{-2}, with a theoretical capacity of 5.0 mAh cm^{-2}) at 25 °C with 1M $LiPF_6$ in FEC/DEC (2:8 v-v) and with two glassfiber separators.

Delithiation of the crystalline $Li_{15}Si_4$ phase is accompanied by a large voltage hysteresis and a large plateau at 450 mV vs. Li^+/Li.[11,30,37] As two-phase regions are associated with high internal stress, causing the particles to crack, the formation of $Li_{15}Si_4$ should be avoided for stable cycling. Delithiation of the amorphous phase is observed as two separated features: the first one corresponding to the delithiation of a higher lithiated $Li_{3.5}Si$ phase to a lower lithiated $Li_{2.0}Si$ phase (< 400 mV) and the second one to the complete delithiation of $Li_{2.0}Si$ to amorphous silicon (> 400 mV) (see **Figure 3**a).[39,40] For subsequent charge/discharge cycles, the situation looks different, as amorphous silicon is already present; the lithiation of this phase already starts at potentials <350 mV vs. Li^+/Li (see **Figure 3**b). This would also be the case for an active material that in its as-received form contains amorphous silicon. It must be mentioned that for the data shown in **Figure 3**, the crystalline silicon phase is still present in the second cycle as the application of this material is based on a partial lithiation strategy, in which a crystalline part of the particle is preserved over cycling. Hence, the pronounced feature for the lithiation of the crystalline silicon is still present in the second cycle. Even though only about on third of the silicon's capacity is used in this approach, limiting the silicon volume expansion and concomitant degradation, the mean potential of (de-) lithiation of such a material is comparable with that of a silicon active material for which 100% of the silicn capacity is used (see dark blue versus bright blue lines in **Figure 4**). As the remaining crystalline phase of the Si particles stays inactive, the active amorphous phase can be lithiated close to ~90% SoC ($Li_{3.5}Si$ – 170 mV vs. Li^+/Li) without further amorphizing the crystalline phase. This is a crucial difference to a partial lithiation strategy of an, e.g., fully amorphous silicon active material with no inactive phase, in which case, the silicon would only be lithiated up to 30% (assuming a capacity usage of 30%). Thus, the voltage curve would only be used to a third (~250 mV vs. Li+/Li), which has a detrimental effect on the cell's energy density (see dotted red line in **Figure 4**).

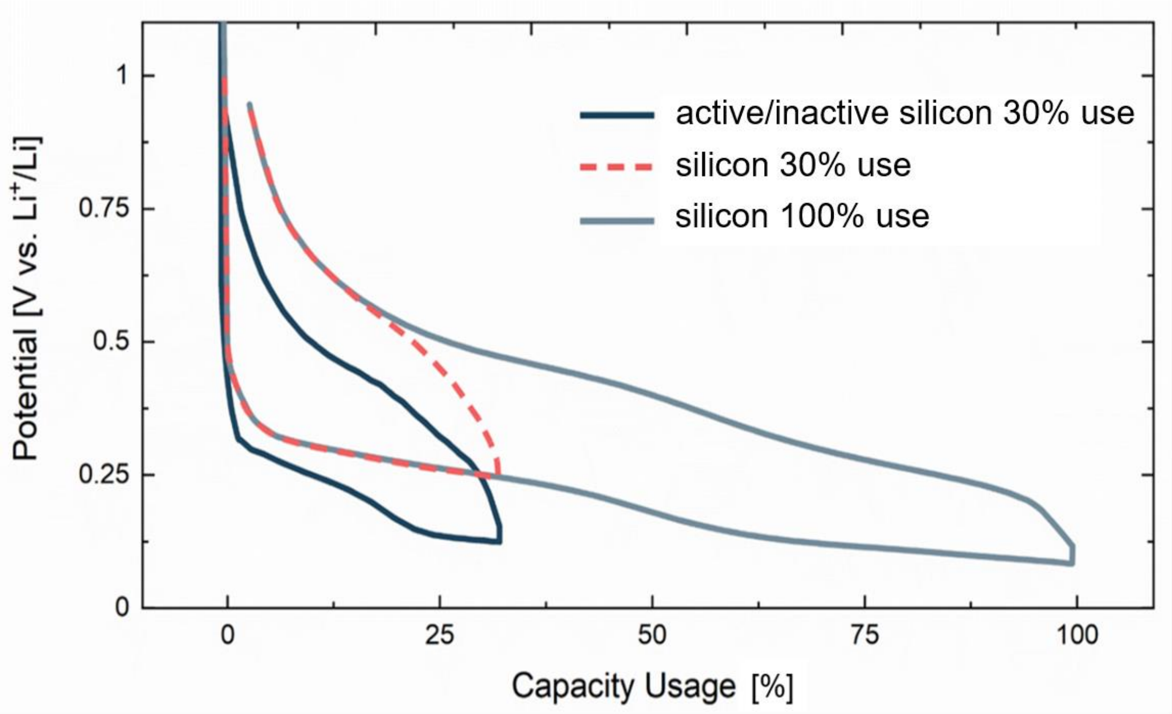

Figure 4 shows the voltage vs. capacity profiles of silicon with 100% capacity usage of silicon (bright gray), restricted to 30% capacity, such that the volume expansion is limited to 100% (dotted red), and an active/inactive silicon material that corresponds to a composite of crystalline and amorphitized silicon, which is produced by setting a silicon referenced capacity limit of 30% (dark blue). Electrochemical testing was done with Si-C65 electrodes (1.4 mg_{Si} cm^{-2}, with a theoretical capacity of 5.0 mAh cm^{-2}) at 25 °C with 1M $LiPF_6$ in FEC/DEC (2:8 v-v) and with two glassfiber separators. The data is shown for the second cycle.

1.3 Design of silicon active materials

1.3.1 Nanosilicon materials

The mitigation of particle pulverization by the volume expansion of silicon through control of the particle size has been known for a long time.[41] Small absolute changes in individual particles dimensions significantly improve the performance of such materials. Huang et al. showed by *in situ* transmission electron microscopy that silicon nanoparticles below a critical diameter of ~150 nm neither cracked nor fractured upon first lithiation.[42] The amount of strain energy released is insufficient for small particles to drive crack propagation. In addition, small diameters reduce the effects of volume expansion and enable fast Li-ion transport, further improving the performance of such materials.[43]

Over the last few years, all kinds of shapes and morphologies of nanostructured silicon materials have been published. Various structural designs such as nanoparticles,[44,45,46,47,48] nanospheres,[49,50] nanowires,[4,43,51] and nanotubes,[52,53] revealed superior performance compared to micron-sized silicon materials. However, nanostructured designs are often challenging to connect electronically within the electrode matrix and the current collector, especially after repetitive volume changes during cycling.[4,54] In addition, a high BET surface area leads to irreversible loss of lithium by SEI formation and thus to low coulombic efiiciencies.

Nanowires, directly bonded to the current collector, offer several advantages over other nanostructured materials: a) the space between adjacent nanowires can accommodate the volume changes upon (de-)lithiation, b) the direct connection to the current collector allows to maintain good electrical contact during cycling, and, c) the direct and one dimensional electronic pathways enable efficient charge transport without the need of conductive additives or binders.[4] In principle, silicon nanowires (SiNWs) can be synthesized using bottom-up methods such as chemical vapor deposition and laser ablation or top-down approaches with metal-assisted chemical etching, which is the most popular technique.[55,56,57,58] Carbon coatings and silicon doping can further enhance the electrochemical properties.[58,59] Next to the attraction of SiNWs amongst researchers in academia over the past few years, they have also made their way into the industry. Amprius Technologies, founded in 2008, finalized its SiNW design in 2014 and commercialized its technology in the past years, building up large-scale production on the kWh scale (see **Figure 5**). With their anode design comprising 100% silicon, cells with energy densities up to 500 Wh kg^{-1} are possible, verified by an independent testing institute (Mobile Power Solutions).[60]

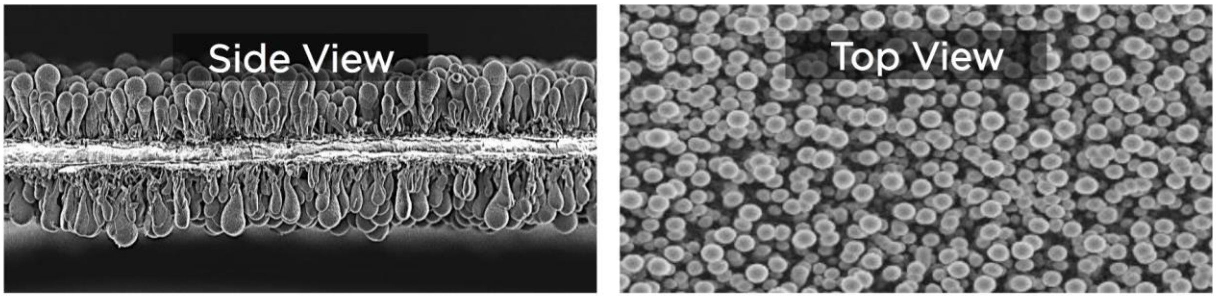

Figure 5 SEM image of the side and top view of silicon nanowires. Reprinted from Amprius Technologies Inc., 10th Annual Electric VTOL Symposium.[61]

However, nanostructured materials bear drawbacks due to their intrinsic property of a large specific surface area. Compared to commercial natural and artificial graphite materials with surface areas of 1-6 m^2 g^{-1},[62,63] similar to bulk silicon materials,[64,65,66] the surface area for nanostructured silicon materials is significantly higher with up to 80 m^2 g^{-1}.[54,65] Low initial coulombic efficiencies (ICE) and high irreversible capacities result from excessive SEI formation and irreversible reactions with SiOx formed as an inherent passivation layer on the surface of silicon.[45,46,65] The proposed reactions of Li^+ with SiO_2 are shown in the following equations:[67,68,69]

$$\mathrm{SiO_2 + 4Li^+ + 4e^- \rightarrow 2Li_2O + Si} \quad 2.2$$

$$\mathrm{2SiO_2 + 4Li^+ + 4e^- \rightarrow Li_4SiO_4 + Si} \quad 2.3$$

$$\mathrm{5SiO_2 + 4Li^+ + 4e^- \rightarrow 2Li_2Si_2O_5 + Si} \quad 2.4$$

Extended SEI formation not only leads to low coulombic efficiencies in the first cycles but also to electrical disconnection of silicon particles and thickening of the electrode over cycling.[45,54]

To evaluate such nano-sized material concepts, one also has to consider the material's properties and its implications on the processability and characteristics at the electrode level. Fabrication of an electrode with a high density is crucial in terms of commercial feasibility. Assuming a constant electrode thickness, a dense electrode has the potential to achieve a significantly higher mass loading than a porous electrode, resulting in a substantial improvement in areal capacity. With decreasing particle size, the tap density decreases considerably: nanostructured silicon materials can achieve tap densities in the range of 0.1-1.2 g cm^{-3}, whereas with microscale silicon materials, tap densities of 0.5-1.2 g cm^{-3} and for commercial graphite densities of 1.3-1.6 g cm^{-3} can be reached.[70] Another critical aspect of commercializing these materials is the ability for drop-in solutions in current process steps. Material concepts such as SiNWs attached to the metal substrate require specific electrode production processes and cannot be manufactured on existing coating lines.[61] Finally, the costs for silicon nanomaterials are usually significantly higher due to complex synthesis methods that are often more complex than those of bulk silicon or commercial graphite.[71] Therefore, these type of materials are still reserved for niche applications with high-performance requirements.

1.3.2 Silicon-carbon nanocomposites

Incorporating silicon into a carbon backbone is an effective method for alleviating the intrinsic disadvantages of silicon as an active material to achieve good cycling stability and high specific capacities.[13,72,73,74] The carbonaceous matrix can minimize electrolyte decomposition and, thus, excessive SEI formation while maintaining the integrity of the electrode. Moreover, the carbon structure can compensate for the impaired electric conductivity of silicon and enable a good connection throughout the electrode.[75,76] Nanocomposites can be synthesized by a variety of different methods, such as ball milling,[77,78] spraying methods,[79,80] high-temperature pyrolysis,[81,82] chemical vapor deposition,[83,84] or hydrothermal[85,86] techniques to name the most common ones. Nanostructured silicon materials can be combined with different types and morphologies of carbon, e.g., amorphous carbon[87], graphitic carbon, carbon nanotubes,[88,89] graphene,[90,91] or carbon shells.[92] The carbon's structural property and morphology is utilized to buffer the volume expansion of the combined silicon material. The carbon matrix leaves free volume for the silicon to grow into and hinders direct contact with the electrolyte. Continuous SEI formation, particle disconnection, and disintegration of the electrode can be prevented effectively by such material designs. Yi Cui and co-workers did groundbreaking work in this area; in 2014, they published a pomegranate-inspired material design with silicon nanoparticles encapsulated by a conductive carbon with void space (see **Figure 6**).[93] For low mass loadings (~0.2 mg cm^{-2}), the material exhibits a reversible capacity of 1200 mAh g_{SiC}^{-1} at C/2 and could retain 97% capacity after 1000 cycles. SEM analysis of the particles after 100 cycles did not show significant particle expansion or disintegration, as observed for pure silicon nanoparticles.[45] However, for industry-relevant, more significant mass loadings (3.1 mg cm^{-2}, corresponding to 3.0 mAh cm^{-2}) the cycling stability decreased to only 100 stable cycles. Later, in 2016, Cui and coworkers showed, with a similar design principle, that graphene cages with void space could significantly improve the cycling performance of micrometer-sized silicon by retaining the electrical contact and avoiding uncontrolled SEI growth.[91]

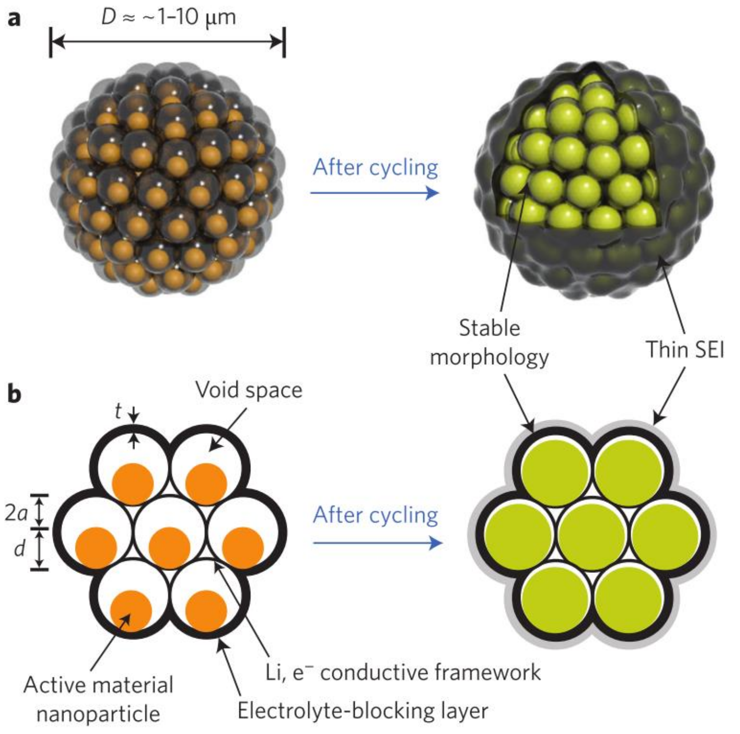

Figure 6 Schematic view of a pomegranate-inspired design. Reprinted from” A pomegranate-inspired nanoscale design for large-volume-change lithium battery anodes” by Cui et al., with permission from Springer Nature.[93]

As mentioned in the nanomaterials section above, scalability and production costs are fundamental aspects of the relevance of such materials for industry. The same year, the groups of Cui and Cho published a work that presented a scalable synthesis of a silicon nanolayer-embedded graphite.[83] In contrast to previous material designs, the carbon matrix is not built around silicon but silicon is instead infiltrated by chemical vapor deposition in an existing carbon host structure. Using silane gas (SiH_4) as the silicon source enables a uniform distribution of a silicon nanolayer on a porous graphite matrix. Most importantly, this approach is suitable for upscaling; 5 kg of material could be produced in one batch with a scalable furnace. Today, one can find materials already in the commercialization based on this approach. Companies like Sila Nanotechnologies or Group14 cooperate with companies in the automotive sector and car manufacturers such as Mercedes or Porsche to bring their material concepts into the market.[94,95] Substitution of graphite with such materials allows for high energy density cells while not compromising on the rate capability, required for fast-charging. Even though the cycling stability of these silicon-based active materials still lags behind that of graphite. However, next to the material's technical performance and production costs, the availability of these type of materials on the market and constant quality are crucial factors for commercialization as well.

1.3.3 Microscale silicon

Microscale silicon particles are scalable and cost-effective; photovoltaic grade silicon often serves as raw material and is thus highly reproducible and reliable.[64] Micro-sized particles are usually made via mechanical milling of polycrystalline silicon, preferably by a jet milling process in air. This is economical compared to a wet ball-milling process used for silicon nanoparticles. In general, production costs increase with decreasing particle size of the product due to elongated milling times. Compared to the aforementioned material designs, microscale silicon particles are more susceptible to the mechanical stress of the volume expansion and thus more prone to particle cracking and pulverization.[39,96]

Unlike the focus on the active material design that is critical for nanomaterials, solutions on the electrode level and operational strategies must be used for microscale particles. On the electrode level, advanced binder systems such as self-healing[97,98] or highly elastic polymers[99,100] can reduce the disintegration of the silicon particles upon volume expansion. Another strategy is to use only a part of the total silicon capacity and thus reduce the volume expansion upon (de)lithiation.[40,64,100,101,102,103] This concept has been known for a long time and was first published by Obrovac and Krause in 2007, at a time when advanced nanostructured designs were unavailable.[104] In this study, the crystalline silicon is lithiated in the first cycle to only 1200 mAh g_{Si}^{-1} corresponding to a lithiation degree of 33% based on a total specific capacity of 3579 mAh g_{Si}^{-1}. Therefore, only a part of the crystalline particle is amorphized while the other part of the silicon remains crystalline. Cycling the silicon anode to different lower lithiation cutoff potentials showed a capacity increase for potentials <170 mV vs. Li^+/Li, while the capacity stayed constant for a cutoff potential of 170 mV and above. This is explained by the fact that for potentials <170 mV vs. Li^+/Li, the crystalline silicon phase is lithiated, thus contributing to the capacity. To directly measure and quantify the crystalline and amorphous Si phase present at different cutoff potentials over cycling is part of the work presented here.[39]

1.3.4 Commercial microscale silicon used in this thesis

The microscale silicon material used in this work exhibits a specific BET surface area of 1.6 $m^2\ g^{-1}$ and a particle size distribution characterized by d_{10} = 2.2 µm, d_{50} = 4.5 µm, and d_{90} = 7.8 µm (CLM 00001, Wacker Chemie AG, Germany).

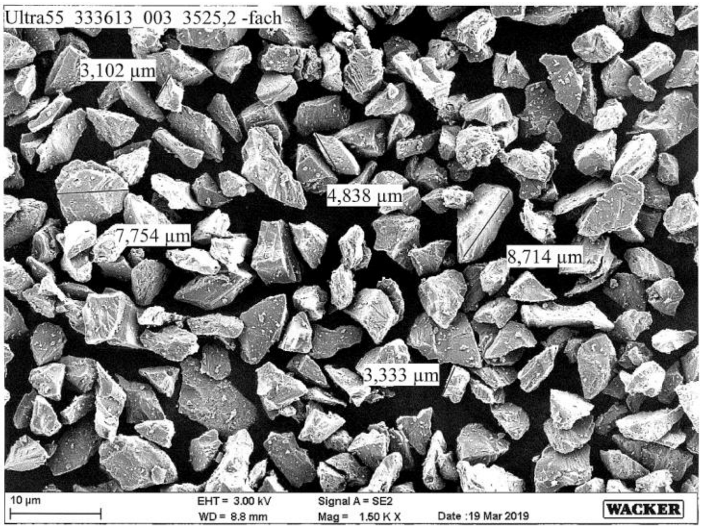

Figure 7 SEM image of the microsilicon material (CLM 00001, Wacker Chemie AG) used in this work. The image was taken using an Ultra 55 from Carl Zeiss Microscopy, Germany, with a thermal field emission cathode in the SE-mode (secondary electrons) at a high vacuum (~10^{-6} mbar) and an electron beam energy of 3 kV.

Jantke et al. investigated different capacity usages for the CLM 00001 silicon material in full-cells with regard to their initial coulombic efficiency and stability over cycling.[64] They found that using 30-40% of the silicon's capacity (i.e., 1200-1500 mAh g^{-1}_{Si} based on 3579 mAh g^{-1}_{Si}) resulted in reasonable specific electrode capacities and good cycling stability. The present study used a three-electrode half-cell setup to evaluate the silicon-based anode's voltage curve against a lithium reference electrode. **Figure 8a** displays the voltage curves of the anode for various capacity usages. Each voltage curve corresponds to an individual cell that was cycled at a low current density of 0.14 mA cm^{-2} (equivalent to C/50 based on 3579 mAh g^{-1}_{Si}) for one hour, followed by an open circuit voltage (OCV) hold of 2 hours, repeating this sequence until the target specific capacity is reached for a given cell. The OCV potential curve for each cell was drawn using the relaxed potential at the end of the OCV holds (see **Figure 8b**). All cells follow the same OCV potential line during lithiation, starting from 170 mV vs. Li$^+$/Li and going to progressively lower potentials. Below 170 mV vs. Li$^+$/Li, a lithium-rich $Li_{3.5}Si$ phase is formed, capable of breaking the strong Si-Si bonds in the crystalline silicon lattice and thus enabling lithiation.[32,35,36,105]

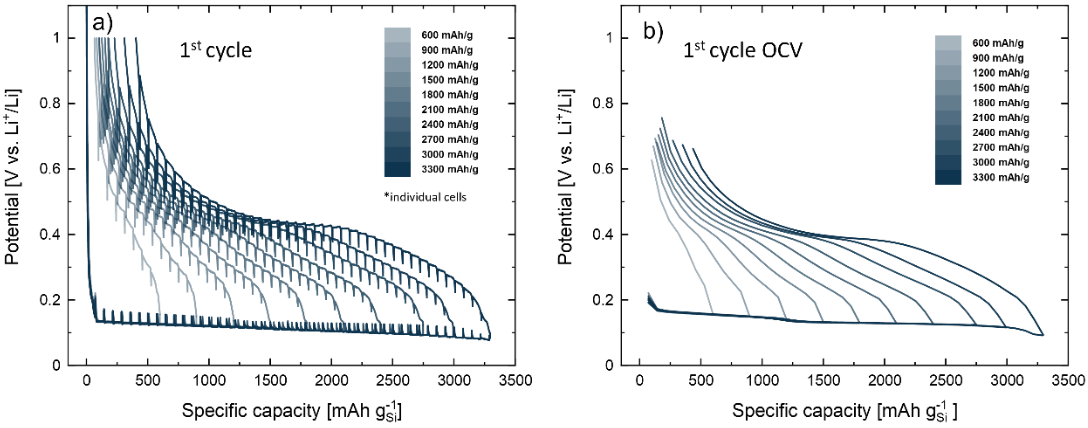

Figure 8 Voltage curve of the first cycle of a microsilicon anode (CLM 00001) in a Swagelok® T-cell with a Li-metal counter electrode and a Li-RE. Cycling was conducted with constant current cycling at C/50 (based on a capacity of 3579 mAh g^{-1}_{Si}) for 1 h, followed by an OCV hold for 2 h. This sequence is repeated until the desired lithiation capacity cutoff ranging from 600-3300 mAh g^{-1}_{Si} is reached. Each voltage curve is represented by an individual cell. b) OCV potential curves of the first cycle taken from the OCV potential after 2 h from panel a).

Contrary to the first cycle shown in **Figure 8a**, the OCV potentials of the second-cycle lithiation curves for the various cells do not follow the same pattern when plotted against the specific capacity, as is shown in **Figure 9a**. This is due to the varying amounts of amorphous phases created in each cell's first cycle. As a result, the same quantity of lithium being alloyed in the second cycle leads to a different phase composition and, therefore, a distinct potential for each cell when plotted against the specific capacity (see **Figure 9a**). In this case, the second cycle was lithiated with the same capacity limit as in the first. For the cell cycled to 3300 mAh $g^{-1}{}_{Si}$, a significant overpotential was observed during the delithiation step, indicating the formation of the $Li_{15}Si_4$ phase. This can be explained by the substantial degradation of the silicon material in the first cycle due to extended capacity usage. Therefore, the remaining intact silicon phase was lithiated even more in the second cycle. Normalizing each cell's maximum capacity to 100% allows it to plot the voltage curve over the state-of-charge (SOC) (refer to **Figure 9b**). The voltage curves for the different cells with varying capacity usage now exhibit the same shape, except for the cell cycled to 3300 mAh $g^{-1}{}_{Si}$, which forms the $Li_{15}Si_4$ phase. Congruent voltage curves can be observed because the partial amorphous and crystalline particle acts as an active/inactive alloy, as described in Chapter 1.2. The amorphous phase is lithiated up to $Li_{3.5}Si$ before further crystalline silicon is lithiated, whereby the remaining crystalline part acts as an inactive phase up to this point.

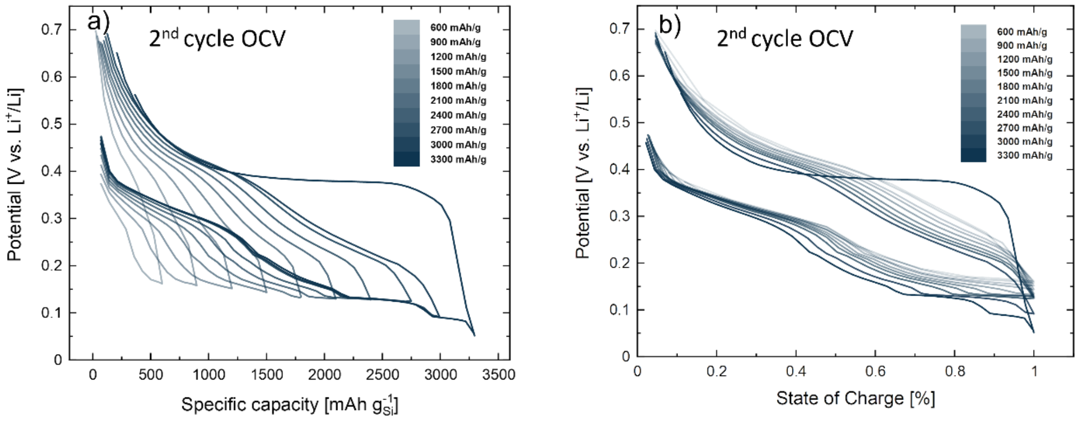

Figure 9 Second-cycle OCV curves of the cells shown in Figure 9: **a)** plotted vs. the specific capacity; **b)** plotted vs. the state of charge (SOC), defined as the percentage of the end-of-lithiation specific capacity.

Figure 10a displays the reversible capacity loss over the first, second, and third cycle of microsilicon anodes to different lithiation capacities. The observed increased irreversible capacity loss with extended capacity usage can be attributed to the significant volume expansion resulting from increased lithium alloying. Notably, the irreversible capacity loss increases exponentially for the two highest lithiation capacities. Particle breakage is likely to occur at high capacity usage, exposing large quantities of fresh surface area to the electrolyte, resulting in large losses of cyclable lithium. This is supported by the observation that, for such high lithiation capacities, a third cycle cannot even be reached due to the failure of the entire electrode. **Figure 10b** shows the capacity loss summed up over the first three cycles and normalized by the first-cycle lithiation capacity. This shows that the highest efficiency, i.e., the least relative capacity loss, is observed at a capacity usage of 1500 mAh g^{-1}_{Si}. Exceptionally large relative capacity losses are observed for the most extended capacity usages of 3000 and 3300 mAh g^{-1}_{Si}, however, also relatively small capacity usages also exhibit poor efficiency, as the absolute capacity loss is significant due to the unfavorable ratio of surface area and capacity usage.

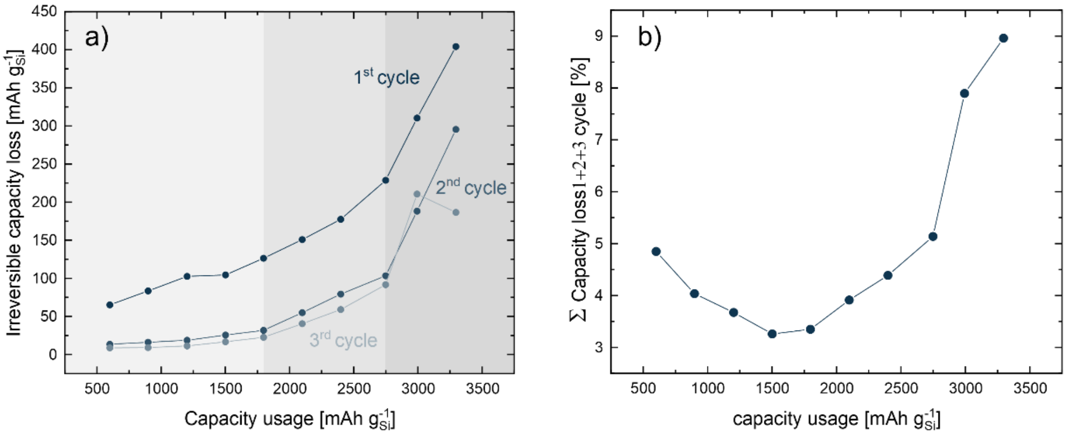

Figure 10 Analysis of the irreversible capacity losses of microsilicon (CLM0001) anodes (2.1 mg$_{Si}$ cm^{-2}, with a theoretical capacity of 7.5 mAh cm^{-2} based on a capacity of 3579 mAh g$^{-1}_{Si}$) in a Swagelok® T-cell with a Li-metal counter electrode and a Li-RE, cycled to different lithiation capacities in the first cycle (x-axis values). Cycling was conducted with constant current cycling at C/50 until the capacity limit was reaches. Delithiation was performed with C/50 until a cutoff of 1.5 V vs Li$^+$/Li. Experiments were conducted at 25 °C with 1M LiPF6 in FEC/DEC (2:8 v-v) and with two glassfiber separators. **a)** Absolute irreversible capacity loss for the first three cycles **b)** Cumulative capacity loss over the first three cycles, normalized to the initial lithiation capacity.

1.4 Electrolyte additives

With the above-described silicon active material designs, the volume expansion of silicon and its effects on particle integrity is pursued to be as low as possible. Next to the electrical disconnection by the fracturing of the particles or disconnection of the whole silicon particle itself from the electrode matrix by the expansion and contraction, the ultimate consequence will always be exposure of the fresh silicon surfaces to the electrolyte. Like most anode materials, a silicon anode operates below the reduction potential of commonly used carbonate-based electrolytes, and a solid electrolyte interface (SEI) readily forms on the freshly exposed surface.[106,107,108,109] Formation of the SEI is essential to the operation of a lithium-ion battery, as it serves as a protective layer for further electrolyte reduction throughout cycling. However, building up an SEI layer consumes lithium, which is no longer available as cyclable lithium, leading to a capacity fading in the cell. Moreover, the SEI contributes an additional resistance to the anode as the lithium ions have to move through the SEI layer. Excessive SEI formation, which can be detached from the active material particle by repeated expansion and extraction, can further clog the electrode's pores, thereby increasing the resistance of Li^+ ion transport to the active material.[54,110] Demands on an effective SEI layer are, therefore: i) high ionic conductivity while beeing electronically insulating, ii) flexibility and mechanical stability, iii) maintaining a good connection to the active material, iv) homogeneous and uniform coverage of the active material particles to prevent further electrolyte decomposition and v) low solubility in the electrolyte.[111]

Typical constituents of the SEI for an $LiPF_6$-based electrolyte in carbonate-based solvents (EC, DEC, DMC) are lithium carbonate (Li_2CO_3), lithium fluoride (LiF), lithium oxide (Li_2O), Li-alkyl carbonates ($ROCO_2Li$) such as lithium ethylene dicarbonate (LEDC) and Li-alkoxides (ROLi). The composition and structure of the SEI depend on the electrolyte (salt, solvent, additives), the active material, and the electrochemical formation procedure. Formation of the SEI is usually governed by a stepwise process, as for typical anode materials, e.g., graphite and silicon, the OCV of the discharged (pristine) state is within the stable voltage window of the electrolyte components. Upon the first charge of the cell, the anode potential continuously decreases, and the specific reduction potentials of the individual electrolyte constituents control the composition and structure of the SEI. Since the first conceptual description of the SEI by Peled[112] in 1979, the SEI has been intensively studied over the past decades.[109,113] Various studies have shown that the initial composition of the SEI will not stay constant over cycling, ultimately, a relatively dense inorganic inner layer near the electrode/SEi interface and a heterogeneous porous organic outer layer at the SEI/electrolyte interface is formed.[109,114,115] The addition of selected components to the electrolyte system can effectively design the composition of the SEI and, thus, the SEI properties.[116]

1.5 Perspective of silicon as anode active material

The electrochemical lithiation of silicon has been studied for more than 50 years now, and since the early 2000s, it has been intensively investigated as an active material for lithium-ion batteries.[24,25,117] Many silicon active material concepts have been employed (described in Chapter 1.3), predominantly in the academic literature. So far, broad application in the industry has been hampered by the intrinsic challenges coming along with silicon. In recent years, various companies have commercialized their silicon active material design and are penetrating the market of anode active materials for lithium-ion batteries. Material designs and concepts can be separated into two categories: a) drop-in solutions, for which the silicon active material can be used for electrode manufacturing with existing infrastructure (mixing and coating equipment) and b) advanced material designs, requiring specific solutions and methods for electrode manufacturing, e.g., chemical vapor deposition (CVD). As drop-in solutions are, silicon-carbon composites are being commercialized, which comprise a porous carbon scaffold filled to a certain extent with silicon to compensate for the volume expansion (see **Figure *11***). For this, the pores of the carbon scaffold are filled and infiltrated with silicon by a CVD process using silane gas. This material concept is used by companies such as Sila Nanotechnologies,[118] Group14,[119] or Nexeon.[120] These companies are already in the ramp-up phase of mass production and have several customers in the automotive sector.[94,95]

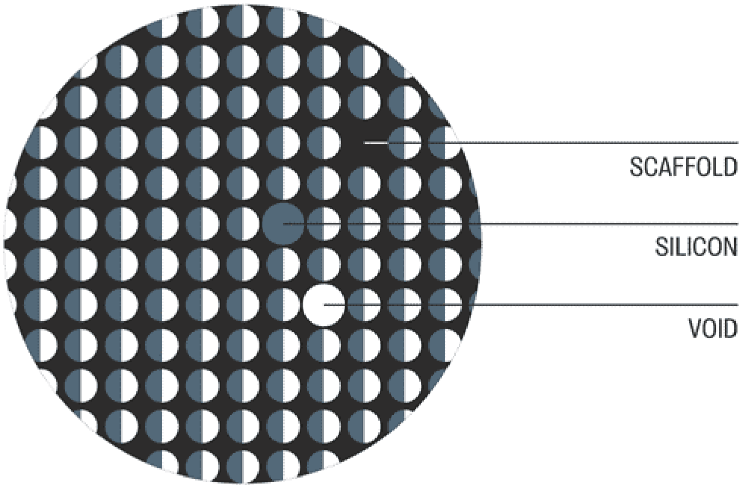

Figure 11 Schematic illustration of a porous carbon scaffold with void space partially filled with silicon. Copyright Group14.[119]

Advanced material designs comprising 100% pure silicon are commercialized by Amprius[121] or Leyden Jar.[122] In the case of Amprius, silicon nanowires are directly attached to the current collector, while in the case of Leyden Jar, nanoporous silicon thin films are used to overcome the volumetric expansion of silicon. These concepts require a CVD process for electrode manufacturing, so that the conventional electrode preparation routes comprising slurry mixing, coating, and calendaring cannot be used.

The industry's demand for silicon based anode active materials is high. Silicon-dominant electrodes can be found in every technology roadmap for next-generation battery cells of major car manufacturers such as Mercedes Benz, BMW, or Porsche.[123,124,125,126,127] Silicon-dominant anodes are seen as enablers for lithium-ion battery cells with higher energy densities until the longer-term envisaged commercialization of solid-state batteries.

1.6 Structure of this Thesis

This section serves as a guideline for the reader to explain this thesis's structure and main topics.

Chapter 1 briefly introduces the current requirements for lithium-ion batteries concerning performance and costs for the automotive sector. Moreover, today's state-of-the-art technology is described, future challenges are addressed, and promising solutions to achieve tomorrow's targets are discussed. Hereby, silicon as an active anode material is analyzed in detail, and different material designs are reviewed. In addition, the crucial function of electrolyte additives, especially for silicon as an active material, is discussed.

Chapter 2 presents a comprehensive overview of the methods and techniques used throughout this thesis. This includes a description of to the working principle of the on-line electrochemical mass spectrometry (OEMS), as well as of X-ray powder diffraction (XRD) with the here developed custom-made cell holder that allows for the in-situ XRD analysis. Furthermore, the theoretical basics of electrochemical impedance spectroscopy (EIS) are explained, and the transmission line model (TLM) application to porous electrodes is exemplified. Simplifications of the TLM for either kinetically controlled or transport-controlled systems are highlighted.

Chapter 3 summarizes the conducted scientific work. In the first part, the amorphization of microscale silicon particles with a partial lithiation strategy is quantitively investigated by in-situ XRD (Chapter 3.1). The second study presents a mechanistic investigation of lithium nitrate as an electrolyte additive in carbonate-based electrolyte systems for silicon anodes (Chapter 3.2). Reduction and oxidation reactions are studied using carbon model electrodes, whereas the effect on the cycling performance is tested in full-cells. The third section focuses on the rate performance of silicon electrodes compared to graphite electrodes (Chapter 3.3). Temperature-dependent contributions of kinetic and transport-related resistances are investigated by impedance measurements.

Chapter 4 summarizes the results and the learnings from this PhD thesis.

2.0 Experimental Methods

2.1 On-line electrochemical mass spectrometry (OEMS)

Understanding the electrochemical reduction and oxidation reactions that occur during the operation of lithium-ion batteries is crucial to elucidate degradation phenomena and develop strategies to mitigate them. Many of these reactions result in the evolution of gaseous species that are difficult to detect in small-scale setups, such as coin cells or Swagelok® T-Cells. For larger cell formats, such as pouch cells, quantification and qualification require significant effort and time-consuming measurements. In order to gain insights into the electrochemical side reactions that occur during cell formation and cycling, it is essential to determine the amount and species of gas produced as well as the onset potentials and gas evolution rates. In some instances, evolved gases can even be consumed again, for example, upon a change in potential. Commonly used post-mortem methods would not be able to detect such processes. On-line electrochemical mass spectrometry (OEMS) enables qualitative and quantitative *operando* gas analysis and can be applied to small-scale electrodes, such as coin cell formats. The method was first presented by Tsiouvaras et al. [128] and further developed by Metzger et al.,[129,130] introducing a 2-compartment OEMS cell with hermetically sealed working and counter electrode compartments, which enables exclusive analysis of the gases evolved at the working electrode.

The here used OEMS cell is a closed system with a volume of approximately 11 mL. During measurement, the gas composition is continuously probed through a capillary with a leak rate of roughly $2x10^{-5}$ $atm{\cdot}cm^3$ s^{-1} (corresponding to ~ 1 µL min^{-1} at 1 bar OEMS cell pressure, Vacuum Technology Inc., USA). Continuous probing reduces the OEMS cell pressure, limiting measurement time to approximately 40 h. The OEMS device comprises a mass spectrometer (QMA 410, Pfeiffer Vacuum Germany) with a closed cross-beam ionization chamber, a quadrupole mass analyzer, and a secondary electron multiplier (SEM) detector. The detector operates at approximately 10^{-7} mbar and can detect currents for each mass-over-charge ratio (m/z) from 1 to 126 at low parts per million (ppm) levels. A calibration procedure is conducted after each measurement to determine the concentration of gas species. For this a cell is purged with an argon calibration gas mixture containing all relevant gas species at a defined concentration of 2000 ppm, which allows for the conversion of measured currents for different gas species into relative concentrations in ppm or µmol, taking into account the cell volume, pressure, and temperature.

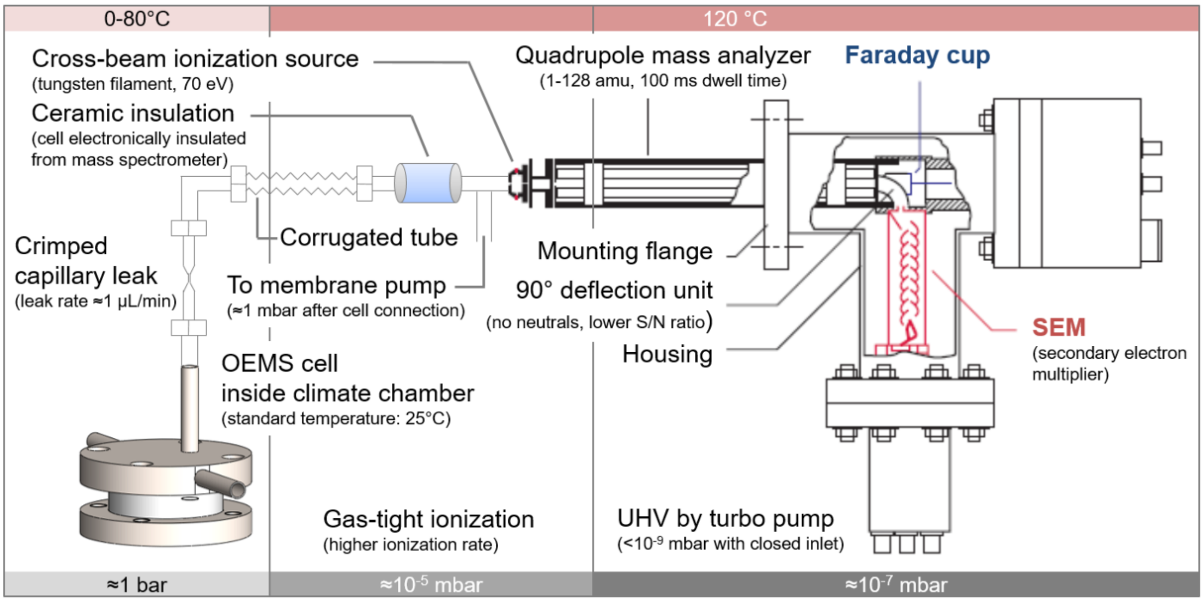

Figure 12 Schematic drawing of the OEMS setup. The electrochemical cell is attached to the crimped capillary and is electronically insulated by the ceramic insulation from the mass spectrometer. Evolved gases are sampled through the capillary and ionized by the cross-beam ionization source. Next, m/z separation is reached by the quadrupole analyzer and finally detected by the secondary electron multiplier (SEM). Reprinted from Strehle.[131]

2.2 X-ray diffraction analysis (XRD)

X-ray diffraction (XRD) is a widely used analytical method for characterizing crystalline materials and investigating various properties, including phase composition, crystal size, and crystal strain. It is particularly suited to analyzing battery materials, as it is a nondestructive technique used in *operando* battery experiments or *ex situ* analysis of pristine or cycled active materials.

X-rays scatter from the lattice planes of a crystal, and the symmetry of the crystal structure, also known as the space group, is determined by the quantity and position of these reflections. The diffractogram shows the reflections as a function of the scattering angle θ, which can be analyzed based on their position, profile, and intensity. Only the scattered waves that constructively interfere contribute to the diffractogram, as their waves are in phase. In this case, the difference in path lengths is equal to an integer multiple (n) of the wavelength (λ), as described by Bragg's law, which correlates this relationship with the interplanar spacing of parallel lattice planes (d) and the angle between the incident beam and the respective lattice planes (θ):

$$n\lambda = 2d\sin\theta \tag{2.5}$$

Figure 13 shows an exemplary XRD o a microscale silicon powder, marking he Miller indices of the various crystal planes.

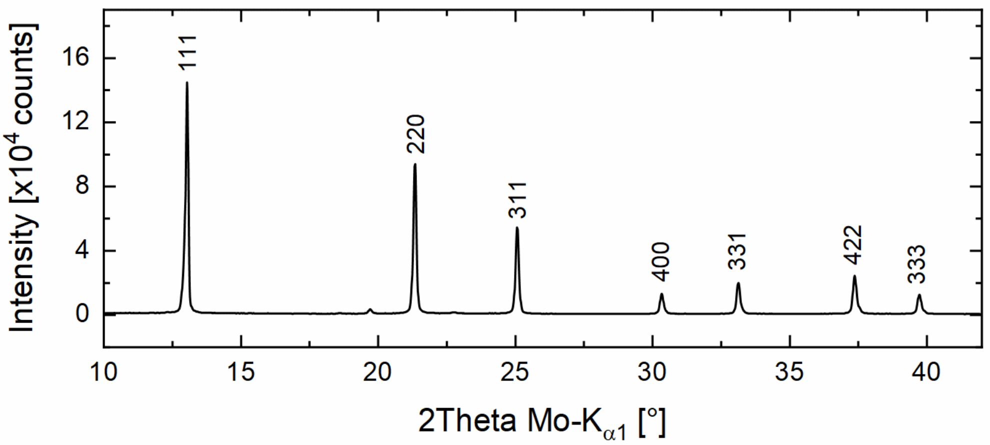

Figure 13 X-ray diffraction pattern of silicon measured of a microscale silicon powder sample on a laboratory diffractometer (STOE STADI P) in transmission mode using Mo-K$_{\alpha1}$ radiation (λ = 0.7093 Å). Reflections are labeled with Miller indices (hkl) from the *Fd*3*m* space group of silicon.

In this study (see Chapter 3.1), XRD was used to trace the amorphization of crystalline microscale silicon used as an anode-active material. Measurements were performed in situ on Si//Li pouch cells (see **Figure 14a**), and data were collected before and in between electrochemical testing. For this, pouch cells were mounted on a home-made holder attached to the diffractometer, providing the X-ray beam access by a 15 mm diameter hole (see **Figure 14b** and **c**). The data were evaluated using the Rietveld refinement software Topas (TOPAS-Academic V6, Coelho Software). The refinement was conducted for the silicon and copper phase using the Thompson-Cox-Hastings pseudo-Voigt function (TCHZ) to describe the peak profiles. The amount of crystalline silicon phase in the microscale silicon based anodes over the course of (extended) lithiation/delithiation cycles was quantified by referencing the silicon reflex intensity of the pristine cell. Refinement parameters are described in Graf et al.[39] To account for slight variations in incident beam intensity between measurements, the intensity of the silicon reflex was also referenced to that of the copper reflex, which served as an internal standard, since the copper current collector remains constant during testing.

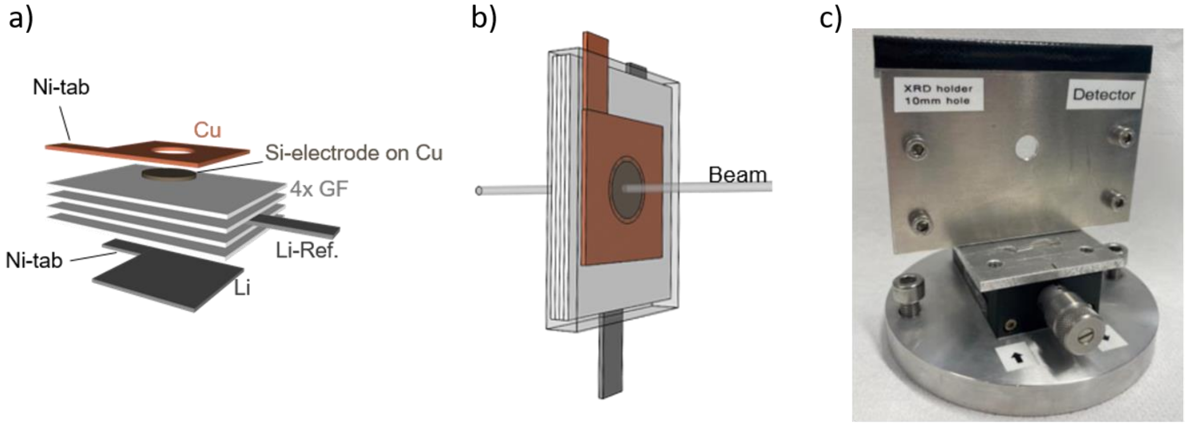

Figure 14 a) Si/Li pouch-cell setup for *in situ* XRD measurements. The cell consisted of a Li-metal (450 µm thick, 30x30 mm^2, 99.9% Rockwood Lithium, USA) counter electrode, four glassfiber separators (Whatman GD type A/E, 45x55 mm^2, USA), and of a Si-KS6L composite working electrode (11mm diameter) coated on a copper foil (11 µm). An additional copper foil with a 10 mm diameter hole was placed on top of the working electrode in order to connect it with the Ni-tab of the pouch cell setup. Thus, the X-ray beam intensity is not further reduced by the copper. A piece of Li-metal attached to a Ni-tab was used as a reference electrode and was placed between the glass fiber separators. b) Configuration of the assembled cell. c) Pouch-cell holder used to mount the cell onto the diffractometer for transmission XRD.

The results of the XRD-based investigations on the amorphization process, as shown in Graf et al.[39], enable precise quantification of the weight fractions of amorphous and crystalline silicon phases (see Chapter 3.1). In-situ measurements allow for quantification during cycling, thus tracking the progress of amorphization. However, this method only captures the average ratio of the amorphous/crystalline phase within the electrode. Next to a quantitative investigation, a particle-resolved qualitative characterization is of interest. The XRD-based study assumes the formation of spherical core/shell particles upon cycling i.e., silicon particles with an amorphous shell and a crystalline core. SEM images of cycled particles indicate that this core-shell structure, as shown in the simplified scheme from Graf et al.[39] is most likely not favored. Since the silicon particles used in this study exhibit a polycrystalline particle morphology, a lithiation and, thus, amorphization along grain boundaries and defects are presumed. **Figure 15** shows the cross-sectional view of silicon particles harvested from an electrode cycled in full cells for 50 cycles. While the particle integrity itself remains intact, showing no larger cracks or formation of a porous structure, as has been observed for the particles cycled to 140 mV, the bulk of the particle shows a structured morphology. The observed pattern resembles ice floes and might originate from amorphous and crystalline parts. In order to verify this hypothesis, a follow up study based on high-resolution TEM measurements is conducted.[132]

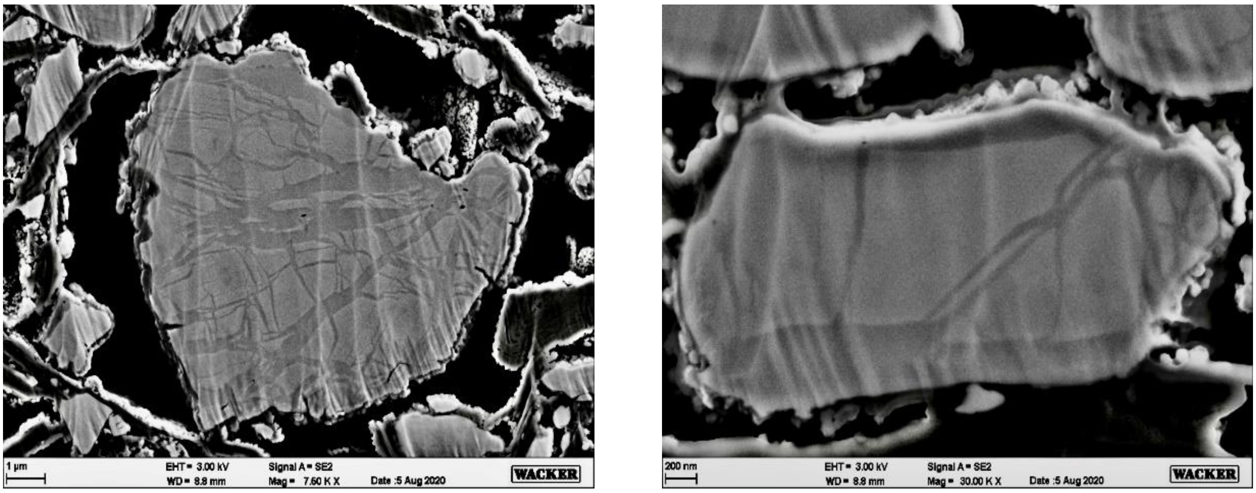

Figure 15 SEM image at 3.0 kV of a cross-sectional view of a silicon electrode cycled in a full-cell to 50 cycles

2.3 Electrochemical impedance spectroscopy (EIS)

Electrochemical impedance spectroscopy (EIS) is a widely used and non-destructive technique to study a broad range of processes such as charge transfer kinetics, lithium-ion transport resistances in the electrolyte phase, and lithium ion solid state diffusion. The method involves applying a sinusoidal potential U(t) or current perturbation I(t) to the cell while recording the current response (in the case of potentiostatic-electrochemical impedance spectroscopy - PEIS) or the potential response (in the case of galvanostatic-electrochemical impedance spectroscopy - GEIS) as a function of frequency, typically ranging from several MHz to the mHz region. The individual time constants of the processes described above allow for their separation and individual analysis through a scan over a range of frequencies. The perturbation and response of potential and current over a specific frequency range can be expressed as a time-dependent sine function with the phase angles ϕ_U and ϕ_I and the amplitudes U_0 and I_0, respectively. The frequency term is described as a radial frequency defined as ω = 2π f.

$$U\,(t) = U_0 \sin(wt + \Phi_U) \tag{2.6}$$

$$I\,(t) = I_0 \sin(wt + \Phi_I) \tag{2.7}$$

Here, U_0 and I_0 are the amplitudes of the potential and of the current, respectively. The phase shift between perturbation and response is then given with:

$$\phi = \phi_U - \phi_I \tag{2.8}$$

The complex, frequency-dependent impedance Z is defined with Ohm´s law as follows:

$$Z = \frac{U\,(0)}{I\,(0)}\, e^{j\phi} = \frac{U\,(0)}{I\,(0)}\,(\cos\Phi + j\sin\Phi) = Re(Z) + j\;Im(Z) \tag{2.9}$$

Here, j is the imaginary unit, Re(Z) is the real part of the impedance, and Im(Z) is the imaginary part. A plot of the negative imaginary part on the y-axis and the real part on the x-axis is a so-called Nyquist plot and is the most common representation of impedance data for battery applications.

To interpret and understand the impedance data for real electrochemical systems, the components of the battery are usually described as equivalent circuit models. The electrochemical interface of electrodes and the electrolyte can be displayed as an *R/C* element, a parallel connection of a resistor and a capacitor. In this context, the resistor represents the charge transfer resistance (R_{CT}), which is responsible for the transfer of Li^+ ions from the liquid electrolyte to the solid active material, upon the uptake of an electron or vice versa. On the other hand, the capacitor represents the electrochemical double layer formed at the interface. The impedance of an ohmic resistor is independent of frequency and is defined as $Z_R = R$, contributing only to the real part. The impedance of a capacitor depends on the frequency and contributes to the imaginary part of the impedance with $Z_C = 1/j\omega C$. When these two circuit elements are connected in parallel as an *R/C* element, it results in a semi-circle in the Nyquist plot, with *R* as the diameter and the apex angular frequency given by:

$$\omega_{max} = \frac{1}{RC} \qquad 3.0$$

Since the real electrochemical systems do not behave like a perfect physical capacitor, the double-layer interface is usually described with a constant phase element (CPE), which includes the phase angle α, a factor that tilts the straight line of an ideal capacitor. The impedance of a CPE is described with $Z_{CPE} = 1/[(j\omega)^{\alpha}Q]$. The impedance of an *R/Q* element ($Z_{R/Q}$) can be derived by Kirchoffs law as:

$$Z_{R/Q} = \frac{R}{1+(j\omega)^{\alpha}RQ} \qquad 3.1$$

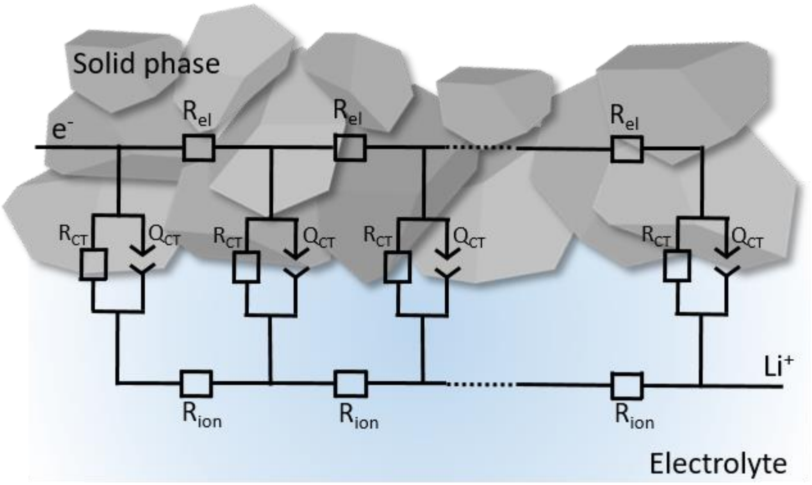

Figure 16 Equivalent circuit for the transmission line model representing a porous electrode. Adapted from Landesfeind et al.[133]

The simple *R/Q* element can be extended to the transmission line model (TLM) shown in **Figure 16**, describing the equivalent circuit of a porous electrode, including the ion transport in electrolyte-filled pores (R_{ion}) and the charge transfer resistance (R_{CT}) of the active material as well as its capacitance (Q_{CT}) , and the electron transport across the electrode (E_{el}). For typical battery electrodes, the electronic resistance across the electrode is significantly smaller than the ionic resistance across the electrode (i.e. $R_{el} << R_{ion}$), in which case the transmission line model is given by equation 3.2:[133]

$$Z_{TLM} = \sqrt{R_{ion}Z_{R/Q}}\ coth\left(\sqrt{\frac{R_{ion}}{Z_{R/Q}}}\right) \qquad 3.2$$

The charge transfer resistance (R_{CT}) of the active material can be derived from the difference of the low frequency resistance (*LFR*) and the high frequency resistance (*HFR*), which is obtained from the individual electrode impedance (see purple line in the Nyquist impedance plots of **Figure 17**). Therefore, R_{ion} needs to be determined separately under so called “blocking conditions” i.e. no faradaic reactions are possible. This is achieved by either using an electrolyte that does not contain any reactive species or recording the impedance at a potential where no faradic reactions occur e.g. before formation (the detailed procedure is described by Morasch et al.).[134]

If the ionic resistance is significantly smaller than the charge transfer resistance R_{CT} ($R_{CT} >> R_{ion}$), the impedance of the TLM can be simplified and is referenced to as the kinetically controlled regime. In this case, the electrode is entirely probed by the impedance measurement over the entire electrode thickness (see **Figure 17a**). This condition usually occurs for thin electrodes at low temperatures, where the charge transfer resistance R_{CT} is dominant compared to the ion transport resistance R_{ion}.

$$LFR - HFR = R_{CT} + \frac{R_{ion}}{3} \tag{3.3}$$

For the other case, when the ionic resistance is significantly larger than the impedance of the *R/Q* element ($R_{ion} >> Z_{R//Q}$), the impedance of the TLM can be reduced to equation 3.4. and is referred to as the transport-controlled regime (see **Figure 17c)**. In this case, the impedance signal does not penetrate the entire electrode thickness. It usually applies to thick electrodes, i.e. electrodes with high active material loadings and at high temperatures.

$$LFR - HFR = \sqrt{R_{ion}R_{CT}} \tag{3.4}$$

For the mixed regime, where the impedance response of the electrode is neither kinetically limited nor transport limited, the full expression of the equation must be used (see **Figure 17c**).

$$LFR - HFR = \sqrt{R_{ion}R_{CT}}\ coth\left(\sqrt{\frac{R_{ion}}{R_{CT}}}\right) \tag{3.5}$$

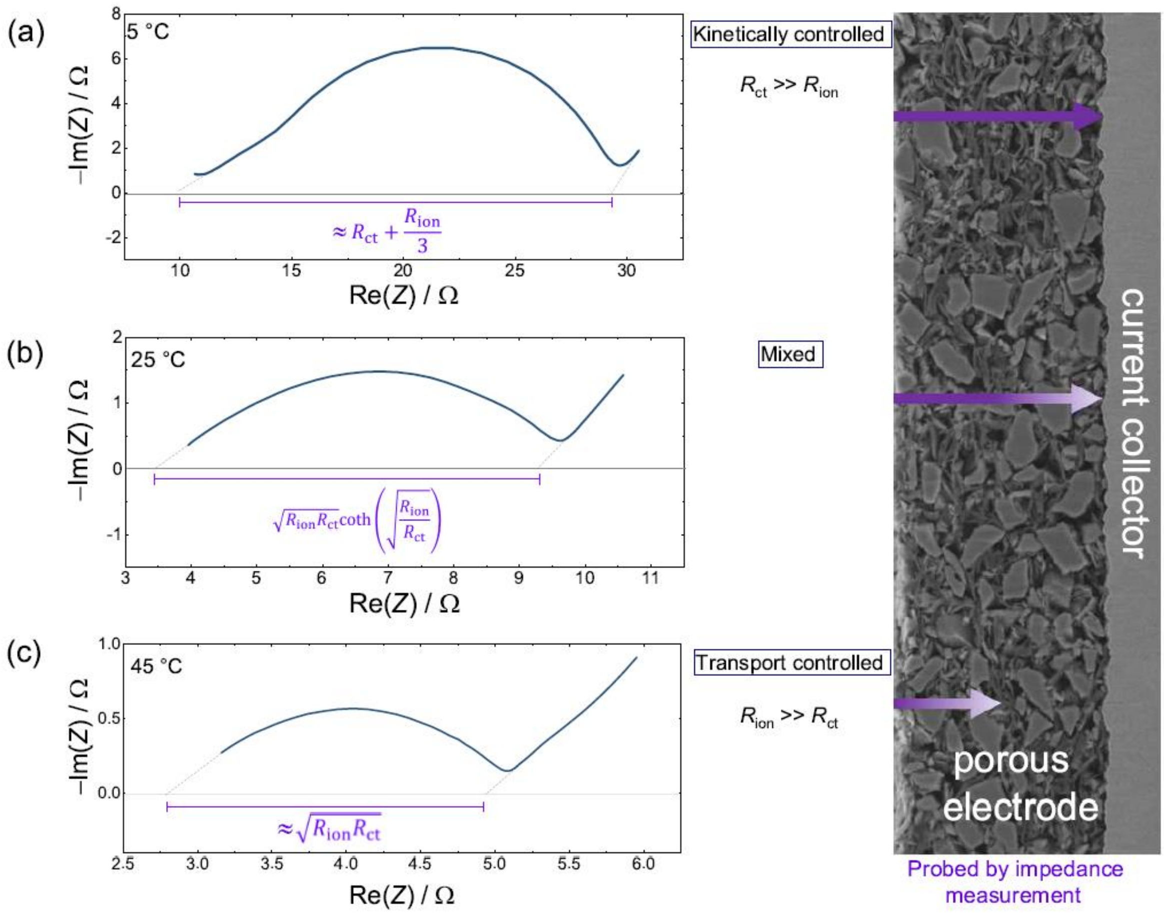

Figure 17 Nyquist impedance plot of a graphite electrode recorded with a gold wire reference electrode (GWRE), measured at 50% SOC at 5 °C, 25 °C and 45°C. Different impedance regimes can be observed at the different temperatures: kinetically controlled **(a)**, mixed **(b)**, and transport controlled **(c)**. For each regime, the value of the difference between the low- and high-frequency resistance (LFR-HFR) of the TLM is given in the Nyquist plot, and the scheme visualizes the corresponding probing depth in the electrode. The figure is reprinted with permission from "Rate Performance and Kinetics of Silicon and Graphite Anodes for Lithium-Ion-Batteries" by Clara Berg.[135]

3.0 Results

The following chapters presents the published results of this thesis. The chapters are thematically separated into three parts:

Chapter 3.1 describes the amorphization process of crystalline silicon using microscale silicon particles as anode active material. The study investigates the progress and degradation of the amorphization process using a partial lithiation strategy. The influence of electrochemical testing parameters, such as the lithiation cutoff potential, was examined using in-situ X-ray spectroscopy to monitor the amorphization process, this newly developed approach allowed to quantify the amount of crystalline and amorphous silicon present during cycling. Based on this study, new insights were gained with regard to the lithiation mechanism and the associated structural changes of µ-sized crystalline silicon particles that are cycled under partial lithiation conditions. The here developed hypothesis led to the initiation of more detailed studies based on high resolution TEM.[132]

Chapter 3.2 focuses on the effect of lithium nitrate ($LiNO_3$) as an electrolyte additive for silicon-based anodes. In this study, the reaction mechanism of the additive is investigated in detail using cyclic voltammetry experiments, X-ray photoelectron spectroscopy (XPS), and on-line electrochemical mass spectrometry (OEMS). $LiNO_3$, which so far has predominantly been used in ether- and ester-based electrolytes for lithium-sulfur (Li-S) or lithium-air batteries, also has remarkably performance-enhancing effect for silicon-based anodes in carbonate-based electrolytes. The results of this study give insights into the reaction principle and identify nitrite (NO_2^-) as one of the active intermediate species formed upon the initial reduction of

NO_3^-. Lithium nitrite ($LiNO_2$) was then directly used as an additive in the electrolyte and was tested in full-cells. The cells revealed a similar performance as the ones cycled with the lithium nitrate-containing electrolyte, validating the findings of the mechanistic investigations.

Chapter 3.3 comprehensively compares graphite and silicon-based anodes with a focus on the temperature-dependent kinetic charge-transfer resistance (R_{CT}) and their ion transport resistance across the electrode thickness through the electrolyte phase (R_{ion}) via impedance measurement. As the charge transfer resistance bears significantly higher activation energy, it is the dominating resistance at low temperatures. The graphite electrodes showed the lowest overall resistance at low temperatures as their charge transfer resistance is slightly smaller than that of silicon-based anodes. However, at elevated temperatures, the ionic resistance controls the overall resistance. The significantly thinner silicon anodes lead to a substantially lower R_{ion} of the silicon electrodes than graphite electrodes. The analysis shows how the contributions of R_{CT} and R_{ion} change from predominantly kinetically-limited at lower temperatures to transport-limited at higher temperatures. In addition, rate performance tests revealed lower overpotentials for the thinner silicon anodes, enabling higher C-rates, particularly during charging.

3.1 Amorphization mechanism of crystalline microscale silicon

The article “Effect and Progress of the Amorphization Process for Microscale Silicon Particles under Partial Lithiation as Active Material in Lithium Ion Batteries” was submitted to the peer-reviewed *Journal of the Electrochemical Society* in October 2021 and published online in February 2022.[39] The article was distributed under the terms of the Creative Commons Attribution 4.0 License, and its permanent weblink can be found at: https://iopscience.iop.org/article/10.1149/1945-7111/ac4b80. An oral presentation of this study was also presented by M. Graf at the PRIME 2020 Meeting of the *Journal of Electrochemical Society* in a virtual format. The link for the Abstract (MA2020-02 357) can be found at: https://iopscience.iop.org/article/10.1149/MA2020-022357mtgabs.

When used as active material in lithium-ion batteries, silicon undergoes significant volumetric changes upon (de-)lithiation. Several different material design strategies, briefly discussed in the introduction chapter, aim to mitigate or diminish the degradation phenomena concomitant with the expansion and contraction of silicon. This thesis focuses on the partial lithiation strategy for microscale silicon particles. Here, a part of the initially crystalline silicon particle remains over the course of extended charge/discharge cycling while the other part of the particle gets amorphized alongside the lithiation process. The preservation of the crystalline silicon phase is dependent on the applied lithiation end potential of the anode. The capacity of silicon anodes cycled to a lithiation cutoff potential of ≥170 mV vs. Li^+/Li remains constant after formation. However, the capacity of electrodes cycled to a cutoff potential <170 mV vs. Li^+/Li continuously increases for each cycle. This increase suggests a consumption of the inactive crystalline phase, in favor of the growth of the amorphous phase that becomes available for lithium (de-)alloying. An in-situ XRD-based method was employed in this study to quantify the consumption of the amorphous phase. For this, Si/Li pouch-cells with a lithium reference electrode were cycled to different lithiation cutoff potentials and measured at selected points in the procedure. To quantify the intensity changes of the silicon diffraction peak over cycling, the silicon diffraction peak intensities were referenced to that of copper derived from the copper current collector. This allows to correct for the absolute intensity variations between the measurements due to unintended but unavoidable variations in cell positioning and beam alignment. In accordance with the observations on the progress of the capacity, a decrease for the crystalline phase can be observed for cells cycled to a cutoff <170 mV vs. Li^+/Li, whereas cells with a cutoff ≥170 mV vs. Li^+/Li show a nearly constant amount of crystalline phase over cycling. While for a cell with the cutoff of 140 mV vs. Li^+/Li, the particle is amorphized to 75 % after 30 cycles, a cell with 170 mV vs. Li^+/Li as the cutoff potential, could retain the 35% amorphous phase, which was set during formation in the beginning. Interestingly, the capacity increase for the cell cycled to 140 mV reaches a peak after 15 cycles, with a decrease in capacity afterward. However, the amorphous phase quantified by XRD continuously increases. The extended capacity increase leads to the disintegration of the particles, causing electric disconnection and thus capacity loss. This could be further validated by cross-sectional SEM images from pristine electrodes and electrodes cycled to different cutoff potentials. The study shows the relevance of the lithiation cutoff potential to the amorphization level of crystalline silicon particles. With the XRD-based method developed in this study, we can quantify and analyze the amorphous phase. Via the quantification of the remaining crystalline phase, the findings help to better understand the degradation mechanisms with such material designs better and give guidance to improve the cycling protocols for cells with such materials.

Author contributions

M.G., R.B., S.H., J.P., and H.A.G. developed the concept of the in-situ XRD-based method. M.G. and C.B. conducted the electrochemical experiments, XRD measurements, and SEM images. M.G. analyzed the data and wrote the manuscript. H.A.G. edited the manuscript. All authors discussed the results and commented on the manuscript.

Journal of The Electrochemical Society, 2022 **169** 020536

Effect and Progress of the Amorphization Process for Microscale Silicon Particles under Partial Lithiation as Active Material in Lithium-Ion Batteries

Maximilian Graf,[1,*,z] Clara Berg,[1] Rebecca Bernhard,[2] Stefan Haufe,[2,]**
Jürgen Pfeiffer,[2] and Hubert A. Gasteiger[1,]**

[1] *Chair of Technical Electrochemistry, Department of Chemistry and Catalysis Research Center, Technical University of Munich, Munich, Germany*
[2] *Wacker Chemie AG, Consortium für Elektrochemische Industrie, Munich Germany*

Microscale silicon particles in lithium-ion battery anodes undergo large volume changes during (de)lithiation, resulting in particle pulverization and surface area increase concomitant with a continuous growth of the solid-electrolyte-interphase. One approach to overcome these phenomena is to operate the silicon anode under capacity-limited conditions (i.e., with partial capacity utilization). Since crystalline silicon is irreversibly transformed into amorphous phases upon lithiation, the purpose of the partial capacity utilization is to maintain a crystalline phase and thus prevent particle disintegration. Here, we investigate the amorphization process of micro-sized silicon particles in a silicon-rich anode (70 wt% silicon) over extended charge/discharge cycling in half-cells with a lithium reference electrode, varying the lower cutoff potential of the Si electrode. While the capacity of Si electrodes after formation remain constant for lithiation cutoffs of $\geqslant$170 mV vs Li^+/Li, their capacity continuously increases over cycling for cutoffs of <170 mV vs Li^+/Li, implying an ongoing amorphization of the crystalline phase. To quantify the ratio of the amorphous phase fraction over cycling, we employed an in-situ XRD method, utilizing the copper reflex of the current collector as internal standard. This allowed to determine the extent of amorphization over the course of cycling depending on the lithiation potentials.
[DOI: 10.1149/1945-7111/ac4b80]

Manuscript submitted October 27, 2021; revised manuscript received December 13, 2021. Published February 11, 2022. *This was Paper 357 presented during PRiME 2020, October 4–9, 2020.*

With a specific electrochemical capacity of 3579 mAh g_{Si}^{-1}, silicon is a promising candidate for next generation Li-ion batteries, as it exceeds the capacity of commonly used graphite by a factor of 10.[1,2] However, large volume changes upon (de-)alloying up to ~300 % lead to mechanical stress in the active material resulting in particle pulverization.[1,3] This causes the loss of electrical contact and excessive electrolyte reduction; the resulting excessive solid-electrolyte-interphase (SEI) formation still hampers a broad application of silicon as anode material up to now.[2,4–6] In the past, several strategies have been proposed to reduce the effect of the volume expansion. Among them, nanostructured silicon has shown to sustain the stress and reduce the degradation phenomena mentioned above.[7] The large surface area of pristine nanostructured silicon however is connected to significant SEI formation and therefore large irreversible lithium losses in the formation process.[6,8] In addition, large-scale production of nanostructured material designs remains difficult and expensive.

To compete against current graphite systems, the production of silicon material needs to be scalable and cost-effective. Microscale silicon particles which meet these requirements are therefore still in the focus of research. To overcome the aforementioned issues, innovative binder systems such as self-healing[9,10] or highly elastic polymers,[11] which can reduce the impact of the volume expansion for μm-sized particles, have been developed. Another promising concept is to use only a part of the total silicon capacity available and therefore reduce the volume expansion upon (de)lithiation, as demonstrated for both Si nanowires[12] and μm-sized silicon particles.[13–16] Some of these studies showed that limiting the utilized silicon anode capacity to 1200 mAh g_{Si}^{-1} (corresponding to ~30% of the theoretical capacity of Si) can improve the cycling stability and significantly reduces pulverization even of μm-sized Si particles.[13,15,16] Next to the limited volume expansion with this approach, another advantage is to prevent formation of the crystalline $Li_{3.75}Si$ phase at low voltages, which is associated with a large overpotential during delithiation.[17] The degree of utilization of silicon in full-cells can be controlled by the balancing of anode and cathode areal capacity, such that upon initial charging only a limited amount of silicon is converted to the amorphous phase, in which case a significant fraction of crystalline silicon could in principle be retained during cycling. As TEM measurements have shown that repeated (de)lithiation of only the amorphous phase results in isotropic expansion that is less prone to lead to particle cracking, whereas the anisotropic expansion of crystalline silicon leads to tensile stress and cracking,[18] retaining a crystalline phase in partially (de)lithiated silicon would be expected to be beneficial. Contrary to a fully amorphous Si particle where the restriction of the capacity would lead to a higher average anode voltage (i.e., to a lower achievable energy density), the crystalline phase in this approach acts as inactive phase.[2] Therefore, the phase composition of the lithiated Si-phase is richer in lithium compared to the case when the silicon particle is completely amorphous, and thus has a lower average anode voltage (i.e. to a higher achievable energy density). That partially lithiated μm-sized silicon particles would be able to retain a crystalline cores was deduced by Obrovac et al.[3] using electrochemical methods, suggesting that the crystalline silicon phase would be preserved for lithiation potentials of $\geqslant$170 mV vs Li^+/Li, where only the amorphous silicon phase is being lithiated. However, this conclusion was not confirmed by a direct quantification of the remaining crystalline phase over the course of extended charge/discharge cycling. Therefore, in this study, we present an in-situ XRD method to track the crystalline phase fraction of partially lithiated μm-sized silicon particles, investigating different lithiation potentials during cycling in relation to the amorphization progress of the remaining crystalline silicon. Furthermore, the degradation of the here used microscale silicon particles caused by progressive amorphization is analyzed, and implications on their cycle-life are discussed.

Experimental

Electrode preparation.—Silicon electrodes with graphite as conductive agent were prepared by suspending 7.0 g Si-powder (BET: 1.6

---

*Electrochemical Society Student Member.
**Electrochemical Society Fellow.
[z] E-mail: Maximilian.graf@tum.de

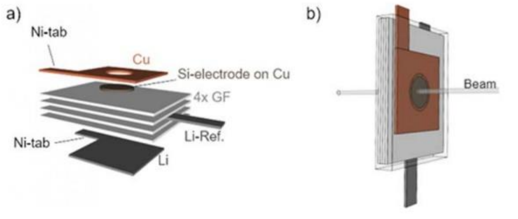

Scheme 1. Setup of the Si//Li pouch-cells for in-situ XRD measurements, (a) The cell is composed of a Li-metal (450 μm thick, 30 × 30 mm^2, 99.9%, Rockwood Lithium, USA) counter electrode (plotted at the bottom), 4 glassfiber separators (Whatman GD type A/E, 45 × 55 mm^2, USA), and a Si-KS6L working electrode (11 mm diameter) coated on a thin copper foil (11 μm). To connect the Si-KS6L working electrode with the Ni-tab, an additional copper foil was used (plotted at the top), containing a hole (10 mm diameter) that is slightly smaller than the size of the Si-KS6L electrode in order to allow for good electronic connection without reducing the X-ray beam intensity. The Li-reference, a Li-metal piece connected to a Ni-tab, was placed in between the glassfiber separators. (b) Configuration of the assembled cell, marking the position of the X-ray beam.

m^2 g^{-1}, d_{10} = 2.2 μm, d_{50} = 4.5 μm, d_{90} = 7.8 μm; CLM 00001, Wacker Chemie AG) in 5.1 g H_2O and 12.5 g of an LiPAA solution (4 wt%) in a dissolver mixer (Dispermat LC30, VMA-Getzmann). The LiPAA solution was prepared by neutralization of PAA solution (polyacrylic acid, M_v = 459 k, Sigma Aldrich) with lithium hydroxide (LiOH, Sigma Aldrich) to a pH of 7. In the next step, 2.5 g graphite (KS6L, Imerys) was added to yield a mass ratio of 70:25:5 Si/KS6L/LiPAA and stirring was continued at 12000 rpm for 30 min.

In addition, silicon model electrodes with carbon black (Super C65, Timcal) as conductive additive were examined, as they allow for a more rigorous analysis of the charge/discharge features of silicon due to the absence of the graphite-derived features in the electrodes with the KS6L graphite. For this, a suspension of 8.5 g Si-powder (CLM 00001, Wacker Chemie AG) in 20.0 g H_2O and 12.5 g of a LiPAA solution (4 wt%) was prepared in a dissolver mixer. Then, 1.0 g Super C65 was added and mixed for 3 × 5 min at 2000 rpm in a planetary mixer (Thinky Corp., USA), yielding a mass ratio of 85:10:5 Si/C65/LiPAA.

For degassing, the slurries were mixed at 2000 rpm for 5 min in a planetary mixer (Thinky Corp., USA). The slurries were coated onto a copper foil (15 μm) with a box-type coating bar (Erichsen, Hemer, Germany) using an automated coater (RK PrintCoat Instruments, UK), and dried at room temperature overnight. Electrodes with a diameter of 11.0 mm were punched out from the above prepared electrode coatings. After drying at 120 C under vacuum over night, the Si electrode coatings with graphite as conductive agent had a loading of 2.1 mg$_{Si}$ cm^{-2} (≡7.5 mAh cm^{-2} based on 3579 mAh g$_{Si}{}^{-1}$) and a thickness of ~34 μm, and will in the following be referred to as "Si-KS6L" electrodes. The electrodes with C65 as conductive additive had a loading of 1.4 mg$_{Si}$ cm^{-2} (≡5.0 mAh cm^{-2} based on 3579 mAh g$_{Si}{}^{-1}$) and a thickness of ~17 μm, and will in the following be referred to as "Si-C65." All electrodes were then transferred to an argon-filled glove box (<1 ppm O_2 and H_2O, MBraun, Germany) without exposure to air.

Cell-assembly.—Differential capacity analysis of the Si-C65 electrodes was conducted in half-cells using a spring-compressed Swagelok® T-cell setup with a metallic lithium reference electrode (RE). The cells were assembled with two glass fiber separators (Whatman GD type A/E, USA) and 90 μl 1M $LiPF_6$ in FEC:DEC 2:8 v/v (<20 ppm H_2O; Gelon, China) against metallic lithium (450 μm thick, 11 mm diameter, 99.9%, Rockwood Lithium, USA). Investigations on the cycling behavior with different lithiation cutoff potentials were conducted with Si-KS6L electrodes containing graphite as conductive agent, using the same cell setup.

In situ XRD experiments were performed on Si//Li pouch cells with a metallic lithium RE, using a thin pouch foil (12 μm thick Al layer) in order to reduce the attenuation of the X-ray beam and the intensity of the Al-derived diffraction peaks. Si-KS6L anodes with 11 mm diameter were assembled vs a lithium counter electrode (450 μm thick, 30 × 30 mm^2, 99.9%, Rockwood Lithium, USA) with four glass fiber separators (Whatman GD type A/E, 45 x 55 mm^2, USA) in 2000 μl 1M $LiPF_6$ in FEC:DEC 2:8 v/v (<20 ppm H_2O; (Gelon, China). A piece of lithium (10 × 5 mm^2) connected to a Ni-tab which was positioned between the separators was used as reference electrode. A sketch of the pouch cell configuration is shown in Scheme 1. To avoid the formation of mossy lithium on the Li-counter electrode, the cells were cycled in a homemade spring-loaded pouch cell holder with a compression of ~25 bar. For in-situ XRD measurements, cell-cycling was stopped at after delithiation to 1.5 V vs Li^+/Li, the pouch cell was removed from the spring-loaded holder and placed into a custom made XRD holder.

Cell testing.—All electrochemical cycling tests were performed in a climate chamber (Binder, Germany) at 25 °C, using a multi-channel potentiostat (Biologic VMP3).

To investigate the silicon phase transition in the dQ/dV plot, the Si-C65 model electrodes were initially lithiated to a specific capacity of 1500 mAh g$_{Si}{}^{-1}$ with constant current cycling at a rate of C/25 (based on 3579 mAh g$_{Si}{}^{-1}$), followed by delithiation to a cutoff potential of 1.5 V vs the lithium reference electrode. For the second cycle, the electrodes were cycled with a rate of C/25, in one case to the same specific capacity limit of 1500 mAh g$_{Si}{}^{-1}$, and in the other case to the lithiation cutoff potential of 170 mV vs Li^+/Li followed by delithiation to 1.5 V vs Li^+/Li.

To study the effect of varying lower lithiation cutoffs on the cycling behavior, the Si-KS6L silicon electrodes (70:25:5 Si/KS6L/LiPAA) were lithiated at a constant current rate of C/60 (based on 3579 mAh g$_{Si}{}^{-1}$) in the first cycle to a specific capacity limit of 600 mAh g$_{Si}{}^{-1}$ for one set of cells and to 1500 mAh g$_{Si}{}^{-1}$; the cells were then delithiated at C/60 until a cutoff of 1.5 V vs Li^+/Li. Subsequent cycling was conducted at C/60 to different lithiation cutoff potentials set in the range of 140-180 mV vs Li^+/Li with a CV step at the end of lithiation until a current of C/120; delithiation was again performed at C/60 until a cutoff of 1.5 V vs Li^+/Li. In order to ensure comparability between the capacity limit of 600 mAh g$_{Si}{}^{-1}$ and 1500 mAh g$_{Si}{}^{-1}$, the same absolute current densities are applied and therefore referred to the maximum theoretical capacity of 3597 mAh g$_{Si}{}^{-1}$ for clarification (i.e. C/60 corresponds to C/10 and C/25 when referred to the actual capacity usage of 600 mAh g$_{Si}{}^{-1}$ and 1500 mAh g$_{Si}{}^{-1}$ respectively).

For the in situ XRD experiments, Si-KS6L silicon electrodes were lithiated to either 600 mAh g$_{Si}{}^{-1}$ or 1500 mAh g$_{Si}{}^{-1}$ at C/60 (based on 3579 mAh g$_{Si}{}^{-1}$), followed by delithiation to 1.5 V vs Li^+/Li at C/60. Consecutive cycles of cells with the different first-cycle capacity limits were lithiated to either 170 mV vs Li^+/Li or 140 mV vs Li^+/Li with a rate of C/30 and a CV step at the end of lithiation until a current of C/120. Prior to the in-situ XRD measurements, the cells were put into open circuit voltage (OCV) hold at the end of selected lithiation cycles.

X-ray powder diffraction measurements.—The in–situ XRD study on the Si//Li pouch cells was performed using a STOE STADI P diffractometer (STOE & Cie GmbH, Darmstadt, Germany) in transmission mode using Mo-K$_{\alpha1}$ radiation (0.7093 Å, 50 kV, 40 mA) and a Mythen 1 K detector. For this, a cycled pouch cell was transferred from the spring-loaded pouch cell holder to a homemade holder for mounting the pouch cell to the diffractometer, equipped with 15 mm diameter holes in the holder fixture to give access to the X-ray beam (for details see reference Strehle et al.[19]). Data collection was performed after delithiating the cells to 1.5 V vs Li^+/Li and comprise the pristine cell (i.e. assembled cell before electrochemical testing), after cycle 1, cycle 11, cycle 21, cycle 31

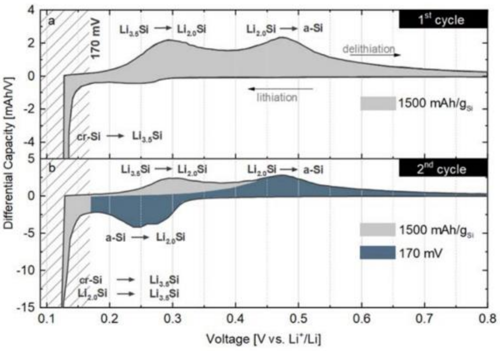

Figure 1. Differential capacity vs Li-Re curves obtained from constant current cycling (C/25, referenced to 3579 mAh g_{Si}^{-1}) of Si-C65//Li (1.4 mg_{Si} cm^{-2}, with a theoretical capacity of 5.0 mAh cm^{-2}) Swagelok® T-cells with a Li-RE: (a) First cycle where, the lithiation step was limited to 1500 mAh g_{Si}^{-1}, followed by consecutive delithiation to a cutoff potential of 1.5 V vs Li^+/Li measured against the Li-RE. (b) Second cycle, where the lithiation was limited either by a capacity cutoff of 1500 mAh g_{Si}^{-1} (gray area) or by a voltage cutoff of 170 mV vs Li^+/Li (blue area). Electrochemical testing was done at 25 °C with 1M $LiPF_6$ in FEC/DEC (2:8 v-v) and with two glassfiber separators.

and cycle 41. Measurements were conducted over night (~14 h) in a 2θ range of 12.5–39° with detector step size/step time of 0.06°/45 s.

The diffraction data were reduced with the software WinXPOW (V3.0.2.1, STOE & Cie GmbH, Darmstadt, Germany 2011) and refined with the software package Topas (TOPAS-Academic V6, Coelho Software, Brisbane, Australia 2016). Rietveld refinement was conducted for the silicon and copper phase using the Thompson-Cox-Hastings pseudo-Voigt function (TCHZ) to describe the peak profiles. The refinements included the following non-structural parameters:

- background: Chebyshev polynomial with 1 β parameters
- instrument: zero shift and axial divergence

The structure-related refinement parameters are the following:

- Cu (225, *Fm*3*m*)
  a. Lattice parameter a_{Cu} (=3.61 Å)
  b. Atomic displacement parameter b_{Cu} (=1.2 Å)
  c. TCHZ peak parameters V_{Cu}, Z_{Cu}, Y_{Cu} are fixed to (0/0/0)
  d. TCHZ peak parameters U_{Cu}, W_{Cu}, X_{Cu} are refined
- Si (227, *Fd*3*m*)
  a. Lattice parameter a_{Si} (=5.40–5.44 Å)
  b. Atomic displacement parameter b_{Si} is fixed to 0.5 Å
  c. TCHZ peak parameters V_{Cu}, Z_{Cu}, Y_{Cu} are fixed to (0/0/0)
  d. TCHZ peak parameters U_{Cu}, W_{Cu}, X_{Cu} are refined

SEM cross-sections.—Sample preparation and post-mortem SEM cross-sections were made at WACKER Chemie AG using a scanning electron microscope (Ultra 55 from Carl Zeiss Microscopy, Germany) with a thermal field emission cathode. The electrode samples were harvested from the cells, rinsed with 3 ml DMC in order to remove remaining conductive salt and dried for 12 h at RT under vacuum. After this, the electrodes were prepared for analysis in an argon filled glove box, and then transferred under inert atmosphere into an IonMill 4000 Plus (Hitachi High Technologies; 6 kV ion beam slope cutting). Via a specimen transfer module (Kammrath & Weiss), samples were transferred under argon atmosphere from the glove box to the measuring chamber of the SEM. Magnifications between 30 x and 30.000 x were chosen using the SE-mode (secondary electrons) at high vacuum (~10^{-6} mbar) with an energy of the electron beam of 3 kV.

Results and Discussion

Effect of lithiation capacity and potential cutoff on electrochemical behavior.—In the following, the lithiation and delithiation behavior of silicon and its phase transitions at different potentials is investigated with the Si-C65 model electrodes containing 85% silicon and 10% C65 as conductive agent, Fig. 1 shows the differential capacity (dQ/dV) plot of the first cycle of a Si-C65||Li Swagelok® T-cell with a Li-RE. In the pristine state, the silicon is present in its crystalline phase. Upon its initial lithiation, the alloying reaction of crystalline silicon with lithium takes place at a potential < 170 mV vs Li^+/Li, marked by the dashed area in the dQ/dV-plot shown in Fig. 1, leading to the formation of amorphous Li_xSi phase. The lithiation potential of crystalline silicon is often reported to be lower than 170 mV,[20,21] as this progress is kinetically hindered and therefore can lead to large polarizations depending on the applied current rate.[3] At very low currents, Limthongkul et al. reported that the first lithiation of crystalline silicon occurred at ~180 mV vs Li^+/Li.[22] In Fig. 1, the lithiation step is terminated at a specific capacity of 1500 mAh g_{Si}^{-1} that corresponds to 42% of the total theoretical capacity of 3579 mAh g_{Si}^{-1} (the maximum for the highest lithiated phase of $Li_{3.75}Si$), so that one would expect a significant fraction of the silicon particles to remain in their crystalline phase. During delithiation two distinct phase transition features can be observed in Fig. 1a between 200–400 mV and 400–600 mV vs Li^+/Li: the former can be ascribed to the delithiation of a higher lithiated phase ($Li_{3.5}Si$) to a lower lithiated phase ($Li_{2.0}Si$), the latter to the consecutive delithiation of the lower lithiated phase to a fully delithiated amorphous Si phase.[20,23–26] The presence of two delithiation features during the first delithiation implies that a highly lithiated phase ($Li_{3.5}Si$) is readily formed once the potential is reached where alloying of crystalline silicon is possible. This was also shown in solid-state NMR studies, where the amorphous phase formed upon lithiating the crystalline phase is highly lithiated, with an average composition of the Li_xSi phase corresponding to $x = 3.4 \pm 0.2$.[21] This is suggested to be due to the required large activation energy and therefore high concentration of Li atoms to break the Si-Si bonds in the crystalline phase.[18,27,28] Therefore, it is kinetically more favorable to first break the remaining Si-Si bonds within the amorphous phase before lithiating the unreacted crystalline Si framework.[29]

When limiting the subsequent second lithiation cycle again to a capacity of 1500 mAh g_{Si}^{-1}, as marked by the sum of the gray and blue area in Fig. 1b, the onset of a lithiation feature is now already observed at potentials below ~350 mV, which has been ascribed to the alloying reaction of the amorphous Si phase and lithium to form the lower lithiated phase with a composition of $Li_{2.0}Si$.[20,26] At potentials below 170 mV, a second feature similar to the one observed in the first cycle appears, corresponding to the further lithiation of crystalline silicon. During the subsequent delithiation, two features are observed again, confirming the formation of the $Li_{3.5}Si$ also in the second cycle when the second-cycle lithiation is terminated at the same capacity as for the first cycle (i.e., at 1500 mAh g_{Si}^{-1}). On the other hand, if the second lithiation cycle terminated at 170 mV, i.e., prior to the second lithiation feature (marked by the blue area in Fig. 1b), the higher lithiated $Li_{3.5}Si$ phase is not formed, and thus only the delithiation feature of the $Li_{2.0}Si$ phase is observed, which is in line with the findings of a former study.[30] In summary, for the capacity-limited lithiation the alloying reaction of crystalline silicon takes place also in the second cycle, implying that further amorphization of the crystalline Si phase is possible in the case of capacity limited cycling even in the second cycle. However, when terminating the second lithiation cycle at a cutoff of 170 mV, the formation of the lithium-rich $Li_{3.5}Si$ phase and thus the amorphization of the remaining crystalline silicon are prevented. In the following, varying lithiation potential cutoff limits are examined and their effect on the retention of the crystalline Si phase are discussed.

To determine the lower cutoff potential at which continuous amorphization of the crystalline silicon occurs upon cycling, Si||Li

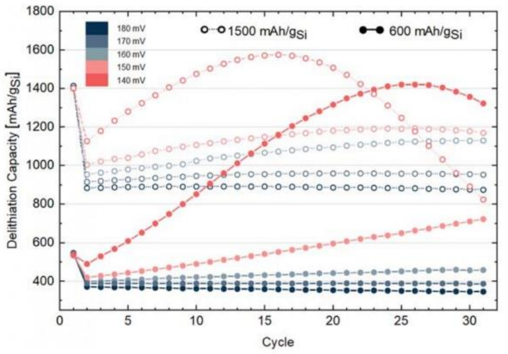

Figure 2. Delithiation capacity of Si-KS6L//Li (2.1 mg$_{Si}$ cm^{-2}, with a theoretical capacity of 7.5 mAh cm^{-2}) Swagelok® T-cells with varying lower cutoff limits for lithiation potentials (set between 180 mV vs Li$^+$/Li (blue) to 140 mV vs Li$^+$/Li (red)). Formation cycles were conducted at C/60 (referenced to 3579 mAh g$_{Si}^{-1}$) until a specific lithiation capacity of either 600 mAh g$_{Si}^{-1}$ (solid symbols) or 1500 mAh g$_{Si}^{-1}$ (open symbols) was reached. Subsequent cycling was conducted at C/60 with a CV step at the end of lithiation until a current of C/120, while delithiation was performed at C/60 until a cutoff of 1.5 V vs Li$^+$/Li. Experiments were conducted at 25 °C with 1M LiPF$_6$ in FEC/DEC (2:8 v-v) and with two glassfiber separators.

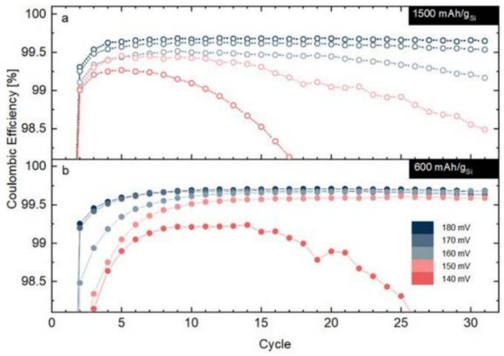

Figure 3. Coulombic-efficiency of the Si-KS6L//Li cells derived from the cycling data shown in Fig. 2 for the two different first-cycle lithiation capacities: (a) 1500 mAh g$_{Si}{}^{-1}{}_{i}$; (b) 600 mAh g$_{Si}^{-1}$. The coulombic-efficiency data is shown for varying lithiation cutoff potential limits ranging from 140–180 mV vs Li$^+$/Li (for further experimental details, see caption of Fig. 2).

cells with a Li-RE were cycled at C/60 with different lithiation cutoff potentials between 140 mV and 180 mV vs Li/Li$^+$ with respect to the Li-RE. To ensure a stable cycling performance, the Si-KS6L electrodes with conductive graphite additive are used instead of the Si-C65 electrodes, as the latter showed only poor cycling stability for longer cycling. It should be noted that the KS6L graphite here only acts as conductive additive, since at these high lithiation potentials the contribution of graphite to the overall electrode capacity are negligible. Figure 2 shows the cycling data for the cells limited to a specific lithiation capacity of either 600 mAh g$_{Si}^{-1}$ (solid symbols) or 1500 mAh g$_{Si}^{-1}$ (open symbols) in the first lithiation cycle, leading to different initial ratios of amorphous and crystalline phase in the first cycle.

For the cells cycled to an initial lithiation capacity of 600 mAh g$_{Si}^{-1}$, the cutoff potentials of 180 and 170 mV (dark blue and blue solid symbols in Fig. 2) show a stable cycling behavior with no capacity increase over 31 cycles. Lowering the lithiation cutoff potential to below 170 mV leads to a continuous capacity increase (light blue, light red, and red solid symbols). Therefore, the lower the cutoff potential, the more pronounced is the capacity increase over cycling, which is in good agreement with the results from Obrovac et al., who reported the same behavior for cells with μm-sized silicon particles cycled to below 170 mV.[3] For the cell with the lowest cutoff potential of 140 mV (red solid symbols), the rate of capacity increase upon cycling decreases until after ~25 cycles the capacity starts to decrease slightly. We believe that at this point a substantial fraction of the crystalline silicon phase has been consumed, so that the mechanical integrity of silicon particles cannot be maintained anymore, leading to degradation and capacity loss. Cells initially lithiated to 1500 mAh g$_{Si}^{-1}$ also show no capacity increase for lithiation cutoff potentials of 170 and 180 mV (dark blue and blue open symbols in Fig. 2) as well as a gradual capacity increase at lower cutoff potentials. For the lowest cutoff potential of 140 mV (dark red open symbols), the rate of capacity increase again gradually declines until the capacity starts to rapidly decrease after ~15 cycles, analogous but more pronounced compared to what was observed for the cells lithiated to an initial capacity of 600 mAh g$_{Si}^{-1}$. This can be explained by the higher amorphous phase fraction formed when the initial lithiation capacity is higher, so that upon continuous cycling to low cutoff voltages the stabilizing crystalline silicon phase gets depleted below a critical amount at a lower number of cycles.

The coulombic efficiency (CE) of the above described Si-KS6L//Li cells is shown in Fig. 3. For both of the initial lithiation capacities of 1500 mAh/g$_{Si}$ (Fig. 3a) and 600 mAh/g$_{Si}$ (Fig. 3b), cells with a cutoff lithiation potential of 180 and 170 mV reveal the highest CE (dark blue an blue symbols), exceeding 99.5% in the third cycle and beyond. On the other hand, lower lithiation cutoffs lead to a proportionally decreasing CE, particularly observed for the cells initially lithiated to 1500 mAh g$_{Si}^{-1}$. This, we believe, is due to silicon particle cracking upon depletion of the stabilizing crystalline silicon phase, leading to enhanced SEI growth and/or a loss of electronic contact of the fractured silicon particles.

To further examine the effect of the lithiation cutoff potential on the amorphization of the silicon particles, we compare the dQ/dV plots over cycling with two different lithiation cutoff potentials, namely with 170 mV and 140 mV, representing two different characteristics: for the former, the capacity remains constant over cycling, while for the latter a continuous capacity increase over cycling is observed, ultimately followed by rapid decrease of the capacity and the CE (see Figs. 2 and 3). Figure 4 depicts the dQ/dV plot of the Si-KS6L/Si cells with a cutoff of 170 mV (blue) and 140 mV (red) over the course of 31 cycles, exemplarily shown for the cells with an initial lithiation capacity of 1500 mAh g$_{Si}^{-1}$ (derived from the data shown in Fig. 2). As already observed for the Si-C65 model electrodes examined in Fig. 1, for a lithiation potential cutoff of 170 mV, only one delithiation feature representative of the delithiation of the Li$_{2.0}$Si phase is observed, implying that the lithiation cutoff potential was too high for the formation of the Li$_{3.5}$Si phase. In this case, the dQ/dV features remain unchanged over the course of the 31 cycles, indicating that the fraction of the amorphous phase does not increase.

On the other hand, when the lithiation potential cutoff is decreased to 140 mV (red lines), the Li$_{3.5}$Si feature during delithiation is increasing over the course of cycling, together with the Li$_{2.0}$Si (de)lithiation features. This continuous increase of the capacity associated with the Li$_{2.0}$Si features can only be explained by a growth of the fraction of the amorphous phase of the silicon particles. Thus, the continuous lithiation of the crystalline silicon phase and the associated formation of an amorphous silicon phase over the course of cycling seems to occur once the Li$_{3.5}$Si feature starts to evolve, implying that the formation of the Li$_{3.5}$Si phase is required for the lithiation of the crystalline silicon phase. These observations support the conclusions that a high lithium

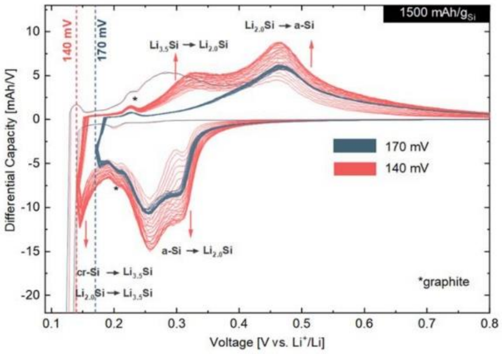

Figure 4. Differential capacity vs Li-RE curves obtained from constant current cycling (C/60, referenced to 3579 mAh g_{Si}^{-1}) of Si-KS6L//Li Swagelok® T-cells lithiated in the first cycle to 1500 mAh g_{Si}^{-1} and subsequently cycled to two different lithiation potential cutoffs: 170 mV vs Li^+/Li (blue) and 140 mV vs Li^+/Li (red); note, the lithiation potential was held until the current decayed to C/120. The delithiation was terminated by a cutoff potential of 1.5 V vs Li^+/Li measured against the Li-RE. The plot is derived from the measurements shown in Fig. 2. The asterisk marks the features due to the graphite component in the electrode.

concentration is needed to break the silicon bonds for the alloying reaction of crystalline silicon with lithium.[18,21,27–29]

***Effect of lithiation capacity and potential cutoff on the silicon particle morphology.*—**In the following, the effect of different cutoff potentials on the silicon particle morphology is investigated and discussed. Figure 5 shows the cross-sectional view of a pristine Si-KS6L electrode and of electrodes harvested after 31 cycles with cutoffs at 170 mV and 140 mV according to the measurements shown in Fig. 2. In the pristine electrode the silicon particles appear in bright gray and exhibit a smooth homogeneous cross sectional surface with no cracks, while the graphite flakes appear in darker gray (see upper and lower panel of Fig. 5a). For both initial lithiation capacities of 600 mAh g_{Si}^{-1} and 1500 mAh g_{Si}^{-1}, silicon particles appear in the delithiated state in bright grey and the graphite flakes in darker grey. The Si-KS6L electrodes harvested after 31 cycles with a lithiation potential cutoff of 170 mV show some minor cracks primarily near the surface of the silicon particles (see upper and lower panels of Figs. 5b and 5c), especially for the cell cycled to 1500 mAh g_{Si}^{-1}. Independent of their initial lithiation capacities, however, the cores of the silicon particles appear to be without structures and cracks, resembling the characteristics of the pristine silicon particles.

In contrast, the silicon particles of the harvested Si-KS6L electrodes cycled with a lithiation cutoff potential of 140 mV reveal a highly structured particle cross-section throughout the whole core of the silicon particles, and only isolated segments of non-structured areas can be observed. This structuring was observed for ~50% of the silicon particles in the cross-sectional images, indicating an inhomogeneous degradation of the silicon particles. This could be explained by the polycrystalline nature of the pristine silicon material, as different crystal orientations show varying lithiation kinetics.[31] The electrodes with 600 mAh g_{Si}^{-1} and 1500 mAh g_{Si}^{-1} harvested after 31 cycles exhibit the same extent of structured areas, which is consistent with the cycling data shown in Fig. 2: while the capacity gain of the cell with 600 mAh g_{Si}^{-1} and a lithiation cutoff potential of 140 mV is larger compared to the one with 1500 mAh g_{Si}^{-1}, the maximum capacity reached is almost the same for both electrodes, suggesting similar extents of particle fracturing. In summary, the cross-sectional views of the silicon particles of the cycled electrodes display a significant degradation of the silicon particles for cells cycled to a lithiation cutoff potential of 140 mV, while no pronounced morphological changes of the silicon particles are observed when the lithiation cutoff potential is restricted to 170 mV.

***XRD analysis on the effect of lithiation capacity and potential cutoff.*—**To further understand and validate the conclusions with regards to the amorphization of the silicon particles upon cycling that were drawn from the analysis of the dQ/dV and the cycling experiments with different lithiation cutoff potentials, we now want to follow the cycling-induced amorphization process of the Si particles by quantifying the amount of the crystalline silicon phase in the pristine and cycled electrodes. For this, in-situ X-ray diffraction (XRD) data were acquired from Si-KS6L/Li pouch cells with a Li-RE, whereby the cells were cycled according to the cycling procedure shown in Fig. 2. The cells were cycled in a pouch cell

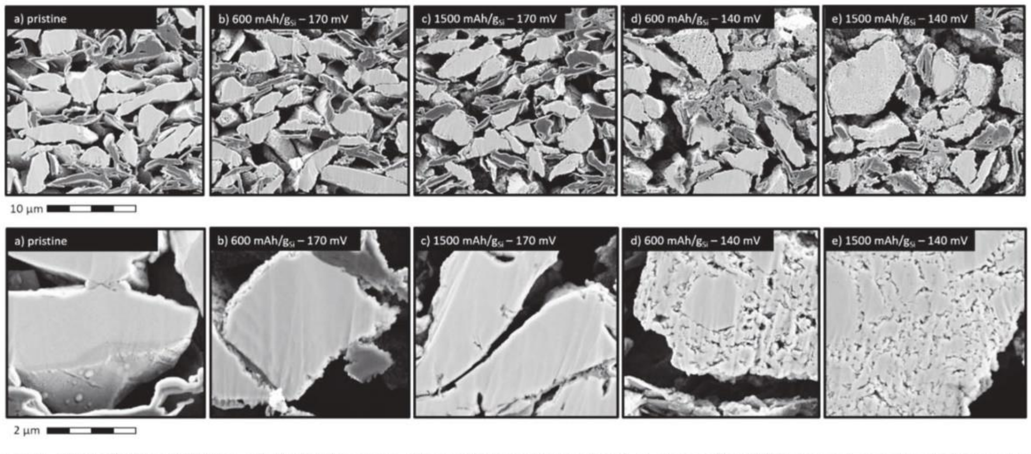

Figure 5. Effect of different lithiation cutoff potentials on the silicon particle morphology based on cross-sectional SEM images (secondary electron mode at 3 kV) of Si-KS6L electrodes in their pristine state or harvested after 31 cycles: (a) pristine electrode; (b) initial lithiation of 600 mAh g_{Si}^{-1} and cycling with a lithiation cutoff potential of 170 mV; (c) initial lithiation of 1500 mAh g_{Si}^{-1} and cycling to 170 mV; (d) initial lithiation of 600 mAh g_{Si}^{-1} and cycling to 140 mV; (e) initial lithiation of 1500 mAh g_{Si}^{-1} and cycling to 140 mV.

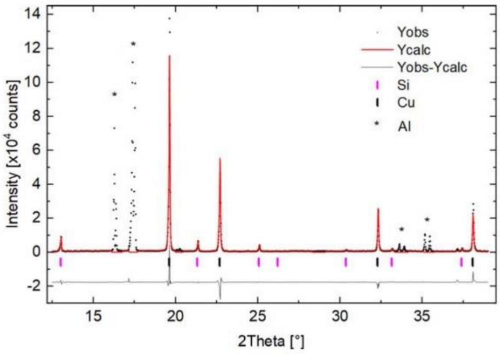

Figure 6. In situ XRD data (black data points) obtained from a pristine Si-KS6L//Li-pouch cell, including a Rietveld refinement fit (red line) and the difference plot (thin black line). Data were collected on an in-house diffractometer in transmission mode using Mo-K$_{\alpha 1}$ radiation. The vertical ticks mark the Bragg peaks of silicon (magenta) in the electrode and of copper (black) from the anode current collector; the asterisks mark the aluminum reflections from the pouch foil. Note that for the refinement only silicon and copper reflections are considered, i.e., the regions near the aluminum peaks were omitted from the fit.

holder (compressed at ~25 bar) and then, either after the first formation cycle (cycle #1) or after sets of 10 cycles (i.e., cycle #11, #21, etc.), they were transferred in their delithiated state to the XRD sample holder for XRD analysis. For the quantification, the cell was also analyzed in the pristine state and the data are reported as cycle #0. To ensure the very same beam position at the electrode within one measurement series of a cell, the exact position of the pouch cell in the XRD holder was marked on the pouch foil on each cell.

Figure 6 shows the diffraction pattern (black dots) of a pristine Si-KS6L/Li pouch cell, where next to the diffraction peaks of crystalline silicon (reflections marked by the magenta ticks), one can observe the copper diffraction peaks from the silicon anode current collector (marked by the black ticks) and the aluminum diffraction peaks from the pouch foil (marked by asterisks). To quantify the amount of crystalline silicon that is being retained over cycling, the silicon diffraction intensity of cells after formation or after cycling is analyzed and referenced to the silicon diffraction intensity obtained with the pristine cell. In order to account for absolute changes of the intensities between each measurement due to small variations of the incident beam intensity, the silicon reflex intensity was referenced to an internal standard. For this, we used the copper diffraction intensity from the Si-KS6L electrode current collector as internal standard, i.e., normalizing the silicon diffraction intensity to the copper diffraction intensity. Previous studies in the literature used nickel powder that was mixed into the silicon electrode as an internal standard in order to conduct quantitative ex-situ XRD experiments with electrodes harvested after lithiation, thereby determining the Li_xSi phases that coexist with crystalline silicon (cr-Si) during the initial lithiation of crystalline silicon.[22] While this is a viable approach, the in-situ XRD method used in the present study is non-destructive and allows for multiple measurements over extended charge/discharge cycling. In addition, using the copper current collector as internal standard eliminates the need for adding an internal reference, so that practically relevant electrodes can be investigated.

The quantification of the diffraction intensities was done by Rietveld refinement of the crystalline silicon and copper phases, and an exemplary Rietveld fit for a pristine Si-KS6L/Li pouch cell is given by the red line in Fig. 6, together with the difference diffraction profiles (thin black line). With the scale factors obtained from the Rietveld fit, the weight percent of the silicon (wt% cr-Si) and the copper phase (wt% Cu) can be deduced and the values are listed in Table I for the different cells and cycles each. The givens errors are based on the error propagation of the refined scale factors by TOPAS. Based on the densities of copper and silicon and a loading of 2.1 $mg_{Si}\ cm^{-2}$ and a copper foil thickness of 11 μm, the expected weight percent of the silicon phase of the pristine cell would be 17.6 % and for the copper phase 82.4 %, this is in good agreement with the experimental values obtained from the measurement (Table I). To quantify the amount of crystalline silicon being consumed during cycling, first the ratio χ of wt% cr-Si with respect to the wt% Cu is calculated by Eq. 1 for each cycle x.

$$\chi_x = \frac{(\text{wt\% cr}-\text{Si})_x}{(\text{wt\% Cu})_x} \qquad [1]$$

Comparison of the ratio χ_x from cycle x to the ratio χ_0 from cycle 0—determined by the weight percent of the silicon and copper phase of the pristine cell before formation—allows to calculate the relative fraction of crystalline silicon (cr—Si) being present at the respective

Table I. Weight percent of crystalline silicon phase (wt% cr-Si) and copper phase (wt% Cu) received by Rietveld refinement of in-situ XRD measurements of pouch cells cycled to 170 mV and 140 mV for 600 mAh g_{Si}^{-1} and 1500 mAh g_{Si}^{-1} initial capacity limit respectively. With Equation 3 the values can be converted into the relative fraction of amorphous silicon phase (a-Si) compared to the crystalline phase being present at each cycle displayed in Fig. 8b. Errors of wt% Cu and wt% cr-Si are based on the errors of the refinement of the scale factors by TOPAS, the error of a-Si was done by error propagation accordingly.

	Cycle 0	Cycle 1	Cycle 11	Cycle 21	Cycle 31	Cycle 41
600 mAh/g_{Si} – 170 mV						
wt% Cu [%]	83.95 ± 0.3	85.52 ± 0.3	85.24 ± 0.4	85.15 ± 0.4	85.55 ± 0.4	85.46 ± 0.3
wt% cr-Si [%]	16.05 ± 0.3	14.48 ± 0.3	14.76 ± 0.4	14.85 ± 0.4	14.45 ± 0.4	14.54 ± 0.3
a-Si [%]	0	11.42 ± 2.3	9.40 ± 2.8	8.78 ± 2.6	11.66 ± 2.8	11.00 ± 2.1
1500 mAh/g_{Si} – 170 mV						
Cu content [%]	84.32 ± 0.4	89.12 ± 1.1	89.40 ± 0.5	89.13 ± 0.5	89.51 ± 0.6	89.71 ± 0.5
Si content [%]	15.68 ± 0.4	10.88 ± 1.1	10.60 ± 0.5	10.87 ± 0.5	10.49 ± 0.6	10.29 ± 0.5
a-Si [%]	0	34.39 ± 7.9	36.23 ± 3.5	34.39 ± 3.3	36.98 ± 4.1	38.36 ± 3.4
600 mAh/g_{Si} – 140 mV						
Cu content [%]	82.76 ± 0.4	84.77 ± 0.5	86.10 ± 0.5	86.32 ± 0.4	87.83 ± 0.4	89.66 ± 0.5
Si content [%]	17.24 ± 0.4	15.23 ± 0.5	13.90 ± 0.5	13.68 ± 0.4	12.17 ± 0.4	10.33 ± 0.5
a-Si [%]	0	13.77 ± 3.1	22.49 ± 3.2	23.94 ± 2.7	33.47 ± 2.4	44.67 ± 3.1
1500 mAh/g_{Si} – 140 mV						
Cu content [%]	85.21 ± 0.4	89.91 ± 0.6	91.20 ± 0.5	93.24 ± 0.6	96.12 ± 0.4	/
Si content [%]	14.79 ± 0.4	10.09 ± 0.6	8.80 ± 0.5	6.76 ± 0.6	3.88 ± 0.4	/
a-Si [%]	0	35.38 ± 4.3	44.47 ± 3.4	58.24 ± 4.2	76.77 ± 2.7	/

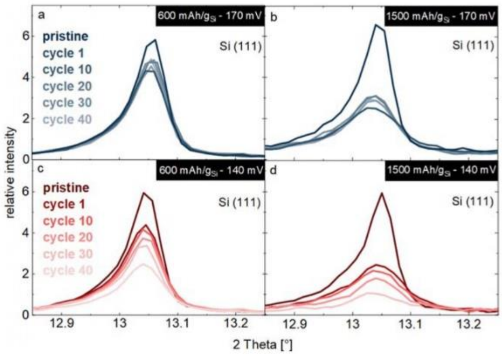

Figure 7. Magnified view of the silicon (111) reflection from in-situ XRD data of Si//Li-pouch cells cycled to a lithiation cutoff of 170 mV (a), (b) and 140 mV (c), (d) for both initial lithiation capacities of 600 mAh g_{Si}^{-1} and 1500 mAh g_{Si}^{-1}. Data were collected in the delithiated state and is shown for the pristine cell, after the first cycle and after each 10 cycles for further cycling. Intensity is normalized to the copper (111) reflection which is set to 100 counts.

cycle compared to the pristine state of the cell (Eq. 2).

$$\text{cr-Si} \equiv \frac{\chi_x}{\chi_0} = \frac{\dfrac{(\text{wt\% cr} - \text{Si})_x}{(\text{wt\% Cu})_x}}{\dfrac{(\text{wt\% cr} - \text{Si})_0}{(\text{wt\% Cu})_0}} = \frac{(\text{wt\% cr} - \text{Si})_x}{(\text{wt\% cr} - \text{Si})_0} * \frac{(\text{wt\% Cu})_0}{(\text{wt\% Cu})_x} \tag{2}$$

The relative fraction of amorphous silicon (a-Si) present at cycle x can then be calculated according to Eq. 3 and are listed in Table I.

$$a\text{-Si} \equiv 1 - \frac{\chi_x}{\chi_0} = 1 - \frac{(\text{wt\% cr} - \text{Si})_x}{(\text{wt\%cr} - \text{Si})_0} * \frac{(\text{wt\% Cu})_0}{(\text{wt\% Cu})_x} \tag{3}$$

(Table I) XRD spectra were taken from cells cycled to 170 mV and 140 mV each for both initial lithiation capacities of 600 mAh g_{Si}^{-1} and 1500 mAh g_{Si}^{-1}. To display the course of the silicon reflex intensity over cycling the most prominent silicon reflection (111) is shown for each cycle in Fig. 7, whereby the reflex intensity is normalized by the copper (111) reflection which is set to 100. The cycling data of these cells is shown in Figure 8a and is in good agreement with the data obtained by the T-cell setup depicted in Fig. 2. Cells cycled with a 170 mV cutoff maintain a constant horizontal capacity course over cycling whereas cells cycled with a cutoff potential of 140 mV exhibit a constant increase until a maximum capacity is reached, followed by a capacity drop. Figure 7a displays the silicon (111) reflection of the cell with an initial capacity of 600 mAh g_{Si}^{-1} and 170 mV cutoff. The pristine state exhibits the highest reflex intensity since the entire silicon is present in its crystalline phase. The silicon reflection obtained after the first cycle shows a decreased intensity for the formation of amorphous silicon phase upon lithiation to 600 mAh g_{Si}^{-1}. For continuous cycling with a cutoff of 170 mV, the measured intensity after every 10 cycles remains equal to the first cycle and does not decrease further on, thus no more additional crystalline silicon is consumed within the investigated numbers of cycles. The cell with an initial capacity of 1500 mAh g_{Si}^{-1} and a cutoff of 170 mV (Fig. 7b) shows the same behavior, even though the reduction of the silicon reflex intensity is more pronounced after the first cycle which is due to the higher initial capacity used in this case. This correlates well with the cycling data received for 170 mV where for both initial capacities 600 mAh g_{Si}^{-1}. and 1500 mAh g_{Si}^{-1} the capacity does not further increase over cycling. Next we want to look at the cells cycled to 140 mV depicted in Figs. 7c and 7d, while the reflex intensity for the first cycle of these cells is analogous the cells described above—as we would expect it since the first cycle is limited by the capacity—the course for the following cycles differ from the cells with a 170 mV cutoff. Here, we observe a significant decrease of the intensity after every 10th cycle, indicating further loss of crystalline phase during cycling. This matches well with the increasing capacity for the cells cycled with a 140 mV cutoff. The XRD data shown here correlate well with the cycling data and reveal a continuous consumption of crystalline phase for the cells cycled to 140 mV whereas cells cycled to 170 mV maintain the amount of crystalline silicon present after the initial cycle.

As described above the loss of crystalline phase during cycling can be quantified by Eq. 2 and is depicted in Figure 8b as the fraction of amorphous phase being present at the corresponding cycle for each cell. After the first lithiation we got a discharge capacity of 526 mAh g_{Si}^{-1} and 1370 mAh g_{Si}^{-1} for the cells lithiated to 600 mAh g_{Si}^{-1} (closed symbols) and 1500 mAh g_{Si}^{-1} (open symbols) respectively. Referring this to the theoretical capacity of the highest lithiated amorphous phase, which was observed by the Dahn group[17] to be $Li_{3.5}Si$ (3350 mAh g_{Si}^{-1}), this would equate to 16% and 41% amorphous phase being present after the first cycle. The experimental values derived by the XRD data show a slightly lower ratio compared to the calculated values, here 11 ± 0.2 % and 14 ± 0.3 % of a-Si is obtained for the cells lithiated to 600 mAh g_{Si}^{-1} and 34 ± 0.8% and 35 ± 0.4 % for cells lithiated to 1500 mAh g_{Si}^{-1}. Since the lithiation end potential of the first cycle is significantly lower than for consecutive cycling, capacity contribution from the graphite is more pronounced in this case. Nevertheless, correcting for the graphite capacity affects the calculated values for the expected amount of amorphous phase only marginally. Taking into consideration that the electrodes contain 25 wt% of graphite and the capacity contribution of graphite is 105 mAh g_C^{-1} at the lithiation end potential of 95 mV vs Li^+/Li for the first cycle, the lithiation degree of silicon is slightly decreased considering the graphite contribution. Therefore, the amorphous phase of the cell with 600 mAh/g_{Si} is calculated with 15% instead of 16% and the ratio of amorphous phase for the cell with 1500 mAh g_{Si}^{-1} gives 40% instead of 41%. Hence, this cannot explain the lower values obtained for the a-Si phase by the experimental data, however this does not affect the observations on the progress of the amorphous phase over cycling.

As already indicated in Fig. 7, the cells cycled to 170 mV (blue symbols) remain a constant ratio of amorphous phase once the initial lithiation cycle is conducted, however the ratio of the cells cycled to 140 mV (red symbols) constantly increases and follows almost the progress of the capacity throughout cycling. In the case of the cell with 600 mAh g_{Si}^{-1}, the ratio of a-Si increases from 14% after the first cycle to 45% after 41 cycles corresponding to a growth of 31% for the amorphous phase. While for the cell with 1500 mAh g_{Si}^{-1} the capacity only increases up to cycle 15 until the capacity drop again - this was already observed in the T-cell setup and discussed above (Fig. 2)—the amount of a-Si further increases. Here the extended capacity usage leads to electrical disconnection of particles causing the collapse of the cell, however crystalline silicon is still present and can be further consumed. At the breakdown of the cell ~50% amorphous phase is determined. This increases further up to 77% for cycle 31 until the sealing of the pouch cell opened due to excessive gas evolution. The cross sectional views in Fig. 5 revealed an increased surface of the silicon particles for the cells cycled to 140 mV, excessive electrolyte reduction on this surface could give an explanation for the gassing of this cell. The XRD data show that cycling silicon only to a lithiation potential of 170 mV allows to maintain the ratio of amorphous phase set in the first cycle with the capacity limit, hence decreasing the lithiation cutoff below 170 mV lead to an ongoing amorphization process during cycling causing a rapid capacity drop once the amorphous phase exceeds a critical ratio.

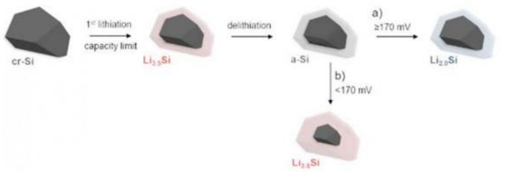

Scheme 2. Progress of the crystalline phase (opaque) and amorphous phase (transparent) of silicon particles upon (de)lithiation. The first lithiation is limited by the capacity forming a particle with remaining crystalline phase and a highly lithiated amorphous phase $Li_{3.5}Si$ (red). For further cycling the progress is shown for case of (a) a cutoff potential of $\geqslant$170 mV vs Li^+/Li, here the crystalline phase is maintained and only the lower lithiated phase $Li_{2.0}Si$ (blue) is formed. In the case of (b) the cutoff potential is limited to $<$170 mV vs Li^+/Li causing continuous amorphization of the crystalline phase and forming the highly lithiated $Li_{3.5}Si$.

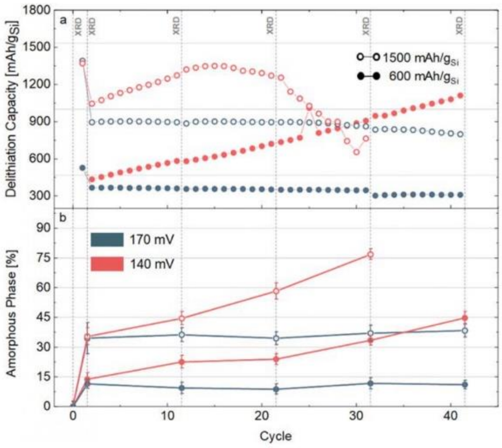

Figure 8. (a) Delithiation capacity of Si//Li pouch-cells (loading: 2.1 mg_{Si} cm^{-2}; with a theoretical capacity of 7.5 mAh cm^{-2}) with a lower cutoff limit for lithiation of either 140 mV vs Li^+/Li (red) or 170 mV vs Li^+/Li (blue) for initial lithiation capacities of 600 mAh g_{Si}^{-1} (closed symbols) and 1500 mAh g_{Si}^{-1} (open symbols). Formation cycles were conducted by cycling at C/60 (with constant-current (CC) lithiation and delithiation), while subsequent cycling was conducted at C/30 with a CV step at the end of lithiation until a current of C/120 (C-rates are referenced to 3579 mAh g_{Si}^{-1}). Experiments were conducted at 25 °C with 1 M $LiPF_6$ in FEC/DEC (2:8 v-v) and with four glassfiber separators (Whatman GD type A/E). (b) Percentage of amorphous Si phase to crystallinic Si and normalized capacity of Si//Li pouch-cells with a lower cutoff limit for lithiation of 140 mV vs Li^+/Li (red) or 170 mV vs Li^+/Li (blue). Ratio of amorphous phase was derived by Rietveld-Refinement of the Si and Cu phase of in-situ X-ray diffraction measurements collected at the in-house Mo-diffractometer (λ = 0.7093 Å). Errors bars are min/max values and are based on the error propagation of the refinement of the scale factors by the TOPAS software.

As a result of this study Scheme 2 depicts the amorphization progress of silicon with a capacity limited material concept adapted from Obrovac et al.,[3] whereby we have added the here estimated Li_xSi phase compositions. Upon first lithiation, crystalline silicon readily forms the highly lithiated $Li_{3.5}Si$ since both the lithiation reaction of cr-Si and the formation of $Li_{3.5}Si$ occur at the same potential, consecutive delithiation results in a two phase particle morphology with crystalline and amorphous silicon. The crystalline phase –preventing the particles to disintegrate- can be maintained by limiting the lithiation potential to 170 mV for further cycling, with this only the first lithiation feature of $Li_{2.0}Si$ is observed.[25] However, when cycling with a cutoff below 170 mV the higher lithiated phase $Li_{3.5}Si$ is formed and ongoing consumption of remaining crystalline phase is observed causing a rapid cell failure once a critical amount of amorphous phase is reached.

Conclusions

In the present study, the amorphization process of partially lithiated silicon anodes is investigated by in-situ X-ray diffraction. First, electrochemical cycling to different lithiation cutoff potentials was analyzed and discussed. With in-situ X-ray diffraction we tracked the ratio of the amorphous and the crystalline silicon phase present during cycling, investigating different lithiation cutoff potentials. The here presented in-situ method is based on the direct measurement of the amount of the crystalline silicon phase, quantified by referencing the silicon reflex intensity to that of the copper current collector that is utilized as internal standard.

The electrochemical cycling showed a continuous capacity increase for cells cycled to a lower lithiation potential of $<$170 mV vs Li^+/Li. Evaluation of the dQ/dV plot of these cells showed the features of the formation of a highly lithiated $Li_{3.5}Si$ phase at these potentials.[20,25,26] The cells cycled only to a potential of 170 mV or higher did not show the characteristic (de-)lithiation features for this highly lithiated phase and revealed a constant delithiation capacity course over the course of cycling. XRD experiments proved that cells cycled to a lithiation cutoff potential of 170 mV maintain the ratio of amorphous and crystalline phase which was set for the capacity-limited formation cycle. On the other hand, cells cycled to 140 mV reveal a constant decrease of the crystalline silicon phase, concomitant with an initial increase of the delithiation capacity over cycling, followed by a rapid capacity decrease. These results are in good agreement with the findings of a previous study by Obrovac and Krause,[3] and confirm that further amorphization of the silicon particles along with an increase of the delithiation capacity will occur for cutoff potentials below 170 mV. Post mortem analysis of harvested electrodes showed severe degradation of the microscale silicon particles after 31 cycles for the cells cycled to a lithiation cutoff of 140 mV, while for the cells cycled to only 170 mV the silicon particle structure remained intact.

To enable a stable long-term cycling performance of partially lithiated micronscale silicon anodes in general, it is crucial to maintain the crystalline structure of the silicon particles in order to prevent their structural disintegration. The study here demonstrates clearly that this is only accomplished by restricting the lithiation cutoff potential of the silicon anode to 170 mV or higher for consecutive cycling.

Acknowledgments

Maximilian Graf greatfully acknowledges WACKER Chemie AG for its financial support. The team would like to acknowledge Christina Peters (WACKER Chemie AG) for her support with SEM sample preparation and measurement, as well as introduction on the microscope and discussion. The authors also kindly thank Benjamin Strehle (Chair of Technical Electrochemistry TUM) for support and discussions with the XRD data treatment.

ORCID

Maximilian Graf https://orcid.org/0000-0002-2252-1216
Stefan Haufe https://orcid.org/0000-0003-3025-1890
Hubert A. Gasteiger https://orcid.org/0000-0001-8199-8703

References

1. U. Kasavajjula, C. Wang, and A. J. Appleby, *J. Power Sources*, **163**, 1003 (2007).
2. M. N. Obrovac and V. L. Chevrier, *Chem. Rev.*, **114**, 11444 (2014).
3. M. N. Obrovac and L. J. Krause, *J. Electrochem. Soc.*, **154**, A103 (2007).
4. M. Wetjen, S. Solchenbach, D. Pritzl, J. Hou, V. Tileli, and H. A. Gasteiger, *J. Electrochem. Soc.*, **165**, A1503 (2018).
5. J. W. Choi and D. Aurbach, *Nat. Rev. Mater.*, **1**, 16013 (2016).

6. M. Wetjen, D. Pritzl, R. Jung, S. Solchenbach, R. Ghadimi, and H. A. Gasteiger, *J. Electrochem. Soc.*, **164**, A2840 (2017).
7. X. H. Liu, L. Zhong, S. Huang, S. X. Mao, T. Zhu, and J. Y. Huang, *ACS Nano*, **6**, 1522 (2012).
8. T. Jaumann, J. Balach, M. Klose, S. Oswald, U. Langklotz, A. Michaelis, J. Eckert, and L. Giebeler, *Phys. Chem. Chem. Phys.*, **17**, 24956 (2015).
9. C. Wang, H. Wu, Z. Chen, M. T. Mcdowell, Y. Cui, and Z. Bao, *Nat. Chem.*, **5**, 1042 (2013).
10. N. Artrith, A. Urban, and G. Ceder, *J. Chem. Phys.*, **148**, 241711 (2018).
11. S. Choi, T. W. Kwon, A. Coskun, and J. W. Choi, *Science (80-).*, **357**, 279 (2017).
12. L. F. Cui, R. Ruffo, C. K. Chan, H. Peng, and Y. Cui, *Nano Lett.*, **9**, 491 (2009).
13. D. Jantke, R. Bernhard, E. Hanelt, T. Buhrmester, J. Pfeiffer, and S. Haufe, *J. Electrochem. Soc.*, **166**, A3881 (2019).
14. S. D. Beattie, M. J. Loveridge, M. J. Lain, S. Ferrari, B. J. Polzin, R. Bhagat, and R. Dashwood, *J. Power Sources*, **302**, 426 (2016).
15. S. Haufe, *EP3335262 B1* (2016), filed July 28, 2016 and published June 20, 2018.
16. S. Haufe, R. Bernhard, and J. Pfeiffer, *J. Electrochem. Soc.*, **168**, 080531 (2021).
17. J. Li and J. R. Dahn, *J. Electrochem. Soc.*, **154**, A156 (2007).
18. M. T. McDowell, S. W. Lee, J. T. Harris, B. A. Korgel, C. Wang, W. D. Nix, and Y. Cui, *Nano Lett.*, **13**, 758 (2013).
19. B. Strehle, T. Zünd, S. Sicolo, A. Kießling, V. Baran, and H. A. Gasteiger, *In Press*.
20. K. Ogata, E. Salager, C. J. Kerr, A. E. Fraser, C. Ducati, A. J. Morris, S. Hofmann, and C. P. Grey, *Nat. Commun.*, **5**, 3217 (2014).
21. B. Key, R. Bhattacharyya, M. Morcrette, V. Seznéc, J. M. Tarascon, and C. P. Grey, *J. Am. Chem. Soc.*, **131**, 9239 (2009).
22. P. Limthongkul, Y. Il Jang, N. J. Dudney, and Y. M. Chiang, *Acta Mater.*, **51**, 1103 (2003).
23. J. Li, A. Smith, R. J. Sanderson, T. D. Hatchard, R. A. Dunlap, and J. R. Dahn, *J. Electrochem. Soc.*, **156**, A283 (2009).
24. V. L. Chevrier and J. R. Dahn, *J. Electrochem. Soc.*, **157**, A392 (2010).
25. M. J. Loveridge, M. J. Lain, I. D. Johnson, A. Roberts, S. D. Beattie, R. Dashwood, J. A. Darr, and R. Bhagat, *Sci. Rep.*, **6**, 1 (2016).
26. M. J. Loveridge, M. J. Lain, Q. Huang, C. Wan, A. J. Roberts, G. S. Pappas, and R. Bhagat, *Phys. Chem. Chem. Phys.*, **18**, 30677 (2016).
27. X. H. Liu et al., *Nat. Nanotechnol.*, **7**, 749 (2012).
28. K. N. Tu, *Appl. Phys. Lett.*, **27**, 221 (1975).
29. B. Key, M. Morcrette, J. M. Tarascon, and C. P. Grey, *J. Am. Chem. Soc.*, **133**, 503 (2011).
30. T. Yoon, C. C. Nguyen, D. M. Seo, and B. L. Lucht, *J. Electrochem. Soc.*, **162**, A2325 (2015).
31. M. Pharr, K. Zhao, X. Wang, Z. Suo, and J. J. Vlassak, *Nano Lett.*, **12**, 5039 (2012).

3.2 Lithium nitrate as electrolyte additive for silicon anodes

The article “Understanding the Effect of Lithium Nitrate As Additive in Carbonate-Based Electrolytes for Silicon Anodes” was submitted to the peer-reviewed *Journal of the Electrochemical Society* in July 2024 and published online September 2024.[136] The article was distributed under the terms of the Creative Commons Attribution 4.0 License, and its permanent weblink can be found under https://iopscience.iop.org/article/10.1149/1945-7111/ad71f7. An oral presentation of this study was also presented by M.Graf at the 240th Meeting of the *Journal of Electrochemical Society* in a virtual format. The link for the Abstract (MA2021-02 379) can be found at: https://iopscience.iop.org/article/10.1149/MA2021-023379mtgabs.

The role of the electrolyte is crucial in operating cells with silicon-based anodes. Compared to graphite anodes, the volumetric expansion upon (de-)lithiation of silicon continuously exposes fresh surface during cycling. Therefore, a robust and flexible SEI is needed to prevent continuous electrolyte consumption and excessive SEI formation. FEC is one of the most commonly used electrolyte additives for silicon-based anode active materials. It has been shown to significantly improve cycling performance.[137] However, the use of FEC leads to considerable gassing due to the evolution of CO_2 upon reduction and FEC also has a limited thermal stability.[138,139] Recently, $LiNO_3$ was found to be an effective electrolyte additive for lithium metal electrodes and was shown to increase the cycling stability of silicon-based anodes significantly.[101,140,141,142] This study aims to investigate and comprehend the reaction mechanism of $LiNO_3$ in carbonate-based electrolyte systems and its impact when used with silicon anodes. To achieve this, the reductive and oxidative reactions of $LiNO_3$ were evaluated within the relevant voltage range, and the reaction species were analyzed using XPS and OEMS. We employed carbon model electrodes to investigate these redox reactions independent of intercalation or alloying reactions. Our findings indicate that $LiNO_2$, the primary reduction product, is the active species and is soluble in the electrolyte solution. Therefore, $LiNO_2$ can be used directly as an additive in the electrolyte. The solubility of $LiNO_2$ in the electrolyte is equal to that of $LiNO_3$. Upon $LiNO_2$ reduction at ~1.39 V vs. Li^+/Li, it forms a passivation layer of Li_2O and Li_3N. Cyclic voltammetry experiments demonstrate that this layer of reduction products can effectively passivate the surface of the anode active material, as no further features for the reduction of EC can be observed. OEMS gas analysis validates this finding, showing significantly reduced gassing connected to EC reduction. Furthermore, the reduction of $LiNO_3$ and $LiNO_2$ species results in minimal gassing, as evidenced by the negligible evolution of N_2O gas.

In addition to the reduction reactions occurring on the anode side, we investigated the relevant oxidation reactions on the cathode side. Our observations reveal a complex cascade of nitrogen redox reactions, beginning with the oxidation of $LiNO_2$ species at 3.5 V vs. Li^+/Li, which leads to the formation of NO_2 gas. $LiNO_3$ can partially be regenerated by these reactions, which could explain the long cycle life of cells with the additive even though the concentration in the electrolyte is relatively low. In addition, the effect of the $LiNO_3$ and $LiNO_2$ additive on the cycling stability of full-cells is evaluated and compared to an electrolyte without the additive and one containing FEC. The cycle life of cells containing the $LiNO_3$ additive could be significantly increased compared to the ones without the additive. Cells with the $LiNO_2$ additive performed similarly to those with the $LiNO_3$ additive.

Author contributions

M.G., R.B., S.H., and H.A.G. developed the study's concept. M.G. conducted the electrochemical experiments. M.G. and T.C. synthesized the $LiNO_2$ and performed the UV/Vis measurements. M.G. and L.R. conducted the OEMS experiments and analyzed and discussed the data. M.G. wrote the manuscript, and L.R. and H.A.G. edited it. All authors discussed the results and commented on the manuscript.

Journal of The Electrochemical Society, 2024 **171** 090514

Understanding the Effect of Lithium Nitrate as Additive in Carbonate-Based Electrolytes for Silicon Anodes

**Maximilian Graf,[1,z] Lennart Reuter,[1,*] Simon Qian,[1] Tom Calmus,[1]
Rebecca Bernhard,[2] Stefan Haufe,[2] and Hubert A. Gasteiger[1,**]**

[1] *Technical University of Munich, Germany; TUM School of Natural Sciences, Department of Chemistry and Catalysis Research Center, Chair of Technical Electrochemistry, Germany*
[2] *Wacker Chemie AG, Consortium für Elektrochemische Industrie, Munich, Germany*

Due to its high specific capacity, silicon is one of the most promising anode materials for next-generation lithium-ion batteries. However, its large volumetric changes upon (de)lithiation of ~300% lead to a rupture/re-formation of the solid-electrolyte interphase (SEI) upon cycling, resulting in continuous electrolyte consumption and irreversible loss of lithium. Therefore, it is crucial to use electrolyte systems that form a more stable SEI that can withstand large volume changes. Here, we investigate lithium nitrate ($LiNO_3$) and lithium nitrite ($LiNO_2$) as electrolyte additives. Linear scan voltammetry on carbon black working electrodes in a half-cell configuration with $LiNO_3$-containing 1 M $LiPF_6$ in EC/DEC (1/2 v/v) revealed a two-step reduction mechanism, whereby the first reduction peak could be attributed to the conversion of $LiNO_3$ to $LiNO_2$, while X-ray photoelectron spectroscopy on harvested electrodes suggests the formation of Li_3N during the second reduction peak. On-line electrochemical mass spectrometry (OEMS) on carbon black electrodes showed that N_2O gas is evolved upon the reduction of $LiNO_3$- and $LiNO_2$-containing electrolytes but that the gassing associated with EC reduction is significantly reduced. Furthermore, OEMS and voltammetry were used to examine the redox chemistry of $LiNO_2$ additive. Finally, $LiNO_3$ and $LiNO_2$ additives significantly improved the cycle-life of Si‖NCM622 full-cells.

[DOI: 10.1149/1945-7111/ad71f7]

Manuscript submitted July 2, 2024; revised manuscript received August 12, 2024. Published September 19, 2024.

Due to its high specific capacity of 3579 mAh g_{Si}^{-1} and its natural abundance, silicon is a promising candidate for replacing commonly used graphite as anode material for next-generation lithium-ion batteries.[1] However, the large volumetric expansion of the silicon upon (de)lithiation leads to mechanical degradation and continuous formation of the solid-electrolyte interphase (SEI). Therefore, the electrolyte is excessively reduced on the repeatedly exposed silicon surface area during prolonged cycling. Thus, silicon anodes typically reveal a lower average coulombic efficiency and decreased cycle-life in full-cells when compared to graphite anodes. It is, therefore, crucial for the application of silicon anodes to form an effective and stable SEI, which is mostly determined by the choice of the electrolyte system. In general, the SEI must have a low electrical conductivity to avoid further electrolyte reduction as well as a sufficiently high but selective permeability for lithium ions to prevent co-intercalation of electrolyte solvent and allow for fast (de)lithiation kinetics.[2] Moreover, the SEI on silicon needs to sustain the mechanical stress upon particle expansion/contraction and prevent an ongoing electrolyte consumption concomitant with the loss of cyclable lithium.[3] One of the most frequently used electrolyte components in carbonate-based electrolyte systems for silicon anodes is the additive fluoroethylene carbonate (FEC). It has been demonstrated to form a highly cross-linked network with elastomeric properties upon reduction and is employed either as an additive with a volume fraction of up to 2% or as a co-solvent.[4–7] However, alternatives to FEC are desired due to its significant gas evolution and its thermal instability at elevated temperatures,[8–10] particularly for battery electric vehicle (BEV) applications where the operating temperature can far exceed 25 °C. Thus, new electrolyte systems and additives need to withstand higher temperatures, and consequently, battery performance, as well as cycle-life, must be evaluated at such conditions.

Recently, lithium nitrate ($LiNO_3$) was introduced as an efficient additive in carbonate-based electrolyte systems for silicon anodes, even though the solubility of $LiNO_3$ in those electrolytes is very low (reported to be as high as ~0.09 M, corresponding to ~0.5 wt%, in 1.2 M $LiPF_6$ in EC/DEC 1/1 w/w).[11] Here, the cycle-life of cells containing $LiNO_3$ additive in the electrolyte is significantly increased compared to the additive-free electrolyte, and $LiNO_3$ was able to improve the capacity retention of cells with an FEC-based electrolyte.

In all of these different battery types—independent of the electrolyte system—the first reduction step of the $LiNO_3$ species was observed at a potential <1.7 V vs. Li^+/Li, where it is reported to be reduced to form $LiNO_2$ and Li_2O.[4,12–15] Li_2O is ascribed to be a major component in an FEC-derived SEI and forms a mechanically robust film with low charge transfer resistance.[16–18] The second reduction step involves the conversion of the in situ formed $LiNO_2$. However, the further reduction step depends on the chemical environment and electrochemical conditions in each system: (i) In lithium-sulfur batteries, generally operated in ether-based electrolytes, $LiNO_2$ is reacting with sulfuric species, leading to the formation of additional Li_2O.[14,19] (ii) In lithium-air systems, also operated in ether-based electrolytes, next to the formation of a passivating Li_2O film on the lithium metal electrode, the produced $LiNO_2$ can regenerate the $LiNO_3$ species by a series of oxidation reactions on the cathode side with dissolved O_2 in the electrolyte.[12,20] (iii) In battery systems operated in carbonate-based electrolytes, however, no detailed reaction pathway is known so far. Analysis of the SEI in these latter systems revealed an increased concentration of Li_2O, Li_3N, and LiN_xO_y species.[16–18,21–23] Employing $LiNO_3$ as an electrolyte additive in carbonate-based electrolyte systems is limited due to the low $LiNO_3$ solubility. In general, the solubility of salt depends on the capability of the solvent to dissociate the anion and cation as well as on the electron donation to the latter. This is quantified by the Gutmann donor number, a parameter of the Lewis basicity of the solvent.[18] In this case, cyclic carbonates such as EC have a much lower Gutman donor number (~16)[24] than NO_3^- (~22)[25] and ether-based solvents like DME (~20).[25] The solubility of $LiNO_3$ in carbonate solvents can be increased by solution promotors such as CuF_2,[22] tris-pentafluorophenyl borane (TPFPB),[16] or triethyl phosphate (TEP),[23] as well as by co-solvents like. γ-butyrolactone (GBL)[26] or crown-ethers.[27] Alternatively, Liu et al. increased the amount of $LiNO_3$ that can be introduced into the electrolyte by the addition of encapsulated $LiNO_3$ nanoparticles onto the separator.[18] While the addition of solution promotors into the electrolyte can be implemented easily

---

[*] Electrochemical Society Student Member.
[**] Electrochemical Society Fellow.
[z] E-mail: Maximilian.graf@tum.de

without additional process steps, adding a coating onto the separator adds additional manufacturing cost.

In the present study, we investigate the effect of $LiNO_3$ electrolyte additive on the performance of silicon anodes in a carbonate-based electrolyte. To understand the fundamental reaction mechanism of $LiNO_3$ in this electrolyte system, we study the reduction and oxidation reactions of $LiNO_3$ additive on high-surface-area carbon black model electrodes using linear scan voltammetry. First, the reduction reaction of $LiNO_3$ is systematically investigated by analyzing the solid and gaseous reduction products formed in the potential window of the anode in a realistic full-cell setup. As $LiNO_2$ is an intermediate in the $LiNO_3$ reduction, the properties of $LiNO_2$-containing electrolyte are also examined. Next, oxidation reactions of $LiNO_3$, of its reduction products, and of $LiNO_2$ are examined, as their oxidation can potentially occur at the positive electrode in full-cells. Finally, the effect of $LiNO_2$ and $LiNO_3$ additives on the cycle-life of full-cells with microscale silicon-based anodes and NCM622-based cathodes will be examined.

Experimental

Electrode preparation.—Silicon electrodes were prepared by suspending 7.0 g microscale silicon particles (BET: 1.6 m^2 g^{-1}, $d_{10} = 2.2$ μm, $d_{50} = 4.5$ μm, $d_{90} = 7.8$ μm; CLM 00001, Wacker Chemie AG) in 5.1 g H_2O, and 12.5 g of an aqueous LiPAA solution (4 wt%) in a dissolver mixer (Dispermat LC30, VMA-Getzmann, Germany). The LiPAA solution was prepared by neutralization of PAA solution (polyacrylic acid, $M_v = 459$k, Sigma Aldrich) with lithium hydroxide (LiOH, Sigma Aldrich) to a pH of 7. In the next step, 2.5 g graphite (BET: 20 m^2 g^{-1}; KS6L, Imerys, France) was added to yield a solids mass ratio of 70:25:5 Si/KS6L/LiPAA, and stirring was continued at 12000 rpm for 30 min. The slurry was degassed by mixing it at 2000 rpm for 5 min in a planetary mixer (Thinky Corp., USA). The slurry was then coated onto a copper foil (11 μm) with a box-type coating bar (Erichsen, Germany) using an automated coater (RK PrintCoat Instruments, UK) and dried at room temperature overnight. Electrodes with a diameter of 15.0 mm were punched out from the above-prepared electrode coatings. After drying at 120 °C under dynamic vacuum overnight, the silicon electrode coatings had a loading of 2.1 ± 0.1 $\text{mg}_{\text{Si}}\,\text{cm}^{-2}$ (≡7.5 ± 0.4 mAh cm^{-2} based on 3579 mAh $\text{g}_{\text{Si}}^{-1}$) and a thickness of ~34 μm, equating to a porosity of ~60% based on the bulk densities of the materials. Practically, only ~32% (≡2.4 mAh cm^{-2}) of the silicon capacity is used, following the partial lithiation strategy for microscale silicon as described by Haufe et al.[28]

For the cyclic voltammetry experiments in coin cells, carbon black model electrodes were prepared by mixing 1.0 g carbon black (BET: 64 m^2 g^{-1};Super C65, Imerys, France) with 1.0 g PVDF (Solef 5130, Solvay, France) to yield a mass ratio of 50:50 C65/PVDF. A higher mass ratio, i.e., 90:10 C65/PVDF that was used for the coating onto a stainless steel mesh current collector (see below) did lead to poor coatings on smooth copper or aluminum foils after drying, so that the binder content was increased to 50 wt%. The mixing consisted of a three-step sequential procedure, starting with the dry components at 500 rpm for 2 min in a planetary mixer before adding N-methyl−2-pyrrolidone (NMP, anhydrous, Sigma Aldrich) stepwise and mixing for 20 min at 2000 rpm. The slurry with a mass ratio of 50:50 C65/PVDF was coated onto a copper foil (11 μm) for electrolyte reduction experiments in coin-cells (i.e., for examining the potential range between 0.1–3.0 V vs. Li^+/Li) and onto an aluminum foil (15 μm) for electrolyte oxidation experiments in coin-cells (i.e., for examining the potential range of >3.0 V vs. Li^+/Li). After drying at 120 °C under dynamic vacuum overnight, the carbon electrode coatings had a loading of either 0.6 ± 0.1 $\text{mg}_{\text{C65}}\,\text{cm}^{-2}$ or 1.0 ± 0.1 $\text{mg}_{\text{C65}}\,\text{cm}^{-2}$.

For the OEMS experiments, carbon model electrodes were prepared by mixing 1.8 g carbon black (BET: 68 m^2 g^{-1}; Super C65, Imerys, France) with 0.2 g PVDF (Solef 5130, Solvay, France) to yield a mass ratio of 90:10 C65/PVDF. The mixing was done analogously to the above-described procedure. The slurry was coated onto a stainless-steel mesh (316 grade, 26 μm aperture, 25 μm wire diameter; The Mesh Company, UK) to allow for short diffusion times of the gas to the head-space of the OEMS cell. Electrodes with a diameter of 15 mm were punched out from the above-prepared electrode coatings. After drying at 120 °C under dynamic vacuum overnight, the carbon electrode coatings had a loading of 2.0 ± 0.1 $\text{mg}_{\text{C65}}\,\text{cm}^{-2}$.

Synthesis of $LiNO_2$.—$LiNO_2$ was synthesized according to Uddin et al.[12] First, 20 mmol of LiCl (Sigma Aldrich, >99.98%) was dissolved in anhydrous methanol (Sigma Aldrich, ⩾99.9%) and 48 mmol of $AgNO_2$ (Sigma Aldrich, 99.98%) was dissolved in anhydrous acetonitrile (Sigma Aldrich, ⩾99.9%). The solution of LiCl in methanol was slowly added to the solution of $AgNO_2$ in acetonitrile in a dried flask under Ar flow. The solution was stirred overnight at room temperature (~18 h) under dark conditions. The precipitate of AgCl was separated by filtration, and the solvent of the filtrate was removed by a rotary evaporator, yielding a white powder. The white powder was re-dissolved in methanol and filtrated with a syringe filter (PTFE 20 μm) to remove unreacted $AgNO_2$ and remaining AgCl before the solvent of the filtrate was removed again by a rotary evaporator. In an additional washing step with acetonitrile, any remaining LiCl was dissolved, whereas $LiNO_2$ would remain as a white powder after decanting the solvent. The white powder was then dried at 120 °C under dynamic vacuum for 12 h, resulting in 0.95 g $LiNO_2$ (90% yield). A quantitative analysis of the Li and N content of the synthesized $LiNO_2$ was done by elemental analysis, yielding 12.13 wt% Li and 25.24 wt% N, which is within ~7% and ~5%, respectively, of the theoretical composition (13.11 wt% Li and 26.45 wt% N). Noteworthy, no chloride and a silver content of <0.5 wt% were found, indicating no significant impurities coming from the educts. UV/Vis measurements of the white $LiNO_2$ powder dissolved in acetonitrile showed a characteristic absorbance with λ_{max}= 345 nm (see the turquoise line in Fig. 1). In contrast, $LiNO_3$ dissolved in acetonitrile exhibits a characteristic absorbance band with λ_{max}= 298 nm (purple line in Fig. 1). These values correlate well with UV/Vis data from Uddin et al.,[12] where $LiNO_2$ and $LiNO_3$ were measured in *N,N*-dimethylacetamide (DMA).

Electrolyte preparation.—Prior to mixing the electrolyte, the white powders of $LiNO_3$ (99.99%, Sigma Aldrich) and $LiNO_2$ were

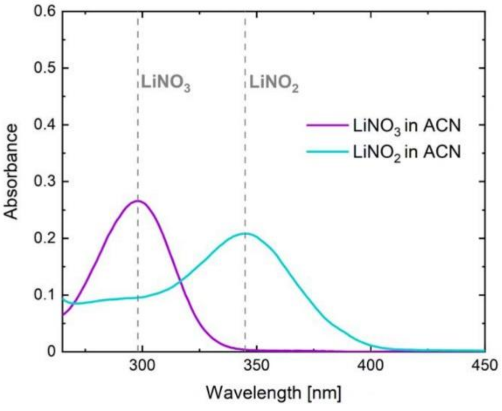

Figure 1. UV/Vis spectra of $LiNO_2$ and $LiNO_3$ in acetonitrile, taken with a Lambda 35 UV/Vis spectrometer (Perkin Elmer, USA). Assignment of the peaks was done based on data from Uddin et al.[12]

dried at 120 °C under dynamic vacuum for 24 h. The powders were then transferred into an argon-filled glovebox (O_2 and H_2O < 0.1 ppm; MBraun, Germany) and added in excess (0.5 wt%) to 1 M $LiPF_6$ in EC/DEC 1/2 v/v (20 ppm H_2O, 42 ppm HF; Gelon, China) each. The saturated solution was stirred for 3 days at 25 °C and afterwards filtrated with a syringe filter (PTFE 20 μm) to remove the undissolved excess of $LiNO_3$ and $LiNO_2$. The concentration of the filtrated solutions was then analyzed by ion chromatography, yielding an NO_3^- concentration of 0.22 wt% (≡0.038 M) for the $LiNO_3$-based electrolyte and an NO_2^- concentration of 0.16 wt% (≡0.036 M) for the $LiNO_2$ based electrolyte. The FEC-based electrolyte was prepared by mixing $LiPF_6$ (99.90%, 6 ppm H_2O, Gotion, China) that was dried at 120 °C under dynamic vacuum for 24 h to a mixture of FEC/DEC 1/4 v/v (20 ppm H_2O; Gelon, China). The nitrosyl tetrafluoroborate ($NOBF_4$) containing electrolyte was prepared by adding $NOBF_4$ (95%, Sigma Aldrich) to 1 M $LiPF_6$ in EC/DEC 1/2 v/v to yield a concentration of 0.038 M. The solution was stirred at 25 °C overnight.

Assembly of full-cells for long-term cycling and testing procedure.—Long-term cycling experiments were conducted in coin-cells (Hohsen Corp., Japan) in a full-cell configuration with: (i) an $Li_{1.0}Ni_{0.6}Co_{0.2}Mn_{0.2}O_2$ (NCM622) based cathode (94.0 wt% active material) coated on Al foil (SEI corp., Japan) at a loading of 14.9 ± 0.1 mg_{NCM} cm^{-2} (≡2.4 ± 0.1 mAh cm^{-2}, based on a nominal specific capacity of 160 mAh g_{NCM}^{-1}) and punched to a diameter of 15 mm; (ii) a microscale silicon-based anode, as described above. The areal capacity of the cathode corresponds to 32% of the nominal capacity of the anode (7.5 ± 0.4 mAh cm^{-2} based on 3579 mAh g_{Si}^{-1}), so that only ∼32% of the nominal silicon capacity is used, which is thus compatible with the partial capacity usage that is needed when employing microscale silicon.[28] Cells were assembled in an argon-filled glovebox (O_2 and H_2O < 0.1 ppm; MBraun, Germany) with a glass fiber separator (Whatman GD type A/E, USA) and 60 μl of one of the following four electrolytes: (i) 1 M $LiPF_6$ in EC/DEC 1/2 v/v (20 ppm H_2O; Gelon, China), (ii) 1 M $LiPF_6$ in EC/DEC 1/2 v/v + 0.22 wt% $LiNO_3$, (iii) 1 M $LiPF_6$ in EC/DEC 1/2 v/v + 0.16 wt% $LiNO_2$, or, (iv) 1 M $LiPF_6$ in FEC/DEC 1/4 v/v.

Electrochemical cycling tests of the full cells at 25 °C were performed in a climate chamber (Binder, Germany) using a multi-channel cycler (Maccor, USA). The cycling tests at 45 °C were performed in a climate chamber (Espec, USA) using a multi-channel potentiostat (Biologic VMP3, France). Two formation cycles of the cells were performed between 3.0–4.2 V, with a 0.1 C constant current and constant voltage (CCCV) charge (with a current limitation of 0.01 C), and with a 0.1 C CC discharge. Subsequently, the cells were cycled in the same voltage window with a 0.5 C CCCV charge (with a current limitation of 0.125 C), and with a 0.5 C CC discharge. C-rates refer to the capacity of the limiting electrode, i.e., the positive electrode (1 C ≡ 160 mA g_{NCM}^{-1} or 2.38 mA cm^{-2}).

Assembly of half-cells for cyclic voltammetry and measurement procedure.—Cyclic voltammetry (CV) analysis was performed in coin-cells using a half-cell setup with a carbon black model electrode against metallic lithium (450 μm thick, 15 mm diameter, 99.9%; Rockwood Lithium, USA). Cells were assembled in an argon-filled glovebox (O_2 and H_2O < 0.1 ppm; MBraun, Germany) with a glass fiber separator (Whatman GD type A/E, USA) using 60 μl of one of the following three electrolytes: (i) 1 M $LiPF_6$ in EC/DEC 1/2 v/v (20 ppm H_2O; Gelon, China), (ii) 1 M $LiPF_6$ in EC/DEC 1/2 v/v + 0.22 wt% $LiNO_3$, or, (iii) 1 M $LiPF_6$ in EC/DEC 1/2 v/v + 0.16 wt% $LiNO_2$. CV measurements were performed at 25 °C in a climate chamber (Binder, Germany) using a multi-channel potentiostat (Biologic VMP, France). The voltametric scans were conducted with a scan rate of 0.1 mV s^{-1} within varying potential windows.

Cell assembly for online electrochemical mass spectrometry and measurement procedure.—For the OEMS experiments, a custom-made two-compartment cell setup was used, where a Li^+-ion conductive glass-ceramic (LICGC, diameter 1 inch, thickness 150 μm, conductivity 10^{-4} S cm^{-1} at 25 °C; Ohara, Japan) is used as a gas/liquid impermeable separator between the working electrode (connected to the mass spectrometer inlet of the OEMS) and the counter electrode in order to suppress any cross-diffusion of liquid or gaseous reaction products between the electrode compartments. A detailed description of the design can be found elsewhere.[29] A metallic lithium counter electrode was placed at the bottom of the OEMS cell and covered with a glass fiber separator (24 mm Whatman GD type A/E, USA) wetted with 100 μl of 1 M $LiPF_6$ in EC/DEC 1/2 v/v. On top of the glass fiber separator, the glass-ceramic was placed as a separator, with PTFE-covered aluminum as a gasket to seal against the counter electrode compartment (i.e., the lower compartment of the OEMS cell). Next, a glass fiber separator (15 mm Whatman GD type A/E, USA) was put onto the glass-ceramic separator and wetted with 50 μl of either one of the following electrolytes: (i) 1 M $LiPF_6$ in EC/DEC 1/2 v/v, (ii) 1 M $LiPF_6$ in EC/DEC 1/2 v/v + 0.22 wt% $LiNO_3$, or, (iii) 1 M $LiPF_6$ in EC/DEC 1/2 v/v + 0.16 wt% $LiNO_2$. Finally, a carbon black model electrode coated onto a stainless steel mesh was placed as a working electrode on top of the stack, which was then compressed by a spring in the sealed OEMS cell.

The cells for the OEMS experiments were placed in a climate chamber (CTS, Germany) at 25 °C, using a multi-channel potentiostat (Biologic SP-300) and a mass spectrometer system (HiQuad QMH 400–1, Pfeiffer Vacuum, Germany) that is described in detail elsewhere.[30] After connecting the cell to the potentiostat and the mass spectrometer system, the cell was purged for 5 min with Ar in order to remove remaining gas traces from the assembly in the glovebox atmosphere. Afterwards, the cell was held at open circuit voltage (OCV ∼3.0 V vs. Li^+/Li) for 4 h to get a stable background of the mass signals. For the measurements, the carbon black working electrode potential was ramped with 0.1 mV s^{-1} from OCV to the desired potential for each experiment.

To convert the measured mass spectrometer currents into concentrations, the OEMS cell was purged after each measurement with the following calibration gases (Westfalen AG, Germany): (i) 2000 ppm nitric oxide (NO) in Ar, (ii) 1000 ppm nitrogen dioxide (NO_2) in Ar, (iii) 2000 ppm nitrous oxide (N_2O) in Ar, and, (iv) 2000 ppm each of carbon dioxide CO_2, carbon monoxide CO, and ethylene (C_2H_4) in Ar. Table I lists the relevant, most pronounced

Table I. Most pronounced *m/z* mass signals and the respective calibration factors based on calibration gases that contain 2000 ppm of the respective gas in Ar, determined for the here used OEMS system. The calibration factor corresponds to the value of the ion current ratio of the respective gas over that of the ^{36}Ar signal (I_Z/I_{36}) for a concentration of 2000 ppm in Ar, which is measured after extensive flushing of the OEMS cell with the respective calibration gas.

Gas	Mass signal m/z	Calibration factor
NO	30	0.56
	16	0.0072
	14	0.03
NO_2	30	0.46
	16	0.0146
	14	0.03
N_2O	44	0.23
	30	0.10
	16	0.014
	14	0.032
CO_2	44	0.80
CO	28	0.57
C_2H_4	26	0.322

m/z signals for each of the gases as well as the respective calibration factors corresponding to 2000 ppm of the respective gas. In addition, the mass signal of CO $m/z = 28$ was corrected for the contribution of C_2H_4 and CO_2 to $m/z = 28$. For this, the fragmentation patterns of C_2H_4 and CO_2 were determined by flushing the headspace of an empty cell with mixtures of CO, C_2H_4, and CO_2 in Ar each at different concentrations of 1000 ppm, 10.000 ppm, and 50.0000 ppm. From this, a constant ratio of I_{28} $(C_2H_4)/I_{26}$ $(C_2H_4) = 1.6$ for C_2H_4, and of I_{28} $(CO_2)/I_{44}$ $(CO_2) = 0.1$ for CO_2 was determined, and the correction conducted according to: $I_{28}(CO) = I_{28} - 0.1 \cdot I_{44}$ $(CO_2) - 1.6 \cdot I_{26}$ (C_2H_4). Similarly, the mass trace $m/z = 44$ shows contributions from CO_2 and N_2O. When no NO and NO_2 are present (both gas species have their major signal on $m/z = 30$), the mass trace $m/z = 44$ can be analyzed with respect to the evolution of CO_2 by subtracting the contribution of N_2O as determined by analyzing the mass trace $m/z = 30$ according to: $I_{44}(CO_2) = I_{44} - 0.23/0.1 \cdot I_{30}(N_2O)$. Consequently, the mass trace at $m/z = 44$ corresponding to N_2O can be obtained according to: $I_{44}(N_2O) = I_{44} - I_{44}(CO_2)$. Since NO and NO_2 both have $m/z = 30$ as the major signal and since they do not significantly differ in their *m/z* patterns, they cannot be distinguished from each other in these OEMS experiments. To convert the gas concentrations in the cell head-space (11 mL) into μmol, the ideal gas law was used.

XPS measurements.—XPS spectra were acquired using an Axis Supra system (Kratos, UK) equipped with a monochromatic Al Kα X-ray source (photon energy = 1486.6 eV) and an emission current of 15 mA. Pass energies of 40 eV for high-resolution spectra and 160 eV for survey spectra were selected with the hybrid lens mode. The beam area was set to $\sim 2 \times 1$ mm^2 using the slot collimation mode. Electrodes were harvested from the cells and rinsed with 1 mL of DMC (⩾99, anhydrous, Sigma Aldrich) and dried for 12 h at room temperature under vacuum. Next, the electrodes were mounted on the XPS sample holder inside an argon-filled glovebox (O_2 and $H_2O < 0.1$ ppm; MBraun, Germany), which was then transferred (air exposure of < 1 min) into the XPS load-lock. The electrodes were kept in the load lock until a pressure of $\sim 10^{-8}$ Torr was achieved. XPS measurements were conducted after transfer into the main chamber at pressures of $\sim 10^{-9}$ Torr.

Survey spectra were first recorded for all samples with a step size of 1.0 eV and a dwell time of 100 ms, while high-resolution spectra of the N 1 s region were collected with 0.05 eV step size and 1000 ms dwell time. All spectra were calibrated to the adventitious carbon peak at the binding energy of 284.8 eV. Charge neutralization was not required, as no binding energy shifts indicative of (differential) charging were observed. The binding energy of the hemispherical analyzer was calibrated with in situ sputter-cleaned silver, gold, and copper standard samples. Thereby, the kinetic energies of the Ag 3d (1118.51 eV), Au 4 f (1402.73 eV), and Cu 2p (554.07 eV) core levels were referenced with an accuracy of 25 meV to the known peak values.

Results and Discussion

Effect of $LiNO_3$ on the cycle-life of full-cells with silicon anodes.—In the following, the effect of $LiNO_3$ on the performance of silicon anodes over extended cycling will be investigated and discussed. The silicon anodes used in this study are comprised of microscale silicon particles which are only lithiated to a certain share of their total capacity (~32%, corresponding to ~1145 mAh g_{Si}^{-1}) in order to limit the volume expansion of the silicon and therefore diminish degradation phenomena.[3,28,31–33] We cycled the silicon anodes in a full-cell configuration against NCM622 cathodes and compared the capacity retention of cells with a $LiNO_3$-containing electrolyte (1 M $LiPF_6$ EC/DEC 1/2 v/v + 0.22 wt% $LiNO_3$) to those cycled with a reference electrolyte (1 M $LiPF_6$ EC/DEC 1/2 v/v) in order to analyze the influence of the $LiNO_3$ electrolyte additive on the cycle-life of the silicon anodes. To be able to compare the performance of the $LiNO_3$ additive to an optimized electrolyte system for silicon anodes, we additionally cycled full-cells containing 1 M $LiPF_6$ in FEC/DEC 1/4 v/v for comparison. To investigate the effect of the temperature of different electrolyte systems on cycling stability, full-cells were cycled at two different temperatures, namely at 25 °C and 45 °C.

Figure 2 shows the mean discharge capacity and coulombic efficiency (CE) of the Si||NCM622 full-cells cycled with the reference electrolyte (1 M $LiPF_6$ in EC/DEC 1/2 v/v; gray), with $LiNO_3$-containing electrolyte (1 M $LiPF_6$ in EC/DEC 1/2 v/v + 0.22 wt% $LiNO_3$; purple), and with an FEC-based electrolyte (1 M $LiPF_6$ in FEC/DEC 1/4 v/v; magenta) at 25 °C. Over the first ~50 cycles, all cells exhibit the same discharge capacity and aging behavior. While cells with the EC/DEC-based electrolyte without $LiNO_3$ additive drop to 80% of their initial capacity already after 104 cycles (gray), the cells containing the $LiNO_3$ additive (purple) sustain 225 cycles before they drop to 80% of their initial capacity (all referenced to the discharge capacity of the first cycle at C/2). This corresponds to an extension of the cycle-life by more than a factor of two. The mean discharge capacity of these cells remains remarkably constant, with a capacity retention of 88% until the 200th cycle, after which the capacity starts to drop more rapidly. In comparison, cells cycled with the FEC electrolyte (magenta) exhibit a capacity retention of only 81% at 200 cycles; however, these cells show a rather continuous capacity decrease and no accelerating capacity decay after some point. Thus, the FEC-based cells outperform the cells cycled with the $LiNO_3$ additive for a higher number of cycles.

The rapid capacity decay of the cells cycled only with the EC/DEC electrolyte after ~50 cycles is also reflected in the coulombic efficiency (CE), as displayed in the upper panel of Fig. 2 (gray). We can rationalize the poor cycling stability by the absence of an electrolyte component that forms a sufficiently stable SEI that is able to withstand the continuous silicon particle expansion/contraction and is, therefore, unable to prevent the continuous reduction of electrolyte components and the associated

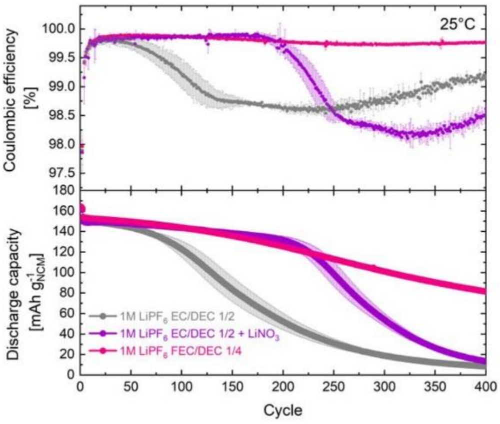

Figure 2. Specific discharge capacities (lower panel) and coulombic efficiencies (upper panel) of Si||NCM622 coin-cells (NCM622 cathodes with 2.4 ± 0.1 mAh cm^{-2} and Si anodes with nominally 7.5 ± 0.4 mAh cm^{-2} utilized to ~32%) cycled at 25 °C. Cells were built with one glass fiber separator (Whatman GD type A/E) and 60 μl of three different electrolytes: (i) 1 M $LiPF_6$ in EC/DEC 1/2 v/v (gray), (ii) 1 M $LiPF_6$ in EC/DEC 1/2 v/v + 0.22 wt% $LiNO_3$ (purple), or, (iii) 1 M $LiPF_6$ in FEC/DEC 1/4 v/v (magenta). The cells were cycled between 3.0–4.2 V, first for two formation cycles with C/10 CCCV charge (until 0.01 C) and a C/10 CC discharge, followed by continuous cycling with C/2 CCCV charge (until C/8) and C/2 CC discharge. Error bars represent the standard deviation of 3 independent repeat measurements.

loss of cyclable lithium. In contrast, the $LiNO_3$ electrolyte system can maintain the initial CE of ~99.85% for almost 200 cycles until a rapid decay is observed (purple). Experiments with different $LiNO_3$ concentrations in the EC/DEC electrolyte have shown that the onset of this rapidly accelerating capacity decrease is directly proportional to the $LiNO_3$ content in the cell (see Fig. A·1 in appendix A1). This is analogous to a study on the effect of the concentration of FEC additive to an EC/EMC electrolyte by Jung et al.,[6] where it was shown that the cycle-life of the cells would directly correlate with the absolute amount of FEC in the cell. Thus, we believe that the rapid drop of the CE efficiency starting at ~200 cycles is caused by a complete depletion of the $LiNO_3$ species in the electrolyte. As shown in the reference electrolyte, the reduction of only EC and DEC apparently forms a less effective SEI, causing a rapid drop in the CE. However, the first-cycle efficiency of the cells cycled only with EC/DEC, amounting to 81.0±1.1%, does not differ significantly from that of the cells containing the $LiNO_3$ additive (80.8±0.3%). This indicates that the initial passivation by the EC/DEC species is not less efficient but does not seem to be as stable over extended cycling. Hence, we believe that the $LiNO_3$ additive forms an SEI that is more persistent against the morphological changes of the silicon. In comparison, the cells cycled with the FEC electrolyte exhibit a similar first-cycle efficiency of 81.5±0.03% as the other two electrolyte systems. Over the course of cycling, the CE of the FEC-based cells is similar to that of the cells cycled with the $LiNO_3$ additive. However, the cells cycled with the FEC additive do not show a rapidly accelerating capacity drop starting at a specific point during cycle-life. This can be explained by the significantly higher concentration of FEC additive (~30 wt%) in the electrolyte compared to that of the more than two orders of magnitude lower concentration of the $LiNO_3$ additive (0.22 wt%; limited by its solubility). In line with the slightly higher CE of the cells containing $LiNO_3$ compared to the cells with the FEC electrolyte, the specific discharge capacity of the FEC-free cells surpasses those containing FEC for approximately 70 cycles. Even though the cells cycled with the $LiNO_3$ electrolyte reveal an accelerating capacity drop after ~200 cycles, the performance of these cells up to this point is impressive when considering the rather low $LiNO_3$ concentration in the cells. The similar performance of both electrolyte systems demonstrates the highly effective passivating properties of the $LiNO_3$ additive for silicon anodes when full-cells are being cycled at room temperature.

Next, the cycle-life of Si||NCM622 full-cells with the different electrolyte systems were tested at 45 °C, using the identical cell setup and cycling procedure. The discharge capacity and coulombic efficiency of these cells are shown in Fig. 3. Cells cycled with the EC/DEC electrolyte without $LiNO_3$ (gray) reach 145 cycles before losing 80% of their initial capacity. Interestingly, this corresponds to a gain of more than 40 cycles compared to their cycle-life at 25 °C (see Fig. 2). Even though the first-cycle efficiency of 80.7 ± 0.0% is similar to the one observed at 25 °C, continuous cycling showed an improved average CE of ~99.7% over the course of ~100 cycles, where the rapidly accelerating capacity decay of the cells begins. For the cells with the $LiNO_3$ additive (purple), a capacity retention of 80% is reached at 227 cycles (similar to what was observed at 25 °C, see Fig. 2 and a first cycle efficiency of 81.5 ± 0.0% (based on three cells) is obtained. The onset of the rapidly accelerating capacity decay occurs at ~225 cycles, which again is similar to what was observed at 25 °C. A striking difference to the $LiNO_3$-free cells is the gradually increasing CE over the first ~75 cycles, which could derive from parasitic oxidation reactions which are not contributing to the capacity. This makes the interpretation of the coulombic efficiency very difficult in this case.

In contrast, the FEC-based cells (magenta) show a more pronounced temperature effect, namely a significantly decreased performance at elevated temperatures. 80% of the initial C/2 discharge capacity is already reached in cycle 144, 65 cycles less than for cycling at 25 °C. FEC decomposition at elevated temperatures was shown to result in the formation of HF and in a significant performance loss of the cells.[34] Under such conditions, the thermal stability of $LiNO_3$ becomes apparently more relevant, and cells cycled with the $LiNO_3$ additive even outperform the ones cycled with the FEC additive. The cycling data shown here demonstrates the advantages of the $LiNO_3$ additive, even though its solubility in carbonate-based electrolyte systems is very low.

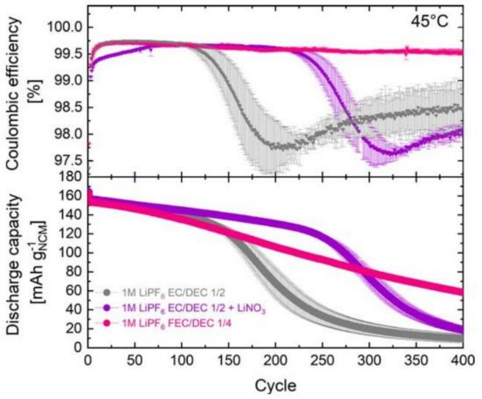

Figure 3. Specific discharge capacities (lower panel) and coulombic efficiencies (upper panel) of Si||NCM622 coin-cells (NCM622 cathodes with 2.4 ± 0.1 mAh cm^{-2} and Si anodes with nominally 7.5 ± 0.4 mAh cm^{-2} utilized to ~32%) cycled at 45 °C. Cells were built with one glass fiber separator (Whatman GD type A/E) and 60 μl of three different electrolytes: (i) 1 M $LiPF_6$ in EC/DEC 1/2 v/v (gray), (ii) 1 M $LiPF_6$ in EC/DEC 1/2 v/v + 0.22 wt% $LiNO_3$ (purple), or, (iii) 1 M $LiPF_6$ in FEC/DEC 1/4 v/v (magenta). The cells were cycled between 3.0–4.2 V, first for two formation cycles with C/10 CCCV charge (until 0.01 C) and a C/10 CC discharge, followed by continuous cycling with C/2 CCCV charge (until C/8) and C/2 CC discharge. Error bars represent the standard deviation of 3 independent repeat measurements.

Comparing the results of our cycle-life test to the literature is difficult, since there is very little published on the use of $LiNO_3$ as an electrolyte additive for microscale silicon anodes in combination with carbonate-based electrolyte systems. Nguyen et al.[11] investigated the effect of $LiNO_3$ additive in 1.2 M $LiPF_6$ in EC/DEC 1/1 w/w on the performance of full-cells with silicon-graphite composite anodes and NCM111 cathodes. A saturated solution of $LiNO_3$ in the electrolyte (in their study, the $LiNO_3$ solubility was given as ~0.5 wt%) increased the capacity retention of these full-cells after 100 cycles from only 8.8% for the additive-free electrolyte to 57.6%, which even outperformed the capacity retention of 44.6% upon the addition of 10 wt% FEC to the electrolyte. As already observed here, the first-cycle efficiency was found to not increase by the addition of $LiNO_3$, which the authors explained by the significant reduction of the $LiNO_3$ species deduced from their dQ/dV analysis. Investigation of the SEI on the silicon-graphite composite electrodes revealed $LiNO_2$, R_3N, and Li_3N species as the main reduction products of the $LiNO_3$ additive. Moreover, XRD and IR-ATR detected an increased lithium carbonate content compared to the additive-free electrolyte. To this day, $LiNO_3$ in carbonate-based electrolyte systems is predominantly used as an additive in lithium metal batteries (LMBs), where the additive could significantly increase the cycle-life of Li||NCA or Li||NCM cells.[18,22] Next to an SEI with fast charge transfer kinetics, attributed to the incorporation of Li_2O and Li_3N as reduction products of $LiNO_3$, a dendrite-free and favorable spherical morphology of Li nuclei was obtained.[17,18,22,23,35]

Investigation of the reduction potential of $LiNO_3$ on carbon black model electrodes.—To gain insights into the reduction mechanism of $LiNO_3$, we examined the reduction processes in the

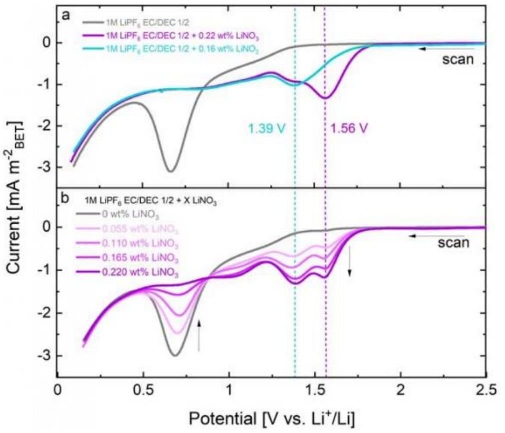

Figure 4. First reductive voltammetric scans from 2.5 to 0.1 V at 0.1 mV s^{-1}, taken for half-cells with carbon black (C65) working electrodes and lithium metal counter electrodes (with a Whatman GD type A/E glass fiber separator), assembled with different electrolytes. (a) First reductive voltammetric scan of C65||Li coin-cells (0.6 ± 0.1 mg_{C65} cm^{-2}, exposing a total carbon surface area of ~0.07 m^2) with 50 μl of: (i) 1 M $LiPF_6$ in EC/DEC 1/2 v/v (gray), (ii) 1 M $LiPF_6$ in EC/DEC 1/2 v/v + 0.22 wt% $LiNO_3$ (purple), or, (iii) 1 M $LiPF_6$ in EC/DEC 1/2 v/v + 0.16 wt% $LiNO_2$ (turquoise). (b) First reductive voltammetric scan of a C65||Li coin-cells (1.0 mg_{C65} cm^{-2}, exposing a total carbon surface area of ~0.11 m^2) with 50 μl of 1 M $LiPF_6$ in EC/DEC 1/2 v/v with varying $LiNO_3$ concentrations: (i) without $LiNO_3$ additive (gray), (ii) with 0.055 wt% $LiNO_3$ additive (very light purple), (iii) with 0.11 wt% $LiNO_3$ (light purple), (iv) with 0.165 wt% $LiNO_3$ (purple), and (v) with 0.22 wt% $LiNO_3$ (dark purple). The current is normalized to the total C65 surface area of the electrodes based on the BET area of C65.

presence of $LiNO_3$ via reductive voltametric scans using carbon black working electrodes in combination with a lithium metal counter electrode (see Fig. 4). The high surface area of the here-used C65 carbon black (BET = 64 m^2 g^{-1}) and the only small contribution of the lithium intercalation reaction for C65, owing to its low degree of graphitization, are both advantageous to investigate the mechanism of the reductive decomposition of the electrolyte (i.e., maximizing surface area while minimizing intercalation). The first reductive scan of the reference electrolyte system without $LiNO_3$ (i.e., 1 M $LiPF_6$ in EC/DEC 1/2 v/v) shown in gray in Fig. 4a reveals the onset of a reduction feature at <0.8 V vs. Li^+/Li, corresponding to the reduction of EC.[29] In contrast, the CV scan of the electrolyte system containing the $LiNO_3$ additive (1 M $LiPF_6$ in EC/DEC 1/2 v/v + 0.22 wt% $LiNO_3$; purple) shows the onset of a reduction feature at already <1.8 V vs. Li^+/Li, with two distinct peak maxima at 1.56 and 1.39 V vs. Li^+/Li. In addition, the reduction peak of the EC species that was observed in the reference electrolyte (gray) completely disappeared, indicating a substantial suppression of the EC reduction process. Hence, the $LiNO_3$ additive appears to effectively passivate the carbon surface before the EC reduction potential is reached. So far, the two clearly distinct features of the reduction of $LiNO_3$ have not been described in detail in the literature: even though dQ/dV analysis of $LiNO_3$-containing full-cell systems could reveal a similar first reduction potential of 1.7 V vs. Li^+/Li, the typically conducted analysis (i.e., without making use of high surface area carbon black electrodes) does not allow to resolve the individual reduction peaks which can be observed in our analysis.[11,13] Several studies suggested the first reduction step of $LiNO_3$ to be the formation of $LiNO_2$ and Li_2O according to reaction 1.1.[13,14,36] In both ether-based as well as carbonate-based electrolytes, Li_yNO_x species are often described to be a component in the passivation film formed upon $LiNO_3$ reduction.[21,22,36,37] In principle, $LiNO_2$ could be one of these Li_yNO_x species, but its measured solubility in EC/DEC electrolyte (0.16 wt%, corresponding to 0.036 M) is very similar to that of $LiNO_3$ (0.22 wt%, corresponding to 0.038 M) so that $LiNO_2$ detected by, e.g., XPS analysis of harvested electrodes, might stem from remaining electrolyte (i.e., residual electrolyte on harvested electrodes), similar to residual NO_3^- species.[11,13]

$$LiNO_3 + 2\,Li^+ + 2\,e^- \rightarrow LiNO_2 + Li_2O \qquad [1.1]$$

To identify the role of the $LiNO_2$ species in the reduction mechanism of $LiNO_3$ and to gain a better understanding of the reduction features observed in Fig. 4a, we examined the reduction of a $LiNO_2$-containing electrolyte separately in an analogously conducted experiment. Since $LiNO_2$ is commercially not available, we synthesized it from LiCl and $AgNO_2$ according to a synthesis described by Uddin et al.,[12] as outlined in the Experimental section. The synthesized $LiNO_2$ was dissolved in a 1 M $LiPF_6$ in EC/DEC 1/2 v/v electrolyte and had a solubility of ~0.16 wt% (corresponding to 0.036 M), rather similar to that of $LiNO_3$ (0.038 M). The first reductive voltametric scan of the $LiNO_2$-containing electrolyte is depicted in turquoise in Fig. 4a. Here, one only observes one reduction peak at 1.39 V vs. Li^+/Li, which aligns with the second reduction feature observed with the $LiNO_3$-containing electrolyte (purple). Analogous to what was observed for the latter, no EC reduction peak is observed for the $LiNO_2$-containing electrolyte, also demonstrating the passivating capability of the $LiNO_2$ reduction product(s). Considering (i) that the first reduction peak at 1.56 V vs. Li^+/Li observed for the $LiNO_3$-containing electrolyte (purple) is not present in case of the $LiNO_2$-containing electrolyte and (ii) that the reduction peak at 1.39 V vs. Li^+/Li is observed for both the $LiNO_3$- and the $LiNO_2$-containing electrolytes provides substantial proof that $LiNO_2$ is a reduction product of $LiNO_3$, formed during the first reduction peak. Thus, we assign the first reduction peak at 1.56 V for the $LiNO_3$-containing electrolyte to the reduction of $LiNO_3$ to $LiNO_2$ according to reaction 1.1, while we ascribe the second reduction peak observed at 1.39 V to the consecutive reduction of $LiNO_2$.

To further investigate the subsequent reduction of $LiNO_2$ and the thereby formed passivating layer on the carbon surface, we performed OEMS measurements to investigate the gas evolution that is accompanied by the reduction of $LiNO_2$ species and conducted *post-mortem* XPS analysis on carbon black electrodes.

Gas evolution during the reduction of $LiNO_3$ - and $LiNO_2$ - containing electrolytes.—Typically, the formation of a solid SEI is accompanied by the evolution of gaseous products resulting from electrolyte decomposition.[38] Studying gas evolution can thus provide insights into the mechanistic reduction pathway. Since gas evolution is observed for most electrolyte systems, depending on the cell type (e.g., pouch-cells) lithium-ion batteries need to undergo a degassing step to remove the evolved gases after cell formation, introducing an additional step in cell manufacturing.[39] In general, it is desired to tailor the electrolyte systems with additives that form a stable and effective SEI but, at the same time, do not release large amounts of gas after the initial formation cycle. Carbonate-based electrolyte systems usually consist of cyclic carbonates such as ethylene carbonate (EC) and linear carbonates, e.g., diethyl carbonates (DEC), both of which lead to the evolution of gases upon their reduction at potentials of typically <1 V. A powerful method to analyze and quantify the gas evolution of electrolytes is online electrochemical mass spectrometry (OEMS).[30,40]

In the following, we will analyze the potential-dependent gassing behavior of $LiNO_3$- and $LiNO_2$-containing electrolytes using carbon black working electrodes in a two-compartment OEMS cell, where only gases evolved at the working electrode are being detected by the mass spectrometer (see Experimental section). Figure 5 shows the current density (upper panel) and the gas evolution (lower panel) during a reductive voltage scan on carbon black working electrodes

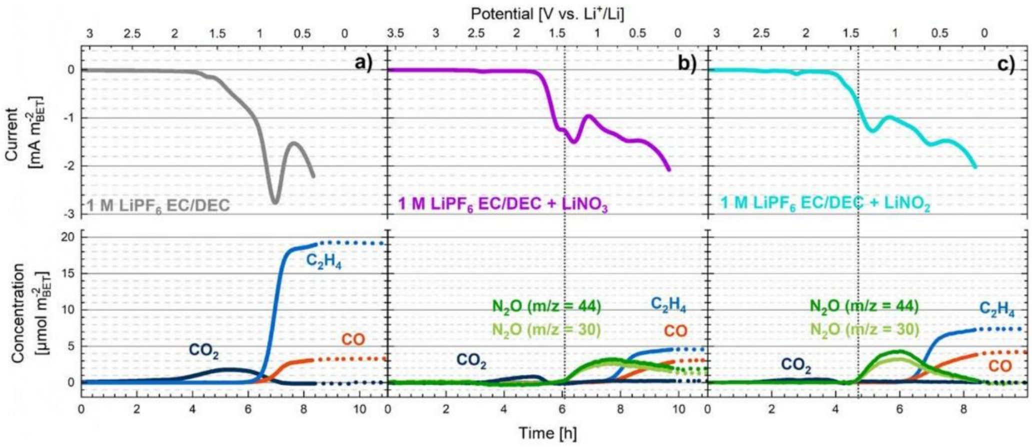

Figure 5. First reductive voltammetric scan (upper panels) and gas evolution (lower panels) of a carbon black working electrode (2.0 ± 0.1 mg$_{C65}$ cm^{-2}, exposing a total carbon surface area of ~0.23 m^2) in a C65||Li two-compartment OEMS cell with three different electrolytes in the working electrode compartment: (a) 1 M LiPF$_6$ in EC/DEC 1/2 v/v, (b) 1 M LiPF$_6$ in EC/DEC 1/2 v/v + 0.22 wt% LiNO$_3$, and, (c) 1 M LiPF$_6$ in EC/DEC 1/2 v/v + 0.16 wt% LiNO$_2$. The voltage scan was performed with 0.1 mV s^{-1} from OCV (~3.0 V vs. Li$^+$/Li) to 0.1 V vs. Li$^+$/Li. The current and the molar quantities of evolved ethylene (determined at $m/z = 26$), carbon monoxide (determined at $m/z = 28$), carbon dioxide (determined at $m/z = 44$), and nitrous oxide (determined at $m/z = 44, 30$) based on the calibration factors in Table I is normalized to the BET surface area of the C65 working electrodes (~0.23 m^2). Note that due to the use of a gas/liquid impermeable, lithium-ion conducting glass-ceramic separator in the two-compartment cell, the detected gases only derive from the carbon working electrode (see Experimental section). Dotted lines represent the mass trace of the gas measured during the OCV period that follows the potential scan.

with three different electrolytes: a) with 1 M LiPF$_6$ in EC/DEC 1/2 v/v, b) with 1 M LiPF$_6$ in EC:DEC 1/2 v/v + LiNO$_3$, and, c) with 1 M LiPF$_6$ in EC:DEC 1/2 v/v + LiNO$_2$. To allow comparability, both current density and the amounts of evolved gas are normalized to the BET surface area of the carbon black electrode (~0.24 m^2). The current profile is shown for a voltammetric scan of the carbon black working electrode from OCV (~3 V) to 0.1 V vs. Li$^+$/Li. The EC/DEC reference system without any additive (Fig. 5a) shows a distinctive reduction peak at 0.8 V vs. Li$^+$/Li (see upper x-axis), accompanied by the evolution of ethylene (blue), whose concentration rapidly increases until a plateau of ~19 µmol m$^{-2}_{BET}$ is reached. The predominant ethylene signal originates from the major reduction pathway of EC to ethylene and lithium ethylene dicarbonate (LEDC).[38] Next to ethylene, the evolution of CO is observed (orange), reaching a total amount of ~3 µmol m$^{-2}_{BET}$; it originates from both a minor, direct 2-electron EC reduction pathway and from the reduction of DEC.[38] In addition, CO$_2$ evolution (dark blue) is observed, starting at ~2 V vs. Li$^+$/Li, until it is consumed again at potentials below 1 V vs. Li$^+$/Li. The initial CO$_2$ evolution can be explained by the reaction of EC with OH$^-$, whereby the latter is produced by the reduction of trace water in the electrolyte;[41,42] below 1.5 V vs. Li$^+$/Li, CO$_2$ can be reduced again, forming Li$_2$CO$_3$ as its main reduction product.[43] No other unique *m/z* signals were observed.

The current response to a reductive voltammetric scan and the gas evolution for an electrolyte system with the LiNO$_3$ additive are shown in Fig. 5b. As already shown in Fig. 4b, during the reductive scan in the presence of LiNO$_3$, two characteristic features at 1.56 V and 1.39 V vs. Li$^+$/Li can be observed, whereas the EC reduction peak at 0.8 V is almost completely suppressed. The EC reduction feature is not entirely suppressed as the mesh-based carbon electrodes for the OEMS cell bear higher mass loadings and thus expose a higher surface area. Consequently the amount of LiNO$_3$ is not sufficiently high enough to fully passivate the carbon surface. For the second reductive feature with its peak at 1.39 V vs. Li$^+$/Li, a parallel gas evolution with the mass of $m/z = 30$ and $m/z = 44$ is observed at ~1.4 V vs. Li$^+$/Li (marked by the vertical dotted line in Fig. 5b). Conceivable gaseous reduction products for LiNO$_3$ and LiNO$_2$ reduction—the latter being the primary reduction product of LiNO$_3$—could be N$_2$O, NO$_2$, and/or NO. As described in the experimental section (Table I), all of these three gases have a mass signal at $m/z = 30$; NO$_2$, as well as NO, has the most pronounced mass signal at $m/z = 30$, while N$_2$O has its strongest signal at $m/z = 44$. When converting the mass trace $m/z = 30$ and 44 with the calibration factor corresponding to N$_2$O (as done in Fig. 5b), both concentrations align very well at potentials below 1.5 V vs. Li$^+$/Li. From that, we can conclude that N$_2$O is formed during the initial reduction of an LiNO$_3$-containing electrolyte. Prior to that, the evolution of CO$_2$ (dark blue in Fig. 5b) is observed again at a potential of ~2 V vs. Li$^+$/Li where no increase at mass trace $m/z = 30$ is observed and, thus, the increase in $m/z = 44$ can be assigned to the evolution of CO$_2$ at potentials above 1.5 V vs. Li$^+$/Li, which qualitatively is similar to the measurement of the reference electrolyte (dark blue in Fig. 5a), where CO$_2$ was also found to get reduced and thus consumed at potentials < 1.5 V vs. Li$^+$/Li. Therefore, the mass signal at $m/z = 44$ over the course of the measurement was treated separately: the first peak of $m/z = 44$ at potentials >1.5 V vs. Li$^+$/Li was assigned to CO$_2$ (dark blue) and, thus, converted into molar quantities with a calibration factor of 0.8 (see Table I); the second peak of $m/z = 44$ was assigned to N$_2$O (dark green) and fitted with a calibration factor of 0.23 (see Table I) and, accordingly, the mass signal of $m/z = 30$ (light green) was converted with the corresponding calibration factor for N$_2$O of 0.1 (see Table I). This yields a consistent maximum N$_2$O concentration of ~3 µmol m$^{-2}_{BET}$ for both the $m/z = 30$ and $m/z = 44$ mass traces, validating our assignment of the mass traces $m/z = 30$ and $m/z = 44$ below 1.5 V vs. Li$^+$/Li to N$_2$O. After reaching a maximum concentration at ~1.0 V vs. Li$^+$/Li, the formed N$_2$O is gradually consumed again when scanning to lower potentials. Mechanistic considerations and proposed reduction reactions are described in the section below, discussing the gas evolution for the LiNO$_2$-based electrolyte.

The OEMS data show that the effective surface passivation by the reduction product(s) of the LiNO$_3$ additive almost completely suppresses the reduction of EC, resulting in an almost 75% decrease in the amount of evolved ethylene (blue) below 0.8 V, reaching only

~5 μmol m^{-2}_{BET} by the end of the scan compared to the ~19 μmol m^{-2}_{BET} that was observed for the $LiNO_3$-free reference electrolyte (see Fig. 5a). Interestingly, the observed amount of CO of ~3 μmol m^{-2}_{BET} is not diminished compared to the reference electrolyte. CO evolution during formation stems either from an alternative EC reduction pathway (as compared to the formation of ethylene gas and LEDC) or the reduction of the linear carbonate.[38] Thus, the presence of $LiNO_3$ in the electrolyte apparently diminish the alternative EC reduction pathway and the reduction of DEC to a smaller extent. The exact origin of this phenomena remains unknown and is beyond the scope of this study. Figure 5c depicts the current density and gas evolution during the reductive voltammetric scan of a C65||Li OEMS cell with $LiNO_2$-containing electrolyte. Consistent with Fig. 4a (turquoise), only one characteristic reduction peak at 1.39 V vs. Li^+/Li is observed. Furthermore, the EC reduction peak at 0.8 V is also diminished (blue), even though slightly larger amounts of ethylene are evolved compared to the $LiNO_3$-containing electrolyte (see Fig. 5b). While the reduction of $LiNO_3$ to $LiNO_2$ already forms Li_2O as a passivating film (see reaction 1.1), the direct use of $LiNO_2$ as additive in the electrolyte bypasses this first reaction, which might explain the slightly higher amount of ethylene produced at the end of the reductive scan with $LiNO_2$- vs. $LiNO_3$-containing electrolyte (~7 vs. ~5 μmol m^{-2}_{BET}); nevertheless, the amount of ethylene is still reduced by more than 60% with respect to the reference electrolyte. Again, small amounts of CO_2 evolved around 2.0 V vs. Li^+/Li and can be traced back to trace amounts of water, as already observed in the case of the reference electrolyte.[41,42] The correction and conversion of mass signal $m/z = 44$ was done analogously to the measurement with $LiNO_3$ (Fig. 5b). The reduction of $LiNO_2$ with its peak at 1.39 V vs. Li^+/Li shows the evolution of N_2O starting from ~1.4 V vs. Li^+/Li at the mass signals $m/z = 44$ and $m/z = 30$ (marked by the vertical dotted line in Fig. 5c). The observation of N_2O gas with the $LiNO_2$-containing electrolyte gives evidence that the N_2O is connected to the reduction of $LiNO_2$ species. This is in line with the observation of the N_2O gas evolution starting at the second reductive feature already in the measurement with the $LiNO_3$-containing electrolyte (see Fig. 5b). We propose that the reduction of $LiNO_2$ to N_2O proceeds according to reaction 1.2: next to N_2O, additional Li_2O is formed, which passivates the surface as a solid reduction product. Jozwiuk et al.[14] already observed the evolution of N_2O in lithium-sulfur battery systems using $LiNO_3$ as an electrolyte additive. In this study, the N_2O gas is formed upon the reaction of $LiNO_2$ with sulfur.

$$2\ LiNO_2 + 4\ e^- + 4\ Li^+ \rightarrow N_2O + 3\ Li_2O \qquad [1.2]$$

Based on this assumption, an N_2O quantity of ~3 μmol m^{-2}_{BET} are being produced, which is supported by the reasonably close correspondence between the N_2O quantities derived from channels $m/z = 44$ and $m/z = 30$ using the calibration factors in Table I. In comparison, the complete conversion of $LiNO_2$ to N_2O according to reaction 1.2 would result in a higher N_2O quantity of ~7.8 μmol m^{-2}_{BET}, based on a total electrolyte amount of 50 μl with 0.16 wt% $LiNO_2$ and a carbon BET surface area of 0.23 m^2. However, N_2O gas is consumed at the same time once it is evolved, as indicated by the strong decrease of the N_2O signal below/near ~1.0 V vs. Li^+/Li (see light/dark green lines in Fig. 5c), so that it cannot be determined at this point whether all or only significant fraction of $LiNO_2$ are being reduced according to reaction 1.2. To identify the reaction products of this competing reaction and to investigate the solid reduction products on the surface of the carbon electrode, we next conducted XPS measurements. Overall, the OEMS data validate the strongly passivating properties of $LiNO_3$ and $LiNO_2$, leading to a significantly reduced ethylene evolution, indicating a strongly suppressed EC reduction, as well as to the formation of N_2O as an intermediate product.

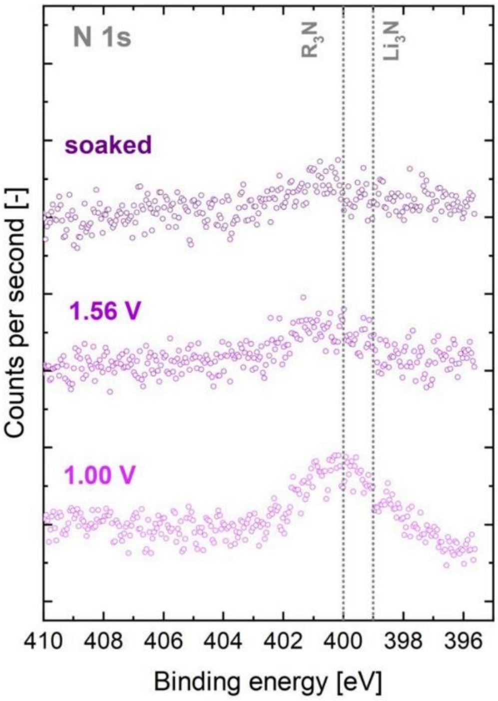

Figure 6. XPS N 1 s spectra of carbon electrodes (0.6 ± 0.1 $mg_{C65}\ cm^{-2}$), harvested either after an overnight soak in 1 M $LiPF_6$ in EC/DEC 1/2 v/v + 0.22 wt% $LiNO_3$ (upper spectrum, dark purple) or harvested from C65||Li coin-cells with 1 M $LiPF_6$ in EC/DEC 1/2 v/v + 0.22 wt% $LiNO_3$ after two voltage scans to 1.56 V (middle spectrum, purple) or 1.00 V vs. Li^+/Li (bottom spectrum, light purple). Counts per second were artificially adjusted for better visualization.

Investigation of solid reduction products by XPS analysis.—To analyze solid reduction products on the surface of the electrodes, we conducted a negative voltammetric scan with C65-electrodes to different voltages in an $LiNO_3$-containing electrolyte and then harvested the electrodes for XPS analysis. The N 1 s spectrum of a carbon electrode soaked overnight in a coin half-cell filled with 1 M $LiPF_6$ in EC/DEC 1/2 v/v + 0.22 wt% $LiNO_3$ does not show any significant signal (see Fig. 6 upper spectrum), confirming the efficacy of the washing procedure applied to the harvested electrodes. We then performed XPS analysis on a carbon black electrode harvested from a C65||Li coin-cell after its voltage had been scanned from OCV to the potential of the first reductive peak at 1.56 V vs. Li^+/Li (see appendix A2). The N 1 s spectrum of this electrode (middle spectrum in Fig. 6 shows the development of a very small signal at ~400 eV, which can be assigned to R_3N/Li_3N species. Li_3N is a known reduction product of $LiNO_2$ in ether- and carbonate-based electrolytes.[11,15,22,36] The presence of Li_3N in the XPS spectrum already at 1.56 V vs. Li^+/Li can be rationalized by the overlap of the reduction peaks of $LiNO_3$ and $LiNO_2$ (compare purple and turquoise curves in Fig. 4a), so that even when the reductive scan is stopped at 1.56 V vs. Li^+/Li, some of the reduced $LiNO_3$ species can already get further reduced to solid R_3N/Li_3N species. Therefore, we believe that the initial reduction reaction of $LiNO_3$ does not form any nitrogen-containing passivation layer, consistent with the conversion of $LiNO_3$ to insoluble Li_2O and soluble $LiNO_2$ species according to reaction 1.1, and that the small

R_3N/Li_3N signal derives from a follow-up reaction of the $LiNO_2$ reduction products.

However, the N 1 s peak assigned to R_3N/Li_3N species significantly increases for a carbon black electrode that is harvested from a C65‖Li coin-cell after its voltage had been scanned from OCV to a potential of 1.0 V vs. Li^+/Li, i.e., to a potential far negative of the $LiNO_2$ reduction peak at 1.39 V vs. Li^+/Li (see the turquoise line in Fig. 4a). This suggests the formation of R_3N/Li_3N as a reduction product of $LiNO_2$ and/or N_2O and its incorporation into the SEI, a follow-up reaction that would be consistent with the N_2O consumption below/near ∼1.0 V vs. Li^+/Li (Fig. 5c). A reasonable explanation for these observations would be electrochemical reduction of N_2O according to reaction 1.3:

$$N_2O + 8\,e^- + 8\,Li^+ \rightarrow 2\,Li_3N + Li_2O \qquad [1.3]$$

The sum of reactions 1.2 and 1.3 then equates to reaction 1.4., which is consistent with the reaction of $LiNO_2$ with lithium ions to Li_3N and Li_2O, as proposed by Fu et al.[15]

$$LiNO_2 + 6\,Li^+ + 6\,e^- \rightarrow Li_3N + 2\,Li_2O \qquad [1.4]$$

In various studies, R_3N/Li_3N species were found as part of the SEI of electrodes cycled in $LiNO_3$-containing electrolyte systems, which is in line with our findings. It has been shown that Li_3N exhibits excellent lithium-ion conductivity, enabling fast Li^+ diffusion through the SEI and poor electronic conductivity.[17,44–46] Next to Li_3N, Li_2O is also often observed in the SEI when using $LiNO_3$ as an electrolyte additive,[13,15,18,47] which again would be consistent with the reactions described above.

We were able to show that the reduction features at both 1.56 V and 1.39 V vs. Li^+/Li can be assigned to the formation of surface passivating species. As a direct consequence, the ratio of the two reduction peaks observed for the reduction of the $LiNO_3$ additive depends on the amount of electrode surface and additive concentration. For an electrode with an overall low amount of total surface area, e.g., 0.07 m^2, as depicted in Fig. 4a (purple line), only a very small second reduction peak can be observed. This can be rationalized by the fact that one equivalent of Li_2O is formed by the reduction of one equivalent of $LiNO_3$ (see reaction 1.1), so that the subsequent reduction of the formed $LiNO_2$ is suppressed. On the other hand, for a larger surface area electrode, e.g., with a total surface of 0.11 m^2 as depicted in Fig. 4b (dark purple line), the surface is less strongly passivated by Li_2O formed during the first reduction step, so that a more pronounced $LiNO_2$ reduction feature due to reaction 1.2 can be seen. Analogously, when the $LiNO_3$ concentration in the electrolyte is being decreased (going from dark to very light purple lines in Fig. 4b), the height of the second reduction peak at 1.39 V relative to the height of the first reduction peak at 1.56 V increases. At the same time, the overall reduction currents in this potential region decrease, indicating an overall reduced surface passivation with decreasing $LiNO_3$ concentration, which is reflected by a simultaneous increase of the EC reduction peak at 0.8 V vs. Li^+/Li. The concentration dependence of the latter suggests that a $LiNO_3$ content of ∼0.22 wt% is just about sufficient to completely passivate the carbon surface area (∼0.11 m^2).

Based on the observation that 0.22 wt% of $LiNO_3$ in the electrolyte is sufficient to passivate a carbon surface area of 0.11 m^2 and the mechanistic findings represented by reactions 1.1 and 1.4, we can estimate the number of monolayers of Li_2O and Li_3N required to suppress EC reduction by (i) considering the total amount of $LiNO_3$ in the cell (namely 1.9 μmol $LiNO_3$ for the 50 μl of added electrolyte with an $LiNO_3$ content of 0.22 wt% and an electrolyte density of ∼1.2 g cm^{-3}) and by (ii) assuming that essentially all of the $LiNO_3$ gets reduced according to reactions 1.1 and 1.4, so that 1 mol $LiNO_3$ would yield 3 mol of Li_2O and 1 mol of Li_3N which are precipitated on the carbon surface. Furthermore, one can estimate the surface covered by one unit cell of Li_2O or Li_3N: (i) by dividing the crystal volume of the cubic $Fm\bar{3}m$ space group for Li_2O by its lattice parameter yields the average surface area occupied by one Li_2O molecule, namely A_{Li_2O} = 101 Å^3/4.66 Å = 21.7 Å^2; (ii) by dividing the crystal volume of the hexagonal P6/mmm space group for Li_3N by its lattice parameter yields the average surface area occupied by on Li_3N molecule, namely A_{Li_3N} = 44.9 Å^3/3.73 Å = 12.0 Å^2. Based on these estimates/assumptions, the total surface area occupied by Li_2O and Li_3N from the complete reduction of 1.9 μmol $LiNO_3$ in the cells would be ∼1.9 μmol·N_A·(3·21.7 Å^2 + 1·12.0 Å^2) ≈ 0.88 m^2 (where N_A is the Avogadro constant). For the here employed total carbon surface area of ∼0.11 m^2, this would amount to approximately 7 monolayers of Li_2O+Li_3N. This would correspond to a thickness of the SEI of ∼3 nm by the passivation of $LiNO_3$, which is in reasonably good agreement with reported values for an adequate passivation of an anode surface.[48] However, such a simplified calculation might underestimate the SEI thickness and thus the amount of monolayers. The electrochemically active surface area of an electrode is typically diminished compared to the single components, as the binder layer covers the surface. Here, the binder content was selected to obtain a reasonable binder layer thickness of ∼ 9 nm.[49]

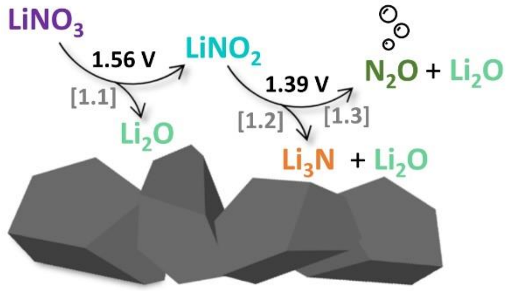

Scheme 1. Reduction reactions of $LiNO_3$ electrolyte additive in carbonate-based electrolyte systems on an anode surface, deduced from the measurements of carbon black model electrodes. The gray numbers in the square brackets refer to the corresponding equations in the main text.

The reduction mechanism of the $LiNO_3$ additive in carbonate-based electrolyte systems on the anode surface is summarized in Scheme 1: First, $LiNO_3$ is reduced at a potential of 1.56 V vs. Li^+/Li to form both Li_2O, passivating the surface of the anode, and $LiNO_2$ that remains dissolved in the electrolyte (reaction 1.1). Then, the dissolved $LiNO_2$ intermediate gets further reduced at a potential of 1.39 V vs. Li^+/Li, yielding N_2O and Li_2O (reaction 1.2), whereby the latter further passivates the anode surface. At the same time, N_2O is reduced to Li_2O and Li_3N (reaction 1.3), leading to additional SEI growth.

Oxidation of $LiNO_3$- and $LiNO_2$-containing electrolytes.— Besides the precise knowledge about the reduction reactions on the anode, the evaluation of the oxidative stability of electrolyte components on the positive electrode is also important.[48] A decomposition of the electrolyte additive at the cathode in combination with a Si anode is particularly undesired, since stable cycling of the silicon requires the permanent presence of effective SEI-forming additives. In contrast, the amount of additive in full-cells with a graphite anode is typically chosen in a way such that the additive is completely consumed during formation, in which case the oxidative stability limit of an additive can be as low as 3.8 V vs. Li^+/Li, where the SEI formation is mostly completed.[48] A typical NCM-based cathode is usually operated with an upper cathode potential of ∼4.3–4.5 V vs. Li^+/Li.[50]

Thus, the oxidative behavior of the $LiNO_3$- and $LiNO_2$-containing electrolytes is analyzed in the following, and implications on full-cell cycling are evaluated. For that, we first performed CV measurements on carbon electrodes with the $LiNO_3$-containing electrolyte in the oxidative scan direction up to 5.0 V vs. Li^+/Li (Fig. 7a). Since we also want to analyze the oxidative stability of the intermediate reduction products of $LiNO_3$ such as $LiNO_2$, we first scanned to different negative potentials to form the reduced species in situ. The negative scans were conducted from OCV (~3.0 V vs. Li^+/Li) to three different negative potential limits in order to generate different $LiNO_3$ reduction species: (i) to 2.0 V vs. Li^+/Li, where we expect no reduction of $LiNO_3$, so that only $LiNO_3$ should be present; (ii) to 1.45 V vs. Li^+/Li, where $LiNO_2$ should have been formed according to reaction 1.1 (see also Fig. 4); and, (iii) to 1.0 V vs. Li^+/Li, where both $LiNO_2$ and $LiNO_3$ should have been consumed to a significant extent. As shown in Fig. 7a (dark purple line), the oxidative CV scan following an initial reductive scan to 2.0 V vs. Li^+/Li does not show any oxidation features in the potential region up to ~4.5 V vs. Li^+/Li, and significant oxidative currents are observed only once the potential is increased to beyond 4.5 V vs. Li^+/Li, where the oxidation of EC initiates.[48,51] If the first reductive scan is continued until 1.45 V vs. Li^+/Li (purple line in Fig. 7a), $LiNO_2$ is expected to be formed in situ by the reduction of $LiNO_3$, while its further reduction should still be very slow (see Fig. 4). Therefore, $LiNO_2$ should be present in the electrolyte for the subsequent oxidative scan, during which a distinct oxidation feature at ~3.5 V vs. Li^+/Li is observed. The magnitude of this oxidation feature strongly decreases again when the initial reductive scan is extended to a lower potential of 1.0 V vs. Li^+/Li (light purple line in Fig. 7a, i.e., going far negative of the reduction peak of the $LiNO_2$ species, where the majority of the $LiNO_2$ intermediate should be consumed. This suggests that the oxidation feature observed at ~3.5 V vs. Li^+/Li can indeed be assigned to the oxidation of the $LiNO_2$ species.

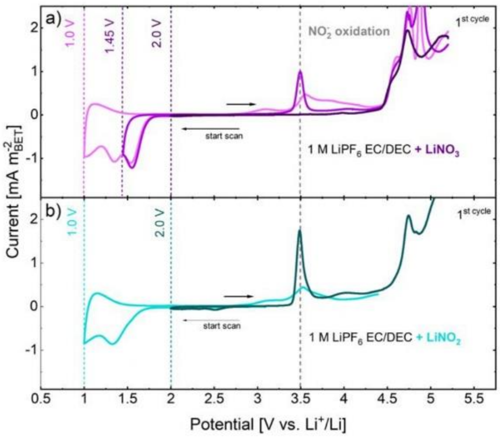

Figure 7. First CV cycle of carbon black electrodes ($0.6 \pm 0.1\ mg_{C65}\ cm^{-2}$, exposing a total carbon surface area of ~0.07 m^2) in C65||Li coin-cells with a glass fiber separator (Whatman GD type A/E) and with 50 μl of: (a) 1 M $LiPF_6$ in EC/DEC 1/2 v/v + 0.22 wt% $LiNO_3$; **b)** 1 M $LiPF_6$ in EC/DEC 1/2 v/v + 0.16 wt% $LiNO_2$. Each scan was conducted with a fresh cell, first scanning from OCV (~3.0 V vs. Li^+/Li) into the negative direction (reductive scan) to either 2.0, 1.45, or 1.0 V vs. Li^+/Li (each marked by a dashed line), and then reversing the scan direction (oxidative scan) until 5.2 V vs. Li^+/Li. The applied scan rate was 0.1 mV s^{-1}. The current is normalized to the BET surface area of the C65 electrodes. The grey dotted line at 3.5 V vs. Li^+/Li marks the oxidation potential of the NO_2^- species.

To get further evidence, we conducted the same experiments with the $LiNO_2$-containing electrolyte. Here, the oxidative scan starting from 2.0 V vs. Li^+/Li already shows the oxidation feature at ~3.5 V vs. Li^+/Li (dark green line in Fig. 7b), confirming the above hypothesis that $LiNO_2$ that is formed as an intermediate during $LiNO_3$ reduction is oxidized at this potential. Consuming the $LiNO_2$ species in a reductive scan to 1.0 V vs. Li^+/Li prior to the oxidative scan results in a significant reduction of the oxidation feature at ~3.5 V vs. Li^+/Li.

A possible oxidation product of the NO_2^- species is gaseous NO_2. Whether this is plausible can be checked by calculating the reversible half-cell potential of the following oxidation reaction:

$$\begin{aligned} &NO^-_{2(l)} \rightarrow NO_{2(g)} + e^- \\ &\text{with } \Delta_R G_{NO^-_{2(l)}/NO_{2(g)}} = ?\ kJ\ mol^{-1} \end{aligned} \tag{2.1}$$

Here, (l) and (g) denote species dissolved in the liquid phase or present in the gas phase, respectively, and $\Delta_R G_{NO^-_{2(l)}/NO_{2(g)}}$ is the free reaction enthalpy of the reaction that we would like to determine. As our potential and thus our free enthalpies are referenced to the Li^+/Li reference potential, reaction 2.1 can be combined with the half-cell reaction describing the Li^+/Li standard reduction reaction:

$$\begin{aligned} &Li^+_{(l)} + e^- \rightarrow Li_{(s)} \\ &\text{with } \Delta_R G_{Li^+_{(l)}/Li_{(s)}} \equiv 0\ kJ\ mol^{-1} \equiv 0V \text{ vs. } Li^+/Li \end{aligned} \tag{2.2}$$

Here, (s) denotes species in a pure solid phase and $\Delta_R G_{Li^+_{(l)}/Li_{(s)}}$ must be zero since we are defining the standard reduction potential of Li^+/Li as 0 V (this implies a lithium-ion activity of one). Adding up reactions 2.1 and 2.2 yields:

$$\begin{aligned} &Li^+_{(l)} + NO^-_{2(l)} \rightarrow Li_{(s)} + NO_{2(g)} \\ &\text{with } \Delta_R G_{react.\ 2.3} = \Delta G_{NO^-_{2(l)}/NO_{(g)}} \end{aligned} \tag{2.3}$$

Here, the free reaction enthalpy of reaction 2.3 corresponds to $\Delta G_{NO^-_{2(l)}/NO_{(g)}}$, since $\Delta_R G_{Li^+_{(l)}/Li_{(s)}} = 0$. Unfortunately, to determine $\Delta G_{NO^-_{2(l)}/NO_{(g)}}$, one would need the free enthalpies of formation of the dissolved $Li^+_{(l)}$ and $NO^-_{2(l)}$ ions, which are not readily available. These can, in principle, be obtained by formulating the dissolution of the $LiNO_2$ salt in the electrolyte:

$$\begin{aligned} &LiNO_{2(s)} \rightarrow Li^+_{(l)} + NO^-_{2(l)} \\ &\text{with } \Delta_{solv.} G_{LiNO_{2(s)}} \end{aligned} \tag{2.4}$$

Here, $\Delta_{solv.} G_{LiNO_{2(s)}}$ is the free enthalpy of dissolution of solid $LiNO_2$ in the electrolyte, which can be obtained from its experimentally determined solubility (see below). By adding up reactions 2.3 and 2.4, one obtains a reaction that now only contains pure solid and pure gaseous substances:

$$\begin{aligned} &LiNO_{2(s)} \rightarrow Li_{(s)} + NO_{2(g)} \\ &\Delta_R G_{react.\ 2.5} = \Delta_f G_{NO_{2(g)}} + \Delta_f G_{Li_{(s)}} - \Delta_f G_{LiNO_{2(s)}} \end{aligned} \tag{2.5}$$

The free enthalpy of reaction for reaction 2.5 can now be obtained easily from the tabulated free enthalpy of formation values of NO_2 ($\Delta_f G_{NO_{2(g)}} = 51.3\ kJ\ mol^{-1}$),[52] Li ($\Delta_f G_{Li_{(s)}} = 51.3\ kJ\ mol^{-1}$),[52] and $LiNO_2$ ($\Delta_f G_{LiNO_{2(s)}} = -302\ kJ\ mol^{-1}$),[52] yielding $\Delta_R G_{react.\ 2.5} = 353.3\ kJ\ mol^{-1}$. As reaction 2.5 was generated by adding up reactions 2.3 and 2.4, $\Delta_R G_{react.\ 2.5}$ must also correspond to:

$$\Delta_R G_{react.\ 2.5} = \Delta_R G_{NO^-_{2(l)}/NO_{2(g)}} + \Delta_{solv.} G_{LiNO_{2(s)}} \tag{2.6}$$

From this, one can calculate $\Delta_R G_{NO^-_{2(l)}/NO_{2(g)}}$, assuming that $\Delta_{solv.} G_{LiNO_{2(s)}}$ can be determined:

$$\begin{aligned} \Delta_R G_{NO^-_{2(l)}/NO_{2(g)}} &= \Delta_R G_{react.\ 2.5} - \Delta_{solv.} G_{LiNO_{2(s)}} \\ &= \Delta_R G_{react.\ 2.5} + R \cdot T \cdot \ln(K_{solub.}) \end{aligned} \tag{2.7}$$

Here, $\Delta_{solv.} G_{LiNO_{2(s)}}$ was replaced by the relationship between $\Delta_{solv.} G_{LiNO_{2(s)}}$ and the thermodynamic solubility constant $K_{solub.}$ of

$LiNO_2$ in the electrolyte (note that T is the temperature in Kelvin and $R = 8.314\ J\ mol^{-1}\ K^{-1}$). The solubility constant can be written in terms of the law of mass action for reaction 2.4:

$$K_{solub.} = \frac{[a_{NO^-_{2(l)}}]\cdot[a_{Li^+_{(l)}}]}{[a_{LiNO_{2(s)}}]} \approx \frac{[(c_{NO^-_{2(l)}})/(1\ mol\ L^{-1})]\cdot[(c_{Li^+_{(l)}})/(1\ mol\ L^{-1})]}{[1]} \approx 0.036 \qquad [2.8]$$

Here, a denotes the activity of the various species, which for a pure solid phase can be taken as one (i.e., $a_{LiNO_{2(s)}} = 1$) and which for the dissolved species can be approximated by their concentration divided by the standard concentration of $1\ mol\ L^{-1}$. Based on the measured NO_2^- concentration of $0.036\ mol\ L^{-1}$ in the 1 M $LiPF_6$ in EC/DEC 1/2 v/v electrolyte (see Experimental section) and the Li^+ concentration of 1 M, $K_{solub.} \approx 0.036$. With this, Eq. 2.7 yields $\Delta_R G_{NO^-_{2(l)}/NO_{2(g)}} = 345.1\ kJ\ mol^{-1}$. Keeping in mind that this value was referenced to $\Delta_R G_{Li^+_{(l)}/Li_{(s)}} = 0$ (see reaction 2.2), i.e., to the Li^+/Li reference potential scale, $\Delta_R G_{NO^-_{2(l)}/NO_{2(g)}}/(-1\cdot F)$ corresponds to the standard oxidation potential of reaction 2.1 or, when multiplied by -1, to the standard reduction potential of reaction 2.1, which equates to 3.58 V vs. Li^+/Li. Considering the here used simplifying assumptions regarding $K_{solub.}$, this calculated value is in quite excellent agreement with the oxidation peak at ~3.5 V vs. Li^+/Li observed for the $LiNO_2$-containing electrolyte (see purple line in Fig. 7b), providing very strong evidence that this peak indeed corresponds to the oxidation of dissolved nitrate ions to NO_2 gas, as described by reaction 2.1. Note that similar values for the oxidation potential of $LiNO_2$ in either acetonitrile or as a molten salt have been reported in the literature.[20,53]

OEMS measurements were conducted to analyze the oxidation reaction in more detail and verify the evolution of NO_2 gas during this reaction, which will be discussed in the following section. Figure 8 depicts the current density of a CV scan on carbon black electrodes in 1 M $LiPF_6$ in EC/DEC 1/2 v/v + 0.16 wt% $LiNO_2$ electrolyte. First, a carbon black electrode was scanned in the oxidative direction from OCV (~3.0 V vs. Li^+/Li) to 3.7 V vs. Li^+/Li, followed by a reductive scan to 0.1 V vs. Li^+/Li (dark green line in Fig. 8). During the oxidative scan, the characteristic oxidation peak of $LiNO_2$ at ~3.5 V vs. Li^+/Li (feature ①) can be observed. In the following reductive scan, two features at 1.56 and 1.39 V vs. Li^+/Li appear, clearly indicating the presence of $LiNO_3$ species after the oxidative scan (compare to Fig. 4). However, the surface of the carbon black electrode does not seem to be passivated completely, since a pronounced EC reduction peak can be observed below 0.8 V.

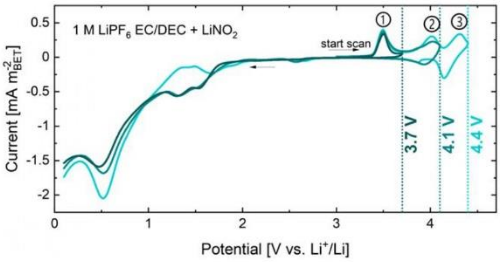

Figure 8. First CV cycle of carbon black working electrodes (2.0 ± 0.1 $mg_{C65}\ cm^{-2}$, exposing a total carbon surface area of ~0.23 m^2) in a C65||Li two-compartment OEMS cell with a glass fiber separator (Whatman GD type A/E) with 50 μl of 1 M $LiPF_6$ in EC/DEC 1/2 v/v + 0.16 wt% $LiNO_2$ electrolyte in the working electrode compartment. Note that in a two-compartment cell, the working and counter electrode compartments are separated by a liquid and gas impermeable glass-ceramic. The scans were conducted at 0.1 mV s^{-1}, starting from OCV (~3.0 V) in oxidative direction to different upper potentials (each measured with a fresh cell) and then reversed in reductive direction to 0.1 V vs. Li^+/Li. The upper potentials were 3.7 V vs. Li^+/Li (dark green), 4.1 V vs. Li^+/Li (green), and 4.4 V vs. Li^+/Li (turquoise). For reference, the different oxidation peaks are marked by ①, ②, and ③ in the figure. The current is normalized to the BET surface area of the C65 electrodes.

The upper panels of Fig. 9 show the same data as in Fig. 8, but this time, the current density of the CV scan is plotted vs. time (rather than vs. potential), and the corresponding gas evolution (lower panel) measured with the OEMS is also shown. Figure 9a shows the cell with the reversal of the scan direction at 3.7 V vs. Li^+/Li (same data as the dark green line in Fig. 8). When passing through the oxidation peak at ~3.5 V vs. Li^+/Li (feature ①), a steep increase in the evolution of a gas with a strong signal at *m/z* = 30 is observed (pink line in Fig. 9a). Based on the above discussion, this increase in the mass signal at *m/z* = 30 could represent the evolution of NO_2 according to Eq. 2.1, but as will be discussed below, there is also the possibility that it is NO or a mixture of NO and NO_2 (mechanistically, there is no evidence for the formation of N_2O during the oxidative scan). Therefore, we used an average calibration factor for the *m/z* = 30 mass signal of NO and NO_2 (i.e., 0.51, see Table I) to convert the *m/z* = 30 mass signal into concentrations; since the average calibration factor differs by only ~10% from the individual calibration factors (see Table I), the error in the quantification of the sum of evolved NO and NO_2 gas is also on the order of only ~10%. Under this premise, the amount of evolved NO+NO_2 reaches a constant value of ~5 μmol m^{-2}_{BET} by the time the potential scan is reversed at 3.7 V vs. Li^+/Li (marked by the dotted vertical line in Fig. 9a). Apart from NO/NO_2, no other gases are evolved during the oxidative scan. During the subsequent reductive scan, the mass signal at *m/z* = 30 decreases at potentials <2.5 V vs. Li^+/Li, suggesting the consumption of NO/NO_2. As already observed in the reductive scans in Fig. 5c, N_2O (dark green) gas is formed (~3.5 μmol m^{-2}_{BET}) upon reduction of $LiNO_2$ species according to reaction 1.2. In addition, C_2H_4 (blue) and CO (orange) are evolved due to EC and DEC reduction at potentials <0.8 V vs. Li^+/Li. However, the total amount of ethylene of ~11 μmol m^{-2}_{BET} is diminished compared to ~19 μmol m^{-2}_{BET} measured for the reference electrolyte, as displayed in Fig. 5a. From that, we conclude that the carbon surface is already partially passivated, which is in good agreement with the observation of the reductive feature for $LiNO_3$ and $LiNO_2$ at 1.56 and 1.39 V vs. Li^+/Li.

Based on the above observations, NO_3^- seems to be produced upon the oxidation of NO_2^- at ~3.5 V vs. Li^+/Li (clearly indicated by the reduction peak at 1.56 V in Fig. 8, dark green line), concomitant with gas formation indicated by the mass signal at *m/z* = 30, which we ascribe to NO/NO_2. Based on the estimated oxidation peak potential for the electrochemical oxidation of NO_2^- to NO_2 (see reaction 2.1) in combination with the strong mass signal of NO_2 at *m/z* = 30, one might assume that the evolved gas is NO_2. However, the investigation of the oxidation of $LiNO_2$ in acetonitrile (AN) and N,N-dimethylacetamide (DMA) on a Pt electrode by Bryantsev et al.[20] and Uddin et al.,[12] respectively, show that NO_2 evolved in AN or DMA upon the oxidation of $LiNO_2$ can undergo a rapid dimerization/autoionization to produce NO^+ and NO_3^-:

$$2\ NO_2 \rightleftharpoons [N_2O_4] \rightleftharpoons NO^+ + NO_3^- \qquad [3.1]$$

The hereby produced NO^+ furthermore undergoes a rapid ionic recombination with residual NO_2^-, leading to the formation of NO_2 and NO:

$$NO_2^- + NO^+ \rightarrow NO_2 + NO \qquad [3.2]$$

Assuming that both reactions proceed, the overall reaction, i.e., the sum of reactions 3.1 and 3.2 is:

$$NO_2^- + NO_2 \rightarrow NO_3^- + NO \quad [3.3]$$

This indeed occurs readily in aprotic electrolytes, as demonstrated by Uddin et al.,[12] showing that the reaction of $LiNO_2$ and NO_2 in DMA yields $LiNO_3$ and NO. If one now assumes that the NO_2 produced by the electrochemical oxidation of NO_2^- (reaction 2.1) quickly reacts further according to reaction 3.3, the summation of reactions 2.1 and 3.3 would reflect the final products,

$$2\,NO_2^- \rightarrow NO_3^- + NO + e^- \quad [3.4]$$

These reaction schemes not only explain the above-observed formation of NO_3^- upon the electrochemical oxidation of NO_2^- (indicated by the reduction peak at 1.56 V in Fig. 8, dark green line), but also show that the mass signal at $m/z = 30$ observed in Fig. 9a must be related to the formation of NO and NO_2, depending on the relative rates of reaction 2.1 vs. reaction 3.3. Two extreme cases may be distinguished: (A) if reaction 3.3 is fast, the overall net reaction for the electrochemical oxidation of NO_2^- is reaction 3.4, which means that 0.5 mol of NO is produced per mol of NO_2^-; (B) if reaction 3.3 is slow, 1 mol of NO_2 is produced per mol of NO_2^- (according to reaction 2.1). For these two cases, the maximum possible amounts of either NO (case A) or NO_2 (case B) that are formed upon the complete consumption of $LiNO_2$ during the OEMS experiment shown in Fig. 9a can be estimated, considering that 1.8 μmol $LiNO_2$ were contained in the working compartment of the OEMS cell (50 μl of electrolyte with an $LiNO_2$ content of 0.16 wt% and an electrolyte density of $\sim$1.2 g cm^{-3}). For case A, $\sim$0.9 μmol NO would be produced, equating to $\sim$3.9 μmol m_{BET}^{-2} (based on the BET surface area of the C65 working electrode of $\sim$0.23 m^2), while for case B, $\sim$1.8 μmol NO_2 would be produced, equating to $\sim$7.8 μmol m_{BET}^{-2}; both gases would be recorded on mass channel $m/z = 30$. Quite clearly, the estimated concentration of the gases corresponding to the $m/z = 30$ signal in Fig. 9a (pink line) of $\sim$5 μmol m_{BET}^{-2} (based on an averaged calibration factor for NO and NO_2, which introduces an absolute error of $\sim$10%) is in between these two extreme cases, which is consistent with the above-described mechanism when one assumes a complete consumption of $LiNO_2$ by the time the positive voltage limit of 3.7 V vs. Li^+/Li is reached. A reversal of reaction 3.4 during the negative going scan could, in principle, explain the vanishing $m/z = 30$ signal observed in Fig. 9a at a potential negative of 2.5 V vs. Li^+/Li; this, however, would require the presence of catalytic amounts of NO_2 (see reaction 3.2).

When increasing the upper cut-off potential of the oxidative scan to 4.1 V vs. Li^+/Li (Fig. 9b or 4.4 V vs. Li^+/Li (Fig. 9c), additional oxidative peaks are observed at 4.0 V vs. Li^+/Li (feature ②) and 4.3 V vs. Li^+/Li (feature ③), respectively. The latter of the two appears to be reversible, with an associated reduction peak developing during the subsequent reductive scan (see turquoise line in Fig. 8). However, when comparing the current response of the oxidative voltammetric scan of the OEMS cell (Fig. 8) to the features in the coin-cell setup (Fig. 7b), one notices that distinct oxidation features are not observable (see also Fig. A·3 in appendix A3). This can be explained by the fact that we employed a liquid and gas impermeable glass-ceramic to separate the working and counter electrode compartments of the OEMS cell, so that evolved NO/NO_2 cannot be consumed at the lithium counter electrode, thereby retaining these gases in the working electrode compartment, where they can undergo further oxidation reactions at potentials beyond 3.5 V vs. Li^+/Li (represented by features ② and ③). While for the subsequent reductive scan after an initial oxidative scan to 3.7 V vs. Li^+/Li, distinct reduction peaks characteristic for the reduction of $LiNO_3$ and $LiNO_2$ are observed (see dark green line in Fig. 8), these reduction peaks smear out but are still present for the case of an initial oxidative scan to 4.1 V vs. Li^+/Li (green line in Fig. 8). However, in the reductive scan following an initial oxidative scan to 4.4 V vs. Li^+/Li (turquoise line in Fig. 8), these reduction peaks disappear completely, suggesting the absence of $LiNO_3$ and $LiNO_2$ in the electrolyte after a prior excursion to 4.4 V vs. Li^+/Li, which is consistent with the strongly pronounced EC reduction peak below 0.8 V vs. Li^+/Li in this case.

Regarding gas evolution, the cell scanned to 4.1 V vs. Li^+/Li shows the same steep initial increase of the mass trace $m/z = 30$ during the oxidative scan (i.e., when passing through feature ①, see Fig. 9b) as already observed for the cell cycled to 3.7 V vs. Li^+/Li. However, after reaching a maximum value for NO/NO_2 of $\sim$6 μmol m_{BET}^{-2}, the gas concentration decreases when scanning through feature ②, reaching a minimum value of $\sim$3 μmol m_{BET}^{-2} at the positive voltage limit of 4.1 V vs. Li^+/Li, which could indicate the complete conversion of the gas phase to NO. Upon reversal of the scan direction, a continuous increase of the $m/z = 30$ signal to a nominal concentration of $\sim$7 μmol m_{BET}^{-2} is observed, which is very close to the maximum possible concentration if only NO_2 had been formed from the $LiNO_2$ contained in the cell (see above). Again, as

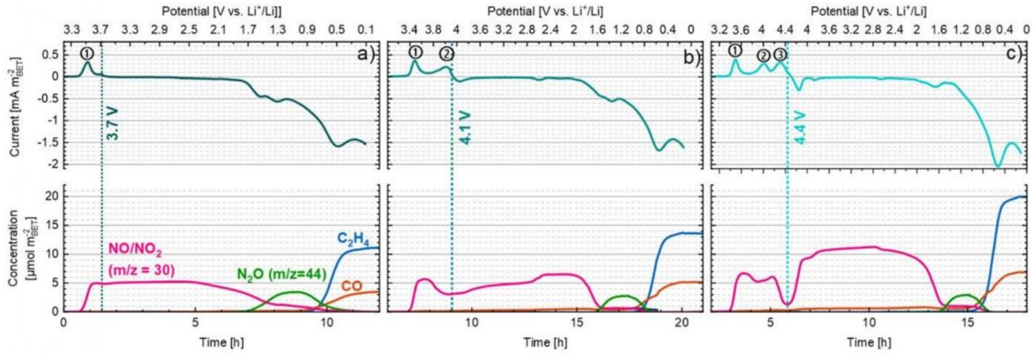

Figure 9. The upper panels depict the first CV cycle data shown in Fig. 8 but plotted against time (lower x-axis) rather than potential; the associated potentials are plotted along the upper x-axis, and the different oxidation peaks are marked by ①, ②, and ③ (corresponding to those marked in Fig. 8). The lower panels show the concomitant gas evolution measured by OEMS: (a) for reversing the scan at a positive potential limit of 3.7 V Li^+/Li (dark green data in Fig. 8); (b) for reversing the scan at a positive potential limit of 4.1 V Li^+/Li (green data in Fig. 8); (c) for reversing the scan at a positive potential limit of 4.4 V Li^+/Li (turquoise data in Fig. 8). The amount of evolved C_2H_4 (determined for $m/z = 26$), CO (determined for $m/z = 28$), N_2O (determined for $m/z = 44$), and NO/NO_2 (determined for $m/z = 30$, using an average calibration factor of 0.51 see Table I) is normalized to the BET surface area of the C65 electrodes.

the potential is decreased below ~2.0 V vs. Li^+/Li, the *m/z* = 30 mass signal starts to decrease and then vanishes below ~1.6 V vs. Li^+/Li. The slightly increased evolution of ethylene and carbon monoxide at low potentials compared to what was observed in Fig. 9a suggests an enhanced EC reduction and, thus, a reduced amount of $LiNO_3/LiNO_2$ in the cell. Again, N_2O gas (dark green) is formed upon the reduction of $LiNO_2$ (reaction 1.3) until it gets further reduced and consumed again.

Going even further with the oxidative scan to 4.4 V vs. Li^+/Li, a drastic decrease and complete consumption of the initially evolved gas with *m/z*=30 is observed as the potential is being scanned through the oxidation peak at ~4.3 V vs. Li^+/Li (feature ③ in Fig. 9c). However, upon reversal of the scan direction at 4.4 V vs. Li^+/Li, a steep increase of the *m/z*=30 mass signal is observed, reaching a maximum value of ~12 μmol m_{BET}^{-2} after the reduction peak associated with feature ③ has been passed. This value actually exceeds our above estimate for the maximum amount of gas, namely of ~7.8 μmol m_{BET}^{-2} for pure NO_2. an observation for which we, unfortunately, have no explanation at the moment. Finally, at the end of the reductive scan, the total amounts of ethylene and carbon monoxide that can be associated with the reduction of EC are at very high levels (blue and orange lines in Fig. 9c), very close to the values observed for the reference electrolyte without $LiNO_3/LiNO_2$ (see Fig. 5a). This indicates the absence of $LiNO_3/LiNO_2$ after having scanned to an upper voltage limit of 4.4 V vs. Li^+/Li. In contrast, the evolution of N_2O gas upon the reductive scan in this case implicates the presence of $LiNO_2$ species at this point (see reaction 1.2), since unless the N_2O gas is formed by an additional reaction, this cannot be explained in the absence of $LiNO_2$.

In order to analyze the redox feature with the oxidation peak at 4.3 V vs. Li^+/Li (feature ③ and the associated reduction peak) in more detail, Fig. 10 shows experiments in a two-compartment OEMS cell with 1 M $LiPF_6$ in EC/DEC 1/2 v/v + 0.16 wt% $LiNO_2$ in the working electrode compartment (turquoise line), starting with a positive scan from OCV (~3.0 V vs. Li^+/Li) to 4.4 V vs. Li^+/Li and then cycling between 4.0–4.4 V vs. Li^+/Li. During the first oxidative scan, the previously observed three oxidation features (①, ②, and ③) can be seen. Within the subsequently restricted voltage window, a rather reversible reaction over several cycles with a half-wave potential of ~4.22 V vs. Li^+/Li can be seen, which are accompanied by a cyclic production (during the oxidative scan) and consumption (during the reductive scan) of the gas recorded at *m/z*=30 (see Fig. A·4 in appendix A4. Based on reaction 3.4, NO_3^- and NO would be expected to be the main species present in the system, whereby the latter can be further oxidized to the nitrosonium ion (NO^+) according to reaction 3.5:[20]

$$NO \rightleftharpoons NO^+ + e^- \qquad [3.5]$$

As a matter of fact, the signal at *m/z* = 30 during the oxidative scans, ascribed to NO, continuously increases for every cycle, reaching a maximum of ~13 μmol m_{BET}^{-2} after the sixth cycle (see Fig. A·4). Depending on the reaction media (electrolyte solvent, salt, and additives) which strongly influence the solvation and stabilization of the NO^+ ion, the reported reversible redox potentials range from 4.05 V,[20] 4.2 V,[54] all the way to 4.6 V,[55,56] which may be compared to the ~4.22 V vs. Li^+/Li that can be seen in Fig. 10 (turquoise line, feature ③) for the EC/DEC based electrolyte used here. Therefore, NO is the most likely gas that is evolved/consumed in feature ③, so that the *m/z*=30 mass signal shown in Fig. A·4 is ascribed to NO and quantified in Fig. A·4 using the calibration factor of NO at *m/z*=30 (i.e., 0.56, see Table I).

$NOBF_4$ is often used as a chemical source for the NO^+ species, so in order to evaluate the redox potential for reaction 3.5, we added $NOBF_4$ salt (0.038 M) to 1 M $LiPF_6$ in EC/DEC 1/2 v/v and conducted analogous CV measurements with a carbon black electrode in the two-compartment OEMS cell setup (see blue line in Fig. 10), this time cycling only between 3.8–4.6 V vs. Li^+/Li. The OCV prior to the CV scan of the cell with the $NOBF_4$-containing electrolyte was measured to be ~4.2 V vs. Li^+/Li, which is in line with the half-wave potential of the NO/NO^+ redox couple. The CV scan for the $NOBF_4$-containing electrolyte showed the same reversible oxidation and reduction peaks at ~4.22 V vs. Li^+/Li (blue line) which were observed for the $LiNO_2$-containing electrolyte (turquoise line). For further examination, the head-space of a two-compartment OEMS cell with a carbon black electrode and with the 1 M $LiPF_6$ in EC/DEC 1/2 v/v reference electrolyte was flushed with the 2000 ppm NO/Ar calibration gas prior to a CV scan in order to introduce NO species (see orange line in Fig. 10). In this case, the OCV of the cell is at the lower value of ~3.0 V vs. Li^+/Li, as in this case the reduced NO species are present in contrast to the NO^+ that are present when using $NOBF_4$. The CV of the carbon electrode under the NO-containing gas atmosphere showed the same features, giving additional proof for the assignment of Eq. 3.5 to the redox feature observed at 4.22 V vs. Li^+/Li.

With these findings, the consumption and consecutive evolution of the mass signal at *m/z* = 30, which is identified to be gaseous NO, can be explained based on reaction 3.5. However, the origin of the oxidative peak observed at 4.0 V vs. Li^+/Li (feature ②) remains unclear. Bryantsev et al. observed two oxidative peaks for the oxidation reaction 3.5 in the presence of NO_2^- and NO_3^-.[20] The first peak was attributed to the fast conversion of NO^+ formed via Eq. 3.1 to NO gas via reaction 3.2, which is then readily oxidized to NO^+ via reaction 3.5. The NO_2 species formed as the second product of reaction 3.2 can react with NO_2^- according to reaction 3.3.[20] Thus, NO can be continuously generated during the oxidation peak at 4.0 V vs. Li^+/Li, which is then oxidized in the following oxidative feature at ~4.22 V vs. Li^+/Li. Going further with the reductive scan into the negative direction, where EC can get reduced (<0.8 V vs. Li^+/Li), a total amount of C_2H_4 (blue) of ~20 μmol m_{BET}^{-2} and CO (orange) of ~7 μmol m_{BET}^{-2} is observed in Fig. 9c. The amount evolved here is similar to the one observed in Fig. 5a, which depicts the OEMS results of the reduction of the reference electrolyte without any $LiNO_3$ or $LiNO_2$ additive. This suggests that the carbon surface is not passivated prior to the EC reduction during the reductive scan, which is in line with the absence of the reductive features of NO_3^- at 1.56 and NO_2^- at 1.39 V vs. Li^+/Li, in contrast to

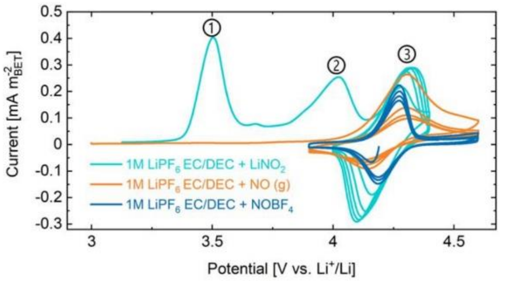

Figure 10. CV scans at 0.1 mV s^{-2} of carbon black working electrodes (2.0 ± 0.1 mg_{C65} cm^{-2}, exposing a total carbon surface area of ~0.23 m^2) in a C65||Li two-compartment OEMS cell, where the working and counter electrode compartments are separated by a liquid and gas impermeable glass-ceramic. The scans were conducted with different electrolytes/gases in the working electrode compartment: (i) 1 M $LiPF_6$ in EC/DEC 1/2 v/v + 0.16 wt % $LiNO_2$ after an initial argon purge of the cell head-space (turquoise); (ii) 1 M $LiPF_6$ in EC/DEC 1/2 v/v + 0.038 M $NOBF_4$ (blue); and, (iii) 1 M $LiPF_6$ in EC/DEC 1/2 v/v after flushing the cell head-space with 2000 ppm NO/Ar (orange). After the initial oxidative scan from OCV (~3.0 V vs. Li^+/Li) to 4.6 V vs. Li^+/Li, the potential was cycled 5 times between 3.8–4.4 V vs. Li^+/Li for the cell with $LiNO_2$-containing electrolyte and between 3.8–4.6 V vs. Li^+/Li for the cells with NO and $NOBF_4$. For reference, the different oxidation peaks are marked by ①, ②, and ③ in the figure and represent the same features that are marked in Figs. 8 and 9.

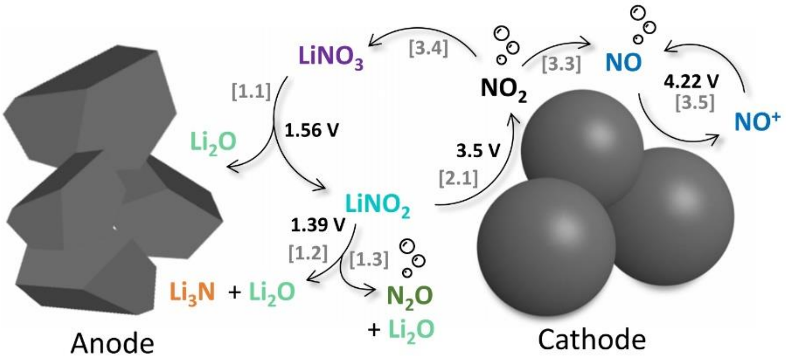

Scheme 2. Overview of the reduction and oxidation reactions occurring on the anode and cathode side when using $LiNO_3$ as electrolyte additive in carbonate-based electrolyte systems. Potentials are referenced to Li^+/Li. The gray numbers in the square brackets refer to the corresponding equations in the main text.

the presence of the features for the cell scanned to only 3.7 V vs. Li^+/Li. The absence of NO_3^- species during the reductive scan suggests that previously formed NO_3^- species from reactions 3.3 and 3.4 react further when the cell is scanned to higher oxidative potentials, basically extinguishing the reductive capability of N-containing species. However, in a realistic full-cell setup, $LiNO_3$ is able to diffuse to the anode and will readily be reduced before reacting with oxidized species on the cathode.[48]

The mechanistic insights obtained in this study are summarized in Scheme 2 and separated into the reactions at the anode and the cathode. In the first step, the $LiNO_3$ additive is reduced on the negative anode to form soluble $LiNO_2$ species and Li_2O (reaction 1.1), which is responsible for the formation of a passivating layer on the anode. Consequently, the subsequent reduction of $LiNO_2$ depends on the surface area of the anode and the additive amount present. Whenever the surface area is not yet completely passivated by Li_2O (formed upon initial reduction of $LiNO_3$), $LiNO_2$ can readily be further reduced to Li_2O and N_2O (reaction 1.2), followed by a further reduction of the latter to Li_3N and Li_2O (reaction 1.3), leading to the deposition of Li_3N and Li_2O on the anode surface. In the case of silicon anode materials, one has to take into account that the initial surface area increases due to the volume expansion of the silicon upon lithiation, so that the complete sequence of reduction reactions is likely to occur. At the same time, when $LiNO_2$ is produced in the electrolyte (reaction 1.1), it can also diffuse to the cathode, where it can lead to a cascade of oxidation reactions, starting at ~3.5 V vs. Li^+/Li to with the formation of NO_2 gas (reaction 2.1). In a series of chemical reactions, the thus produced NO_2 can be converted to NO_3^- and NO (reactions 3.3 and 3.4), whereby the latter can further reversibly be oxidized at ~4.2 V vs. Li^+/Li to NO^+ (reaction 3.5). Hence, $LiNO_3$ can partially be regenerated. Going to high oxidative potentials (>4.1 V vs. Li^+/Li), NO_3^- is absent for a consecutive reductive scan, as no characteristic reductive features was observed, and as the same amount of evolved is observed as in the additive-free electrolyte. In addition, NO gas—generated during the oxidative scan—is completely consumed again during the reductive scan. However, passivating effects on the carbon surface were not observed.

Cycle-life of Si||NCM622 full-cells in $LiNO_3$- vs. $LiNO_2$-containing electrolytes.—Finally, we evaluate the $LiNO_2$ additive in NCM622|Si full-cells (Fig. A·1). The performance is evaluated with respect to cells cycled with the $LiNO_3$ (purple) additive and the additive-free EC/DEC reference electrolyte (gray), which were shown in Fig. 11. Figure A·1 shows that cells cycled with the $LiNO_2$ additive (turquoise) have an improved cycle-life when compared to the reference electrolyte (gray), with 84 more cycles until they reach 80% capacity retention after 188 cycles. The first-cycle efficiency of 80.0±0.3% and the average CE over cycling of ~99.85% with the $LiNO_2$ additive is equal to the one observed for the $LiNO_3$ additive (purple). However, the capacity drop of the cells with $LiNO_2$ additive occurs earlier than with $LiNO_3$ additive. This could be explained by a more comprehensive passivation with the $LiNO_3$-based electrolyte, as additional Li_2O species are formed upon the first reduction step of $LiNO_3$ (reaction 1.1). Nevertheless, a significant increase in cycle-life by the addition of $LiNO_2$ to the electrolyte validates the finding that the NO_2^- species plays a key role in the passivation mechanism of the $LiNO_3$ additive in carbonate-based electrolyte systems.

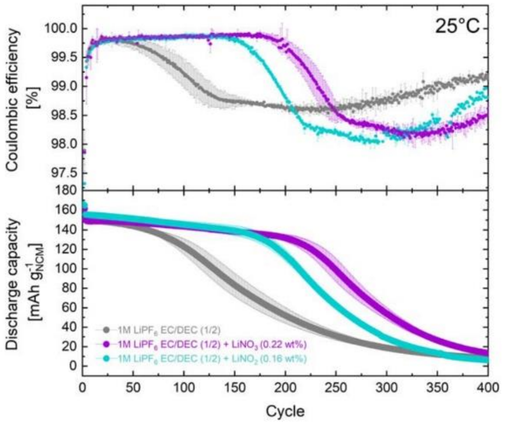

Figure 11. Specific discharge capacities (lower panel) and coulombic efficiencies (upper panel) of Si||NCM622 coin-cells (NCM622 cathodes with 2.4 ± 0.1 mAh cm^{-2} and Si anodes (with nominally 7.5 ± 0.4 mAh cm^{-2} utilized to ~32%) cycled at 25 °C. Cells were built with one glass fiber separator (Whatman GD type A/E) and 60 µl of three different electrolytes: (i) 1 M $LiPF_6$ in EC/DEC 1/2 v/v (gray, same as in Fig. 2), (ii) 1 M $LiPF_6$ in EC/DEC 1/2 v/v + 0.22 wt% $LiNO_3$ (purple, same as in Fig. 2), or, (iii) 1 M $LiPF_6$ in EC/DEC 1/2 v/v + 0.16 wt% $LiNO_2$ (turquoise). The cells were cycled between 3.0–4.2 V, first for two formation cycles with C/10 CCCV charge until 0.01 C and a C/10 CC discharge, followed by continuous cycling with C/2 CCCV charge until C/8 and C/2 CC discharge. Error bars represent the standard deviation of 3 independent repeat measurements.

However, oxidation of the $LiNO_2$ species on the cathode (reactions 3.2–3.4) can lead to a fast depletion of the $LiNO_2$ additive in the electrolyte. It seems unlikely that the initial reduction of the $LiNO_2$ additive in the first cycle creates such a long-lasting anode passivation layer that the oxidation of the remaining $LiNO_2$ species would play no role. The OEMS experiments in this study showed that by the oxidation of the $LiNO_2$ species, products such as NO_3^- can be regenerated, and NO gas being present in the cell can be consumed on the anode. Further studies need to be conducted to investigate and evaluate the effect of the oxidation products of this reaction to more comprehensively understand the effect of $LiNO_2$ in a realistic full-cell. The results presented here show that $LiNO_2$ is a reasonably effective additive for silicon-based anodes and is also able to significantly increase the cycle-life in full-cells.

Conclusions

We investigated the effect of $LiNO_3$ in silicon anodes in carbonate-based electrolyte systems and observed a significant increase of the cycle-life when adding $LiNO_3$ to the electrolyte. At elevated temperatures, the cells with the $LiNO_3$ additive outperformed the cells cycled with an FEC-based electrolyte, since the degradation of FEC at higher temperatures (>40 °C) leads to faster capacity fading.

We further conducted fundamental mechanistic experiments with carbon model electrodes to elucidate the reaction mechanism of the $LiNO_3$ additive in carbonate-based electrolytes. Hereby, $LiNO_2$ was found to be the primary reduction product, which is soluble in the electrolyte and can thus undergo reactions at both anode and cathode; the concomitantly produced Li_2O forms a passivating layer on the anode surface. Further reduction of the $LiNO_2$ species generates next to gaseous N_2O additional passivating Li_2O. The gaseous N_2O species was observed to be consumed at the same time once it is evolved. The reduction reaction of the intermediate N_2O species generates Li_3N and more Li_2O, both passivating the surface further. Therefore, the final reduction products of $LiNO_3$ being Li_3N and Li_2O which contribute to the property of the SEI and explain the beneficial effect of the additive to the cycling stability. However, while $LiNO_3$ is not oxidized in the usual operating potential window for the operation of full-cells (i.e., up to cathode potentials of ~4.4 V vs. Li^+/Li), $LiNO_2$ can be oxidized at ~3.5 V vs. Li^+/Li to NO_2. In a series of complex reactions, NO_2 is further converted to NO and NO_3^-. The latter can again be reduced on the anode surface and thus still provides the passivating properties. Finally, for the first time, $LiNO_2$ was used as an electrolyte additive and showed a similar improvement in the cycling performance of SiC||NCM full-cells when compared to the addition of $LiNO_3$. Already very little amount of the additive (0.036 M) could increase the cycling stability significantly. Future work should focus on increasing the concentration of the additive in order to further improve the cycle life.

Acknowledgments

Maximilian Graf gratefully acknowledges Wacker Chemie AG for financial support. Lennart Reuter gratefully acknowledges BMW Group for funding. Simon Qian acknowledges funding from the Deutsche Forschungsgemeinschaft (DFG, German Research Foundation) under Germany's Excellence Strategy (EXC 2089/1–390776260).

Appendix

A1: Variation of $LiNO_3$ concentration.—In order to investigate whether the rapidly accelerating capacity drop of $LiNO_3$-containing Si||NCM622 coin-cells after a specific number of cycles is related to a depletion of $LiNO_3$, a number of cells with different $LiNO_3$ concentrations in the EC/DEC electrolyte were built. As a baseline, an electrolyte solution with 0.22 wt% of $LiNO_3$ (corresponding to the $LiNO_3$ solubility limit) was used; the data of these cells is shown as dark purple line in Fig. A·1 and corresponds to the data shown in Figs. 2 and 11. With a dilution series of this $LiNO_3$-containing baseline electrolyte and the same electrolyte without $LiNO_3$ additive, an electrolyte with 0.11 wt% $LiNO_3$ (50% of the saturated solution) and one with 0.055 wt% $LiNO_3$ (25% of the saturated solution) were made. The discharge capacities of the cells assembled with the electrolyte containing 0.11 wt% $LiNO_3$ (purple) and of the cells with the electrolyte containing 0.055 wt% $LiNO_3$ (light purple) are shown in Fig. A·1. The cycling data shows a clear correlation between the onset of the rapidly accelerating capacity drop and the amount of $LiNO_3$ in the cells. The onset of the rapidly accelerating capacity drop of the cells cycled with only 0.055 wt% of $LiNO_3$ in the electrolyte is already observed at ~80 cycles, whereas for the cells with twice the amount of $LiNO_3$ (0.11 wt%), this onset occurs at ~160 cycles. However, for a perfectly linear correlation, one would expect the onset of the rapidly accelerating capacity drop for the cells with 0.22 wt% $LiNO_3$ to occur after ~320 cycles, but in fact, the drop is already observed at ~200 cycles. Thus, it seems that for extended cycling, other degradation phenomena also play a role that might induce a faster consumption of $LiNO_3$.

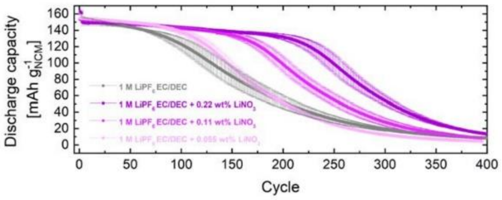

Figure A·1. The specific discharge capacity of Si||NCM622 coin-cells (NCM622 cathodes with 2.4 ± 0.1 mAh cm^{-2} and Si anodes with nominally 7.5 ± 0.4 mAh cm^{-2} utilized to ~32%) cycled at 25 °C. Cells were built with one glass fiber separator (Whatman GD type A/E) and 60 μl of four different electrolytes: (i) 1 M $LiPF_6$ in EC/DEC 1/2 v/v (gray); (ii) 1 M $LiPF_6$ in EC/DEC 1/2 v/v + 0.22 wt% $LiNO_3$ (dark purple), (iii) 1 M $LiPF_6$ in EC/DEC 1/2 v/v + 0.11 wt% $LiNO_3$ (purple), or, iv) 1 M $LiPF_6$ in EC/DEC 1/2 v/v + 0.055 wt% $LiNO_3$ (light purple). The cells were cycled between 3.0–4.2 V, first for two formation cycles with a C/10 CCCV charge (until 0.01 C) and a C/2 CC discharge, followed by continuous cycling with a C/2 CCCV charge (until C/8) and C/2 CC discharge. Error bars represent the standard deviation of 3 independent repeat measurements.

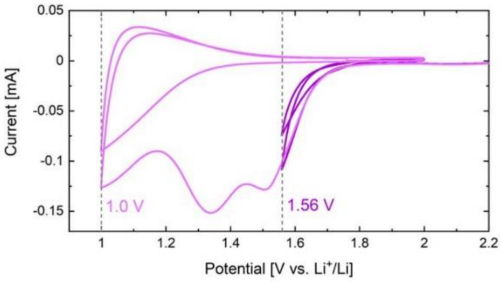

Figure A·2. Voltammetric cycles were conducted in a C65||Li half-cell prior to harvesting the carbon black electrodes (0.6 ± 0.1 mg_{C65} cm^{-2}) for the XPS measurements. The potential was cycled at 0.1 mV s^{-1} from OCV (~3.0 V vs. Li^+/Li) to either 1.56 V (dark red line) or 1.0 V vs. Li^+/Li (magenta line), scanned back to 2.0 V vs. Li^+/Li, and then cycled once more between 2.0 V vs. Li^+/Li and the respective lower cutoff voltage. The coin-cells were built with a glass fiber separator (Whatman GD type A/E) and with 50 μl of 1 M $LiPF_6$ in EC/DEC1/2 v/v + 0.22 wt% $LiNO_3$.

A2: CV data for XPS measurement.—Prior to harvesting the carbon black electrodes for XPS measurements, the electrodes were cycled in a C65||Li half-cell to either 1.56 V or 1.0 V vs. Li^+/Li in order to investigate the solid species in the SEI, which are presumable formed by reactions 1.1 and 1.2. The cells were cycled at 0.1 mV s^{-1} from OCV (~3.0 V vs. Li^+/Li) to their lower cutoff potential of either 1.56 V (dark red line) or to 1.0 V vs. Li^+/Li (magenta line) scanned

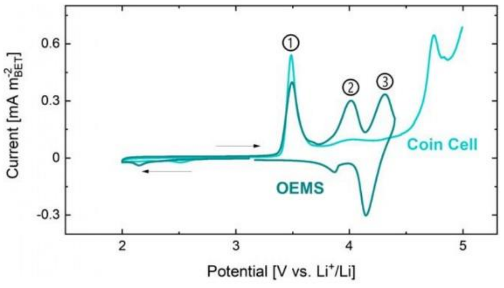

Figure A·3. Voltammetric scan of a carbon black working electrode (2.0 ± 0.1 mg$_{C65}$ cm^{-2}) in a C65||Li half-cell configuration with 1 M LiPF$_6$ in EC/DEC 1/2 v/v + 0.16 wt% LiNO$_2$, comparing data obtained in a coin-cell (light green) with those obtained in a two-compartment OEMS cell. The potential was first scanned negatively from OCV (~3.0 V vs. Li$^+$/Li) to 2.0 V vs. Li$^+$/Li and then scanned positively at 0.1 mV s^{-1}. The oxidation peaks marked by ①, ②, and ③ correspond to those marked by the same symbols in Figs. 8 and 9.

back to 2.0 V vs. Li$^+$/Li, and then cycled once more between 2.0 V vs. Li$^+$/Li and the respective lower cutoff voltage. These two cycles for each of the cells are shown in Fig. A·2. Two cycles were conducted in order to ensure complete passivation of the surface; accordingly, the second cycle of the cell scanned to 1.0 V vs. Li$^+$/Li shows no LiNO$_3$/LiNO$_2$ reduction features anymore. The electrodes were harvested at the final cell voltage of 2.0 V vs. Li$^+$/Li.

A3: Comparison of voltammetric scans recorded in a coin cell vs. an OEMS cell.—Figure A·3 compares the CVs of carbon black electrodes scanned at 0.1 mV s^{-1} in a C65||Li half-cell configuration obtained in a coin-cell vs. in a two-compartment OEMS cell. Both cells contain 1 M LiPF$_6$ in EC/DEC 1/2 v/v + 0.16 wt% LiNO$_2$ as the electrolyte. The scans were started from OCV (~3.0 V vs. Li$^+$/Li) first in the reductive direction to 2.0 V to ensure the same starting voltage, then scanning positively. The oxidative peak at ~3.5 V vs. Li$^+$/Li, marking the oxidation of LiNO$_2$, can be observed in both cell setups. However, for the coin-cell setup, the products of the LiNO$_2$ oxidation can readily be consumed on the lithium counter electrode, while in the OEMS cell setup, the carbon black working electrode compartment is separated from the lithium counter electrode compartment by a liquid and gas impermeable glass-ceramic. Thus, in the OEMS cell, the initially formed NO$_2$ (see reaction 2.1) can react further according to reactions 3.1 and 3.2, leading to the observation of the well-pronounced oxidation peaks at ~4.0 and ~4.2 V vs. Li$^+$/Li shown in Fig. A·3.

A4: Reversibility of the NO/NO$^+$ feature.—To show not only the reversible behavior of the electrochemical feature at 4.22 V (also depicted in Fig. 10), the corresponding OEMS measurement, including gas concentration of m/z = 30 and gas evolution rate, is shown in Fig. A·4. The carbon electrode was scanned in a two-compartment OEMS cell setup from OCV (~3.0 V) to 4.6 V vs. Li$^+$/Li and then cycled 7 times between 3.8 V and 4.6 V. Panel a shows the current signal plotted vs. potential; here, the reversibility of feature ③ is very apparent. Panel b shows the same current data but now plotted vs. time, whereby panel c shows the corresponding gas evolution/consumption detected at *m/z* = 30; based on the discussion in the main text, the *m/z* = 30 mass signal near feature ③ is most likely ascribed to NO gas, so that the molar quantities given in panel b were determined using the calibration factor for NO at *m/z* = 30 of 0.56 (see Table I). Panel c depicts the gas evolution rate, i.e., the time derivative of the data in panel b.

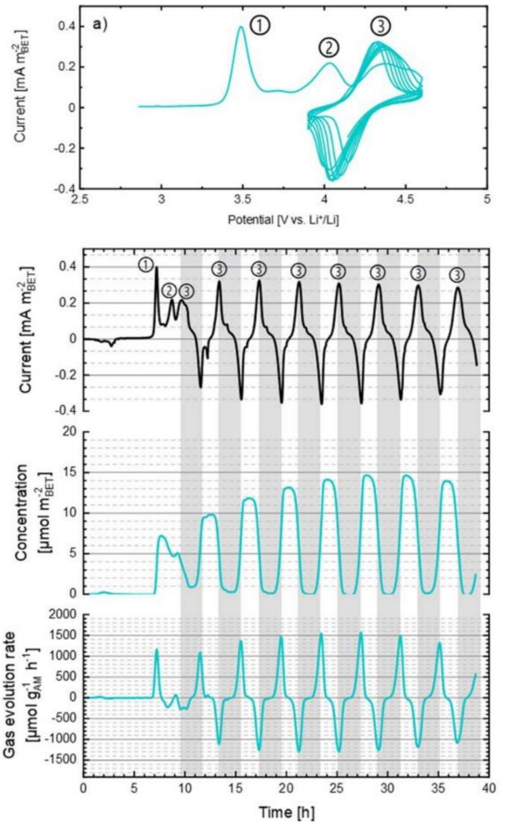

Figure A·4. (a) CV cycles of a carbon black working electrode (2.0 ± 0.1 mg$_{C65}$ cm^{-2}) in a two-compartment OEMS cell, with 50 µl of 1 M LiPF$_6$ in EC/DEC 1/2 v/v + 0.16 wt% LiNO$_2$ in the working electrode compartment (with a Whatman GD type A/E glass fiber separator), which is separated from the lithium metal counter electrode compartment by a liquid and gas impermeable glass-ceramic. The voltage scan was conducted at 0.1 mV s^{-1} from OCV (~3.0 V vs. Li$^+$/Li) in oxidative direction to 4.6 V vs. Li$^+$/Li, after which the scan was reversed, and cycling was continued between 3.8 and 4.6 V vs. Li$^+$/Li for 7 cycles. (b) Identical data, as in panel a, but plotted vs. time. (c) Associated mass signals for *m/z* = 30, converted into a molar gas amount using the calibration factor for NO of 0.56, see Table I. (d) Gas evolution rate, corresponding to the time derivate of the data in panel c. Note that the current and total amount of evolved gas at *m/z* =30 are normalized to the BET surface area of the C65 electrode; on the other hand, the gas evolution rate is normalized to the carbon mass of the C65 carbon black electrode.

ORCID

Maximilian Graf https://orcid.org/0000-0002-2252-1216
Lennart Reuter https://orcid.org/0000-0002-6240-5893
Simon Qian https://orcid.org/0000-0003-3459-9683
Stefan Haufe https://orcid.org/0000-0003-3025-1890
Hubert A. Gasteiger https://orcid.org/0000-0001-8199-8703

References

1. V. L. Chevrier, L. Liu, D. B. Le, J. Lund, B. Molla, K. Reimer, L. J. Krause, L. D. Jensen, E. Figgemeier, and K. W. Eberman, *J. Electrochem. Soc.*, **161**, A783 (2014).
2. E. Peled and S. Menkin, *J. Electrochem. Soc.*, **164**, A1703 (2017).

3. M. Wetjen, D. Pritzl, R. Jung, S. Solchenbach, R. Ghadimi, and H. A. Gasteiger, *J. Electrochem. Soc.*, **164**, A2840 (2017).
4. V. Etacheri, O. Haik, Y. Goffer, G. A. Roberts, I. C. Stefan, R. Fasching, and D. Aurbach, *Langmuir*, **28**, 965 (2012).
5. C. Xu, F. Lindgren, B. Philippe, M. Gorgoi, F. Björefors, K. Edström, and T. Gustafsson, *Chem. Mater.*, **27**, 2591 (2015).
6. R. Jung, M. Metzger, D. Haering, S. Solchenbach, C. Marino, N. Tsiouvaras, C. Stinner, and H. A. Gasteiger, *J. Electrochem. Soc.*, **163**, A1705 (2016).
7. A. L. Michan, B. S. Parimalam, M. Leskes, R. N. Kerber, T. Yoon, C. P. Grey, and B. L. Lucht, *Chem. Mater.*, **28**, 8149 (2016).
8. T. Teufl, D. J. Pritzl, L. Hartmann, S. Solchenbach, M. Mendez, and H. A. Gasteiger, *J. Electrochem. Soc.*, **170**, 020531 (2023).
9. C. Xu, G. Hernández, S. Abbrent, L. Kobera, R. Konefal, J. Brus, K. Edström, D. Brandell, and J. Mindemark, *ACS Appl. Energy Mater.*, **2**, 4925 (2019).
10. A. Schiele, B. Breitung, T. Hatsukade, B. B. Berkes, P. Hartmann, J. Janek, and T. Brezesinski, *ACS Energy Lett.*, **2**, 2228 (2017).
11. C. C. Nguyen and B. L. Lucht, *J. Electrochem. Soc.*, **165**, A2154 (2018).
12. J. Uddin, V. S. Bryantsev, V. Giordani, W. Walker, G. V. Chase, and D. Addison, *J. Phys. Chem. Lett.*, **4**, 3760 (2013).
13. T. Jaumann, J. Balach, M. Klose, S. Oswald, J. Eckert, and L. Giebeler, *J. Electrochem. Soc.*, **163**, A557 (2016).
14. A. Jozwiuk, B. B. Berkes, T. Weiß, H. Sommer, J. Janek, and T. Brezesinski, *Energy Environ. Sci.*, **9**, 2603 (2016).
15. L. Fu et al., *Adv. Funct. Mater.*, **31**, 1 2010602 (2021).
16. S. Li, W. Zhang, Q. Wu, L. Fan, X. Wang, X. Wang, Z. Shen, Y. He, and Y. Lu, *Angew. Chemie - Int. Ed.*, **59**, 14935 (2020).
17. D. Liu, X. Xiong, Q. Liang, X. Wu, H. Fu, and R. Li, *Chem. Commun.*, 9232 (2021).
18. Y. Liu, D. Lin, Y. Li, G. Chen, A. Pei, O. Nix, Y. Li, and Y. Cui, *Nat. Commun.*, **9**, 1 (2018).
19. D. Aurbach, E. Pollak, R. Elazari, G. Salitra, C. S. Kelley, and J. Affinito, *J. Electrochem. Soc.*, **156**, A694 (2009).
20. V. S. Bryantsev, J. Uddin, V. Giordani, W. Walker, G. V. Chase, and D. Addison, *J. Am. Chem. Soc.*, **136**, 3087 (2014).
21. S. Liu et al., *Angew. Chemie - Int. Ed.*, **60**, 3661 (2021).
22. C. Yan, Y. X. Yao, X. Chen, X. B. Cheng, X. Q. Zhang, J. Q. Huang, and Q. Zhang, *Angew. Chemie - Int. Ed.*, **57**, 14055 (2018).
23. Z. L. Brown, S. Heiskanen, and B. L. Lucht, *J. Electrochem. Soc.*, **166**, A2523 (2019).
24. S. S. Sekhon, N. Arora, and H. P. Singh, *Solid State Ionics*, **160**, 301 (2003).
25. C. M. Burke, V. Pande, A. Khetan, V. Viswanathan, and B. D. McCloskey, *Proc. Natl. Acad. Sci. U. S. A.*, **112**, 9293 (2015).
26. Y. Jie, X. Liu, Z. Lei, S. Wang, Y. Chen, F. Huang, R. Cao, G. Zhang, and S. Jiao, *Angew. Chemie*, **132**, 3533 (2020).
27. B. Daniel, B. Irmgard, and D. Jantke, *Lithium Ion Batteries*, GermanyWO2019105544A1 (2017).
28. D. Jantke, R. Bernhard, E. Hanelt, T. Buhrmester, J. Pfeiffer, and S. Haufe, *J. Electrochem. Soc.*, **166**, A3881 (2019).
29. M. Metzger, B. Strehle, S. Solchenbach, and H. A. Gasteiger, *J. Electrochem. Soc.*, **163**, A798 (2016).
30. N. Tsiouvaras, S. Meini, I. Buchberger, and H. A. Gasteiger, *J. Electrochem. Soc.*, **160**, A471 (2013).
31. M. N. Obrovac and V. L. Chevrier, *Chem. Rev.*, **114**, 11444 (2014).
32. M. Wetjen, *PhD Thesis*, Technische Universität München, https://mediatum.ub.tum.de/?id=1443160 (2018).
33. S. Haufe, R. Bernhard, and J. Pfeiffer, *J. Electrochem. Soc.*, **168**, 080531 (2021).
34. K. Kim, I. Park, S. Y. Ha, Y. Kim, M. H. Woo, M. H. Jeong, W. C. Shin, M. Ue, S. Y. Hong, and N. S. Choi, *Electrochim. Acta*, **225**, 358 (2017).
35. L. N. Wu, J. Peng, Y. K. Sun, F. M. Han, Y. F. Wen, C. G. Shi, J. J. Fan, L. Huang, J. T. Li, and S. G. Sun, *ACS Appl. Mater. Interfaces*, **11**, 18504 (2019).
36. W. Qi, L. Ben, H. Yu, Y. Zhan, W. Zhao, and X. Huang, *J. Power Sources*, **424**, 150 (2019).
37. V. Etacheri, U. Geiger, Y. Gofer, G. A. Roberts, I. C. Stefan, R. Fasching, and D. Aurbach, *Langmuir*, **28**, 6175 (2012).
38. B. Strehle, S. Solchenbach, M. Metzger, K. U. Schwenke, and H. A. Gasteiger, *J. Electrochem. Soc.*, **164**, A2513 (2017).
39. D. L. Wood, J. Li, and C. Daniel, *J. Power Sources*, **275**, 234 (2015).
40. L. Reuter, J. L. S. Dickmanns, B. Strehle, L. Hartmann, F. Maglia, R. Jung, B. Suthar, and H. A. Gasteiger, *J. Electrochem. Soc.*, **171**, 050551 (2024).
41. R. Bernhard, M. Metzger, and H. A. Gasteiger, *J. Electrochem. Soc.*, **162**, A1984 (2015).
42. M. Metzger, B. Strehle, S. Solchenbach, and H. A. Gasteiger, *J. Electrochem. Soc.*, **163**, A1219 (2016).
43. K. U. Schwenke, S. Solchenbach, J. Demeaux, B. L. Lucht, and H. A. Gasteiger, *J. Electrochem. Soc.*, **166**, A2035 (2019).
44. U. V. Alpen, A. Rabenau, and G. H. Talat, *Appl. Phys. Lett.*, **30**, 621 (1977).
45. K. Park and J. B. Goodenough, *Adv. Energy Mater.*, **7**, 1 (2017).
46. G. Ma, Z. Wen, M. Wu, C. Shen, Q. Wang, J. Jin, and X. Wu, *Chem. Commun.*, **50**, 14209 (2014).
47. X. Ma, J. Yu, X. Zou, Y. Hu, M. Yang, F. Zhang, and F. Yan, *Cell Reports Phys. Sci.*, **4**, 101379 (2023).
48. D. Pritzl, S. Solchenbach, M. Wetjen, and H. A. Gasteiger, *J. Electrochem. Soc.*, **164**, A2625 (2017).
49. J. Landesfeind, A. Eldiven, and H. A. Gasteiger, *Journal of The Electrochemical Society*, **165**, 1122 (2018).
50. R. Jung, M. Metzger, F. Maglia, C. Stinner, and H. A. Gasteiger, *J. Electrochem. Soc.*, **164**, A1361 (2017).
51. M. Metzger, P. Walke, S. Solchenbach, G. Salitra, D. Aurbach, and H. A. Gasteiger, *J. Electrochem. Soc.*, **167**, 160522 (2020).
52. J. R. Rumble, *CRC Handbook of Chemistry and Physics* (CRC Press, Boca Raton, FL) 99th ed. (2018).
53. J. Poris, I. D. Raistrick, and R. A. Huggins, *ECS Proceedings Volumes*, **1984-2**, 313 (1984).
54. A. Boughriet and M. Wartel, *J. Electroanal. Chem.*, **362**, 167 (1993).
55. G. Bontempelli, G. A. Mazzocchin, and F. Magno, *J. Electroanal. Chem.*, **55**, 91 (1974).
56. K. Y. Lee, D. J. Kuchynka, and J. K. Kochi, *Inorg. Chem.*, **29**, 4196 (1990).

3.3 Impedance and rate capabilities of silicon anodes

The article "Comparison of Silicon and Graphite Anodes: Temperature-Dependence of Impedance Characteristics and Rate Performance" was submitted to the peer-reviewed *Journal of the Electrochemical Society* in November 2022 and published online in March 2023.[144] The article was distributed under the terms of the Creative Commons Attribution 4.0 License, and its permanent weblink can be found at: https://iopscience.iop.org/article/10.1149/1945-7111/acc09d

The almost tenfold higher specific capacity for silicon as active material (3576 mAh g_{Si}^{-1}) compared to graphite (374 mAh g_{LiC6}^{-1}) results in significantly thinner electrodes while maintaining the same areal capacity. As the thickness of electrodes, specifically on the anode side, often limits the rate-capability of lithium-ion battery cells, employing silicon as an active material can bring valuable benefits regarding rate-capability. In this study, we compared graphite-based and microsilicon-based anodes with application relevant areal capacities (2.8 mAh cm^{-2}) with regards to their temperature-dependent kinetic charge-transfer resistances (R_{CT}) and their ion transport resistances in the electrolyte phase (R_{ion}). We used impedance spectroscopy to separate the kinetic resistance from the temperature-dependent ion resistance by measuring them at different temperatures between -5 and +45 °C. The contributions of R_{CT} and R_{ion} at various temperature regimes are quantified, showing that the latter dominates at higher temperatures due to the higher activation energies of R_{CT}.

Rate performance tests show superior rate-capabilities for the thinner silicon anodes, predominantly at higher temperatures. The silicon anodes revealed an overall two-fold higher lithiation rate-capability until reaching 0 V vs. Li^+/Li compared to graphite electrodes.

C.B., R.M., M.G., and H.A.G. developed the concept of the study. C.B. conducted the electrochemical experiments. C.B. and R.M. wrote the manuscript and M.G. and H.A.G. edited the manuscript. All authors discussed the results and commented on the manuscript.

Journal of The Electrochemical Society, 2023 **170** 030534

Comparison of Silicon and Graphite Anodes: Temperature-Dependence of Impedance Characteristics and Rate Performance

Clara Berg,[=,*] **Robert Morasch,**[=,z] **Maximilian Graf,** and **Hubert A. Gasteiger**[**]

Chair of Technical Electrochemistry, Department of Chemistry and Catalysis Research Center, Technical University of Munich, Munich, Germany

A meaningful benchmarking of battery active materials with inherently different properties requires knowledge of both their intrinsic electrochemical properties as well as of the differences in the resulting porous electrode structures for equal, practically relevant areal capacities. Here we compare graphite and microsilicon anodes with practical areal capacities of 2.8 mAh cm^{-2} for lithium-ion batteries with regard to their temperature-dependent kinetic charge-transfer resistances (R_{ct}) and their ion transport resistances through the electrolyte phase within the pores of the electrodes (R_{ion}), measured via impedance spectroscopy. We deconvolute the kinetic resistance from the impedance spectra by individually measuring the temperature-dependent pore resistance between −5 and +45 °C, showing that the charge-transfer resistance dominates at low temperatures, while at high temperatures the pore resistance dominates for both electrode types due to the significantly higher activation energy of R_{ct}. An analysis of the potential profile of the electrodes at different lithiation rates shows how the thinner silicon electrode is significantly less affected by R_{ion}-induced transport losses compared to a thicker graphite electrode, resulting in lower overpotentials when fast-charging at high temperatures, despite similar kinetic resistances. Overall the silicon electrodes could be charged up to two times faster than graphite before reaching 0 V vs Li$^+$/Li.

[DOI: 10.1149/1945-7111/acc09d]

Manuscript submitted November 4, 2022; revised manuscript received January 28, 2023. Published March 29, 2023.

Silicon is a promising anode active material for next-generation lithium-ion batteries.[1,2] By electrochemically alloying silicon with lithium, the $Li_{15}Si_4$ phase can be obtained, which equates to a theoretical capacity of 3579 mAh g_{Si}^{-1} (2194 Ah l^{-1}).[3–5] Compared to the state-of-the-art graphite anode material which intercalates lithium to a composition of LiC_6 (372 mAh g^{-1}, 719 Ah l^{-1}), the use of silicon-rich anodes can significantly improve the gravimetric and volumetric capacity of a lithium-ion battery (LIB). Next to the goal of an improved energy density, the use of silicon is also being considered for the improvement of a cell's fast-charging capability.

Fast-charging of lithium-ion batteries is predominantly limited by lithium plating on the anode, which is possible once the anode potential drops below 0 V vs Li$^+$/Li. If the total overpotentials of graphite and silicon electrodes were to be identical, silicon anodes would allow for higher lithiation rates, as the average lithiation potential of amorphous silicon is substantially higher than that of graphite. In addition, when comparing anodes with the same areal capacity, the higher specific capacity of silicon results in anode electrodes that are substantially thinner than graphite based electrodes, so that the reduced path length of the ions in the electrolyte phase within the pores of the anode electrodes should result in lower mass-transport overpotentials (assuming comparable electrode porosities and tortuosities). Finally, the alloying of silicon can occur in three dimensions, whereas the intercalation into the graphite planes is two-dimensional.

The rate performance of a silicon-containing electrode is largely dependent on the type of silicon electrode used. Over the years, a large variety of strategies have been developed for the implementation of silicon into electrodes to enable a stable cycling performance despite the large volumetric changes of the material upon its (de-)lithiation; many of which include the usage of silicon as a composite material or as an additive.[6] In this study we investigate a microsilicon electrode for which most of the capacity is accounted for by the silicon. Jantke et al.[7] showed that pulverization of the here used μm-scale crystalline silicon can be avoided by only partially lithiating the silicon particles, whereby a partial lithiation to ~30% (corresponding to ~1200 mAh g_{Si}^{-1}) enables the reversible cycling of silicon-rich anodes (70%$_{wt}$) in full-cells for up to 250 cycles without particle pulverization and with little initial irreversible capacity losses.[5,7,8] For this limited degree of lithiation, the microscale silicon particles retain their crystalline core over cycling,[8,9] and the electrode-level specific capacity of such silicon electrodes (~840 mAh $g_{electrode}^{-1}$) is still ~2.5-fold higher than that of typical graphite electrodes (~340 mAh $g_{electrode}^{-1}$). However, it must be noted that due to the substantially higher delithiation voltage, the use of this silicon strategy on a cell level only leads to small improvements in the cell's energy density. While other silicon strategies might lead to more significant improvements in the cell's energy density, this study focuses on the potential improvements in rate capability of such a silicon-dominant electrode compared to graphite. For this, we aim to discuss both material intrinsic advantages (i.e. higher thermodynamic lithiation voltage of silicon) and potential geometric advantages arising from the higher gravimetric capacity and thus, lower loading of the silicon electrode.

The silicon electrodes used in the present study were made with microscale silicon (70%$_{wt}$) and were partially lithiated to 1200 mAh g_{Si}^{-1}. Figure 1a shows the potential profile at C/10 of such a silicon electrode compared to that of a graphite electrode. The lithiation potential of silicon is more than 100 mV higher over most of the state-of-charge (SOC) range. Figure 1b shows the cross-section scanning electron microscopy (SEM) image of the two pristine electrodes. The 70%$_{wt}$ microscale silicon electrode is depicted on the left and the 95.8%$_{wt}$ graphite electrode is depicted on the right. Both electrodes have a reversible areal capacity of 2.8 mAh/cm^2, which in the case of the silicon electrode is based on a ~30% utilization of the theoretical silicon capacity (1200 mAh g_{Si}^{-1}). Both electrodes are uncalendered and have similar porosities of approximately 60%. In this state, they differ in thickness by more than a factor of two (~40 μm for the silicon vs ~95 μm for the graphite electrode).

Since the pore resistance is a major factor that affects the electrode performance, we will first compare the resistance contributions of the ionic pore resistance (R_{ion}) and the kinetic charge-transfer resistance (R_{ct}, here assumed to also contain the SEI resistance) of both silicon and graphite electrodes of practical areal capacities (2.8 mAh cm^{-2}) via electrochemical impedance spectroscopy (EIS). The EIS analysis is done using a transmission line model approach as shown in Refs. 10 and 11. As R_{ion} is influenced

---

[=] Equal Contribution.

[*] Electrochemical Society Student Member.

[**] Electrochemical Society Fellow.

[z] E-mail: robert.morasch@tum.de

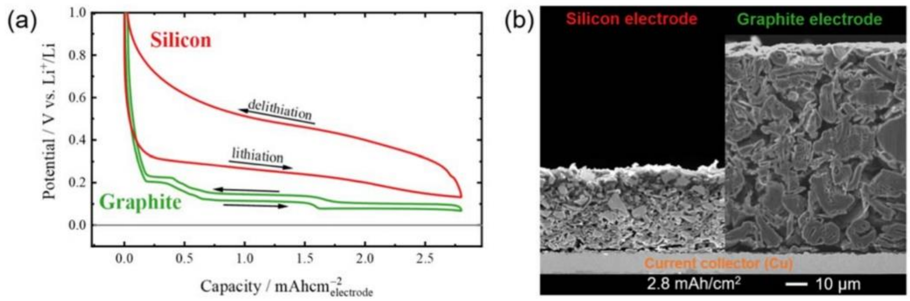

Figure 1. (a) Potential profiles of microscale silicon (red) and graphite (green) working electrodes vs capacity during galvanostatic cycling at C/10 (5th cycle) of electrodes with an areal capacity of 2.8 mAh cm^{-2}, calculated by referring to the reversible capacities of 1200 mAh $g_{Si}{}^{-1}$ for silicon (i.e., using ~30% of the theoretical capacity of Si) and 350 mAh $g_{Gra}{}^{-1}$ for graphite. The potentials are referenced to a lithium metal reference electrode and the counter electrode is composed of metallic lithium and a free-standing graphite (FSG) electrode (see Experimental section). (b) Scanning electron microscopy (SEM) images, showing the cross-sections of pristine and uncalendered silicon and graphite electrodes with 2.8 mAh cm^{-2}, illustrating the reduced thickness of the silicon electrode (~40 μm) compared to that of the graphite electrode (~95 μm) at comparable estimated porosities (~60%).

by the structure and morphology of the electrodes (i.e., thickness, porosity, and tortuosity), and since R_{ct} is dependent on the type of active material and its specific surface area, we show how silicon and graphite electrodes exhibit different contributions from each of these two resistances. This results in different temperature-dependent behavior of the electrodes due to the significantly higher activation energy of R_{ct} compared to R_{ion} (shown, e.g., for NCA cathode electrodes[12] as well as graphite anode electrodes[13,14]), rendering R_{ion} as the dominating resistance at high temperatures.

In a second part, we will compare the effect of the differences in R_{ct} and R_{ion} on the lithiation rate capability of silicon and graphite anodes. As the lithiation potential of silicon (especially when operating it at partial lithiation of only ~30%) is higher than that of graphite over the entire state-of-charge (SOC) region, directly comparing the lithiation capacities reached at 0 V vs Li$^+$/Li is not sufficient to deduce the effect of R_{ct} and R_{ion} on the lithiation rate capability. Thus, we analyze the potential profiles of the electrodes at different lithiation rates (expressed as C-rates) and at different temperatures in order to disentangle the electrode performance from the potential profile, showing how R_{ct} causes a downshift in the potential, while R_{ion} causes a constant increase in electrode overpotential with SOC, ultimately limiting the graphite electrode performance. Lastly, we compare the silicon and graphite rate performance at different temperatures and show how silicon electrodes show a performance improvement by a factor of two.

Experimental

***Silicon electrode preparation.*—**The targeted weight percentages of the electrode were 70%$_{wt}$ silicon, 25%$_{wt}$ conductive graphite additive, and 5%$_{wt}$ acrylate binder. First, 7.0 g of silicon (d_{50} = 4.5 μm, A_{BET} = 2.9 m^2 g^{-1}, Wacker Chemie AG, Germany), 12.5 g of an aqueous 4%$_{wt}$ LiPAA solution (prepared by neutralizing a polyacrylic acid (PAA; M_v = 459 k, Sigma Aldrich) solution with LiOH to pH 7), and 5.1 ml of deionized water (18 MΩcm, Merck Millipore) were added to a mixing beaker (125 ml). After mixing the materials in a dissolver mixer (Dispermat LC30, VMA-Getzmann) at 4500 rpm for 5 min, 2.5 g of graphite (KS6L, A_{BET} = 23.2 m^2 g^{-1}, Imerys) were added in small portions by gently stirring the mixture using a spatula, followed by another mixing step at 4500 rpm for 5 min and finally at 12000 rpm for 30 min. In a last step, the ink was degassed by mixing it in a planetary orbital mixer (Thinky Corp., USA) for 5 min at 2000 rpm. The slurry was coated onto copper foil (MTI, 12 μm) with a box-type coating bar (Erichsen, Hemer, Germany) using an automated coater (RK PrintCoat Instruments). Wet-film thicknesses of 110 μm resulted in the desired capacity loading of ~2.8 mAh cm^{-2} based on the reversible capacity of 1200 mAh $g_{Si}{}^{-1}$. After drying the coating at room temperature for 12 h, electrodes were punched out to a diameter of 10.95 mm (equating to an area of ~0.94 cm^2) using an electrode punch (Hohsen Corp. OSAKA, Japan), and then dried overnight under vacuum in a glass oven (Büchi, B-585) at 120 °C and transferred into the glove box (note that the electrodes were not calendered or compressed).

The punched-out electrodes were individually characterized by weight (Sartorius Cubis I MSA225S) and thickness (Mitutoyo, Japan), with estimated absolute measurement errors of ±0.015 mg and ±1 μm, respectively. The copper foil areal weight (8.57 ± 0.02 mg cm^{-2}) and thickness (10 ± 1 μm) were determined from copper foil sampled in close proximity to the punched-out electrodes and subtracted from the measured electrode weight and thickness. The capacities of all analyzed electrodes ranged between 2.83 ± 0.08 mAh cm^{-2} (based on 1200 mAh $g_{Si}{}^{-1}$), and for each of the studied electrodes the areal capacity was determined with a calculated measurement error of ±0.02 mAh cm^{-2}. From the determined electrode thickness, the areal weight of all electrode components, and the bulk densities of the electrode components ($\rho_{Si} \approx 2.34$ g cm^{-3}, $\rho_{KS6L} \approx 2.26$ g cm^{-3}, and $\rho_{LiPAA} \approx 1.5$ g cm^{-3}), an average porosity of 62.0% with a maximum deviation of ±0.5 percentage points was obtained. Here the resulting absolute error from the uncertainties in weight and thickness measurement was estimated as ±2.2 percentage points.

***Graphite electrode preparation.*—**The targeted weight percentages were 95.8%$_{wt}$ graphite, 1%$_{wt}$ carbon black, 1%$_{wt}$ sodium carboxymethyl cellulose (CMC), and 2.2%$_{wt}$ polystyrene-co-butadiene rubber (SBR). First, 0.2 g of CMC (MAC200HC, D.o.S = 0.85–0.95 mol/C$_6$, SUNROSE) were added to 10 ml of DI water and mixed twice for 10 min until the CMC was well dissolved. 19.16 g of surface-modified graphite (SMG, d_{50} = 18.1 μm, A_{BET} = 3.1 m^2 g^{-1}, Hitachi, Japan) and 0.2 g of carbon black (Super C65, A_{BET} = 62 m^2 g^{-1}, TIMCAL, Switzerland) were mixed in a separate beaker for 10 min at 1500 rpm. The resulting powder mixture was added to the CMC solution and everything was mixed in three steps in a planetary orbital mixer (Thinky Corp., USA): (1) 10 min at 1000 rpm, (2) 10 min at 1500 rpm, (3) 5 min at 1500 rpm, and (4) 5 min at 2000 rpm. Before the second and third mixing step, water (2 × 3.75 ml) was added. The cup was weighed before and after each mixing step and any water vapour losses were compensated for. Finally, 0.88 g of SBR (Sigma-Aldrich, Germany) were added and all was mixed for 5 min at 500 rpm. Wet-film thicknesses of 140 μm resulted in a loading of ~2.8 mAh cm^{-2} based on a reversible capacity of graphite of 350 mAh $g_{Gra}{}^{-1}$. The coating was dried and electrodes were punched to 10.95 mm diameter. Subsequently, they were dried overnight under vacuum in a glass oven (Büchi, B-585) at

120 °C (note that the electrodes were not calendered or compressed) and transferred into the glove box.

Electrodes with an average capacity of 2.82 mAh cm^{-2} (based on a reversible capacity of 350 mAh $g_{Gra}{}^{-1}$) with a maximum deviation of ±0.05 mAh cm^{-2} were obtained. Each electrode's capacity was determined with a calculated measurement error of ±0.01 mAh cm^{-2}. From the determined electrode thickness, the areal weight of all electrode components, and the bulk densities of the electrode materials ($\rho_{Gra} \approx 2.26$ g cm^{-3}, $\rho_{C65} \approx 2.26$ g cm^{-3}, $\rho_{CMC} \approx 1.6$ g cm^{-3}, and $\rho_{SBR} \approx 1.04$ g cm^{-3}), an average porosity of 59.0% with a maximum deviation of ±0.2 percentage points was obtained. Here the resulting absolute error from errors in weight and thickness measurements was estimated as ±0.9 percentage points for each electrode.

The free-standing graphite (FSG) electrodes used on the counter electrode were prepared analogously to the method described in our previous publication.[15] The ∼105 μm thick FSG electrodes were composed of 95$\%_{wt}$ graphite (T311 type from SGL) and 5$\%_{wt}$ polymer binder (polyvinylidene fluoride (PVDF), Arkema); they had a graphite loading of ∼10.31 mg cm^{-2}.

Test cell assembly.—For electrochemical impedance analysis (EIS) and rate capability tests, three-electrode cell setups (Swagelok® T-cell) with reference electrodes were used, either with a gold-wire reference electrode (GWRE) for EIS measurements[16] or with a lithium metal reference electrode for rate capability tests. The cells were built inside an argon-filled glove box (MBraun, 25 ± 1 °C, oxygen and water content <0.1 ppm, Ar 5.0, Westfalen). All test cell components were dried at 80 °C overnight in an oven (Binder, Germany), while the glass fiber (GF) separators (11 mm diameter, 250 μm thickness, ∼90% porosity; VWR) were dried overnight under vacuum in a glass oven (Büchi, B-585) at 300 °C. The here used electrolytes were LP57 (1 M $LiPF_6$ in EC:EMC 3:7 (w:w), BASF, Germany), and 1 M $LiPF_6$ in a 1:4 mixture (v:v) of fluoroethylene carbonate (FEC, Gotion, USA) and diethyl carbonate (DEC, Gotion, USA).

Test cells for the electrochemical impedance measurements were assembled with a working electrode (silicon or graphite), four glass fiber separators, and a counter electrode consisting of a free-standing graphite electrode firmly attached to the metallic lithium foil (11 mm diameter, 0.45 mm thickness; Rockwood Lithium, 99.9% battery grade). 160 μl electrolyte were added to the four separators between the working and counter electrode.

Cells for rate capability tests were assembled analogously to the cells used for the impedance measurements (i.e., with a lithium counter electrode attached to a FSG electrode). Instead of the GWRE, metallic lithium was used as a reference electrode (6 mm diameter) and an additional 30 μl were added to the separator at the reference electrode.

Cell formation, impedance measurements, and rate capability tests.—Before electrochemical testing, all cells were left for 3 h at open circuit voltage (OCV) after assembly in order to allow for complete wetting of the electrode. Formation cycles and rate tests at 25 °C and 45 °C were performed in climate chambers (Binder, Germany). Temperature-dependent impedance measurements and rate tests at –5 °C were performed in a programmable low-temperature cabinet (ESPEC, LU-114, Japan). Electrochemical cycling and impedance measurements were conducted using a potentiostat (Bio-Logic Science Instruments, France). For cells with a gold wire reference electrode, the GWRE was lithiated by applying 150 nA for 1 h at 25 °C via the counter electrode.

Figure 2 schematically illustrates the formation of the silicon and graphite electrodes and the procedure for the impedance analysis. The same formation procedure was carried out for all cells, i.e., also for those that were used for rate capability tests. Two galvanostatic (constant current (CC) (de-)lithiation) formation cycles were performed at C/10, with the first cycle at 25 °C and the second cycle at 45 °C. For the graphite electrodes, formation cycling was done between 30 mV and 1.5 V vs Li^+/Li. The working electrode potentials were measured against the reference electrode whereby the GWRE potential was determined as 0.311 V vs Li^+/Li.[16] For simplicity, all potentials are given with respect to the Li^+/Li potential. In case of the silicon electrodes, a partial lithiation of the microscale silicon was achieved by capacitively limiting the lithiation to 1200 mAh $g_{Si}{}^{-1}$, while for the delithiation a potential cutoff of 1 V vs Li^+/Li was chosen.

Potentiostatic electrochemical impedance spectra (PEIS) were recorded by applying a sinusoidal voltage perturbation of 10 mV at frequencies in the range of 30 kHz—0.1 Hz. Before formation, PEIS was measured under blocking conditions (2 V vs Li^+/Li). After formation, the working electrodes were lithiated once more (to 1200 mAh/g_{Si} in the case of silicon and to 350 mAh $g_{Gra}{}^{-1}$ in the case of graphite) and then delithitated to 50% SOC (600 mAh $g_{Si}{}^{-1}$ and 175 mAh $g_{Gra}{}^{-1}$) at a rate of C/10 at 25 °C. Then, PEIS was recorded at OCV at 50% SOC (see right-most segments in Fig. 2). All PEIS measurements (i.e., before formation and at 50% SOC) were performed in the following sequence: 25 °C, −5 °C, 5 °C °C, 15 °C, 25 °C, 35 °C, 45 °C, 25 °C. Before each impedance measurement, the cell was left to adapt to the respective temperature for 2 h. All impedance spectra were fitted to a simplified, reflecting, transmission line model (TLM, see e.g. Pritzl et al.[10]) using the software RelaxIS (rhd instruments, Version 3.0.20). The ionic pore resistances (R_{ion}) were determined from a fit of the spectra recorded in blocking conditions before formation. The charge-transfer resistances (R_{ct}) at 50% SOC were obtained from a non-blocking TLM fit with the variable for R_{ion} fixed to the values determined before formation.

For half-cell rate capability tests, the working electrode (silicon or graphite) was lithiated using a CC procedure, applying the current corresponding to each respective rate until the total capacity equaled 1200 mAh $g_{Si}{}^{-1}$ or 350 mA $g_{Gra}{}^{-1}$. The CC delithiation was performed to a cut-off voltage of 1 V and 1.5 V vs the Li^+/Li reference electrode for silicon and graphite electrodes, respectively. This was followed by a constant voltage (CV) step until the measured current dropped below C/40. After formation (Fig. 2), three lithiation/delithiation cycles were carried out for each lithiation rate: C/10, C/5, C/2, 1C, 1.33C, 1.66C, 2C, 2.5C, 3C, and 4C. The delithiation was performed at C/10 for the C/10 cycles and at C/5 for all other cycles. These rate capability tests were performed at −5, 25, and 45 °C using two cells at each temperature.

Electrolyte conductivity measurements.—The ionic conductivities of the electrolytes were determined in a commercially available Pt microelectrode setup consisting of a Pt beaker and electrode (rhd Instruments, TSC 1600 closed, Germany). 0.9 ml of electrolyte were added to the Pt beaker inside the glovebox. The setup was then transferred to a programmable low-temperature cabinet (ESPEC, LU-114, Japan) and connected to a potentiostat (Bio-Logic Science Instruments, France). Cell impedances were measured after a thermal equilibration for 2 h at the temperatures −5 °C, 5 °C, 15 °C, 25 °C, 35 °C, and 45 °C. The obtained cell resistances were converted to conductivity values using the calibration constant $k_c = 1370 \pm 20$ Ω mS cm^{-1} which was previously determined for a KCl calibration solution (Mettler Toledo, conductivity standard, 12.88 mS cm^{-1}).

Results and Discussion

Quantification of R_{ion} and R_{ct} for graphite and silicon electrodes.—This section describes the impedance analysis and the thereby determined differences in the ionic pore resistance (R_{ion}) as well as the charge-transfer resistance (R_{ct}) between the graphite and silicon electrodes. As this analysis is done for electrodes with practically relevant areal capacities of 2.8 mAh cm^{-2} that have a significant thickness, R_{ion} is of the same order as R_{ct} near room temperature (illustrated for graphite anodes in Ref. 11) and thus will have a strong impact on electrode performance. For a better

(a) Silicon (C/10, 1200 mAh/g_{Si})

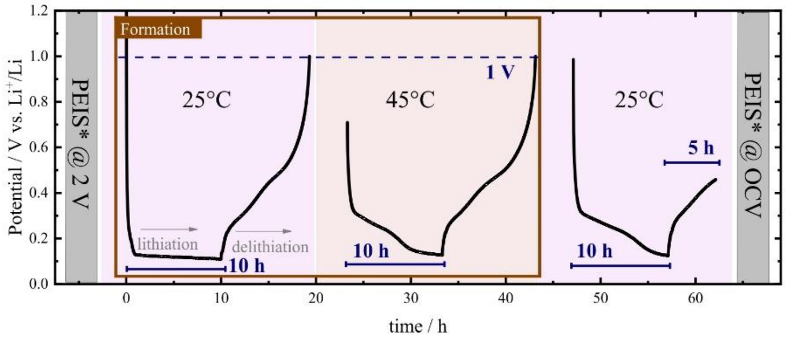

(b) Graphite (C/10, 350 mAh/g_{Gra})

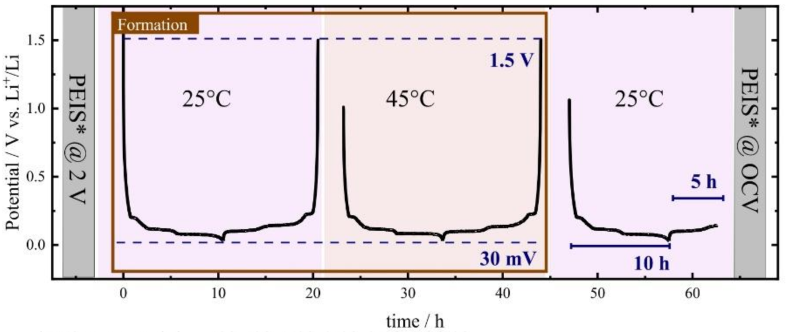

*PEIS were recorded at −5°C, 5°C, 15°C, 25°C, 35°C and 45°C

Figure 2. Illustration of the potential curves during the formation procedure done for all cells (1st cycle at 25 °C and 2nd cycle at 45 °C) and during setting of the 50% SOC point (in delithiation direction) for the EIS measurements in T-cells with a GWRE (right-most segments) for: (a) silicon; (b) graphite. Galvanostatic cycling was performed at C/10, based on specific capacities of 1200 mAh g_{Si}^{-1} and 350 mAh g_{Gra}^{-1} for silicon and graphite electrodes, respectively (for details see text).

comparison, LP57 was used as electrolyte for both Si and graphite electrodes. However, since Si electrodes are typically used with FEC-based electrolyte, the Si electrodes were also examined using FEC:DEC 1:4 (v:v) with 1 M $LiPF_6$; for any analyses pertaining to the silicon electrode measured with this electrolyte, we denote the electrode as Si_{FEC}.

Figures 3a and 3b show exemplary impedance spectra of a graphite electrode in LP57 (green) and of silicon electrodes in either LP57 (red) or in the FEC-based electrolyte (orange), acquired at 25 °C prior to formation as well as at 50% SOC (after two formation cycles). R_{ion} and R_{ct} were determined by an EIS analysis that was performed according to Ref. 11: (i) first, the value of R_{ion} was determined under blocking conditions (i.e., prior to formation), using a transmission line model (TLM) with only capacitive and ionic resistance elements (neglecting electrical resistances) as well as a resistor representing the separator resistance (including electrical contact resistances); (ii) subsequently, the value of R_{ct} was determined at 50% SOC (see right-most segments of Fig. 2), using the above TLM but including charge-transfer resistance elements, whereby the TLM was fitted using the R_{ion} value determined under blocking conditions (a necessary step for low values of R_{ct} compared to R_{ion} as described in Ref. 11). The shift in the high-frequency resistance (HFR) for the Si electrode impedance spectra in FEC-based electrolyte (Si_{FEC}) in Figs. 3a, 3b is a result of the lower ionic conductivity of the FEC-based electrolyte (6.8 ± 0.1 mS cm^{-1}) compared to the LP57 electrolyte (9.1 ± 0.1 mS cm^{-1}) at 25 °C.

Figure 3a shows the 25 °C impedance spectra under blocking conditions of the electrodes prior to electrode formation, allowing the determination of R_{ion}, as, e.g. described in the literature.[12,17] The R_{ion} value obtained from Fig. 3a for the graphite electrode is 6.9 $\Omega cm^2_{electrode}$, whereas R_{ion} for the Si electrode measured in the same LP57 electrolyte is 2.3 $\Omega cm^2_{electrode}$ (see Table I). These differences can be understood by considering the most general mathematical description of R_{ion}:

$$R_{ion} = \frac{\tau \cdot t}{\varepsilon \cdot A \cdot \kappa} \quad [1]$$

where τ is the tortuosity, t is the electrode thickness, ε is the porosity (here ~60% for all electrodes, see Table I), A is the geometric surface area of the electrodes (0.94 cm^2), and κ is the electrolyte conductivity. The most apparent factor that would lower R_{ion} of the Si electrodes is their nearly 2.5-fold lower thickness (~40 vs ~95 μm, see Table I and Fig. 1). Additionally, particle shape, binder type, and electrode preparation can be an important factor influencing the electrode tortuosity values,[17–19] which can be determined from Eq. 1 using the measured values of R_{ion}, the geometric parameters of the electrodes (ε, t, and A), and the electrolyte bulk conductivities. The resulting tortuosity values for silicon (~3.2) are roughly 20% smaller than those obtained for graphite (~3.9), indicating that the structure of the silicon electrodes offers slightly better intrinsic ionic transport properties. Ultimately,

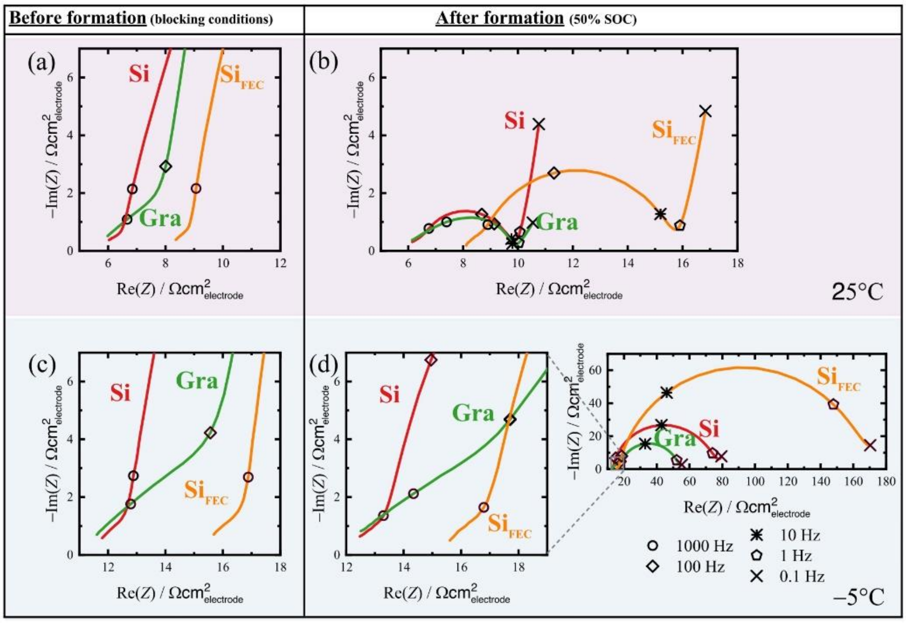

Figure 3. Nyquist plots of the impedances of silicon and graphite working electrodes with areal capacities of 2.8 mAh cm^{-2}, measured by means of a micro-reference electrode (GWRE) in half-cells with a lithium metal counter electrode attached to a free-standing graphite electrode (Li/FSG): (a) measured at 25 °C before formation at 2 V vs Li$^+$/Li, i.e., under blocking conditions; (b) measured at 25 °C after formation at 50% SOC (see Fig. 2). The graphite electrode was measured with LP57 electrolyte (green), while the Si electrode was measured with both LP57 (red) and with an FEC-based electrolyte (orange; 1 M LiPF$_6$ in FEC:DEC 1:4 (v:v)). (c) and (d): Same type of EIS data, but acquired at −5 °C.

Table I. Structural characterization of the graphite and silicon electrodes that were analyzed by impedance spectroscopy for their electrochemical properties in LP57 electrolyte and, in the case of the silicon electrodes, also in FEC-based electrolyte (1 M LiPF$_6$ in FEC:DEC 1:4 (v:v); the corresponding data are referred to as Si$_{FEC}$). The table lists the reversible capacities, electrode thicknesses ($t_{coating}$), calculated porosities (ε), the ionic pore resistances (R$_{ion}$) obtained at 25 °C from the impedance spectrum in blocking conditions, and the tortuosity (τ) determined from Eq. 1. For each electrode/electrolyte combination, two independent samples were measured and analyzed (labelled as #1 and #2) and the ionic conductivites (κ) at 25 °C are 9.1 ± 0.1 mS cm^{-1} for LP57 and 6.8 ± 0.1 mS cm^{-1} for the FEC-based electrolyte. The errors correspond to the measurement errors for each sample, including the error propagation in case of ε and τ.

System		Capacity [mAh/cm$^2_{electrode}$]	$t_{coating}$ [μm]	ε [%]	R_{ion} [Ωcm$^2_{electrode}$]	τ [−]
Gra (LP57 electrolyte)	#1	2.85 ± 0.01	94 ± 1	59 ± 1	6.9 ± 0.10	3.9 ± 0.1
	#2	2.86 ± 0.01	95 ± 1	59 ± 1	6.8 ± 0.05	3.8 ± 0.1
Si (LP57 electrolyte)	#1	2.86 ± 0.02	40 ± 1	62 ± 2	2.3 ± 0.09	3.2 ± 0.2
	#2	2.84 ± 0.02	39 ± 1	62 ± 2	2.2 ± 0.05	3.2 ± 0.2
Si$_{FEC}$ (FEC-based electrolyte)	#1	2.78 ± 0.02	39 ± 1	62 ± 2	2.9 ± 0.10	3.1 ± 0.2
	#2	2.92 ± 0.02	40 ± 1	62 ± 2	3.0 ± 0.10	3.2 ± 0.2

the major effect responsible for the ~3-fold lower R_{ion} of the silicon compared to the graphite electrodes in the LP57 electrolyte (see green and red highlighted segments in Table I) is simply their difference in electrode thickness. It must be noted that the measured values of R_{ion} are descriptive of the pristine and uncalendered electrodes (Fig. 1b) and are probably subject to change over cycling. Especially for silicon, the volumetric changes during lithiation lead to changes in porosity and electrode thickness as a function of SOC and electrode ageing. In addition, it must be kept in mind that in a commercial cell, the electrodes would be calendered. While the silicon electrode likely needs to be operated at higher porosities (~50%), the graphite is commonly compressed to porosities in the range 20%–30%. However, a reduced thickness would still yield an R_{ion} higher than the one measured here due to the non-linear decrease in porosity with electrode thickness (even when assuming constant tortuosity). Thus, the graphite is expected to perform equally or worse if it was compressed.

Figure 3b shows the impedance of the graphite and silicon electrodes after formation at 50% SOC (for conditions, see right-most segments in Figs. 2a, 2b). Both silicon measurements show an initial 45°-slope at high frequencies of above 1 kHz (for frequency assignments see legend given in the lower right-hand corner of Fig. 3), followed by a transition into a semicircle (between 1 kHz and 1 Hz), and a final diffusive branch (below 1 Hz).

Assuming that the value for R_{ion} does not change significantly upon formation (e.g., via volumetric expansion), the data in Fig. 3b yield charge-transfer resistances in LP57 electrolyte at 25 °C of 2.7

$\Omega cm^2_{electrode}$ for graphite and 3.4 $\Omega cm^2_{electrode}$ for silicon. On the other hand, when using the FEC-based electrolyte, the charge-transfer resistance of the Si electrodes is approximately twice as high, at 7.0 $\Omega cm^2_{electrode}$, which is presumably due to the formation of an SEI with different composition and/or more resistive solid electrolyte interphase (SEI).[20,21] To move this analysis from the electrode level to the material level, one would need to consider the intrinsic charge-transfer resistance of the different active materials, i.e., the charge-transfer resistance normalized to the electrochemically active surface area which, a zero-order estimate would be the BET surface area of the active material. With this assumption, the electrode roughness factor multiplied with the above given charge-transfer resistance referenced to the geometric surface area yields the intrinsic charge-transfer resistance. The graphite electrode roughness factor is calculated as ~250 $cm^2{}_{BET}$ $cm^{-2}{}_{electrode}$ (based on the graphite BET surface area of 3.1 m^2 g^{-1} and the graphite loading), while that of the silicon electrodes with ~70 $cm^2{}_{BET}$ $cm^{-2}{}_{electrode}$ (based on a BET surface area of 2.9 m^2 g^{-1} and the silicon loading) is more than 3-fold smaller. This yields intrinsic charge-transfer resistances in LP57 of 675 Ωcm^2_{BET} for graphite, which is ~3-fold larger than the 238 Ωcm^2_{BET} for silicon. However, since the silicon surface area is subject to change over cycling[22] and since the graphite basal planes are not expected to be electrochemically active, this comparison of the active materials intrinsic charge-transfer resistances needs to be studied in more detail to yield further understanding. It should be noted that, while the silicon electrodes contain graphite as conductive additive, the potential of the silicon electrode at 50% SOC (450 mV vs Li^+/Li) lies above the threshold at which intercalation into the graphite is possible and we expect no notable influence of the graphite on the charge-transfer analysis of the silicon electrodes (i.e., the graphite is under blocking conditions).

Figure 3c depicts the blocking impedance measurement of the electrodes at −5 °C, showing the roughly twofold increase in R_{ion} due to the temperature-induced decrease in electrolyte conductivity. Comparing the impedance responses at 50% SOC obtained at −5 °C (Fig. 3d) with those obtained at 25 °C reveals a drastic increase in the charge-transfer resistance of the electrodes. The strong temperature dependence of R_{ct} (discussed further in the section below) results in a greater increase of R_{ct} compared to R_{ion} with decreasing temperatures. As this leads to a better separation of the contributions of R_{ion} and R_{ct} in the frequency domain (i.e., to a clearly visible 45°-line at high frequencies followed by a well-pronounced semicircle at lower frequencies), R_{ion} can be determined in a straightforward

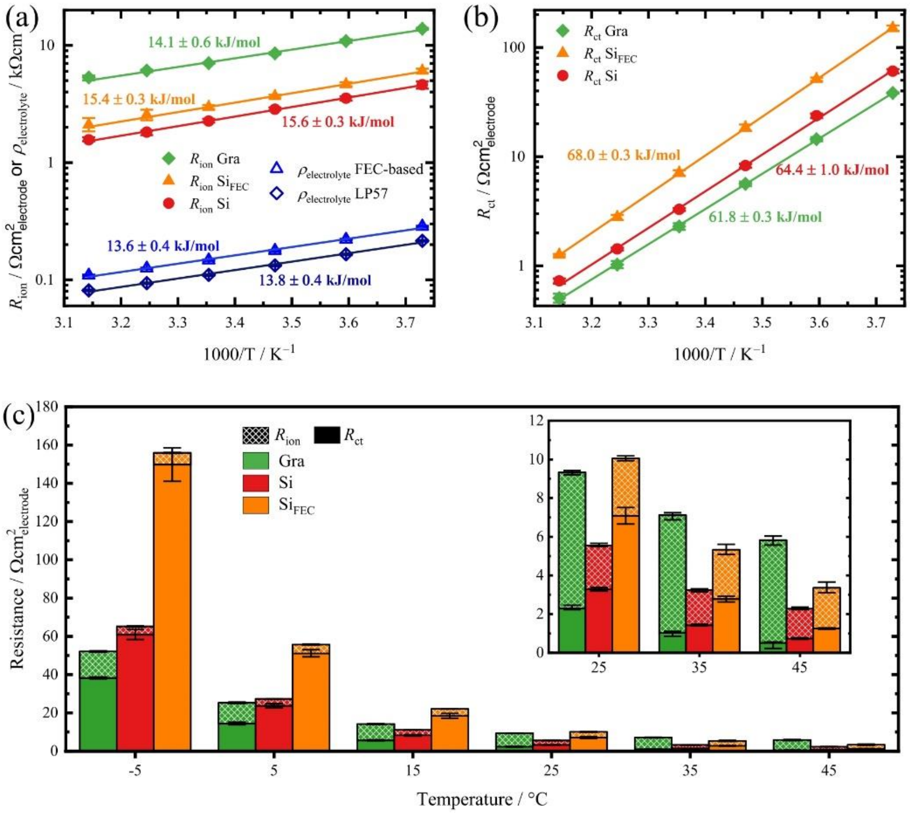

Figure 4. The obtained values for R_{ct} and R_{ion} from the impedance analysis conducted at −5 to +45 °C with graphite and silicon electrodes (2.8 mAh cm^{-2}) in LP57 and with silicon electrodes in 1 M $LiPF_6$ in FEC:DEC 1:4 (referred to as Si_{FEC}). (a) Arrhenius plots for R_{ion} and the electrolyte resistivities ρ; (b) Arrhenius plot for R_{ct}; (c) Bar chart showing the absolute contributions of R_{ion} and R_{ct} for each system and temperature, with R_{ct} represented by the lower part of the bar and R_{ion} represented by the upper hatched part of the bar. The data shows the change of resistance contribution, with R_{ct} dominating at lower temperatures and R_{ion} dominating at higher temperatures. The average obtained from two measurements in separate cells is plotted. The plotted error bars span the deviation of each resistance value from the mean plus the error obtained from each impedance fit.

manner even from measurements under non-blocking conditions.[11] This allows for comparison of R_{ion} obtained under blocking conditions before formation (Fig. 3c) and obtained under non-blocking conditions after formation at 50% SOC (left plot in Fig. 3d). For all cells analyzed herein, the R_{ion} value obtained at −5 °C either from blocking conditions before formation (see Fig. 3c) or at 50% SOC after two formation cycles (see Fig. 3d) deviated by less than 15%. This means that our above stated assumption used to determine R_{ct}, namely that R_{ion} does not change significantly over the course of the two formation cycles, is reasonably accurate, i.e., that fixing the value for R_{ion} to that obtained before formation is reasonable. Due to the expected volumetric changes of the silicon particles during (de-)lithiation it is probable that reversible and irreversible changes in porosity and thickness occur in the electrode over formation, as a function of SOC and during the ageing of the electrode. Thus, while the R_{ion} deviates by less than 15% at 50% SOC compared to that measured before formation, it is probable that changes in microstructure exist which account for these small deviations. Furthermore, it is expected that larger deviations are present at higher SOCs or aged electrodes. It must be noted that the electrode has a large initial porosity (∼62%) which may be able to accommodate a major part of the volumetric expansion of the silicon which is expected to be in the order of 100% for a lithiation to 1200 mAh g_{Si}^{-1} (based on the assumption of ∼300% expansion upon full lithiation and a linear volume expansion). Thus, larger changes in microstructure and resulting R_{ion} could occur during formation of calendered electrodes of lower porosities which are, however, not investigated in this study.

Temperature-dependent impedance.—This section describes the temperature-dependent behavior of the two resistances, R_{ct} and R_{ion}. The resistances were extracted by individually measuring R_{ion} before formation at all temperatures and then analyzing the spectra at 50% SOC to extract the charge-transfer resistance.

As described above, the main differences in electrode properties between the graphite and silicon electrodes is their difference in pore resistance, which is lower for the much thinner silicon electrodes, as well as in charge-transfer resistance, which is slightly higher for the silicon electrodes in the same electrolyte (i.e., in LP57) and substantially higher when using an FEC-based electrolyte that is commonly used for silicon electrodes. This difference plays a key role when it comes to the temperature-dependent behavior of the electrode performance. Figure 4 shows the temperature dependence of the two resistances, R_{ion} and R_{ct}, which were extracted from the EIS measurements.

First, Fig. 4a shows the temperature-dependence of R_{ion} of the different electrodes as well as of the resistivity ($\rho_{\mathrm{electrolyte}} = 1/\kappa$) of the pure electrolytes (i.e., of LP57 and the FEC-based electrolyte), together with the thereof calculated activation energies. For the graphite electrodes in LP57, the activation energy for R_{ion} of 14.1 kJ mol^{-1} (Fig. 4a, green text/symbols) is in very good agreement with the activation energy determined for the ionic resistivity of LP57 of 13.8 kJ mol^{-1} (dark blue text/symbols; reasonably close to the 13.2 kJ mol^{-1} determined by Solchenbach et al. from Swagelok* T-cell measurements[14]), as one would expect on the basis of Eq. 1. On the other hand, for the silicon electrode in LP57, the activation energy for R_{ion} (15.6 kJ mol^{-1}, red text/symbols) is ∼13% higher than the activation energy of the ionic resistivity of LP57. This deviation is likely due to a non-negligible error in the analysis of the impedance data R_{ion}, since the ∼3.5-fold lower R_{ion} value for the silicon electrodes in LP57 makes it difficult to accurately analyze the spectra (this is especially the case at higher temperatures, which in turn may lead to an apparently higher slope). For the silicon electrodes with the FEC-based electrolyte, the same discrepancy between the activation energy for R_{ion} (15.4 kJ mol^{-1}, orange text/symbols) and for $\rho_{\mathrm{electrolyte}}$ (13.6 kJ mol^{-1}, blue text/symbols) is observed, presumably for the same reason. Overall, however, it can be stated that the activation energies for R_{ion} are rather low and, as expected, very close to the activation energy for $\rho_{\mathrm{electrolyte}}$.

Figure 4b shows the change of the charge-transfer resistance with temperature. The graphite and the Si electrodes with LP57 electrolyte show activation energies for R_{ct} of 61.8 and 64.4 kJ mol^{-1}, respectively. The $\mathrm{Si_{FEC}}$ electrodes show a slightly higher activation energy for the charge-transfer reaction (68.0 kJ mol^{-1}), but reasonably similar to that of the silicon electrodes with LP57 electrolyte, despite an expected difference in SEI composition.[20,21]

To better highlight the differences in electrode resistances, Fig. 4c shows the sum of R_{ct} (fully colored lower part of the bars) and R_{ion} (hatched upper part of the bars) at each temperature. At −5 °C, R_{ct} is the dominating resistance for all electrodes/electrolytes, most prominently for the Si electrodes, for which the ratio of $R_{\mathrm{ct}}/R_{\mathrm{ion}}$ is ∼13 (LP57) and ∼25 (FEC), whereas it is only ∼2.8 for the graphite electrodes. With increasing temperature, the charge-transfer resistance changes drastically due to their higher activation energy, so that the ratio of $R_{\mathrm{ct}}/R_{\mathrm{ion}}$ at 45 °C decreases to 0.47, 0.58, and 0.11 for the Si, $\mathrm{Si_{FEC}}$, and graphite electrodes, respectively. At these elevated temperatures, the dominating resistance is now R_{ion}, i.e., the material is expected to be limited by the lithium ion transport in the electrolyte phase within the pores of the electrodes rather than by the reaction resistance. While at −5 °C the sum of R_{ct} and R_{ion} was lowest for the graphite electrode, at 35 °C and 45 °C this is reversed and the graphite electrode shows the largest total resistance compared to Si in either one of the electrolytes. This is explained by the difference in activation energies and the differences in R_{ct} and R_{ion} for the graphite and silicon electrodes. At low temperatures, R_{ct} is increased significantly and the silicon electrodes show larger resistances compared to graphite. At high temperatures, R_{ct} is significantly reduced, so that the differences between the kinetic resistances become negligibly small, leaving R_{ion} as the dominating resistance, which is smallest for the thin silicon electrodes.

Electrode potential profile comparison in lithiation rate tests.—This section describes the observed influence of the two resistances R_{ct} and R_{ion} on the potential profile and the performance of the electrodes. While the resistances shown in the previous section were measured after being delithiated to 50% SOC and only show the resistance at 50% SOC, they can still be used as guidelines and reference points to understand the behavior of the potential curves of the electrodes under load, even though they are not necessarily representative of the overpotentials of the electrodes at all SOCs. Additionally, the diffusion overpotentials from Li^{+} concentration gradients in the electrodes and the separator, which are not part of the measured R_{ion}, will contribute to the measured overpotential.[23,24]

The effects of the resistances R_{ct} and R_{ion} on the potential profile are expected to be different. The charge-transfer resistance is a resistance connected in series to the reaction path, i.e., every Li^{+}-ion has to overcome the reaction resistance to be intercalated (in case of graphite) or alloyed (in case of silicon). The kinetics may change as a function of SOC (assuming e.g. Doyle-Fuller-Newman (DFN) -type kinetics[25]), but between applying a lower and higher C-rate, the difference in their respective overpotential from faradaic reactions should result in the electrode potential being shifted downward, as changes in the applied current correspond to changes in Butler-Volmer (BV) type overpotential. The linear region of the BV kinetics, where the kinetic overpotential equates to the product of R_{ct} and the current density, extends to overpotentials of up to roughly one third of the Tafel slope. Assuming a kinetic transfer coefficient of $\alpha = 0.5$, the Tafel slope (*TS*) at room temperature is ∼120 mV (based on $\mathrm{TS} = 2.303 \cdot R \cdot T/(\alpha \cdot F)$, with R being the ideal gas constant, F the Faraday constant, and T the temperature in Kelvin), so that the linear region should extend to up to roughly ± 40 mV.[26] At 25 °C, the R_{ct} of the silicon electrode with LP57 is ∼3 $\Omega\mathrm{cm}^{2}_{\mathrm{electrode}}$, resulting in a kinetic overpotential of ∼8 mV at a rate of 1C (i.e., at a current density of 2.8 mA $\mathrm{cm}^{-2}_{\mathrm{electrode}}$), i.e., still being in the linear BV region. At −5 °C however, the charge-transfer resistance of the silicon electrode with LP57 increases to R_{ct}

~60 $\Omega\text{cm}^2_{\text{electrode}}$, resulting in a linearly extrapolated kinetic overpotential at 1C of ~170 mV; as the latter is outside the linear region, the actual kinetic overpotential would be lower. In either case (i.e., whether in the linear or non-linear BV region), higher rates will lead to an increased down-shift of the potential curve (i.e., of E vs SOC). Furthermore, if R_{ct} does not vary strongly with the SOC, the potential curve retains its specific shape. The change in R_{ct} with SOC is not shown in this work but has been measured to be below a factor 2 for most parts of the SOC window measured in LP57, similarly to the DFN model which predicts a max. change of factor 2 in kinetics between 10%–90% SOC, represented by Eq. 2:[25,27]

$$i_0 = Fk(c_{s,\,\max} - c_s)^{\alpha_c}(c_s)^{\alpha_a}(c_1)^{\alpha_a} \qquad [2]$$

with k as the reaction rate, c_s and $c_{s,\,\max}$ as the solid concentration and maximum solic concentration of Li and c_1 as the Li^+ concentration in the electrolyte. α_c and α_c are the kinetic transfer coefficients and usually assumed 0.5.

In contrast, the electrolyte ionic resistance in the pores of the electrode is connecting the active material particles through the electrode, and not all ions have to pass through the entire electrode for the reaction to occur. For example, only 10% of the total Li^+ exchanged needs to reach the bottom 10% of the electrode near the electrode/current collector interface. Thus, one might assume that the ionic resistance is less important compared to the charge-transfer resistance. However, high currents can lead to concentration gradients across the electrode and thus to an inhomogeneous use of the electrode, i.e., it is more difficult for Li^+ to reach the region of the electrode near the current collector vs the region of the electrode near the separator, which is reflected in a downward-sloping potential profile.[24] Additionally, R_{ion} is only a representation of the electrolyte conductivity, whereas during operation of a battery cell additional diffusion resistances will contribute to the mass transport overpotential. These diffusion overpotentials not only play a role in the porous electrodes but also across the separator. The concentration difference across the separator can be estimated via

$$\frac{\partial c}{\partial x} = -\frac{I(1-t_+)\tau}{D\varepsilon F} \qquad [3]$$

with c being the electrolyte concentration, x being the path length (e. g., the separator thickness), F being the Faraday constant, I being the applied current (in A/m^2), t_+ being the transference number, and D being the salt diffusion coefficient (in $\text{m}^2\text{/s}$). Combined with the equation

$$\frac{\partial \phi_{diff}}{\partial x} = \frac{\frac{2RT}{F}(\text{TDF})(1-t_+)}{c}\frac{\partial c}{\partial x} \qquad [4]$$

with R being the ideal gas constant, T the electrolyte temperature (in Kelvin), and TDF being the thermodynamic factor of the electrolyte, the potential drop ϕ across the separator can be estimated.[28] This equation represents the part of the MacInnes equation which represents the diffusion overpotential, as the ohmic resistance of the electrolyte has been incorporated in the HFR of the EIS measurement. The path length (travel distance) of ions through the separator, x, can be estimated from the thickness of the separator and its tortuosity. The tortuosity of the separator can be calculated using Eq. 1 assuming $\varepsilon = 0.9$, separator thickness $\sim 2 \times 200\ \mu\text{m}$ (two separators measured from the reference electrode to the working electrode), electrolyte conductivity 9.1 mS cm^{-1} and a resistance of ~6 $\Omega\text{cm}^2_{\text{electrode}}$ (HFR), giving $\tau \approx 1.15$. From there, using electrolyte values for 25 °C measured by Landesfeind et al.[29] for LP57, ($D = 3{*}10^{-10} m^2/s$, $t_+ = 0.25$, TDF = 1.5), the overpotential at C/5 ($\equiv$0.56 mA $\text{cm}^{-2}_{\text{electrode}}$) across two glass fiber separators is estimated to be ~4.3 mV, which corresponds to an areal resistance of ~7.7 $\Omega\text{cm}^2_{\text{electrode}}$. The Warburg diffusion resistance is dependent on the same geometric and electrolyte properties as the HFR, meaning that an increase in HFR would directly follow an increase in the Warburg diffusion resistance, with the Warburg resistance giving 1.3× HFR. This means that under load the separator exhibits a total resistance 2.3 times the measured HFR. Following this, the factor 2.3 can be used with any resistance stemming from the electrolyte under load, including R_{ion}. It should be mentioned that changes in Li^+ concentration in the electrolyte are also assumed to have an effect on the kinetics, with a locally decreased Li^+ concentration increasing the local R_{ct}, as, e.g., expected during fast-charging on the anode side. This highlights the importance of the porous aspect of the electrode, as it has an effect on local current homogeneity,[11,24] kinetic resistances, as well as transport resistances. In summary, electrodes which are mostly limited by kinetic resistances are expected to keep the shape of their potential profile, with the potential vs SOC curve only being shifted downward (assuming no drastic changes in SOC-dependent kinetics). In contrast, electrodes which show strong transport limitations in the electrolyte phase are subject to inhomogeneous current distributions in the electrode and show time dependent concentration gradients, which are expected to increase the electrode overpotential over time, i.e., over SOC when conducting a constant-current charge or discharge curve. In this work the solid diffusion resistance was not measured, as diffusion coefficient measurements need to be performed over the whole SoC range and fitted to a model, an analysis which is outside of the scope of this work. As will be shown below,

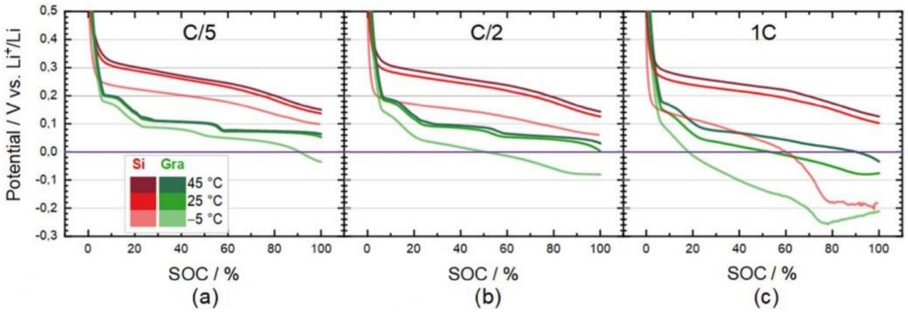

Figure 5. Lithiation potentials vs SOC for silicon (red colored line) and graphite electrodes (green colored lines) in LP57 at 45 °C, 25 °C and −5 °C at various C-rates: (a) C/5, (b) C/2, and (c) 1C. The silicon and graphite electrode potentials are referenced to the reference electrode in Swagelok® T-cells, with graphite or silicon as working electrodes (2.8 mAh cm^{-2}) and a lithium metal foil with a free-standing graphite electrode as counter electrode. Note that the silicon in the silicon electrodes is utilized only partially, i.e., only up to 1200 mAh $\text{g}_{\text{Si}}^{-1}$.

the electrodes limitations are often visible already at SOCs below or around 50%, a region where the diffusion limitation is expected to still be low.

To show the influence of R_{ct} and R_{ion} on the electrode performance, the electrodes were tested for their rate capability during lithiation (corresponding to the charging of a battery cell). Figure 5 shows the potential profiles of the graphite and silicon electrode measured with LP57 electrolyte at different temperatures and C-rates, whereby the graphite and silicon electrode potentials are measured vs the reference electrode in the cell. The silicon electrode (red colored lines) shows the expected behavior of electrodes that are limited by their charge-transfer kinetics, where the electrode potential vs SOC curve retains its shape but is shifted downward, visible most clearly for the −5 °C data at C/5 (Fig. 5a) and C/2 (Fig. 5b). Only at a rate of 1C at −5 °C, the silicon electrode shows an increase in overpotential with SOC (i.e., with lithiation time) and the electrode potential ultimately falls below 0 V vs Li^+/Li, where lithium plating can occur.

The graphite electrodes only retain the shape of their open circuit potential vs SOC profile for C/5 and C/2 at 25 °C and 45 °C, suggesting a constant overpotential over the entire SOC range under these conditions. However, while the graphite potential profile at −5 °C is downshifted at C/5 in a similar fashion at low SOCs (see Fig. 5a), it starts to become more sloped at higher SOCs (around 80% SOC), suggesting stronger concentration overpotentials at high SOCs. This effect is even more pronounced at C/2 and −5 °C (see Fig. 5b), where a substantial sloping and smearing out of the plateaus of the different lithiation stages can be observed already beyond ∼20% SOC. At 1C (see Fig. 5c), the graphite electrodes show a constantly increasing overpotential over all temperature ranges and even at the highest temperature of 45 °C, the electrode cannot be fully charged before reaching 0 V vs Li^+/Li. The resistances derived from the impedance data (Fig. 4c) between 25 °C and 45 °C show that the graphite and silicon charge-transfer resistances (for LP57) are similar, and that the electrodes differ most prominently in their ionic pore resistance which are ∼3-fold smaller for the silicon electrodes. This results in a poor lithiation performance at 1C of the graphite electrode, but does not yet limit the performance of the thinner silicon electrode. Analyzing the electrode potential at 100% SOC, the effect of the difference in ionic pore resistance becomes apparent: at 45 °C, the potential difference between C/5 and 1C for the silicon electrodes is ∼30 mV at 100% SOC, while it is ∼100 mV for the graphite electrode, i.e., ∼3-fold larger. It should be noted that the cells used here are flooded with electrolyte, and any commercially relevant system might show influences of electrolyte starvation not seen in this analysis.

The comparison of the effect of temperature and of the individual resistances (i.e., R_{ct} and R_{ion}) on the potential vs SOC profile is important when comparing the performance of different materials, as it allows to deconvolute the influence of their open circuit potentials from the influence of their charge-transport and ionic pore resistances on the rate performane of the electrodes. By virtue of having a potential profile which lies significantly higher than graphite, silicon electrodes (particularly silicon electrodes where the silicon is utilized only partially, as is the case here) allow higher overpotentials than graphite before reaching the lithium plating potential of 0 V vs Li^+/Li. The above analysis shows that it is not only the potential vs SOC profile, but also the reduced ionic pore resistance that allows higher rate capabilities of the material.

To give an overview over the lithiation rate capability of the graphite (in LP57) and of the silicon (in LP57 and the FEC-based electrolyte) electrodes, Fig. 6 shows the SOC values of the electrodes at which their potential reaches 0 V vs Li^+/Li (determined by the lithium metal reference electrode), i.e., the SOC beyond which the plating of lithium becomes possible. This analysis shows the combined effect of the higher potential of the silicon electrode (based on a ∼30% silicon utilization) as well as its lower ionic pore resistance (i.e., its lower transport overpotential) on its lithiation rate capability. The graphite electrode (Fig. 6a) shows a performance improvement of a factor ∼4 from the lowest (−5 °C) to the highest (+45 °C) temperature, with 50% SOC reached for C/2 at −5 °C and for ∼1.8C (interpolated C-rate) at 45 °C. The silicon electrode measured in LP57 (Fig. 6b) generally allows for higher C-rates, giving 50% SOC at ∼1.2C when measured at −5 °C. At higher temperatures, the electrode limitation is ultimately expected to be also caused by ionic transport limitations, as kinetic resistances are very low at high temperatures, and at 45 °C the silicon electrode reaches 50% of its capacity at ∼3.2C (i.e., a factor of ∼2.5 improvement from −5 °C to 45 °C). The silicon electrode with the FEC-based electrolyte (Si_{FEC}, see Fig. 6c) shows a very similar behavior.

Comparing the lithiation rate capabilities of the various electrodes at a given temperature, one can see that at −5 °C it is similar for the silicon electrodes in the two different electrolytes and ∼2-fold higher than that of the graphite electrode (i.e., 50% SOC are reached for the silicon electrodes at ∼1C and for the graphite electrode at ∼0.5C; see Fig. 6d). The overall electrode resistance of the silicon electrode in FEC-based electrolyte at −5 °C is dominated by R_{ct} and is ∼3-fold higher than that of the graphite electrode (see Fig. 4c), yet it still performs clearly better than the graphite electrode. Thus, the higher OCV of silicon compensates for the high kinetic overpotentials at low temperatures. Comparing graphite and silicon at 25 °C (Fig. 6e) and 45 °C (Fig. 6f), the temperature-induced reduction in kinetic overpotential strongly improves the rate capability of the silicon electrodes in both electrolytes, which only show a reduced capacity above 2C at 25 °C and 2.5C at 45 °C. In contrast, graphite is limited above ∼0.75C at both 25 and 45 °C, which can be explained by the kinetics becoming negligible at higher temperatures. As the pore resistance is significantly less affected by changes in temperature, it becomes the dominant factor in determining the electrodes limitation at higher temperatures.

Conclusions

In this publication we analyzed and compared graphite and silicon electrodes of practical areal capacities (2.8 mAh cm^{-2}) for their kinetic and transport resistances at temperatures between −5 to 45 °C via electrochemical impedance spectroscopy (EIS) with a micro-reference electrode to quantify the anode (graphite or silicon) impedance. For the here studied silicon elecrodes ($70\%_{wt}$ silicon), only ∼30% of the full capacity of silicon was utilized (i.e., 1200 mAh g_{Si}^{-1}). LP57 was used as reference electrolyte for both graphite and silicon, the latter also being measured in an FEC-based electrolyte which is generally used for silicon electrodes.

Using EIS we showed that the graphite anode has a ∼2.5 times higher ionic resistance (R_{ion}) for lithium ion conduction in the electrolyte phase within the pores of the electrode, mostly due to its ∼2.5-fold larger electrode thickness at the same areal capacity as the silicon-based electrode. Furthermore, the graphite electrode exhibits only slightly lower kinetic resistances (R_{ct}) compared to silicon when measured in LP57 at 25 °C. The temperature-dependent impedance analysis showed how the ratio of R_{ct} to R_{ion} changes from predominantly kinetically limited at lower temperatures to transport limited at higher temperature, due to high activation energies for R_{ct} of ∼62–68 kJ mol^{-1} compared to the ionic resistance R_{ion} of ∼14–16 kJ mol^{-1}.

We subsequently explored the lithiation rate limiting properties of the graphite and silicon electrodes by comparing the resulting potential profiles at different C-rates to the findings from the EIS analysis. We showed how the kinetically dominated silicon electrodes mostly retain their potential shape, as the kinetic overpotential only generates an offset in overpotential, while the graphite electrodes, which show a much greater transport limitation, show a smearing of the potential profile and an increase in overpotential over SOC when cycled at higher C-rates. Only at −5 °C, the graphite electrode exhibited a kinetic limitation at C/5 but already showed additional transport overpotentials starting at C/2. At 1C the graphite potential showed transport limitations even at 45 °C and did not

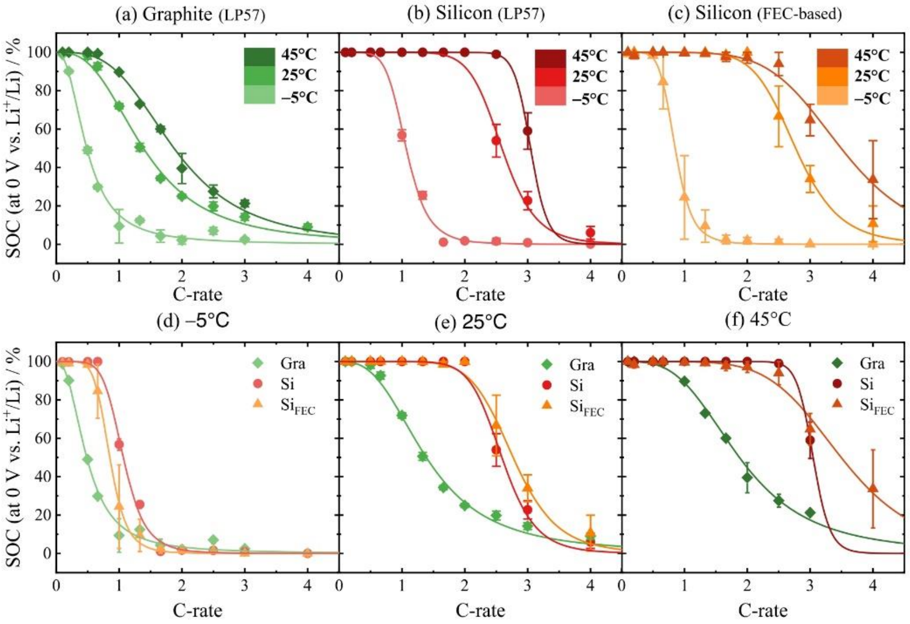

Figure 6. SOC obtained at 0 V vs Li$^+$/Li for silicon and graphite electrodes at different temperatures and C-rates. (a)–(c) Lithiation rate vs SOC at which 0 V vs Li$^+$/Li are reached for graphite in LP57, silicon in LP57, and silicon in FEC-based electrolyte (Si$_{FEC}$), acquired at −5 °C, 25 °C, and 45 °C. (d)–(f) Lithiation rate test data for the three sets of electrodes/electrolytes at each of the three temperatures. Error bars indicate the standard error of the mean of two independent measurements with electrodes of identical composition. A sigmoidal fit was added as a guide-to-the-eye according to the mathematical description described in Ref. 1. Measurements were conducted with Swagelok* T-cells equipped with a GWRE, with graphite or silicon as working electrodes (2.8 mAh cm^{-2}), and a lithium metal foil with a free-standing graphite electrode as counter electrode. Note that the silicon in the silicon electrodes is utilized only partially, i.e., only up to 1200 mAh g$_{Si}$$^{-1}$.

reach the full capacity before reaching 0 V vs Li$^+$/Li. In contrast, the thinner silicon electrodes only showed transport overpotentials at −5 °C for a 1C lithiation. Comparing the end-of-charge overpotential of the two electrode types at 45 °C and 1C, the graphite overpotential of ∼100 mV was three times greater than that of the silicon (∼30 mV), highlighting how the silicon electrodes' decreased transport resistance is contributing significantly to its greater lithiation rate capability. This potential profile analysis showed that the better performance of silicon is not only due to its higher reversible potential, which allows for higher overpotentials before the onset of Li-plating, but also due to its significantly smaller thickness.

Additional analysis of the temperature-dependent lithiation rate tests gave insight into the overall performance of the electrodes. While the graphite electrodes could not reach the full capacity at 1C and 45 °C, the silicon electrodes allowed a lithiation at 2C already at 25 °C and still reached the full capacity at 2.5 °C and 45 °C. Overall the silicon electrodes showed a roughly 2-fold increase in lithiation rate capability compared to graphite.

Acknowledgments

C. B. gratefully acknowledges funding by Wacker Chemie AG. R. M. gratefully acknowledges funding by BMW AG. M. G. gratefully acknowledges funding by Wacker Chemie AG. We gratefully acknowledge Jonas Dickmanns for his help with the conductivity measurements.

ORCID

Clara Berg https://orcid.org/0000-0002-5416-3396
Robert Morasch https://orcid.org/0000-0002-9931-1022
Maximilian Graf https://orcid.org/0000-0002-2252-1216
Hubert A. Gasteiger https://orcid.org/0000-0001-8199-8703

References

1. M. N. Obrovac, "Si-alloy negative electrodes for Li-ion batteries." *Current Opinion in Electrochemistry*, **9**, 8 (2018).
2. O. Gröger, H. A. Gasteiger, and J.-P. Suchsland, "Review—Electromobility: Batteries or Fuel Cells?" *J. Electrochem. Soc.*, **162**, A2605 (2015).
3. M. N. Obrovac and L. Christensen, "Structural changes in silicon anodes during lithium insertion/extraction." *Electrochem. Solid-State Lett.*, **7**, A93 (2004).
4. J. Li and J. R. Dahn, "An in situ X-ray diffraction study of the reaction of Li with crystalline Si." *J. Electrochem. Soc.*, **154**, A156 (2007).
5. M. N. Obrovac, L. Christensen, D. B. Le, and J. R. Dahn, "Alloy design for lithium-ion battery anodes." *J. Electrochem. Soc.*, **154**, A849 (2007).
6. J. Guo et al., "Silicon-based lithium ion battery systems: state-of-the-art from half and full cell viewpoint." *Adv. Funct. Mater.*, **31**, 1 (2021).
7. D. Jantke et al., "Silicon-dominant anodes based on microscale silicon particles under partial lithiation with high capacity and cycle stability." *J. Electrochem. Soc.*, **166**, A3881 (2019).
8. S. Haufe, R. Bernhard, and J. Pfeiffer, "Revealing the failure mechanism of partially lithiated silicon-dominant anodes based on microscale silicon particles." *J. Electrochem. Soc.*, **168**, 080531 (2021).
9. M. Graf et al., "Effect and progress of the amorphization process for microscale silicon particles under partial lithiation as active material in lithium-ion batteries." *J. Electrochem. Soc.*, **169**, 020536 (2022).
10. J. Landesfeind, D. Pritzl, and H. A. Gasteiger, "An analysis protocol for three-electrode li-ion battery impedance spectra: part I. analysis of a high-voltage positive electrode." *J. Electrochem. Soc.*, **164**, A1773 (2017).
11. R. Morasch, J. Keilhofer, H. A. Gasteiger, and B. Suthar, "Methods—understanding porous electrode impedance and the implications for the impedance analysis of Li-Ion battery electrodes." *J. Electrochem. Soc.*, **168**, 080519 (2021).
12. N. Ogihara et al., "Theoretical and experimental analysis of porous electrodes for lithium-ion batteries by electrochemical impedance spectroscopy using a symmetric cell." *J. Electrochem. Soc.*, **159**, A1034 (2012).
13. J. Illig, M. Ender, A. Weber, and E. Ivers-Tiffée, "Modeling graphite anodes with serial and transmission line models." *J. Power Sources*, **282**, 335 (2015).

14. S. Solchenbach, X. Huang, D. Pritzl, J. Landesfeind, and H. A. Gasteiger, "Monitoring SEI formation on graphite electrodes in lithium-ion cells by impedance spectroscopy." *J. Electrochem. Soc.*, **168**, 110503 (2021).
15. R. Morasch, B. Suthar, and H. A. Gasteiger, "Simple way of making free-standing battery electrodes and their use in enabling half-cell impedance measurements via μ-reference electrode." *J. Electrochem. Soc.*, **167**, 100540 (2020).
16. S. Solchenbach, D. Pritzl, E. J. Y. Kong, J. Landesfeind, and H. A. Gasteiger, "A Gold micro-reference electrode for impedance and potential measurements in lithium ion batteries." *J. Electrochem. Soc.*, **163**, A2265 (2016).
17. J. Landesfeind, J. Hattendorff, A. Ehrl, W. A. Wall, and H. A. Gasteiger, "Tortuosity determination of battery electrodes and separators by impedance spectroscopy." *J. Electrochem. Soc.*, **163**, A1373 (2016).
18. J. Landesfeind, A. Eldiven, and H. A. Gasteiger, "Influence of the binder on lithium ion battery electrode tortuosity and performance." *J. Electrochem. Soc.*, **165**, A1122 (2018).
19. R. Morasch, J. Landesfeind, B. Suthar, and H. A. Gasteiger, "Detection of binder gradients using impedance spectroscopy and their influence on the tortuosity of li-ion battery graphite electrodes." *J. Electrochem. Soc.*, **165**, A3459 (2018).
20. K. U. Schwenke, S. Solchenbach, J. Demeaux, B. L. Lucht, and H. A. Gasteiger, "The impact of CO 2 evolved from VC and FEC during formation of graphite anodes in lithium-ion batteries." *J. Electrochem. Soc.*, **166**, A2035 (2019).
21. S. K. Heiskanen, J. Kim, and B. L. Lucht, "Generation and evolution of the solid electrolyte interphase of lithium-ion batteries." *Joule*, **3**, 2322 (2019).
22. M. Wetjen et al., "Morphological changes of silicon nanoparticles and the influence of cutoff potentials in silicon-graphite electrodes." *J. Electrochem. Soc.*, **165**, A1503 (2018).
23. J. Moškon and M. Gaberšček, "Transmission line models for evaluation of impedance response of insertion battery electrodes and cells." *J. Power Sources Advances*, **7**, 100047 (2021).
24. S. Malifarge, B. Delobel, and C. Delacourt, "Experimental and modeling analysis of graphite electrodes with various thicknesses and porosities for high-energy-density li-ion batteries." *J. Electrochem. Soc.*, **165**, A1275 (2018).
25. T. F. Fuller, M. Doyle, and J. Newman, "Simulation and optimization of the dual lithium ion insertion cell." *J. Electrochem. Soc.*, **141**, 1 (1994).
26. J. Newman and K. E. Thomas-Alyea, *Electrochemical Systems* (Wiley-VCH Verlag GmbH & Co. KGaA, New Jersey) (2004).
27. M. Doyle, T. F. Fuller, and J. Newman, "Modeling of galvanostatic charge and discharge of the lithium/polymer/insertion cell." *J. Electrochem. Soc.*, **140**, 1526 (1993).
28. T. S. Chadha, B. Suthar, D. Rife, V. R. Subramanian, and P. Biswas, "Model based analysis of one-dimensional oriented lithium-ion battery electrodes." *J. Electrochem. Soc.*, **164**, E3114 (2017).
29. J. Landesfeind and H. A. Gasteiger, "Temperature and concentration dependence of the ionic transport properties of lithium-ion battery electrolytes." *J. Electrochem. Soc.*, **166**, A3079 (2019).

4.0 Conclusions

The main objective of this work was to gain a fundamental understanding of a new type of silicon active material employed by the group in a research project funded by WACKER Chemie AG. The here investigated microscale silicon material aims to address the intrinsic challenges associated with the volume expansion of silicon upon lithiation.[11,14,31,54,104,143] Microscale silicon particles are characterized by a low specific surface area, which has the advantage of lower first-cycle irreversible capacity losses compared to nanoscale silicon materials.[64] In addition, microscale silicon also offers advantages from a production and cost perspective. However, to achieve a reasonable electrochemical performance, microscale silicon-based anodes must be operated under partial lithiation conditions, i.e., using only a part of the silicon's capacity. The resulting preservation of a crystalline phase in the silicon particles enables the maintenance of the integrity of the material over cycling and, therefore, diminishes the degradation phenomena such as particle fracturing and electrical isolation (see upper part of **Figure 18**).

To track and understand the amorphization of the crystalline silicon particles, we employed an XRD-based in-situ method described in Chapter 3.1. The amorphization process was investigated using varying lower lithiation cutoff potentials for the silicon-based anodes. For lithiation cutoff potentials ≥ 170 mV vs. Li^+/Li, a constant capacity is observed for the electrodes over cycling. However, decreasing the lower lithiation cutoff potential to < 170 mV vs. Li^+/Li leads to a continuous capacity increase over cycling until a threshold is reached where the material collapses, after which point the capacity drops again. Using Si//Li pouch-cells allows conducting in-situ XRD measurements of the electrodes in between cycling. Accurate quantification of the crystalline phase is accomplished by taking the diffraction peak intensity of the internal copper current collector as an internal reference that was used to normalize the diffraction peak intensity if the crystalline silicon phase for the silicon phase. In accordance with the capacity increase for the lower cutoff potential, a decrease for the crystalline silicon phase, i.e., an increase for amorphous silicon, is detected by XRD. At the same time, electrodes with a restricted lithiation cutoff potential of ≥ 170 mV vs. Li+/Li retained the amount of crystalline phase that was set by the capacity-limited cycle. The quantitative study on the evolution of the crystalline and amorphous silicon phases of microscale silicon over cycling provided valuable information on how to operate microsilicon-based anodes using the partial lithiation principle. Moreover, the insights can help to improve the material designs to enable longer cycle life.

Such approaches or specific material designs can diminish volumetric expansion upon lithiation; however, rupturing the SEI accompanied by irreversible Li-loss through consecutive electrolyte reduction remains challenging (see lower part of **Figure 18**). Developing effective and robust electrolyte systems alongside with new silicon materials is crucial for the commercialization of the latter. Additives in the electrolyte play a pivotal role in tuning an SEI's properties. Recently, $LiNO_3$ was employed as an effective additive in carbonate-based electrolytes for silicon-active materials. The mechanism and working principle of $LiNO_3$ in such electrolyte systems is investigated in Chapter 3.2. Voltammetric scans on carbon electrodes revealed two distinct reduction features at 1.56 V vs. Li^+/Li and 1.39 V vs. Li^+/Li. The first feature can be assigned to the reduction of $LiNO_3$ to $LiNO_2$; the latter turned out to be soluble in the electrolyte and is thus not incorporated as a solid reduction product in the SEI. Consecutively, the second peak is ascribed to the reduction of $LiNO_2$ instead of $LiNO_3$, which was validated by applying $LiNO_2$ as an electrolyte additive. Analysis of gaseous and solid reduction products by OEMS and XPS showed that $LiNO_2$ is further reduced to Li_3N and Li_2O, with N_2O as a gaseous intermediate species. This mechanistic investigation revealed $LiNO_2$ as the actual active species when $LiNO_3$ was applied as an additive. Full-cell cycling experiments with silicon anodes, NCM622 cathodes, and $LiNO_2$ as additive in the electrolyte showed impressive cycling stability. Similar performance of the $LiNO_2$ additive was achieved compared to cells cycled with the $LiNO_3$ additive. Both electrolyte systems could even outperform FEC at elevated temperatures, which is the most used additive for silicon-based anodes. The significant impact of these additives on the cycling stability of the cells underlines the critical role of well-designed electrolyte systems on the performance of silicon-based anodes. The mechanistic insights gained in this study help develop and tailor electrolytes for demanding materials like silicon and thereby to accelerate their commercialization.

Not only active material designs but also electrode designs have a significant impact on the final performance of a cell. Fast-charging capability can be achieved with low electrode loadings and high porosities, whereas high energy densities are accomplished with more densified electrodes with higher loadings. With its high specific capacity, silicon enables both high energy densities and high rate-capabilities with thin electrode designs. To evaluate and benchmark electrode properties and the porous electrode structure, electrochemical impedance spectroscopy allows to determine the limiting resistances independently from each other. In this study, we compared silicon-based electrodes with graphite electrodes with the same areal capacities with regard to their temperature-dependent charge transfer resistances (R_{CT}) and ion transport resistance (R_{ion}) in the electrolyte phase within the pores of the anode electrode. The pore resistance for the thinner silicon-based and thicker graphite electrodes dominates at higher temperatures. The higher activation energy of the kinetic charge transfer resistance reduces the influence at high temperatures but controls the lower temperatures even more. In other words, thin electrodes are even more advantageous at high temperatures, since the ion resistance strongly depends on the thickness of the coating. Fast-charging processes, in principle, cause the cells to heat up, and the ion resistance and, thus, the thickness of the electrodes is the determining parameter for such an application. The benchmarking against graphite anodes conducted in this study shows that silicon-based electrodes have superior performance for fast-charging applications, making them particularly relevant, especially for the automotive applications.

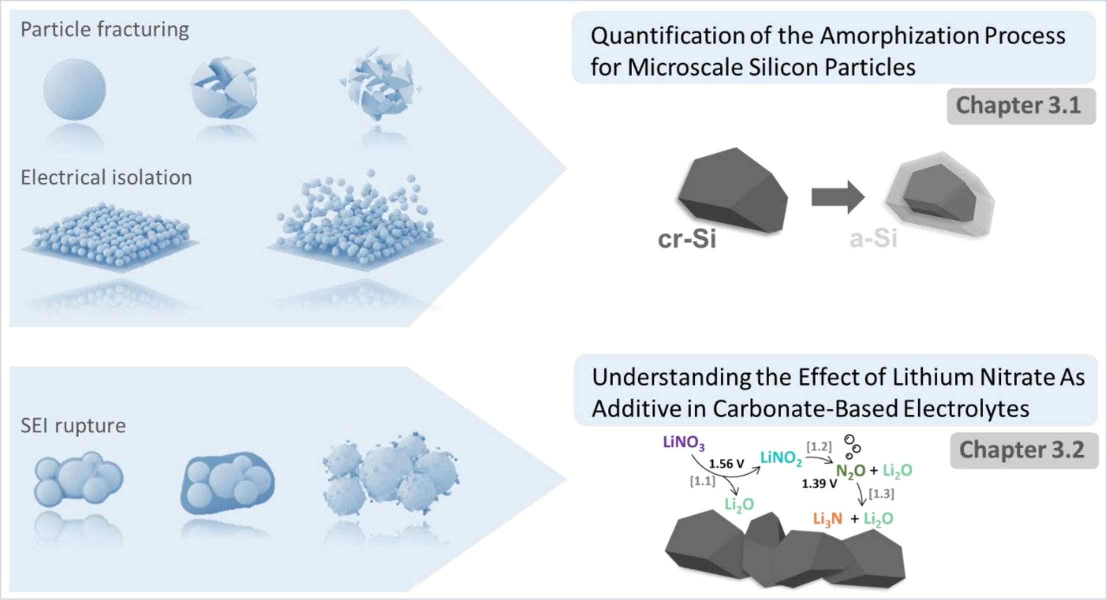

Figure 18 Degradation phenomena of silicon anodes arising from the volume expansion upon (de-)lithiation and graphical overview of the mitigation strategies presented in this work (right part of the figure). Left part of the figure; reprinted from Choi et al. with permission from Nature Review Materials.[14]

References

[1] McKinsey & Company. (2021). Why the future automotive future is electric. *McKinsey Center for Future Mobility*, *September*. https://www.mckinsey.com/industries/automotive-and-assembly/our-insights/why-the-automotive-future-is-electric (accessed: 10/23/2023)

[2] Eshetu, G. G., Zhang, H., Judez, X., Adenusi, H., Armand, M., Passerini, S., & Figgemeier, E. (2021). Production of high-energy Li-ion batteries comprising silicon-containing anodes and insertion-type cathodes. *Nature Communications*, *12*(1), 1–14. https://doi.org/10.1038/s41467-021-25334-8

[3] Office of Energy Efficiency & Renewable Energy. (2023). *Electric Vehicle Battery Pack Costs in 2022 Are Nearly 90% Lower than in 2008, according to DOE Estimates*. https://www.energy.gov/eere/vehicles/articles/fotw-1272-january-9-2023-electric-vehicle-battery-pack-costs-2022-are-nearly (accessed: 10/23/2023)

[4] Wu, H., & Cui, Y. (2012). Designing nanostructured Si anodes for high energy lithium ion batteries. *Nano Today*, *7*(5), 414–429. https://doi.org/10.1016/j.nantod.2012.08.004

[5] Chevrier, V. L., Liu, L., Le, D. B., Lund, J., Molla, B., Reimer, K., Krause, L. J., Jensen, L. D., Figgemeier, E., & Eberman, K. W. (2014). Evaluating Si-Based Materials for Li-Ion Batteries in Commercially Relevant Negative Electrodes. *Journal of The Electrochemical Society*, *161*(5), A783–A791. https://doi.org/10.1149/2.066405jes

[6] Asenbauer, J., Eisenmann, T., Kuenzel, M., Kazzazi, A., Chen, Z., & Bresser, D. (2020). The success story of graphite as a lithium-ion anode material-fundamentals, remaining challenges, and recent developments including silicon (oxide) composites. *Sustainable Energy and Fuels*, *4*(11), 5387–5416. https://doi.org/10.1039/d0se00175a

[7] Huggins, R. A. (1999). Lithium alloy negative electrodes. *Journal of Power Sources*, *81-82*, 13–19. https://doi.org/10.1016/S0378-7753(99)00124-X

[8] Li, X., Zhang, M., Yuan, S., & Lu, C. (2020). Research Progress of Silicon/Carbon Anode Materials for Lithium-Ion Batteries: Structure Design and Synthesis Method. *ChemElectroChem*, *7*(21), 4289–4302. https://doi.org/10.1002/celc.202001060

[9] Obrovac, M. N., Christensen, L., Le, D. B., & Dahn, J. R. (2007). Alloy Design for Lithium-Ion Battery Anodes. *Journal of The Electrochemical Society*, *154*(9), A849. https://doi.org/10.1149/1.2752985

[10] Iaboni, D. S. M., & Obrovac, M. N. (2016). Li 15 Si 4 Formation in Silicon Thin Film Negative Electrodes . *Journal of The Electrochemical Society*, *163*(2), A255–A261. https://doi.org/10.1149/2.0551602jes

[11] Obrovac, M. N., & Chevrier, V. L. (2014). Research Progress. *Chemical Reviews*, *114*(23), 11444–11502. https://doi.org/10.1021/cr500207g

[12] Dou, F., Shi, L., Chen, G., & Zhang, D. (2019). Silicon/Carbon Composite Anode Materials for Lithium-Ion Batteries. In *Electrochemical Energy Reviews* (Vol. 2, Issue 1). Springer Singapore. https://doi.org/10.1007/s41918-018-00028-w

[13] Shi, Q., Zhou, J., Ullah, S., Yang, X., Tokarska, K., Trzebicka, B., Ta, H. Q., & Rümmeli, M. H. (2021). A review of recent developments in Si/C composite materials for Li-ion batteries. *Energy Storage Materials*, *34*, 735–754. https://doi.org/10.1016/J.ENSM.2020.10.026

[14] Choi, J. W., & Aurbach, D. (2016). Promise and reality of post-lithium-ion batteries with high energy densities. In *Nature Reviews Materials* (Vol. 1). https://doi.org/10.1038/natrevmats.2016.13

[15] Nishi, Y. (2016). The Dawn of Lithium-Ion Batteries. *Journal of Electrochemical Society Interface*, *25*, 71.

[16] The Royal Swedish Academy of Sciences. (2019). *The Nobel Prize in Chemistry 2019*. *Press Release*, 1. https://www.nobelprize.org/prizes/chemistry/2019/press-release/ (accessed: 10/23/2023)

[17] Whittingham, M. S. (1976). Electrical Energy Storage and Intercalation Chemistry. *Science*, *192*, 1126–1127. https://science.sciencemag.org/content/192/4244/1126/tab-pdf

[18] Blomgren, G. E. (2017). The Development and Future of Lithium Ion Batteries. *Journal of The Electrochemical Society*, *164*(1), A5019–A5025. https://doi.org/10.1149/2.0251701jes

[19] Giesige, J. (2021). *How a Lithium Ion Battery Actually Works*. The Limiting Factor. https://www.youtube.com/watch?v=4-1psMHSpKs (accessed: 06/02/2024)

[20] Xiao, J., Li, Q., Bi, Y., Cai, M., Dunn, B., Glossmann, T., Liu, J., Osaka, T., Sugiura, R., Wu, B., Yang, J., Zhang, J. G., & Whittingham, M. S. (2020). Understanding and applying coulombic efficiency in lithium metal batteries. *Nature Energy*, *5*(8), 561–568. https://doi.org/10.1038/s41560-020-0648-z

[21] Andre, D., Hain, H., Lamp, P., Maglia, F., & Stiaszny, B. (2017). Future high-energy density anode materials from an automotive application perspective. *Journal of Materials Chemistry A*, *5*(33), 17174–17198. https://doi.org/10.1039/c7ta03108d

[22] Nitta, N., Wu, F., Lee, J. T., & Yushin, G. (2015). Li-ion battery materials: Present and future. *Materials Today*, *18*(5), 252–264. https://doi.org/10.1016/j.mattod.2014.10.040

[23] Deng, D., Kim, M. G., Lee, J. Y., & Cho, J. (2009). Green energy storage materials: Nanostructured TiO_2 and Sn-based anodes for lithium-ion batteries. *Energy and Environmental Science*, *2*(8), 818–837. https://doi.org/10.1039/b823474d

[24] Seefurth, R. N., & Sharma, R. A. (1977). Investigation of Lithium Utilization from A Lithium-Silicon Electrode. *Journal of The Electrochemical Society*, *124*(8), 1207–1214. https://doi.org/10.1149/1.2133529

[25] Sharma, R. a., & Seefurth, R. N. (1976). Thermodynamic Properties of the Lithium-Silicon System. *Journal of The Electrochemical Society*, *123*(12), 1763. https://doi.org/10.1149/1.2132692

[26] Wen, C. J., & Huggins, R. a. (1981). Chemical diffusion in intermediate phases in the lithium-silicon system. *Journal of Solid State Chemistry*, *37*(3), 271–278. https://doi.org/10.1016/0022-4596(81)90487-4

[27] Limthongkul, P., Jang, Y. Il, Dudney, N. J., & Chiang, Y. M. (2003). Electrochemically-driven solid-state amorphization in lithium-silicon alloys and implications for lithium storage. *Acta Materialia*, *51*(4), 1103–1113. https://doi.org/10.1016/S1359-6454(02)00514-1

[28] Wilson, a. M., Way, B. M., Dahn, J. R., & Van Buuren, T. (1995). Nanodispersed silicon in pregraphitic carbons. *Journal of Applied Physics*, *77*(6), 2363–2369. https://doi.org/10.1063/1.358759

[29] McDowell, M. T., Lee, S. W., Nix, W. D., & Cui, Y. (2013). 25th anniversary article: Understanding the lithiation of silicon and other alloying anodes for lithium-ion batteries. *Advanced Materials*, *25*(36), 4966–4985. https://doi.org/10.1002/adma.201301795

[30] Obrovac, M. N., & Christensen, L. (2004). Structural Changes in Silicon Anodes during Lithium Insertion/Extraction. *Electrochemical and Solid-State Letters*, *7*(5), A93. https://doi.org/10.1149/1.1652421

[31] Kasavajjula, U., Wang, C., & Appleby, A. J. (2007). Nano- and bulk-silicon-based insertion anodes for lithium-ion secondary cells. In *Journal of Power Sources* (Vol. 163, Issue 2, pp. 1003–1039). https://doi.org/10.1016/j.jpowsour.2006.09.084

[32] Key, B., Morcrette, M., Tarascon, J. M., & Grey, C. P. (2011). Pair distribution function analysis and solid state NMR studies of silicon electrodes for lithium ion batteries: Understanding the (de)lithiation mechanisms. *Journal of the American Chemical Society*, *133*(3), 503–512. https://doi.org/10.1021/ja108085d

[33] Chon, M. J., Sethuraman, V. a., McCormick, a., Srinivasan, V., & Guduru, P. R. (2011). Real-time measurement of stress and damage evolution during initial lithiation of crystalline silicon. *Physical Review Letters*, *107*(4), 1–4. https://doi.org/10.1103/PhysRevLett.107.045503

[34] Mcdowell, M. T., Lee, S. W., Harris, J. T., Korgel, B. A., Wang, C., Nix, W. D., & Cui, Y. (2013). In Situ TEM of Two-Phase Lithiation of Amorphous Silicon Nanospheres. *Nano Letters*, *13*, 758–764. https://doi.org/10.1021/nl3044508

[35] Liu, X. H., Wang, J. W., Huang, S., Fan, F., Huang, X., Liu, Y., Krylyuk, S., Yoo, J., Dayeh, S. A., Davydov, A. V., Mao, S. X., Picraux, S. T., Zhang, S., Li, J., Zhu, T., & Huang, J. Y. (2012). In situ atomic-scale imaging of electrochemical lithiation in silicon. *Nature Nanotechnology*, *7*(11), 749–756. https://doi.org/10.1038/nnano.2012.170

[36] Tu, K. N. (1975). Selective growth of metal-rich silicide of near-noble metals. *Applied Physics Letters*, *27*(4), 221–224. https://doi.org/10.1063/1.88436

[37] Li, J., & Dahn, J. R. (2007). An In Situ X-Ray Diffraction Study of the Reaction of Li with Crystalline Si. *Journal of The Electrochemical Society*, *154*(3), A156. https://doi.org/10.1149/1.2409862

[38] Key, B., Bhattacharyya, R., Morcrette, M., Seznéc, V., Tarascon, J. M., & Grey, C. P. (2009). Real-time NMR investigations of structural changes in silicon electrodes for lithium-ion batteries. *Journal of the American Chemical Society*, *131*(26), 9239–9249. https://doi.org/10.1021/ja8086278

[39] Graf, M., Berg, C., Bernhard, R., Haufe, S., Pfeiffer, J., & Gasteiger, H. A. (2022). Effect and Progress of the Amorphization Process for Microscale Silicon Particles under Partial Lithiation as Active

Material in Lithium-Ion Batteries. *Journal of The Electrochemical Society*, *169*(2), 020536. https://doi.org/10.1149/1945-7111/ac4b80

[40] Beattie, S. D., Loveridge, M. J., Lain, M. J., Ferrari, S., Polzin, B. J., Bhagat, R., & Dashwood, R. (2016). Understanding capacity fade in silicon based electrodes for lithium-ion batteries using three electrode cells and upper cut-off voltage studies. *Journal of Power Sources*, *302*, 426–430. https://doi.org/10.1016/j.jpowsour.2015.10.066

[41] Besenhard, J. O., Yang, J., & Winter, M. (1997). Will advanced lithium-alloy anodes have a chance in lithium-ion batteries? *Journal of Power Sources*, *68*(1), 87–90. https://doi.org/10.1016/S0378-7753(96)02547-5

[42] Liu, X. H., Zhong, L., Huang, S., Mao, S. X., Zhu, T., & Huang, J. Y. (2012). Size-dependent fracture of silicon nanoparticles during lithiation. *ACS Nano*, *6*(2), 1522–1531. https://doi.org/10.1021/nn204476h

[43] Chan, C. K., Peng, H., Liu, G., McIlwrath, K., Zhang, X. F., Huggins, R. a., & Cui, Y. (2008). High-performance lithium battery anodes using silicon nanowires. *Nature Nanotechnology*, *3*(1), 31–35. https://doi.org/10.1038/nnano.2007.411

[44] Li, H., Huang, X., Chen, L., Wu, Z., & Liang, Y. (1999). High capacity nano-Si composite anode material for lithium rechargeable batteries. *Electrochemical and Solid-State Letters*, *2*(11), 547–549. https://doi.org/10.1149/1.1390899

[45] Wetjen, M., Solchenbach, S., Pritzl, D., Hou, J., Tileli, V., & Gasteiger, H. A. (2018). Morphological Changes of Silicon Nanoparticles and the Influence of Cutoff Potentials in Silicon-Graphite Electrodes. *Journal of The Electrochemical Society*, *165*(7), A1503–A1514. https://doi.org/10.1149/2.1261807jes

[46] Kim, H., Seo, M., Park, M. H., & Cho, J. (2010). A critical size of silicon nano-anodes for lithium rechargeable batteries. *Angewandte Chemie - International Edition*, *49*(12), 2146–2149. https://doi.org/10.1002/anie.200906287

[47] Ng, S. H., Wang, J., Wexler, D., Konstantinov, K., Guo, Z. P., & Liu, H. K. (2006). Highly reversible lithium storage in spheroidal carbon-coated silicon nanocomposites as anodes for lithium-ion batteries. *Angewandte Chemie - International Edition*, *45*(41), 6896–6899. https://doi.org/10.1002/anie.200601676

[48] Gan, C., Zhang, C., Liu, P., Liu, Y., Wen, W., Liu, B., Xie, Q., Huang, L., & Luo, X. (2019). Polymeric carbon encapsulated Si nanoparticles from waste Si as a battery anode with enhanced electrochemical properties. *Electrochimica Acta*, *307*, 107–117. https://doi.org/10.1016/j.electacta.2019.03.186

[49] Yao, Y., McDowell, M. T., Ryu, I., Wu, H., Liu, N., Hu, L., Nix, W. D., & Cui, Y. (2011). Interconnected silicon hollow nanospheres for lithium-ion battery anodes with long cycle life. *Nano Letters*, *11*(7), 2949–2954. https://doi.org/10.1021/nl201470j

[50] Ma, H., Cheng, F., Chen, J., Zhao, J., Li, C., Tao, Z., & Liang, J. (2007). Nest-like silicon nanospheres for high-capacity lithium storage. *Advanced Materials*, *19*(22), 4067–4070. https://doi.org/10.1002/adma.200700621

[51] Kim, H., & Cho, J. (2008). Superior Lithium Electroactive Mesoporous Si. *Nano Letters*, *8*(11), 3688–3691.

[52] Wu, H., Chan, G., Choi, J. W., Ryu, I., Yao, Y., Mcdowell, M. T., Lee, S. W., Jackson, A., Yang, Y., Hu, L., & Cui, Y. (2012). Stable cycling of double-walled silicon nanotube battery anodes through solid-electrolyte interphase control. *Nature Nanotechnology*, *7*(5), 310–315. https://doi.org/10.1038/nnano.2012.35

[53] Park, M. H., Kim, M. G., Joo, J., Kim, K., Kim, J., Ahn, S., Cui, Y., & Cho, J. (2009). Silicon nanotube battery anodes. *Nano Letters*, *9*(11), 3844–3847. https://doi.org/10.1021/nl902058c

[54] Wetjen, M., Pritzl, D., Jung, R., Solchenbach, S., Ghadimi, R., & Gasteiger, H. A. (2017). Differentiating the Degradation Phenomena in Silicon-Graphite Electrodes for Lithium-Ion Batteries. *Journal of The Electrochemical Society*, *164*(12), A2840–A2852. https://doi.org/10.1149/2.1921712jes

[55] Schmidt, V., Wittemann, J. V., Senz, S., & Gósele, U. (2009). Silicon nanowires: A review on aspects of their growth and their electrical properties. *Advanced Materials*, *21*(25-26), 2681–2702. https://doi.org/10.1002/adma.200803754

[56] Yang, Y., Yuan, W., Kang, W., Ye, Y., Pan, Q., Zhang, X., Ke, Y., Wang, C., Qiu, Z., & Tang, Y. (2020). A review on silicon nanowire-based anodes for next-generation high-performance lithium-ion batteries from a material-based perspective. *Sustainable Energy and Fuels*, *4*(4), 1577–1594. https://doi.org/10.1039/c9se01165j

[57] Ramanujam, J., Shiri, D., & Verma, A. (2011). Silicon nanowire growth and properties: A review. *Materials Express*, *1*(2), 105–126. https://doi.org/10.1166/mex.2011.1013

[58] Ge, M., Rong, J., Fang, X., & Zhou, C. (2012). Porous doped silicon nanowires for lithium ion battery anode with long cycle life. *Nano Letters*, *12*(5), 2318–2323. https://doi.org/10.1021/nl300206e

[59] Wang, X., Li, G., Seo, M. H., Lui, G., Hassan, F. M., Feng, K., Xiao, X., & Chen, Z. (2017). Carbon-Coated Silicon Nanowires on Carbon Fabric as Self-Supported Electrodes for Flexible Lithium-Ion Batteries. *ACS Applied Materials and Interfaces*, *9*(11), 9551–9558. https://doi.org/10.1021/acsami.6b12080

[60] Poff, S. (2023). *Energy Density Report for Amprius Technologies*. Mobile Power Solutions. https://amprius.com/500whenergydensityreport/(accessed: 2024-06-02)

[61] Amprius Inc. (2023). Amprius - Transforming electric mobility. *10th Annual Electric VTOL Symposium*, *January*. https://amprius.com/wp-content/uploads/2023/02/Amprius_Technologies_10th_Annual_eVTOL-Symposium.pdf (accessed: 06/02/2024)

[62] Eldesoky, a., Bauer, M., Azam, S., Zsoldos, E., Song, W., Weber, R., Hy, S., Johnson, M. B., Metzger, M., & Dahn, J. R. (2021). Impact of Graphite Materials on the Lifetime of NMC811/Graphite Pouch Cells: Part I. Material Properties, ARC Safety Tests, Gas Generation, and Room Temperature Cycling. *Journal of The Electrochemical Society*, *168*(11), 110543. https://doi.org/10.1149/1945-7111/ac39fc

[63] Mao, C., Wood, M., David, L., An, S. J., Sheng, Y., Du, Z., Meyer, H. M., Ruther, R. E., & Wood, D. L. (2018). Selecting the Best Graphite for Long-Life, High-Energy Li-Ion Batteries. *Journal of The Electrochemical Society*, *165*(9), A1837–A1845. https://doi.org/10.1149/2.1111809jes

[64] Jantke, D., Bernhard, R., Hanelt, E., Buhrmester, T., Pfeiffer, J., & Haufe, S. (2019). Silicon-Dominant Anodes Based on Microscale Silicon Particles under Partial Lithiation with High Capacity and Cycle Stability. *Journal of The Electrochemical Society*, *166*(16), A3881–A3885. https://doi.org/10.1149/2.1311915jes

[65] Zhao, X., & Lehto, V. P. (2021). Challenges and prospects of nanosized silicon anodes in lithium-ion batteries. *Nanotechnology*, *32*(4). https://doi.org/10.1088/1361-6528/abb850

[66] Zhang, Z., Han, X., Li, L., Su, P., Huang, W., Wang, J., Xu, J., Li, C., Chen, S., & Yang, Y. (2020). Tailoring the interfaces of silicon/carbon nanotube for high rate lithium-ion battery anodes. *Journal of Power Sources*, *450*, 227593. https://doi.org/10.1016/j.jpowsour.2019.227593

[67] Han, Y., Liu, X., & Lu, Z. (2018). Systematic investigation of prelithiated SiO2 particles for high-performance anodes in lithium-ion battery. *Applied Sciences*, *8*(8), 1245. https://doi.org/10.3390/app8081245

[68] Xun, S., Song, X., Wang, L., Grass, M. E., Liu, Z., Battaglia, V. S., & Liu, G. (2011). The Effects of Native Oxide Surface Layer on the Electrochemical Performance of Si Nanoparticle-Based Electrodes. *Journal of The Electrochemical Society*, *158*(12), A1260. https://doi.org/10.1149/2.007112jes

[69] Tang, C., Liu, Y., Xu, C., Zhu, J., Wei, X., Zhou, L., He, L., Yang, W., & Mai, L. (2018). Ultrafine Nickel-Nanoparticle-Enabled SiO2 Hierarchical Hollow Spheres for High-Performance Lithium Storage. *Advanced Functional Materials*, *28*(3), 1–8. https://doi.org/10.1002/adfm.201704561

[70] Zhu, G., Chao, D., Xu, W., Wu, M., & Zhang, H. (2021). Microscale Silicon-Based Anodes: Fundamental Understanding and Industrial Prospects for Practical High-Energy Lithium-Ion Batteries. *ACS Nano*, *15*(10), 15567–15593. https://doi.org/10.1021/acsnano.1c05898

[71] Wang, W., Favors, Z., Li, C., Liu, C., Ye, R., Fu, C., Bozhilov, K., Guo, J., Ozkan, M., & Ozkan, C. S. (2017). Silicon and Carbon Nanocomposite Spheres with Enhanced Electrochemical Performance for Full Cell Lithium Ion Batteries. *Scientific Reports*, *7*, 1–9. https://doi.org/10.1038/srep44838

[72] Jung, C. H., Choi, J., Kim, W. S., & Hong, S. H. (2018). A nanopore-embedded graphitic carbon shell on silicon anode for high performance lithium ion batteries. *Journal of Materials Chemistry A*, *6*(17), 8013–8020. https://doi.org/10.1039/c8ta01471j

[73] Mei, Y., He, Y., Zhu, H., Ma, Z., Pu, Y., Chen, Z., Li, P., He, L., Wang, W., & Tang, H. (2023). Recent Advances in the Structural Design of Silicon/Carbon Anodes for Lithium Ion Batteries: A Review. *Coatings*, *13*(2). https://doi.org/10.3390/coatings13020436

[74] Yang, Y., Yang, X., Chen, S., Zou, M., Li, Z., Cao, A., & Yuan, Q. (2017). Rational Design of Hierarchical Carbon/Mesoporous Silicon Composite Sponges as High-Performance Flexible Energy Storage Electrodes. *ACS Applied Materials and Interfaces*, *9*(27), 22819–22825. https://doi.org/10.1021/ACSAMI.7B05032/SUPPL_FILE/AM7B05032_SI_001.PDF

[75] Hu, Y., Yu, B., Qi, X., Shi, B., Fang, S., Yu, Z., & Yang, J. (2020). The preparation of graphite/silicon@carbon composites for lithium-ion batteries through molten salts electrolysis.

Journal of Materials Science, *55*(23), 10155–10167. https://doi.org/10.1007/s10853-020-04756-7

[76] Li, P., Kim, H., Myung, S. T., & Sun, Y. K. (2021). Diverting Exploration of Silicon Anode into Practical Way: A Review Focused on Silicon-Graphite Composite for Lithium Ion Batteries. *Energy Storage Materials*, *35*, 550–576. https://doi.org/10.1016/j.ensm.2020.11.028

[77] Zhao, L., Bennett, J. C., George, a., & Obrovac, M. N. (2019). SiC-Free Carbon-Silicon Alloys Prepared by Delithiation as Lithium-Ion Battery Negative Electrodes. *Chemistry of Materials*, *31*(11), 3883–3890. https://doi.org/10.1021/acs.chemmater.8b03898

[78] Parekh, M. H., Sediako, A. D., Naseri, A., Thomson, M. J., & Pol, V. G. (2020). In Situ Mechanistic Elucidation of Superior Si-C-Graphite Li-Ion Battery Anode Formation with Thermal Safety Aspects. *Advanced Energy Materials*, *10*(2), 1–12. https://doi.org/10.1002/aenm.201902799

[79] Zhou, R., Guo, H., Yang, Y., Wang, Z., Li, X., & Zhou, Y. (2016). N-doped carbon layer derived from polydopamine to improve the electrochemical performance of spray-dried Si/graphite composite anode material for lithium ion batteries. *Journal of Alloys and Compounds*, *689*, 130–137. https://doi.org/10.1016/j.jallcom.2016.07.315

[80] Guan, P., Li, J., Lu, T., Guan, T., Ma, Z., Peng, Z., Zhu, X., & Zhang, L. (2018). Facile and Scalable Approach to Fabricate Granadilla-like Porous-Structured Silicon-Based Anode for Lithium Ion Batteries. *ACS Applied Materials and Interfaces*, *10*(40), 34283–34290. https://doi.org/10.1021/acsami.8b12071

[81] Su, J., Zhang, C., Chen, X., Liu, S., Huang, T., & Yu, A. (2018). Carbon-shell-constrained silicon cluster derived from Al-Si alloy as long-cycling life lithium ion batteries anode. *Journal of Power Sources*, *381*, 66–71. https://doi.org/10.1016/j.jpowsour.2018.02.010

[82] Zhang, C., Cai, X., Chen, W., Yang, S., Xu, D., Fang, Y., & Yu, X. (2018). 3D Porous Silicon/N-Doped Carbon Composite Derived from Bamboo Charcoal as High-Performance Anode Material for Lithium-Ion Batteries. *ACS Sustainable Chemistry and Engineering*, *6*(8), 9930–9939. https://doi.org/10.1021/acssuschemeng.8b01189

[83] Ko, M., Chae, S., Ma, J., Kim, N., Lee, H. W., Cui, Y., & Cho, J. (2016). Scalable synthesis of silicon-nanolayer-embedded graphite for high-energy lithium-ion batteries. *Nature Energy*, *1*(9), 1–8. https://doi.org/10.1038/nenergy.2016.113

[84] Suresh, S., Wu, Z. P., Bartolucci, S. F., Basu, S., Mukherjee, R., Gupta, T., Hundekar, P., Shi, Y., Lu, T. M., & Koratkar, N. (2017). Protecting Silicon Film Anodes in Lithium-Ion Batteries Using an Atomically Thin Graphene Drape. *ACS Nano*, *11*(5), 5051–5061. https://doi.org/10.1021/acsnano.7b01780

[85] Shen, T., Xia, X. H., Xie, D., Yao, Z. J., Zhong, Y., Zhan, J. Y., Wang, D. H., Wu, J. B., Wang, X. L., & Tu, J. P. (2017). Encapsulating silicon nanoparticles into mesoporous carbon forming pomegranate-structured microspheres as a high-performance anode for lithium ion batteries. *Journal of Materials Chemistry A*, *5*(22), 11197–11203. https://doi.org/10.1039/c7ta03294c

[86] Wang, B., Yuan, F., Wang, J., Wang, Q., Li, Z., Zhao, W., Li, Y., Feng, J., & Li, W. (2020). Synthesis of pomegranate-structured Si/C microspheres using P123 as surfactant for high-energy lithium-ion batteries. *Journal of Electroanalytical Chemistry*, *864*, 114102. https://doi.org/10.1016/j.jelechem.2020.114102

[87] Nie, P., Liu, X., Fu, R., Wu, Y., Jiang, J., Dou, H., & Zhang, X. (2017). Mesoporous Silicon Anodes by Using Polybenzimidazole Derived Pyrrolic N-Enriched Carbon toward High-Energy Li-Ion Batteries. *ACS Energy Letters*, *2*(6), 1279–1287. https://doi.org/10.1021/acsenergylett.7b00286

[88] Harpak, N., Davidi, G., Melamed, Y., Cohen, A., & Patolsky, F. (2020). Self-Catalyzed Vertically Aligned Carbon Nanotube-Silicon Core-Shell Array for Highly Stable, High-Capacity Lithium-Ion Batteries. *Langmuir*, *36*(4), 889–896. https://doi.org/10.1021/acs.langmuir.9b03424

[89] Li, P., Hwang, J. Y., & Sun, Y. K. (2019). Nano/microstructured silicon-graphite composite anode for high-energy-density li-ion battery. *ACS Nano*, *13*(2), 2624–2633. https://doi.org/10.1021/acsnano.9b00169

[90] Nie, P., Le, Z., Chen, G., Liu, D., Liu, X., Wu, H. Bin, Xu, P., Li, X., Liu, F., Chang, L., Zhang, X., & Lu, Y. (2018). Graphene Caging Silicon Particles for High-Performance Lithium-Ion Batteries. *Small*, *14*(25), 1–8. https://doi.org/10.1002/smll.201800635

[91] Li, Y., Yan, K., Lee, H. W., Lu, Z., Liu, N., & Cui, Y. (2016). Growth of conformal graphene cages on micrometre-sized silicon particles as stable battery anodes. *Nature Energy*, *1*(2), 15029. https://doi.org/10.1038/nenergy.2015.29

[92] Nava, G., Schwan, J., Boebinger, M. G., McDowell, M. T., & Mangolini, L. (2019). Silicon-Core-Carbon-Shell Nanoparticles for Lithium-Ion Batteries: Rational Comparison between Amorphous and Graphitic Carbon Coatings. *Nano Letters*, *19*(10), 7236–7245. https://doi.org/10.1021/acs.nanolett.9b02835

[93] Liu, N., Lu, Z., Zhao, J., Mcdowell, M. T., Lee, H. W., Zhao, W., & Cui, Y. (2014). A pomegranate-inspired nanoscale design for large-volume-change lithium battery anodes. *Nature Nanotechnology*, *9*(3), 187–192. https://doi.org/10.1038/nnano.2014.6

[94] Mercedes-Benz Group Unternehmen News. (2022). *Mercedes-Benz und Sila erzielen Durchbruch bei Hochvoltbatterie mit Silizium-Hochleistungszellen*. https://group.mercedes-benz.com/unternehmen/news/mercedes-benz-und-sila.html (accessed: 03/25/2024)

[95] Mayr-Uhlmann, S. (2022). *Porsche AG beteiligt sich an innovativem Produzenten von Batteriematerial*. https://newsroom.porsche.com/de/2022/unternehmen/porsche-group14-technologies-produzent-batteriematerial-investition-28206.htm l(accessed: 03/25/2024)

[96] Poetke, S., Cangaz, S., Hippauf, F., Haufe, S., Dörfler, S., Althues, H., & Kaskel, S. (2023). Partially Lithiated Microscale Silicon Particles as Anode Material for High-Energy. *Energy Technology*, *11*, 2202330.

[97] Wang, C., Wu, H., Chen, Z., Mcdowell, M. T., Cui, Y., & Bao, Z. (2013). Self-healing chemistry enables the stable operation of silicon microparticle anodes for high-energy lithium-ion batteries. *Nature Chemistry*, *5*(12), 1042–1048. https://doi.org/10.1038/nchem.1802

[98] Artrith, N., Urban, A., & Ceder, G. (2018). Constructing first-principles phase diagrams of amorphous LixSi using machine-learning-assisted sampling with an evolutionary algorithm. *Journal of Chemical Physics*, *148*(24), 241711. https://doi.org/10.1063/1.5017661

[99] Choi, S., Kwon, T. W., Coskun, A., & Choi, J. W. (2017). Highly elastic binders integrating polyrotaxanes for silicon microparticle anodes in lithium ion batteries. *Science*, *357*(6348), 279–283. https://doi.org/10.1126/science.aal4373

[100] Cui, L. F., Ruffo, R., Chan, C. K., Peng, H., & Cui, Y. (2009). Crystalline-amorphous core-shell silicon nanowires for high capacity and high current battery electrodes. *Nano Letters*, *9*(1), 491–495. https://doi.org/10.1021/nl8036323

[101] Daniel, B., Irmgard, B., & Jantke, D. (2017). *Lithium ion batteries* (WO2019105544A1).

[102] Haufe, S. (2016). *Siliciumpartikel enthaltende Anodenmaterialien für Lithium-Ionen-Batterien* (EP 3 335 262 B1).

[103] Haufe, S., Bernhard, R., & Pfeiffer, J. (2021). Revealing the Failure Mechanism of Partially Lithiated Silicon-Dominant Anodes Based on Microscale Silicon Particles. *Journal of The Electrochemical Society*, *168*(8), 080531. https://doi.org/10.1149/1945-7111/ac1491

[104] Obrovac, M. N., & Krause, L. J. (2007). Reversible Cycling of Crystalline Silicon Powder. *Journal of The Electrochemical Society*, *154*(2), A103. https://doi.org/10.1149/1.2402112

[105] McDowell, M. T., Lee, S. W., Harris, J. T., Korgel, B. A., Wang, C., Nix, W. D., & Cui, Y. (2013). In situ TEM of two-phase lithiation of amorphous silicon nanospheres. *Nano Letters*, *13*(2), 758–764. https://doi.org/10.1021/nl3044508

[106] An, S. J., Li, J., Daniel, C., Mohanty, D., Nagpure, S., & Wood, D. L. (2016). The state of understanding of the lithium-ion-battery graphite solid electrolyte interphase (SEI) and its relationship to formation cycling. *Carbon*, *105*, 52–76. https://doi.org/10.1016/j.carbon.2016.04.008

[107] Peled, E. (1983). Film forming reaction at the lithium/electrolyte interface. *Journal of Power Sources*, *9*(3), 253–266. https://doi.org/10.1016/0378-7753(83)87026-8

[108] Peled, E., Golodnitsky, D., & Ardel, G. (1997). Advanced Model for Solid Electrolyte Interphase Electrodes in Liquid and Polymer Electrolytes. *Journal of The Electrochemical Society*, *144*(8), L208–L210. https://doi.org/10.1149/1.1837858

[109] Peled, E., & Menkin, S. (2017). Review—SEI: Past, Present and Future. *Journal of The Electrochemical Society*, *164*(7), A1703–A1719. https://doi.org/10.1149/2.1441707jes

[110] Wetjen, M., Trunk, M., Werner, L., Gernhäuser, R., Märkisch, B., Révay, Z., Gilles, R., & Gasteiger, H. A. (2018). Quantifying the Distribution of Electrolyte Decomposition Products in Silicon-Graphite Electrodes by Neutron Depth Profiling. *Journal of The Electrochemical Society*, *165*(10), A2340–A2348. https://doi.org/10.1149/2.1341810jes

[111] Eshetu, G. G., & Figgemeier, E. (2019). Confronting the Challenges of Next-Generation Silicon Anode-Based Lithium-Ion Batteries: Role of Designer Electrolyte Additives and Polymeric Binders. *ChemSusChem*, *12*(12), 2515–2539. https://doi.org/10.1002/cssc.201900209

[112] Peled, E. (1979). The Electrochemical Behavior of Alkali and Alkaline Earth Metals in Nonaqueous Battery Systems—The Solid Electrolyte Interphase Model. *Journal of The Electrochemical Society*, *126*(12), 2047–2051. https://doi.org/10.1149/1.2128859

[113] Wang, A., Kadam, S., Li, H., Shi, S., & Qi, Y. (2018). Review on modeling of the anode solid electrolyte interphase (SEI) for lithium-ion batteries. *Npj Computational Materials*, *4*(1), 15. https://doi.org/10.1038/s41524-018-0064-0

[114] Xu, K. (2014). Electrolytes and interphases in Li-ion batteries and beyond. *Chemical Reviews*, *114*(23), 11503–11618. https://doi.org/10.1021/cr500003w

[115] Lu, P., & Harris, S. J. (2011). Lithium transport within the solid electrolyte interphase. *Electrochemistry Communications*, *13*(10), 1035–1037. https://doi.org/10.1016/j.elecom.2011.06.026

[116] Pritzl, D., Solchenbach, S., Wetjen, M., & Gasteiger, H. A. (2017). Analysis of Vinylene Carbonate (VC) as Additive in Graphite/$LiNi_{0.5}Mn_{1.5}O_4$ Cells. *Journal of The Electrochemical Society*, *164*(12), A2625–A2635. https://doi.org/10.1149/2.1441712jes

[117] Hatchard, T. D., & Dahn, J. R. (2004). In Situ XRD and Electrochemical Study of the Reaction of Lithium with Amorphous Silicon. *Journal of The Electrochemical Society*, *151*(6), A838. https://doi.org/10.1149/1.1739217

[118] Sila Technology. (2024). *Titan Silicon: Next-Generation Battery Materials*. https://www.silanano.com/our-solutions/titan-silicon-anode (accessed: 06/02/2024)

[119] Group14.(2024). *The Transition to Lithium-Silicon Batteries*. https://www.group14.technology/resources/whitepapers/whitepaper-the-transition-to-lithium-silicon-batteries/ (accessed: 06/02/2024)

[120] Nexeon. (2024). *Transformative siliconbasierte Anode-Technologie*. https://www.nexeonglobal.com/technology (accessed: 06/02/2024)

[121] Amprius. (2024). *100% Silicon Nanowire Batteries from Amprius Technology*. https://amprius.com/technology/(accessed: 06/02/2024)

[122] LeydenJar. (2022). *Our Technology - Pure Silicon Anode*. https://leyden-jar.com/storage/uploads/2022/09/LJT-Technology-White-Paper-2022-1.pdf (accessed: 06/02/2024)

[123] Vandeputte, K. (2024). *AABC Presentation 2024, "Battery Technologies for Automotive Applications – BMW Group Status 2024*.

[124] *Mercedes Benz Strategy Update: electric drive*. (2021). https://group.mercedes-benz.com/company/strategy/mercedes-benz-strategy-update-electric-drive.htm (accessed: 06/02/2024)

[125] *Die Zukunft der Zelle: Leistungsfähige Batterien als zentrales Element von Elektrofahrzeugen*. (2023). https://newsroom.porsche.com/de/2023/innovation/porsche-engineering-die-zukunft-der-zelle-30801.html (accessed: 06/02/2024)

[126] Hettesheimer, T., Neef, C., Rosellón Inclán, I., Link, S., Schmaltz, T., Schuckert, F., Stephan, A., Stephan, M., Thielmann, A., Weymann, L., & Wicke, T. (2023). *Lithium-Ion Battery Roadmap – Industrialization Perspectives Toward 2030*. https://www.isi.fraunhofer.de/content/dam/isi/dokumente/cct/2023/Fraunhofer-ISI_LIB-Roadmap-2023.pdf (accessed: 06/02/2024)

[127] Fleischmann, J., Hanicke, M., Horetsky, E., Ibrahim, D., Jautelat, S., Linder, M., Schaufuss, P., Torscht, L., & van de Rijt, A. (2023). *Battery 2030: Resilient, sustainable, and circular*. https://www.mckinsey.com/industries/automotive-and-assembly/our-insights/battery-2030-resilient-sustainable-and-circular (accessed: 06/02/2024)

[128] Tsiouvaras, N., Meini, S., Buchberger, I., & Gasteiger, H. A. (2013). A Novel On-Line Mass Spectrometer Design for the Study of Multiple Charging Cycles of a Li-O_2 Battery. *Journal of The Electrochemical Society*, *160*(3), A471–A477. https://doi.org/10.1149/2.042303jes

[129] Metzger, M., Strehle, B., Solchenbach, S., & Gasteiger, H. A. (2016). Origin of H_2 Evolution in LIBs: H_2O Reduction vs. Electrolyte Oxidation. *Journal of The Electrochemical Society*, *163*(5), A798–A809. https://doi.org/10.1149/2.1151605jes

[130] Metzger, M., Marino, C., Sicklinger, J., Haering, D., & Gasteiger, H. A. (2015). Anodic Oxidation of Conductive Carbon and Ethylene Carbonate in High-Voltage Li-Ion Batteries Quantified by On-Line Electrochemical Mass Spectrometry. *Journal of the Electrochemical Society*, *162*(7), A1123–A1134. https://doi.org/10.1149/2.0951506jes

[131] Strehle, B. (2022). *Degradation Mechanisms of Layered Oxides Used as Cathode Active Materials in Lithium-Ion Batteries*. PhD Thesis, Technical University of Munich.

[132] Valencia, H., Rapp, P., Graf, M., Mayer, J., & Gasteiger, H. A. *Elucidating the Morphology of Partially Lithiated Microscale Silicon Particles using Transmission Electron Microscopy*. submitted

[133] Landesfeind, J., Hattendorff, J., Ehrl, A., Wall, W. A., & Gasteiger, H. A. (2016). Tortuosity Determination of Battery Electrodes and Separators by Impedance Spectroscopy. *Journal of The Electrochemical Society*, *163*(7), A1373–A1387. https://doi.org/10.1149/2.1141607jes

[134] Morasch, R., Keilhofer, J., Gasteiger, H. A., & Suthar, B. (2021). Methods—Understanding Porous Electrode Impedance and the Implications for the Impedance Analysis of Li-Ion Battery Electrodes. *Journal of The Electrochemical Society*, *168*(8), 080519. https://doi.org/10.1149/1945-7111/ac1892

[135] Clara, B. (2020). *Rate Performance and Kinetics of Silicon and Graphite Anodes for Lithium-Ion Batteries*. Master Thesis, Technical University of Munich.

[136] Graf, M., Reuter, L., Qian, S., Calmus, T., Ghamlouche, A., Maibach, J., Bernhard, R., & Gasteiger, H. A. (2021). Understanding the Effect of Lithium Nitrate As Additive in Carbonate Based Electrolytes for Silicon Anodes. *ECS Meeting Abstracts*, *MA2021-02*(3), 379–379. https://doi.org/10.1149/ma2021-023379mtgabs

[137] Jung, R., Metzger, M., Haering, D., Solchenbach, S., Marino, C., Tsiouvaras, N., Stinner, C., & Gasteiger, H. A. (2016). Consumption of Fluoroethylene Carbonate (FEC) on Si-C Composite Electrodes for Li-Ion Batteries. *Journal of The Electrochemical Society*, *163*(8), A1705–A1716. https://doi.org/10.1149/2.0951608jes

[138] Wang, D. Y., Sinha, N. N., Petibon, R., Burns, J. C., & Dahn, J. R. (2014). A systematic study of well-known electrolyte additives in $LiCoO_2$/graphite pouch cells. *Journal of Power Sources*, *251*, 311–318. https://doi.org/10.1016/j.jpowsour.2013.11.064

[139] Kim, K., Park, I., Ha, S. Y., Kim, Y., Woo, M. H., Jeong, M. H., Shin, W. C., Ue, M., Hong, S. Y., & Choi, N. S. (2017). Understanding the thermal instability of fluoroethylene carbonate in LiPF6-based electrolytes for lithium ion batteries. *Electrochimica Acta*, *225*, 358–368. https://doi.org/10.1016/j.electacta.2016.12.126

[140] Uddin, J., Bryantsev, V. S., Giordani, V., Walker, W., Chase, G. V, & Addison, D. (2013). Lithium Nitrate As Regenerable SEI Stabilizing Agent for Rechargeable Li/O_2 Batteries. *The Journal of Physical Chemistry Letters*, *4*(21), 3760–3765.

[141] Jozwiuk, A., Berkes, B. B., Weiß, T., Sommer, H., Janek, J., & Brezesinski, T. (2016). The critical role of lithium nitrate in the gas evolution of lithium-sulfur batteries. *Energy and Environmental Science*, *9*(8), 2603–2608. https://doi.org/10.1039/c6ee00789a

[142] Nguyen, C. C., & Lucht, B. L. (2018). Development of Electrolytes for Si-Graphite Composite Electrodes. *Journal of The Electrochemical Society*, *165*(10), A2154–A2161. https://doi.org/10.1149/2.0621810jes

[143] Wetjen, M. (2018). *Studies on the Differentiation and Quantification of Degradation Phenomena in Silicon-Graphite Anodes for Lithium-Ion Batteries*. PhD Thesis, Technical University Munich

[144] Berg, C., Morasch, R., Graf, M., & Gasteiger, H. A. (2023). Comparison of Silicon and Graphite Anodes: Temperature-Dependence of Impedance Characteristics and Rate Performance. *Journal of The Electrochemical Society*, *170*(3), 030534. https://doi.org/10.1149/1945-7111/acc09d

List of Figures

Acknowledgements

First and foremost, I would like to express my deepest gratitude to **Prof. Hubert A. Gasteiger** for the exceptional opportunity to work and learn within your group. Your unwavering passion for science, especially electrochemistry, is truly inspiring. I am immensely thankful for your outstanding guidance and invaluable support throughout these years. Your ability to share your vast knowledge, combined with your talent for fostering critical thinking, encourages us not to choose the easy path but to think creatively—all while maintaining a sense of fun and excitement in the work.

The atmosphere of mutual trust and the freedom you provide for developing our own ideas are remarkable. You have cultivated a group dynamic where scientific exploration thrives, and I am particularly grateful for the way you are always on hand with advice and technical insight when needed. My PhD journey under your supervision has been a joyful and enriching experience, both scientifically and personally. For that, I will always be deeply grateful. It was an intense but exciting journey—one I would gladly undertake again!

I would also like to extend my heartfelt thanks to **Veronika Pritzl**, whose endless patience and exceptional organizational skills keep the entire group running smoothly. Your support in navigating the complexities of administrative and organizational tasks allowed us to focus entirely on our research. Beyond your professional contributions, I genuinely enjoyed our lively, non-scientific discussions. Your good mood and sense of humor have been a constant source of positivity in our group. Thank you for everything!

In addition, I owe the success of my PhD to the many people who contributed along the way—without you, this work would not have been possible and definitely with less fun.

First I want to thank my supervisors of my Bachelor's thesis **Johannes Landesfeind** and Master's thesis **Daniel Pritzl** for introducing me to the field of lithium-ion batteries. I couldn’t have asked for better mentors—thank you both for sharing your knowledge and approach to science with me.

I also want to thank Wacker Chemie AG for their financial support and making this project possible. I want to express my special gratitude to **Rebecca Bernhard**, **Stefan Haufe** and **Jürgen Pfeiffer** for the great work we accomplished together. Your dedication, collaboration, and commitment made this project not only successful but also a truly enjoyable experience.

A big thank you to all my former students **Clara Berg, Jonas Dickmanns, Tom Calmus** and **Louis Hartmann** your contributions are invaluable for this thesis.

A huge shoutout and thank you to all my current and former colleagues at TEC for creating such a fun and inspiring atmosphere at the chair. You all made work feel a lot less like work! Special thanks go to **Lennart Reuter**, **Christian Sedlmeier**, **Timon Lazaridis**, **Carla Harzer**, **Franziska Hnyk**, **Tanja Zünd**, **Stefan Oswald, Ceren Tok, Mohammad Fathi Tovini** and **Ana Marija Damjanovic** for keeping the good vibes going, both in and out of the office. Whether we were having fun on the squash court, going cycling, climbing, or hitting the slopes on a ski tour, it was always an absolute blast.

I want to express my deepest gratitude to my parents **Kathy** and **Andreas** and my sister **Hannah** for their support throughout my studies and beyond. Your backing has been a tremendous source of strength and motivation to me. Thank you!

Lastly, I want to thank **Lilly** for your unwavering support, for being the way you are and for being part of my life.

Scientific Contributions

Peer-reviewed Publications

1. **M. Graf**, C. Berg, R. Bernhard, S. Haufe, J. Pfeiffer, H. A. Gasteiger, "Effect and Progress of the Amorphization Process for Microscale Silicon Particles Under Partial Lithiation As Active Material in Lithium-Ion Batteries", *J. Electrochemical Society.* **169,** 020536 (2022) DOI: 10.1149/1945-7111/ac4b80
2. **M. Graf**, L. Reuter, S. Qian, T. Calmus, R. Bernhard, S. Haufe, H. A. Gasteiger, "Understanding the Effect of Lithium Nitrate As Additive in Carbonate Electrolytes for Silicon Anodes" *J. Electrochemical Society,* **171** *,* 090514 (2024) DOI: 10.1149/1945-7111/ad71f7
3. H. Valencia, P. Rapp, **M. Graf**, J. Mayer, H. A. Gasteiger*, "*Elucidating the Morphology of Partially Lithiated Silicon Microparticles using Transmission Electron Microscopy*", in submission*
4. C. Berg, R. Morasch, **M. Graf**, H. A. Gasteiger, "Comparison of Silicon and Graphite Anodes on their Temperature-Dependent Impedance and Rate Performance", *J. Electrochemical Society.* **170,** 030534 (2023) DOI: 10.1149/1945-7111/acc09d
5. J. Landesfeind, T. Hosaka, **M. Graf,** K. Kubota, S. Komaba, H. A. Gasteiger, "Comparison of Ionic Transport Properties of Non-Aqueous Lithium and Sodium Hexafluorophosphate Electrolytes", *J. Electrochemical Society* **168** , 040538 (2021), DOI: 10.1149/1945-7111/abf8d9
6. J. Landesfeind, A. Ehrl, **M. Graf**, W. A. Wall, H. A. Gasteiger , "Direct Electrochemical Determination of Thermodynamic Factors in Aprotic Binary Electrolytes", *J. Electrochemical Society* **163** (7), A1254-A1264 (2016), DOI: 10.1149/2.0651607jes.

Oral Presentations

1. **M. Graf**, L. Reuter, S. Qian, T. Calmus, A. Ghamlouche, J. Maibach, R. Bernhard, H. A. Gasteiger, “Understanding the Effect of Lithium Nitrate As Additive in Carbonate Electrolytes for Silicon Anodes, Meeting Abstracts MA2021-02 379
2. **M. Graf**, C. Berg, R. Bernhard, S. Haufe, J. Pfeiffer, H. A. Gasteiger, “Effect and Progress of the Amorphization Process for Microscale Silicon Particles Under Partial Lithiation As Active Material in Lithium-Ion Batteries“, Meeting Abstracts, MA2020-02, 357.
3. L. Hartmann, S. Oswald, **M. Graf**, D. Pritzl, H. A. Gasteiger, “Washing of Ni-Rich Cathode Active Materials for Lithium-Ion-Batteries: Mechanistic Understanding“, Meeting Abstracts, MA2020-01, 214.
4. J. Landesfeind, **M. Graf**, H. A. Gasteiger, “Transport Limitations in Binary Electrolytes: The Temperature Dependence of the Electrolyte Transport Parameters“, Meeting Abstracts, MA2017-01, 2006.
5. J. Landesfeind, **M. Graf**, M. Dahbi, K. Kubota, S. Komaba, H. A. Gasteiger, “Transport Limitations in Binary Electrolytes: EC-Free Solvents and NaPF6 vs. LiPF6 Salts“, Meeting Abstracts,MA2017-01,211